Title

Design of an Esophageal Deflection and Thermal Monitoring Device for use during Cardiac Ablation Procedures

Author

Morris, Karcher

Publication Date

2021

Peer reviewed|Thesis/dissertation

UNIVERSITY OF CALIFORNIA SAN DIEGO

Design of an Esophageal Deflection and Thermal Monitoring Device for use during Cardiac Ablation Procedures

Doctor of Philosophy

in

Engineering Sciences (Mechanical Engineering)

by

Karcher Morris

Committee in charge:

Professor Frank E. Talke, Chair
Professor David A. Gough
Professor Vlado A. Lubarda
Professor Thomas J. Savides
Professor Michael T. Tolley

2021

The dissertation of Karcher Morris is approved, and it is acceptable in quality and form for publication on microfilm and electronically:

University of California San Diego

2021

DEDICATION

To all healthcare workers

TABLE OF CONTENTS

LIST OF FIGURES

LIST OF TABLES

ACKNOWLEDGMENTS

I am very grateful for all of the support I have received during my time as a Ph.D. candidate. This dissertation would not have been possible as an individual. Thank you to all of those who have helped me.

First, I would like to thank my advisor and mentor Professor Frank Talke. I will always remember the day I knocked on his office door to see whether or not I could be involved in research to finish my undergraduate career. He was so welcoming on day one, and so supportive every day after, that I found myself in an ideal situation to grow and develop as an engineer and a leader. At the time, I did not realize what the road ahead entailed, but I knew I would have a very caring and supportive team around me, including him and the other students in his lab. I am grateful for every single opportunity Professor Talke worked to provide me and for his constant dedication to his students so that we all can succeed.

As I am able to complete my Ph.D. work, I am very grateful to my thesis committee. Dr. Savides, Prof. Michael Tolley, Prof. Vlado Lubarda and Prof. David Gough. With their guidance, I learned a great deal, from gastroenterology, to design, to mechanics, and to medical devices. I am fortunate to have such accomplished and knowledgeable professors on my committee.

I also must thank the medical community here at UC San Diego. Most especially Drs. Thomas Savides and Gregory Feld. They are the reason that I am working in the field of medical devices and, specifically, have been able to work on such a fascinating and meaningful medical device project, the Esophageal Deflection Device. I am grateful for their wealth of knowledge, ideas, and, more importantly, their willingness to share them with me and help make the design process a truly meaningful one.

The medical community that has supported me is very large. So many medical doctors, nurses, and bioengineers that I could not name them all. Each conversation has meant a great deal to me. I thank them for their support, and for the work they do every day. Some of the medical doctors and bioengineers I have been able to work with more recently include: Dr. Shanglei Liu, Dr. Jenny Lam, Dr. Jyoti Mayadev, Dr. Milan Makale, Prof. David Gough, Dr. Jaime Chen, Dr. Travis Desa, Dr. Madhu Alagiri, and Dr. Farshad Ahadian. I appreciate all of their time and energy that they shared with me.

I have had many stellar lab mates over the years who have helped me become who I am today. Initially, Dr. Liane Matthes, Dr. Youyi Fu, Benjamin Suen, Dr. Young Seo and Dr. Tan Trinh helped me as I entered the lab and explored the world of hard disk drive technology. Dr. Alex Phan and Phuong Truong joined the lab and were trailblazers for medical device research, setting the bar very high on the way. Anay Pandit began exploring 3D printed endoscopes for his master's work with Dr. Savides, and as one thing led to another, Scott Garner, Weilun Hseih, Oren Gotlib and Matthew Kohanfars all earned their masters while working on medical technology in the Talke Lab. Lars Ringel was a visiting scholar who could design, model, simulate, and build any medical device. We had many excellent undergraduate students as well including Camille Lee, Minghui (Scott) Zhao, Tanvir Reza, Dora Trieu, Simonas Vaitkus, Rafaela Simoes-Torigoe, and Yu (Brian) Li. Meeran Fehmi, who was a high school student when he worked in our lab, also contributed to our research effort. More recent students include Po-han (Jackie) Chen, Shengfan Hu, Avinash Laha, and Luke Lindgren who are keeping the energy up even during COVID times. I have been fortunate to work with all of them, making research a team activity. It was all of these students who made the lab culture something we could be proud of and enjoy.

During my research, three individuals had an especially significant influence on my learning and the papers I was able to work on and write. Prof. Andreas Rosenkranz is a materials and design expert who spent night after night helping me understand how to characterize 3D printed material. Dr. Fred Spada was always at CMRR between the times of 10pm and 2am and every single thing he shared was so valuable from hard disk drive experimentation techniques to antimicrobial thin film ideas for catheters. Prof. Vlado Lubarda, was my instructor for C programming, then I was able to TA for him for C and MATLAB programming courses for countless quarters, and a couple of years ago I found myself spending many afternoons with him as he shared with me everything I wanted to know about solid mechanics and its relation to the Esophageal Deflection Device. I am so fortunate to have had these three help me throughout my Ph.D. years.

Jesse Dewald built the EnVision MakerStudio, both the place and the community, where I spent countless days teaching and building projects with students. He also helped me with many of my ups and downs when it came to both research and teaching. Ben Shih, Dylan Drotman, and Paul Glick always invited me to their fun lab activities and also let me ask them a million research related questions during those times. Steve Porter and Jessica Tuazon shared the nicest undergraduate lab equipment I know of. This, paired with Steve and Jessica's immense engineering knowledge and their passion for teaching it, made materials testing a much more enjoyable activity.

Thank you to all those at the Center for Memory and Recording Research. This was a fascinating place to work at every day and I would like to especially thank Iris Villanueva, Marina Robenko, Octavio Ochoa, Prof. Eric Fullerton, Prof. Paul Siegel, Prof. Oscar Vazquez Mena, and Prof. Ping Liu.

The Electrical and Computer Engineering Department provided me with my second home thanks to Stefanie Battaglia, Beatriz Valenzuela-Guzman, Prof. Truong Nguyen, Prof. Drew Hall, Prof. Vikash Gilja, Dr. John Eldon, Prof. Curt Schurgers, Prof. Sahar Baghdachi, and Prof. Paul Siegel. I have also had the pleasure to work alongside some amazing TAs and Tutors including: Scott Zhao, Raul Pegan, Ella Kan, Joshua Jain, Kien Nguyen, Camille Lee, Brittany Nguyen, Tina Kafel, Eugene Arabadzhi, Katie Hsieh, Farnia Nafarifard, Tanvir Reza, Brea Torquato, Payal Singh, Victor Miranda, Sarp User, Willy Ma, Zhaowei Yu, Quoc-Zuy Do, Sarah Kinney, Brooke Dybicz, Ilya Petrov, Vince Chen, Hector Murguia-gastelum and Keshav Rungta. They turned my teaching hobby into a career path.

Thank you to the School of Global Policy and Strategy for their support as I had the opportunity to work with Liz Lyons and Roger Bohn to explore policy, regulation and innovation related to 3D printing of medical Devices. Thank you also to the Institute for the Global Entrepreneur and the Rady School of Management for their support as we aimed to commercialize our efforts, most especially Prof. Vish Krishnan, Dennis Abremski, Dr. Michael Krupp, and Marie Christensen.

These were not the only ones who have supported me during this time. There are many important people to me that I have not mentioned here. Thank you so much for all of your support.

Chapter 2, in part, is a reprint of the materials as they appear in “Esophageal Deflection Device”, Karcher Morris, Scott Garner, Youyi Fu, Anay Pandit, Young Seo, Gregory Feld, Thomas Savides, Frank E. Talke, Ser. 62/468,697, 8 March 2018 (Published Patent (Pending) – US20200029822A1). The dissertation author was the primary investigator and author of this patent publication.

Chapter 3, in part, is a reprint of the materials as they appear in "Uniaxial and biaxial testing of 3D printed hyperelastic photopolymers." Morris, K., Rosenkranz, A., Seibert, H., Ringel, L., Diebels, S., Talke, F. E. (2020), Journal of Applied Polymer Science, 137, 48400. The dissertation author was the primary investigator and author of this patent publication.

Chapter 4, in part, is a reprint of the materials as they appear in "Design of an esophageal deflection device for use during atrial ablation procedures." Morris, K., Lubarda, V.A., Talke, F.E. Journal of Materials Research and Technology, 9(6) pp. 13801-12, 2020. The dissertation author was the primary investigator and author of this patent publication.

Chapter 5 and 6, in part are a reprint of the materials as they appear in "Experimental and Numerical Investigation of Heat Transfer through Porcine Heart and Esophageal Tissue" Morris, K., Hu, S., Kohanfars, M., and Talke, F.E., Proceedings for ASME 2021 Conference on Information Storage and Processing Systems. Online Virtual. June 2–3, 2021.

VITA

12/2010-03/2012	Research Equipment Assistant, Scripps Institution of Oceanography, Marine Physical Laboratory, La Jolla, CA, USA
03/2010-03/2012	Undergraduate Student Researcher, Center for Memory and Recording Research, Talke Lab, La Jolla, CA, USA
06/2013	Bachelor of Science in Aerospace Engineering and Bachelor of Science in Management Science (Economics), University of California San Diego, La Jolla, CA, USA
06/2013-09/2013	Full-time summer intern, Western Digital Corporation, San Jose, CA, USA
09/2013-09/2020	Research and Teaching Assistant, Center for Memory and Recording Research Talke Lab, Jacobs School of Engineering, University of California San Diego, La Jolla, CA, USA
06/2014-09/2014	Full-time summer intern, Northrop Grumman Corporation, Woodland Hills, CA, USA
09/2015	Master of Science in Engineering Sciences (Mechanical Engineering), University of California San Diego, La Jolla, CA, USA
06/2019-09/2019	Full-time summer associate, RAND Corporation, Santa Monica, CA, USA
11/2020-Present	Assistant Teaching Professor, Department of Electrical and Computer Engineering, Jacobs School of Engineering, University of California San Diego, La Jolla, CA, USA
06/2021	Doctor of Philosophy in Engineering Sciences (Mechanical Engineering), University of California San Diego, La Jolla, CA, USA

PUBLICATIONS

Journal Papers

"Design and optimization of collocated dual stage suspensions." Wang, Y., Li, L., Morris, K., Hogan, J., Talke, F.E. Microsyst Technol 21, 2657–2662 (2015). https://doi.org/10.1007/s00542-015-2519-2

"Simulation of Lift Tab/Ramp Contact During Load/Unload." Y. Fu, K. Morris and F. E. Talke, in IEEE Transactions on Magnetics, vol. 53, no. 4, pp. 1-5, April 2017, Art no. 3301705. https://doi.org/10.1109/TMAG.2016.2634549

"Uniaxial and biaxial testing of 3D printed hyperelastic photopolymers." Morris, K., Rosenkranz, A., Seibert, H., Ringel, L., Diebels, S., Talke, F. E. (2020), Journal of Applied Polymer Science, 137, 48400. https://doi.org/10.1002/app.48400

"Design of an esophageal deflection device for use during atrial ablation procedures." Morris, K., Lubarda, V.A., Talke, F.E. Journal of Materials Research and Technology, 9(6) pp. 13801-12, 2020. https://doi.org/10.1016/j.jmrt.2020.09.123

"Investigation of an improved electricidal coating for inhibiting biofilm formation on urinary catheters." Gotlib, O., Vaitkus, S., Simoes-Torigoe, R., Morris, K., Bodnar, A., Spada, F.E., Alagiri, M., Talke, F.E. Journal of Materials Research and Technology, V10,pp. 339-48 (2021). https://doi.org/10.1016/j.jmrt.2020.11.089

"A comparative study of experimental urinary catheters containing silver and zinc for biofilm inhibition." Vaitkus, S., Simoes-Torigoe, R., Wong, N., Morris, K., Spada, F.E., Alagiri, M., Talke, F.E. Journal of Biomaterials Applications. January 2021. https://doi.org/10.1177/0885328221989553

Conference Papers

"Design of a Collocated Dual Stage Suspension in a Hard Disk Drive." Li, L, Morris, K, Hogan, J, & Talke, FE. Proceedings of the ASME 2014 Conference on Information Storage and Processing Systems. Santa Clara, California, USA. June 23–24, 2014. V001T01A025. ASME. https://doi.org/10.1115/ISPS2014-6991

"Effect of Slider Bias Voltage and Humidity on Wear and Contact Potential." Morris, K, Matthes, L, Spada, FE, Ovcharenko, A, Knigge, BE, & Talke, FE. Proceedings of the ASME 2016 Conference on Information Storage and Processing Systems. Santa Clara, California, USA. June 20–21, 2016. V001T01A018. ASME. https://doi.org/10.1115/ISPS2016-9620

"Molecular Dynamics Study of Lubricant Evaporation and Fragmentation in Heat-Assisted Magnetic Recording With Pulsed Laser Heating." Seo, YW, Rosenkranz, A, Morris, K, & Talke, FE. Proceedings of the ASME 2017 Conference on Information Storage and Processing Systems, San Francisco, California, USA. August 29–30, 2017. V001T01A017. ASME. https://doi.org/10.1115/ISPS2017-5473

"Development of a New Endoscope Distal Attachment Cap for Converting a Front Viewing Scope into a Side Viewing Scope", Lars Ringel, Karcher Morris, Thomas Savides, Frank E. Talke, Gastrointestinal Endoscopy June 18 2018 V. 87, Is. 6 pp AB246-AB247

"Development of a Luminal Esophageal Temperature Monitoring Device for Use During Treatment for Atrial Fibrillation." Garner, S, Morris, K, Pegan, R, Savides, T, & Talke, FE. Proceedings of the ASME-JSME 2018 Joint International Conference on Information Storage and Processing Systems and Micromechatronics for Information and Precision Equipment. San Francisco, California, USA. August 29–30, 2018. V001T05A005. ASME. https://doi.org/10.1115/ISPS-MIPE2018-8578

"A Wearable Neck Measurement Device and Monitoring System to Improve Ergonomic Performance of Surgeons." Morris, K, Zhao, M, Lam, J, Jacobsen, G, Horgan, S, & Talke, FE. Proceedings of the ASME 2019 28th Conference on Information Storage and Processing Systems. San Diego, California, USA. June 27–28, 2019. V001T09A002. ASME. https://doi.org/10.1115/ISPS2019-7513

"Investigation of Zinc-Silver Oxide-Thermoplastic Composite for Application in a Biofilm Retardant Urinary Catheter." Gotlib, O, Morris, K, Spada, FE, Alagiri, M, Patras, K, & Talke, FE. Proceedings of the ASME 2019 28th Conference on Information Storage and Processing Systems. San Diego, California, USA. June 27–28, 2019. V001T07A004. ASME. https://doi.org/10.1115/ISPS2019-7517

"Investigation of Biofilm-Inhibiting Zinc-Silver Oxide Urinary Catheter Coatings." Vaitkus, S, Simoes-Torigoe, R, Gotlib, O, Morris, K, Spada, FE, Alagiri, M, & Talke, FE. Proceedings of the ASME 2020 29th Conference on Information Storage and Processing Systems. Virtual, Online. June 24–25, 2020. V001T06A007. ASME. https://doi.org/10.1115/ISPS2020-1963

Patents (Pending)

"Esophageal Deflection Device", Karcher Morris, Scott Garner, Youyi Fu, Anay Pandit, Young Seo, Gregory Feld, Thomas Savides, Frank E. Talke, Ser. 62/468,697, 8 March 2018 (Published Patent (Pending) – US20200029822A1)

"Detachable Control Handle Scope with Distal Sensors Disposed On Elongate Insertion Tube", Matthew Kohanfars, Yu Li, Karcher Morris, Farshad Ahadian, Frank E. Talke, Ser. 62/949,876, 17 December 2019

"Antimicrobial Coating", Oren Gotlib, Frederick Spada, Karcher Morris, Rafaela Simoes-Torigoe, Simonas Vaitkus, Adriane Minori, Michael Tolley, Madhu Alagiri, Frank E. Talke, Ser. 62/968,096, 20 January 2020

ABSTRACT OF THE DISSERTATION

Design of an Esophageal Deflection and Thermal Monitoring Device for use during Cardiac Ablation Procedures

by

Karcher Morris

Doctor of Philosophy in Engineering Sciences (Mechanical Engineering)

University of California San Diego, 2021

Professor Frank E. Talke, Chair

Cardiac ablation is a common procedure performed by cardiac electrophysiologists. The clinician will use a device, such as a radiofrequency ablation catheter, to thermally ablate or burn off defective heart tissue (myocardium). During the procedure, the esophagus can be in close proximity to the heart tissue. As heat transfers through the myocardium, it can also transfer to the esophagus, potentially damaging the esophagus tissue. The damage results in thermal lesions and,

in worst-case scenarios, atrioesophageal fistulae. The work reported in this thesis was performed to devise a tool and method to protect the esophagus during the ablation procedure.

The Esophageal Deflection Device (EDD) was designed and manufactured to move the esophagus away from the ablation location. The device comprises of a straight rod and a precurved overtube. If the rod is inserted into the overtube, the overtube is straightened out by the rod. If the assembled device is inserted into the esophagus, and the rod is retracted, the elastic memory effect will cause the tube to reassume its original curved shape, thereby moving the esophagus safely away from its close position to the heart.

In this dissertation, the medical problem along with the design tools needed to address the above problem of moving the esophagus are investigated. The materials used for the Esophageal Deflection Device are reviewed, and the testing of 3D printed hyperelastic photopolymers used during preliminary designs is performed. Theoretical, experimental, and numerical methods were used to characterize the bending behavior of the Esophageal Deflection Device, and the Mooney-Rivlin materials properties for the hyperelastic tube material are determined. Thereafter, a temperature sensing Esophageal Deflection Device is described and tested. The temperature distribution during ablation is simulated using finite element analysis. Experimental and numerical results are discussed and compared. Finally, a summary and future direction of this work and our research is provided.

Chapter 1 Introduction to Medical Device Design and the Problem of Esophageal Thermal Damage

In order to develop medical devices to solve current medical challenges, we need to review design tools, manufacturing methods, and theoretical concepts pertaining to medical devices. As defined by United States Food and Drug Administration (FDA) [1] in Section 201(h) of the Food, Drug, and Cosmetic Act, a medical device is

> *"an instrument, apparatus, implement, machine, contrivance, implant, in vitro reagent, or other similar or related article, including a component part, or accessory which is:*
>
> 1. *recognized in the official National Formulary, or the United States Pharmacopoeia, or any supplement to them,*
> 2. *intended for use in the diagnosis of disease or other conditions, or in the cure, mitigation, treatment, or prevention of disease, in man or other animals, or*
> 3. *intended to affect the structure or any function of the body of man or other animals, and which does not achieve its primary intended purposes through chemical action within or on the body of man or other animals and*
>
> *which does not achieve its primary intended purposes through chemical action within or on the body of man or other animals and which is not dependent upon being metabolized for the achievement of its primary intended purposes..."*

A detailed method must be followed to first identify a medical challenge, and then to design, manufacture and implement a medical device solution. In this chapter, a current medical problem is discussed, esophageal thermal damage during cardiac ablation procedures. Special attention is then given to the medical device design process which emphasizes the use of prototyping and development techniques needed to resolve such an important issue in the field of cardiac electrophysiology.

1.1 Esophageal Thermal Damage During Cardiac Ablation Procedures

Atrial fibrillation (AF) is a very common heart arrhythmia that impacts tens of millions of people worldwide [2]. Antiarrhythmic medication is most commonly used to mitigate symptoms. However, the medication is not nearly as effective as one would hope and can have additional problematic side effects [3]. Pulmonary vein isolation with catheter ablation is an increasingly practiced option that is usually encouraged for symptomatic patients and has a strong success rate [3, 4].

During the cardiac ablation procedure, an electrophysiologist will use a radiofrequency (RF) ablation catheter or cryoablation catheter to purposefully inflict thermal damage on the defective heart tissue [5]. This can eliminate the arrhythmia and cause a “re-wiring” by altering the tissue mechanisms that propagate the heart’s electrical signals.

A major problem arises when the esophagus is in close proximity to the left atrial tissue. The left atrial tissue is nominally about 2mm thick. When the RF heat source is ablating (or burning) the heart tissue, the esophageal tissue can be unintentionally damaged [6, 7]. Thermal lesions may develop causing pain for the patient and potential infection. A rare, most acute complication with

a very high mortality rate can occur, called atrioesophageal fistula [8]. Figure 1 shows a schematic of an atrioesophageal fistula occurring, which is a hole between the esophagus and the left atrium of the heart [9]. In order to reduce the occurrence of complications related to cardiac ablation, it is necessary to monitor the heat transferring from the heart to the esophagus and move the esophagus away from the ablation site when there is risk of thermal damage.

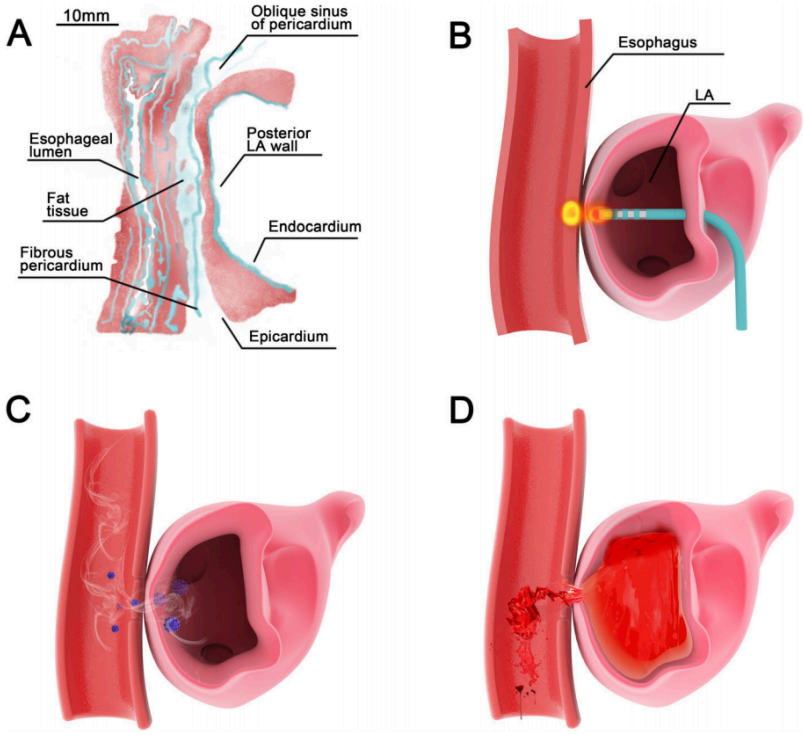

Figure 1: A diagram illustrating a) the types of tissue at the heart-esophagus interface, b) a radiofrequency ablation catheter heating the heart and esophagus tissue, c) atrioesophageal fistula with food from the esophagus entering the heart, and d) atrioesophageal fistula with blood entering the esophagus. [9]

Cardiac electrophysiologists currently use temperature probes, such as the Circa S-Cath™, to monitor esophageal temperature throughout an ablation procedure [10]. If an increase in temperature is indicated, the clinician will stop the ablation procedure and attempt to deviate the

esophagus. Current devices used to perform such an esophageal deviation include endoscopes operated by a gastroenterologist, repurposed endotracheal stylets, or pre-shaped nitinol embedded rods [11-13]. These approaches are not optimal due to cost, time constraints, accessibility, or increased risk to the patient. It is the purpose of this thesis to develop an improved solution to prevent the potentially fatal medical problem of atrioesophageal fistula.

1.2 Brief History of Relevant Medical Devices for Cardiac Electrophysiology and Gastroenterology

Medical devices have been an important part of human history, as many tools have been developed or repurposed to diagnose or treat a person in medical need. An example of a simple, early medical device would be woven materials used to cover a wound. Still to this day, bandages (and a wide variety of them) are useful medical devices from the more simplistic Band-Aid™ adhesive bandage to the more complex Procellera™ wound dressing that incorporates silver and zinc battery technology to reduce infection [14-16]. Medical device technology has rapidly developed over time, and a number of key technologies in the fields of gastroenterology and cardiac electrophysiology are worth reviewing.

Atrial ablation procedures are now very common and a number of medical technologies were needed to enable the current approach to understanding and curing arrythmias. Some important technologies include flexible catheters (Cornelius Solingen, Benjamin Franklin) [17], X-rays (Wilhelm Conrad Röntgen) [18], electrocardiograms (Willem Einthoven) [19], pacemakers (Albert S. Hyman & Seymour Furman) [20], etc. Photographs from [17-20] are shown in Figure 2. In particular, Figure 2a shows a flexible catheter used by Dutch Surgeon Cornelius Solingen in

the 17th century [17]. Figure 2b shows a pacemaker designed by Albert Hyman [20]. Figure 2c shows an X-ray of the human hand made by Wilhelm Röntgen [18]. Figure 2d shows electrocardiograms using electrometer and galvanometer readings from Willem Einthoven [19].

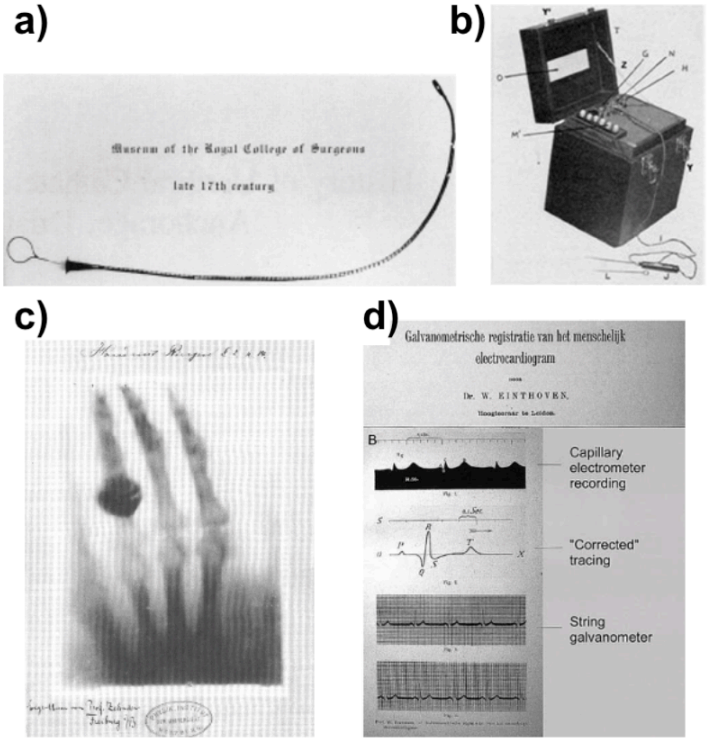

Figure 2: Photographs from historical references showing a) flexible catheters [17], b) pacemakers [20], c) an x-ray of a human hand [18] and d) electrocardiograms [19].

In the 1980s, Dr. Melvin Scheinman used catheters to apply high energy direct current (DC) shocks, or ablation, to accessory pathways of the heart. Mueller and Sanborn [21] reviewed the history of interventional cardiology covering several of the most important technological milestones. As a safer alternative to DC ablation, alternating current (AC) was implemented using high frequencies, or radiofrequencies (RF) between 300 and 750 kHz [22]. Driving current through human tissue at these frequencies produces resistive heating, increasing temperature above 50ºC and causing irreversible damage of the tissue. This radiofrequency ablation technology is

commonly used today across a wide variety of medical fields. Examples of current cardiac RF ablation catheter technology are illustrated in Figure 3. Figure 3 shows radiofrequency ablation catheters where multiple electrodes are depicted in different arrangements [23-26]. Irrigation ports, contact force sensors, and location or mapping sensors are also shown on these catheters.

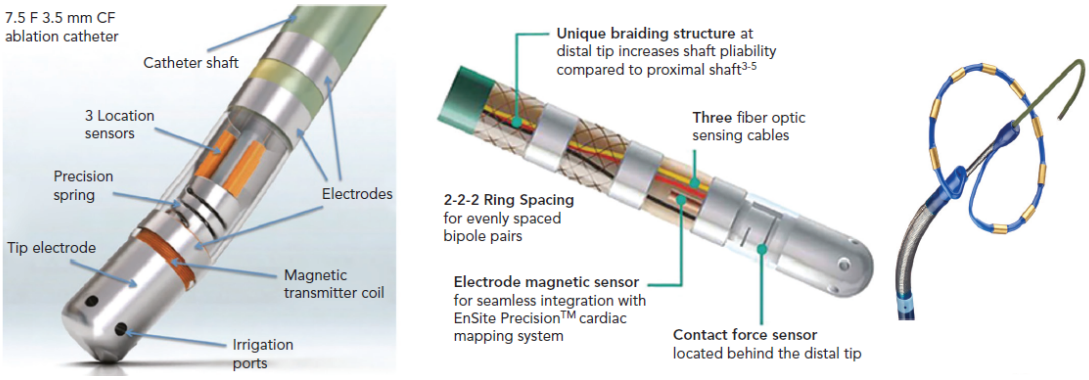

Figure 3: Radiofrequency ablation devices with contact force detection and multi-electrode ablation catheters [23-26].

There have recently been advanced developments in RF catheter technology (as well as cryoablation) and techniques which allow for heating (or freezing) to damage the heart tissue. There have also been advances in mapping techniques using low impedance electrodes and ultrasonic sensors that have improved efficacy of the minimally invasive surgical procedure. Recent catheter ablation and mapping technology is reviewed in [27] and [28]. In both reviews [27,28], the concern for esophageal thermal damage is also discussed.

Thermal damage from RF ablation or cryoablation has been observed on the esophagus by using an endoscope after the cardiac ablation procedures [29, 30]. Endoscopy is an important technology that has developed over the years to assist with esophageal visual monitoring and even esophageal protection. Endoscopy was first introduced by Phillip Bozzini [32], a medical doctor, who designed and developed the first endoscope. At the time of Bozzini's first endoscope, called

the “Lichtleiter”, there was a significant amount of “pushback” for such a novel tool. The device was being derogatorily called a “new toy” [32]. Now, endoscopes are being used for a variety of medical examinations including identification of inflammation, ulcers and tumors. Endoscopes can be especially useful for minimally invasive surgeries, avoiding often more risky open surgeries. [33]

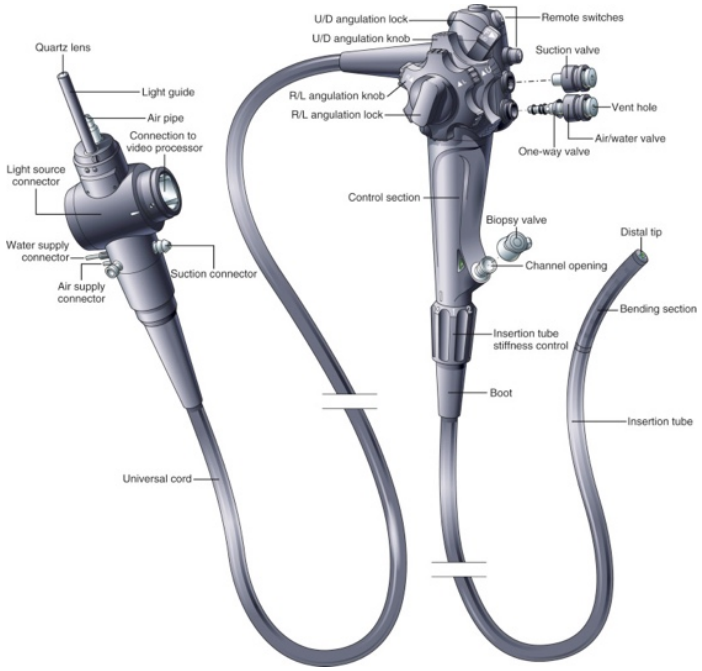

Figure 4: Schematic of an endoscope commonly used in gastroenterology [34].

A schematic of a current and commonly used endoscope is shown in Figure 4 [34]. Endoscopes like this one are entered into the esophagus through the mouth and pharynx. Using endoscopes, thermal lesions have been witnessed on the inner esophageal wall caused by cardiac ablation [29]. A photograph taken from an endoscope is shown in Figure 5 revealing thermal lesions on the inner wall of the esophagus [29]. Clinical studies have also shown that an endoscope

can be an effective tool to protect the esophagus during the ablation procedure by articulating the distal end of the endoscope resulting in movement of the esophagus.

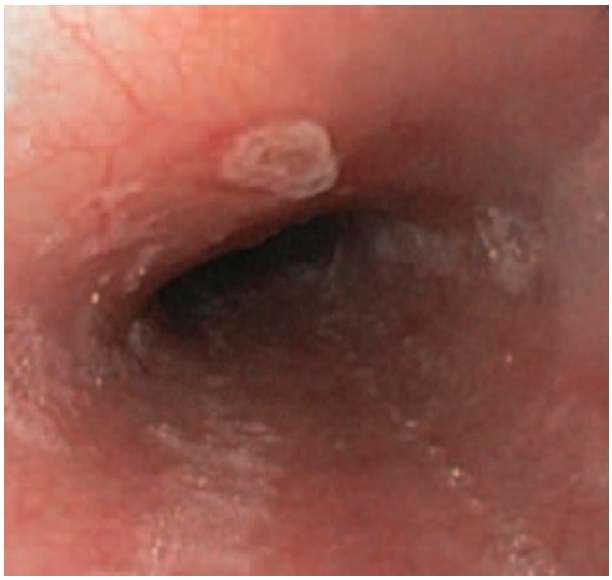

Figure 5: Thermal lesions found on the inside of the esophagus after cardiac ablation procedure [29].

All of these technologies are important for understanding the medical problem of thermal damage on the esophagus during RF ablation procedures. Medical devices are constantly being designed and re-designed to meet existing medical needs. The individuals, companies or institutions that are working to meet these needs have a good understanding of the previously implemented technologies and iteratively work through a design process to develop an innovative, useful medical product.

1.3 Important Aspects of Medical Device Design

1.3.1 The Design Process

The design process can vary for each research laboratory or working group in academia or industry. No matter the team, an organized roadmap and the discipline to follow it is required to achieve an innovative final product. A schematic illustrating the steps of a typical design process is shown in Figure 6 [35]. This generalized procedure begins with the "recognition of a need" and concludes at the "production release." It is often the case that teams of engineers must work on each of the design process steps to achieve the desired goal of product implementation. Teams must work cooperatively and rely on "feedback" throughout the process as design requirements are revised, as prototypes are iterated on and tested, and as customers gain experience using the product.

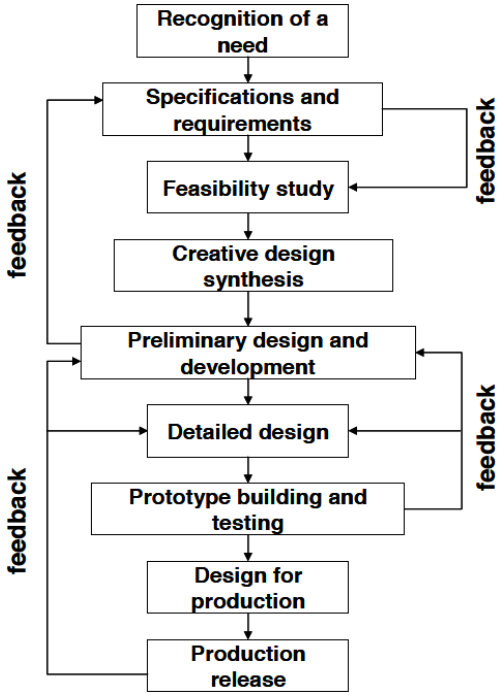

Figure 6: Schematic of a typical design process [35]

Another example schematic of a typical design process is shown in Figure 7. Deborah Forster, along with many other influential designers, have shared the concepts behind the “double diamond” of design to designers across disciplines [36].

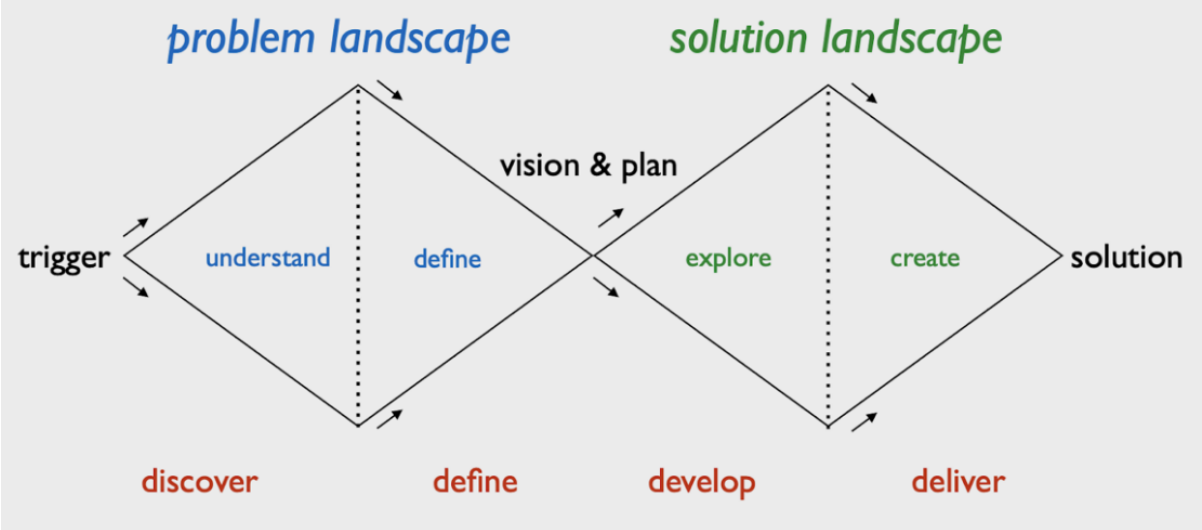

Figure 7: Schematic of a typical design process - the "Double Diamond" of Design. [36]

The “double diamond” of design consists of the widening and narrowing of the problem landscape and then the solution landscape. It is often the case that a problem is difficult to fully conceptualize and define. As time is given to a designer or, more preferably a diverse team of designers, the problem definition could be refined and focused. This process allows for a well-directed solution that meets the necessary design requirements. A strong design team provides time to explore potential solutions. Certain constraints or motivations, for example, manufacturability, cost, or safety, can help narrow feasible prospects toward an optimal solution.

1.3.2 Design Considerations for Medical Devices

Yock et al. [37] elaborate on the design process as it relates to medical devices in the textbook: “Biodesign: The process for innovating medical technologies.” The authors have

organized the book to follow a modified design process with a schematic shown in Figure 8, covering three steps: *Identify*, *Invent*, and *Implement*.

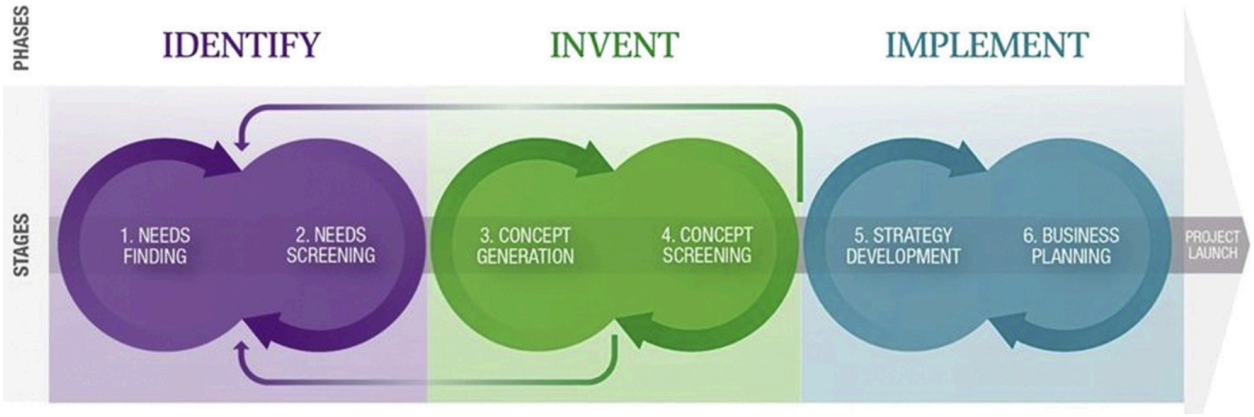

Figure 8: Additional schematic of a typical design process for medical devices. [37]

The "identify" phase incorporates exploring prevalent medical problems and challenges. This phase includes screening problems for existing solutions and understanding their scope in science as well as the consumer market. The "invent" phase provides a general view of device ideation and prototyping, and emphasizes the medical device design "landscape" including the necessary understanding of intellectual property, regulations, and reimbursement. Finally, with a completed "minimum viable product (MVP)", it is important to develop a business strategy that is curated for the particular medical device environment. Teixeira complements this work and offers additional perspective of medical device design highlighted in [38] with the schematic shown in Figure 9.

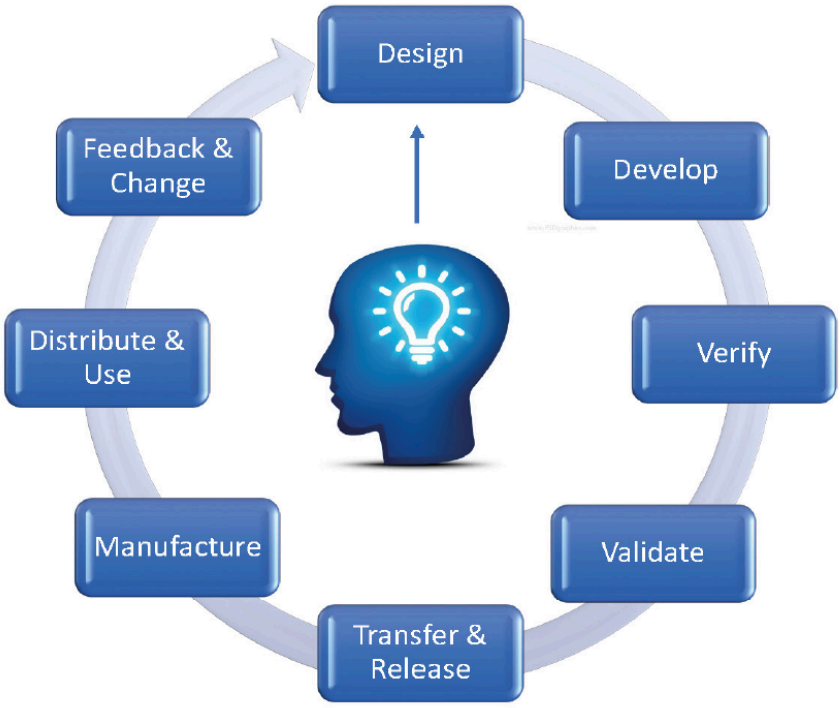

Figure 9: An additional example of the medical device design process. [38]

In the following subsections, a more detailed overview will be provided for the design topics of device safety, reliability, reimbursement, and intellectual property.

1.3.3 Safety of Medical Devices

Regulation by the Food and Drug Administration

The Food and Drug Administration (FDA) is responsible for regulating the medical device market in the United States. Any device used as a diagnostic or therapeutic tool in medicine will fall into one of the three categories: Class I, Class II, or Class III. These classes are primarily organized in terms of risk and examples of such devices are provided in Table 1.

Table 1: Medical Device Classification [39]

Device Classification	Examples	Safety/Effectiveness Controls	Required Submission
Class I	elastic bandages, examination gloves, hand-held surgical instruments	General Controls	Registration only unless 510(k) specifically required
Class II	powered wheelchairs, infusion pumps, surgical drapes	General Controls & Special Controls	510(k) notification unless exempt -IDE possible
Class III	heart valves, silicone gel-filled breast implants, implanted cerebella stimulators	General Controls & Premarket Approval	PMA application -IDE probable
	metal-on-metal hip joint, certain dental implants	*General Controls*	*510(k) notification*

Source: FDA, Overview of Medical Device Regulation, General and Special Controls, at http://www.fda.gov/MedicalDevices/DeviceRegulationandGuidance/Overview/GeneralandSpecialControls/default.htm.

Note: IDE means investigational device exemption. Some Class III devices have been cleared via the 510(k) process; these are Class III devices that entered the market prior to regulation calling for a PMA application.

Johnson [39] provides an overview of the FDA's medical device regulation process including discussion on pre- and post-market requirements for the medical device industry to adhere to. The design constraints, time to market, testing and manufacturing costs can be significantly influenced by the chosen regulatory pathway. A "510(k)" submission can help expedite a regulatory path by leveraging a predicate device that is already marketed and available for clinical use. For a research endeavor, it may be necessary for an FDA submission and approval beyond the assessment by an institutional review board (IRB). This FDA submission, for research activities, is labeled as an investigational device exemption (IDE) and requires for certain manufacturing and testing precautions to be taken before the device is used in a clinical setting [40].

Biocompatibility of Medical Devices

"Biocompatibility" is a common design requirement that engineers must consider for any medical device that comes into contact with the human body. ISO-10993 is an international standard frequently referenced by engineers to guide their decision-making on how to evaluate the

biocompatibility of a device material. Table 2 shows the factors that need to be considered to determine whether a device is safe in a certain medical environment. To determine the biological effects that need to be tested for, the duration and location of device use must be known [41].

Table 2: Medical Device Classification – Biocompatibility Testing Endpoints [41]

Medical device categorization by			Biological Effect [a]							
Nature of body contact		Contact duration								
Category	Contact	A - limited (≤ 24 h) B - prolonged (> 24 h to 30 d) C - permanent (> 30 d)	Cytotoxicity	Sensitization	Irritation or intracutaneous reactivity	Systemic toxicity (acute)	Subchronic toxicity (subacute toxicity)	Genotoxicity	Implantation	Haemocompatibility
Surface device	Skin	A	X	X	X					
		B	X	X	X					
		C	X	X	X					
	Mucosal membrane	A	X	X	X					
		B	X	X	X					
		C	X	X	X		X	X		
	Breached or compromised surface	A	X	X	X					
		B	X	X	X					
		C	X	X	X		X	X		
External communicating device	Blood path, indirect	A	X	X	X	X				X
		B	X	X	X	X				X
		C	X	X		X	X	X		X
	Tissue/bone/ dentin	A	X	X	X					
		B	X	X	X	X	X	X	X	
		C	X	X	X	X	X	X	X	
	Circulating blood	A	X	X	X	X				X
		B	X	X	X	X	X	X	X	
		C	X	X	X	X	X	X	X	
Implant device	Tissue/bone	A	X	X	X					
		B	X	X	X	X	X	X	X	
		C	X	X	X	X	X	X	X	
	Blood	A	X	X	X	X	X		X	X
		B	X	X	X	X	X	X	X	X
		C	X	X	X	X	X	X	X	X

Note:
a The "X" indicates data endpoint that can be necessary for a biological safety evaluation, based on a risk analysis. Where existing data are adequate, additional testing is not required.

It is important to note that a material alone cannot determine whether a device is compatible in a specific bio-system [42]. The entire complex system must be considered, and even with the standards described in ISO-10993 being met, more system level testing may be required to ensure an adequate safety assessment is made before fully deploying a medical device.

Manufacturing and Quality of Medical Devices

The FDA requires medical device approval submissions to include information on the manufacturing quality of the device including "methods, facilities, and controls" [43]. A design control program must be implemented to ensure all design decisions (including inputs, modifications, validations, certifications, etc.) are properly documented. Furthermore, a quality system must be in place and outlined in the FDA submission. Internal audit procedures and management review procedures must also be submitted. The FDA offers "Guidance" documentation to assist many manufacturers with defining their "Current Good Manufacturing Practices" (CGMP) [43] .

Further guidance documentation can be found for areas of specific concern for the FDA. A good example for guidance documentation related to rapid prototyping was recently published on "Technical Considerations for Additive Manufactured Medical Devices" [44]. Figure 10 shows a schematic of the medical device manufacturing workflow when including additive manufacturing methods. Boxed items including materials, software workflow, build, and post processing are important manufacturing steps to consider and discussed in a later section of this chapter.

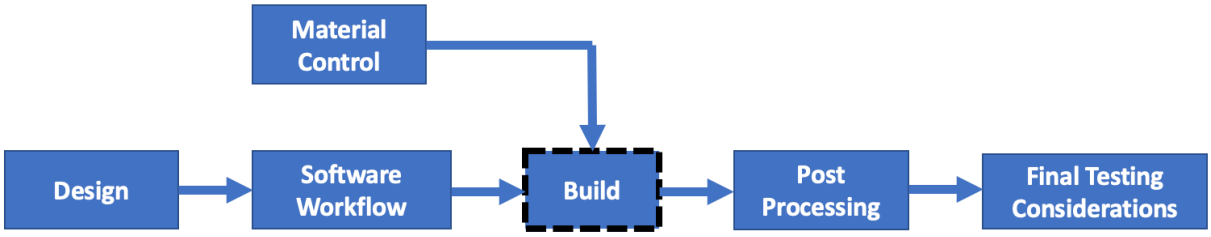

Figure 10: Flow chart of the Additive Manufacturing Process per FDA Technical Guidance. [modified from 44]

1.3.4 Reliability of Medical Devices

Regulation by the Food and Drug Administration

Reliability is an increasingly valued and implemented part of the product design process. Reliability is succinctly defined by Dhillon [45] as "the probability that an item will carry out its assigned mission satisfactorily for the stated time period when used under the specific conditions." At a given moment in time, an "item" or designed product, will have either failed or maintained its reliability. Failure occurs when the product is no longer functioning as intended.

Statistical Methods and Probability Distributions

Failure can be mathematically and statistically modeled over time under specific conditions with a cumulative density function. Dhillon and Kececioglu [45,46] describe the mathematical concepts to assist engineers with monitoring and improving reliability and failure. The failure cumulative distribution function $F(t)$ with respect to time is defined by

$$F(t) = \int_{-\infty}^{t} f(x)dx \tag{1.1}$$

where $f(x)$ is the probability density function.

The reliability $R(t)$ can be expressed as a function of $F(t)$ as

$$R(t) = 1 - F(t) \tag{1.2}$$

$$= 1 - \int_{-\infty}^{t} f(x)dx \tag{1.3}$$

where $R(t)$ is the reliability function. A number of models have been used in order to improve understanding of failure during a product's lifecycle. An often-used term is hazard rate $\lambda(t)$, which is defined by

$$\lambda(t) = \frac{f(t)}{R(t)} \tag{1.4}$$

$$= \frac{f(t)}{1-F(t)} \tag{1.5}$$

Maybe the most common distribution that uses a constant hazard rate, or failure rate, is the exponential distribution. The probability density function of the exponential distribution can be defined by

$$f(t) = \lambda e^{-\lambda t} \qquad t \geq 0, \lambda > 0 \tag{1.6}$$

$$F(t) = 1 - e^{-\lambda t} \tag{1.7}$$

The Weibull distribution is also commonly used in reliability analysis due to its ability to follow the failure in a phenomenological context and is defined as

$$f(t) = \frac{\beta}{\eta}\left(\frac{t-\gamma}{\eta}\right)^{\beta-1} e^{-\left(\frac{t-\gamma}{\eta}\right)^{\beta}} \qquad f(t) \geq 0, t \geq \gamma, \beta > 0, \eta > 0, -\infty < \gamma < \infty \tag{1.8}$$

where β is the shape parameter, η is the scale parameter, and γ is the location parameter. Figure 11 shows the probability density function with respect to time at three distinct shape parameter values: $\beta = 0.5$, $\beta = 1$, and $\beta = 3$.

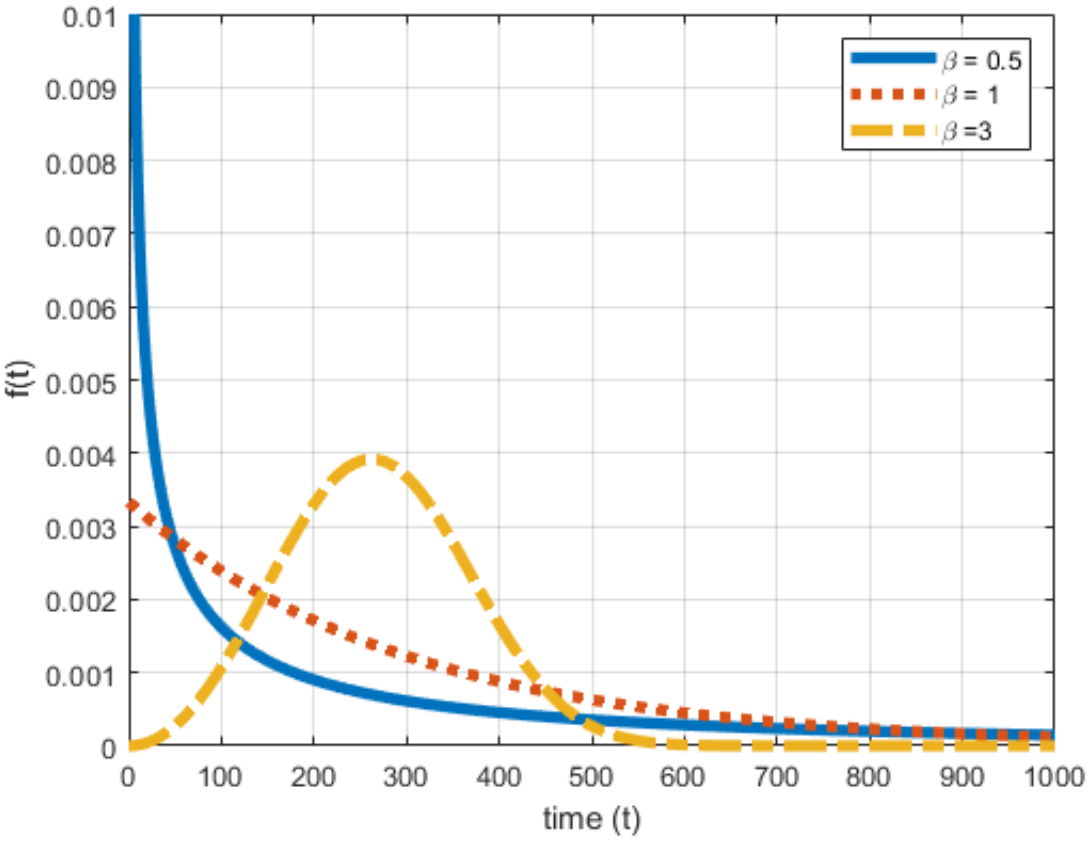

Figure 11: Example probability density functions for three Weibull distributions.

Also, a normal distribution is commonly used in statistical analysis. This distribution is often referred to as a Gaussian distribution and the probability density function can be defined with the expression

$$f(t) = \frac{1}{\sigma_t\sqrt{2\pi}} e^{-\frac{1}{2}\left(\frac{t-\bar{t}}{\sigma_t}\right)^2} \qquad f(t) \geq 0, \sigma_t > 0, -\infty < \bar{t} < \infty, -\infty < t < \infty \qquad (1.9)$$

where $\bar{t}$ is the mean of the normal time to failure and σ_t is the standard deviation of the time to failure.

Reliability is an important consideration to measure, model, and evaluate medical devices. Medical devices, naturally, are required to be reliable and this reliability needs to be quantified. The definition of reliability goes beyond personally driven ethical beliefs and has been largely influenced by the Food and Drug Administration as well as a United States Supreme Court case

between Medtronic Inc. vs Lohr about a failed pacemaker that placed a significant portion of liability for failure of a medical device on a medical device designer and manufacturer [47]. Also, medical device recalls have become increasingly prevalent and costly to medical device companies. Thus, it makes financial sense to have a strong reliability and quality assurance program integrated with the design and manufacturing teams. The risk of a medical device's failure must be mitigated and, thus, both theoretical and practical knowledge of reliability should be held by any medical device designer.

Figure 12, adapted from [48], eloquently embeds the reliability growth curve in the design process. Again, the evaluation of reliability for a medical device must be made when the device is first being prototyped. Reliability should be monitored and improved throughout the product design lifecycle. For a medical device, post-approval alterations to any design usually need review and approval by the FDA, but are likely to be accepted when the reliability is quantitatively shown to improve.

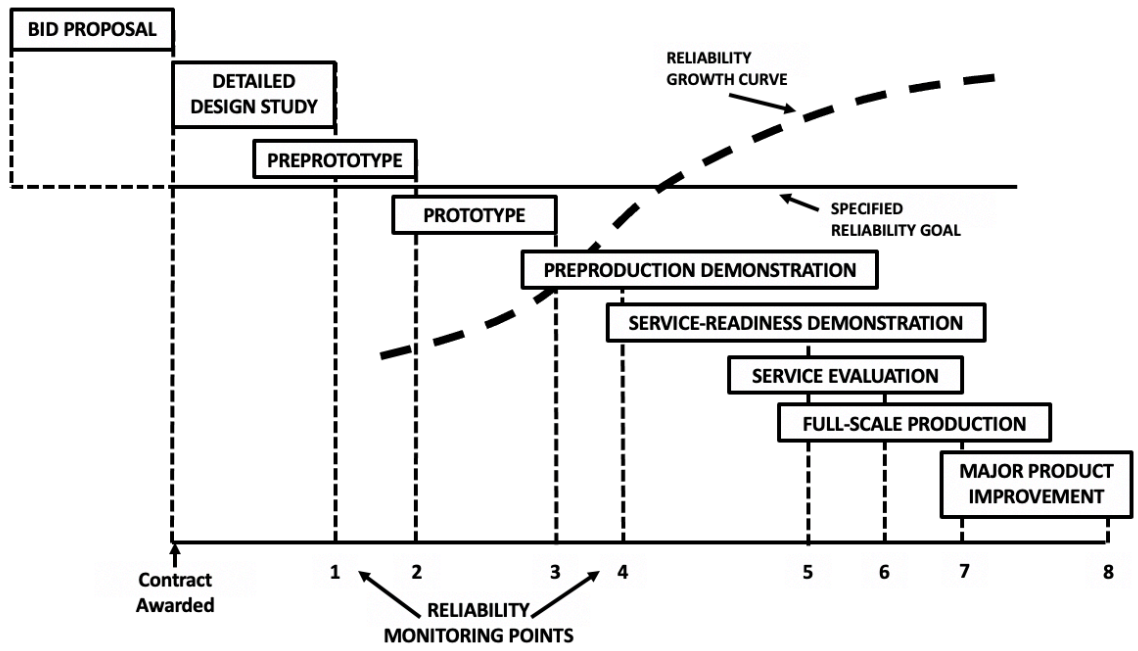

Figure 12: Reliability growth tests and their schedule adapted from [modified from 48]

1.3.5 Cost and Reimbursement

Beyond the life altering possibilities, the value of a medical device design can, fortunately or unfortunately, have monetary considerations that are commonly founded in the terms coding, coverage and payment [49]. “Coding” refers to a Current Procedural Terminology (CPT) code which is used by a medical practitioner to distinguish and communicate the type of diagnosis or therapy provided to the hospital or billing department. This code is then communicated to an insurer, where “coverage” is necessary in order for the insurer to be willing to pay. There are procedures that may have a code, yet not be covered by the insurer. “Payment” can be provided by the insurer to the hospital and can vary depending on the insurer. As a designer is developing a product to meet the needs of a patient or medical practitioner, it is important to consider each of these three areas so that a monetary value can be associated with the life altering value.

1.3.6 Intellectual Property for Medical Devices

Intellectual property (IP) is a term to describe the value of ideas. A patent is a form of intellectual property that can be granted by a government and provides the exclusive rights to sell a good that is based on specifically claimed ideas. [50,51]. Trademarks, copyrights, and trade secrets are other forms of intellectual property that may also be useful to a medical device designer. In order to obtain a patent, three primary properties of the idea or ideas must be considered: utility, novelty, and obviousness. Utility may be the simplest for a medical device designer and requires that a device must be useful, which is usually the premise of designing a medical device. Novelty, potentially more difficult property to achieve, relies on differentiation from dated “prior art”. Prior art can come in the form of previous patents or publicly available descriptions or products. Finally,

obviousness requires the potential IP to not be an obvious extension from prior art to anyone of ordinary skill in the pertinent field. If these three requirements have any potential to be met, a patent may be a useful tool to a medical device designer and innovator. The decision to apply for a patent usually is one that pertains to the value a patent might hold, and a larger discussion would be necessary here, involving relevant business-oriented decisions. If the decision is made to pursue a patent, the first step is most often a provisional patent, which is a formal filing (usually at a lower cost) to provide a more preferred "filing date" on the IP. Within one year, a full patent application must be submitted. A useful timeline, adapted from [51], is illustrated in Figure 13.

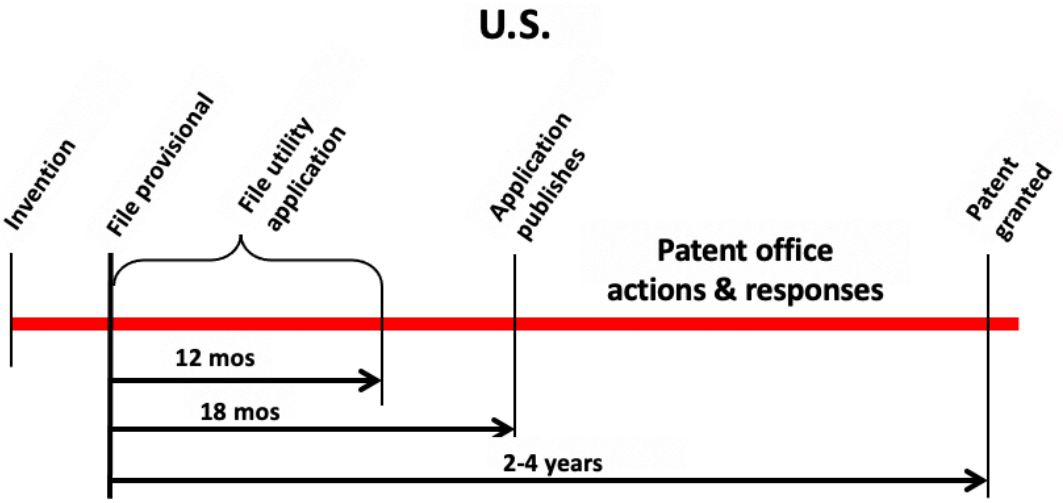

Figure 13: General U.S. Patent timeline adapted from [51]

1.4 Computer-Aided Design

Computer-Aided Design (CAD) is, now, ubiquitous across all engineering disciplines due to computers being an essential part of the design process. CAD software has developed significantly in the last 50 years and can currently support the initial conceptualization of a design,

assist with modifying and optimizing the design, and can be further integrated into testing, simulations and manufacturing. Medical device design companies rely heavily on the use of CAD as well.

1.4.1 CAD History

Over the years, computers have increasingly influenced the design process. Some especially notable developments, influential to CAD, can be found in the works of Ivan Sutherland and Pierre Bezier in the mid 20th century.

Sutherland [52] developed what is known as the “SketchPad”. The novel device worked like a modern-day tablet, incorporating a display monitor and a stylet shown in Figure 14.

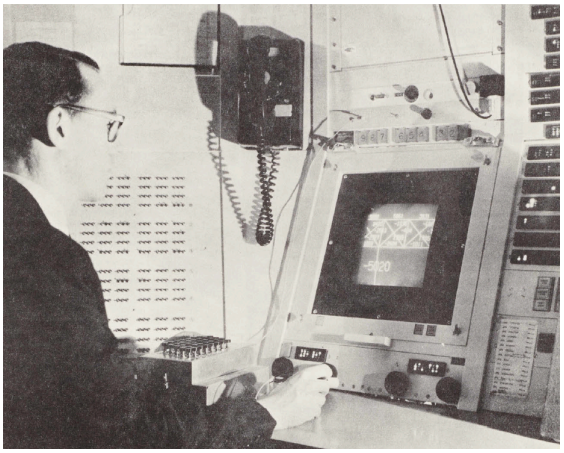

Figure 14: Ivan Sutherland demonstrating Sketchpad [52]

With the SketchPad, Sutherland proved that a human could communicate an envisioned design to a computer, where it can be stored, visualized on a monitor, and further manipulated. This computer software package captured the *design intent* of the user. *Design intent* is now a common feature of modern-day CAD software.

Bezier was a mathematician and engineer, who applied polynomial curve fitting to automobile design. “Bezier curves” are mathematically defined and, more recently, computer-generated. The new approach to defining curves has proven useful in industry, most notably for the design and manufacturing processes in the automobile industry which is where Bezier was employed. Figure 15 shows a computer-generated illustration, using SolidWorks 2020, implementing the Bezier curve technology.

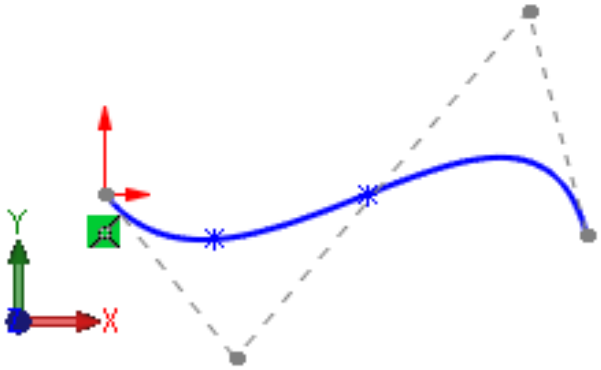

Figure 15: A cubic Bezier Polynomial Curves implemented in modern-day CAD software (created in SolidWorks 2020).

A cubic Bezier curve, $p(t)$, is mathematically represented by control points p_i:

$$p(t) = (1-t)^3 p_0 + 3t(1-t)^2 p_1 + 3t^2(1-t)p_2 + t^3 p_3 \qquad (10)$$

with t moving between 0 and 1 and using control points p_0, p_1, p_2, and p_3. This mathematically defined curve can be shown to equal p_0 at $t = 0$ and p_3 at $t = 1$. Between those points a smooth curve is generated using weighted averages of the four points.

These are only a couple of examples of early innovation in computer-aided design, but the potential was clear then, and now it is highly likely that an engineering design firm in any field would have computers aiding their design efforts. Industry has implemented so many valuable

forms of CAD, that for this thesis work, it is important to focus on especially relevant areas including those for developing geometry and numerically solving problems in solid mechanics and heat transfer.

1.4.2 Geometry in CAD (Mechanical CAD or MCAD)

Mechanical CAD or MCAD software packages incorporate important aspects of modern-day CAD tools, often including the properties for communicating design intent, being feature-based, and acting parametrically.

Design intent is the property which enables a human user to convey all geometric properties of a design with a computer. If computer software has captured all of the user's design intent, then the geometry will respond to any dimension or relation changes, as the user would expect. MCAD software strives to capture all of the user's design intent as seamlessly as possible, usually with a clean and clear graphical user interface. Many MCAD packages improve the communication of design intent by being feature-based and parametric. Feature-based is the idea that the user will begin creating a feature that only depends on built-in features, such as pre-existing reference planes and an origin. Features will continue to be developed by referencing the previous features. A user can add, edit, or delete any feature they designed. Parametric is the concept that the dependencies between the features can be defined formally, again to engage with the user's design intent. If the user changes the dimension of one entity or relationship between entities, it should propagate through to other aspects of the design, preferably with well-defined design intent.

SolidWorks (see Figure 16), OnShape (see Figure 17), and CreoParametric (see Figure 18) each incorporate the previously discussed aspects of design intent, feature-based, and parametric. Figure 16-18 show the current layout of the software tools, each of which aiming to seamlessly

capture the design intent. Features are notably in the corresponding “design trees” (on the left of each figure). The parametric properties of each design are defined through the dependences between the features.

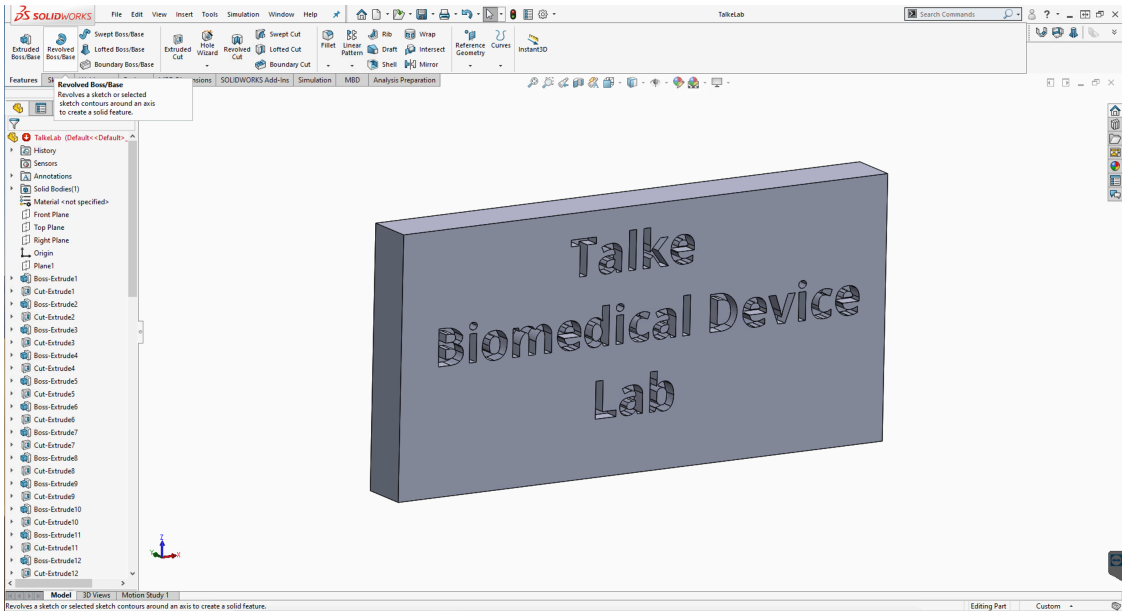

Figure 16: An example of a SolidWorks Part.

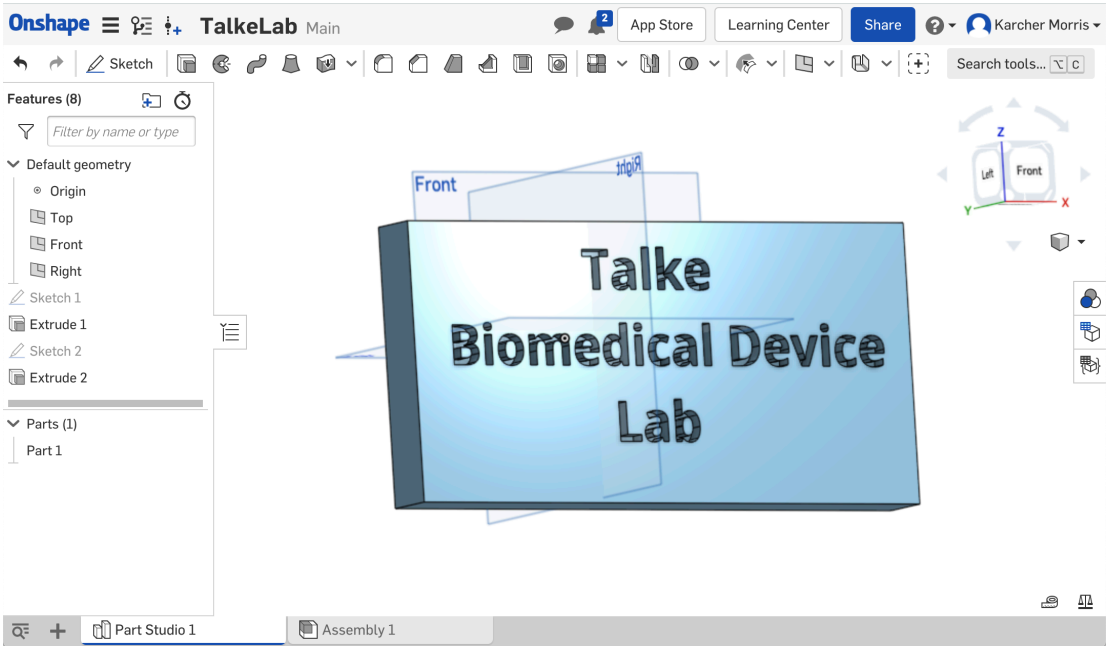

Figure 17: An example of an OnShape Part.

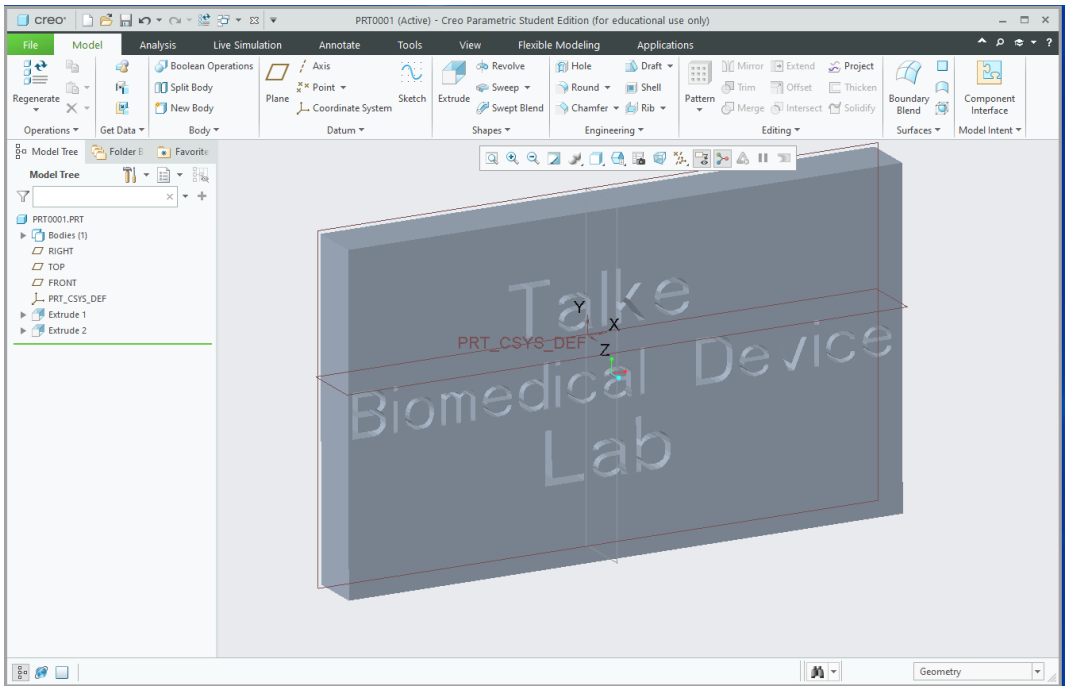

Figure 18: An example of a Creo Parametric Part

There is an extensive list of other MCAD packages that are commercially available. The use of one software package over another can be due to what the user is most familiar with, or previously prescribed relationships between MCAD companies and their targeted companies or fields.

1.4.3 Mechanical CAD Simulation Software

A variety of numerical or simulation methods have been developed including finite element analysis, kinematic modeling, optimization, computational fluid dynamics and multi-physics solvers. The finite element method is a powerful mathematical tool that assists with finding solutions for boundary value problems in structural mechanics, heat transfer, fluid flow, and electromagnetics. [53, 54].

A continua, or body, can be discretized into a number of "finite" elements in order to solve a very complicated structural problem. These elements with a number of nodes hold mathematical properties associated with the degrees of freedom and constitutive equation for the material of the body being discretized. These elements each provide stiffness matrices that can be integrated into a larger linear system of equations. A result, by solving this system, can be further analyzed and marched forward in time. The results are numerical estimates, but if built properly, can be extremely accurate and produce relevant information capable of driving design.

Commercially available finite element analysis software includes NASTRAN, SolidWorks (COSMOS), Abaqus, Altair, ANSYS, and LSDYNA. An example of the SolidWorks finite element tool is shown in Figure 19. In this case the tool is being used to understand how a hole in a plate with specific boundary conditions (i.e., constraints and applied forces) can influence the von Mises stress profile. Figure 20 shows a typical result.

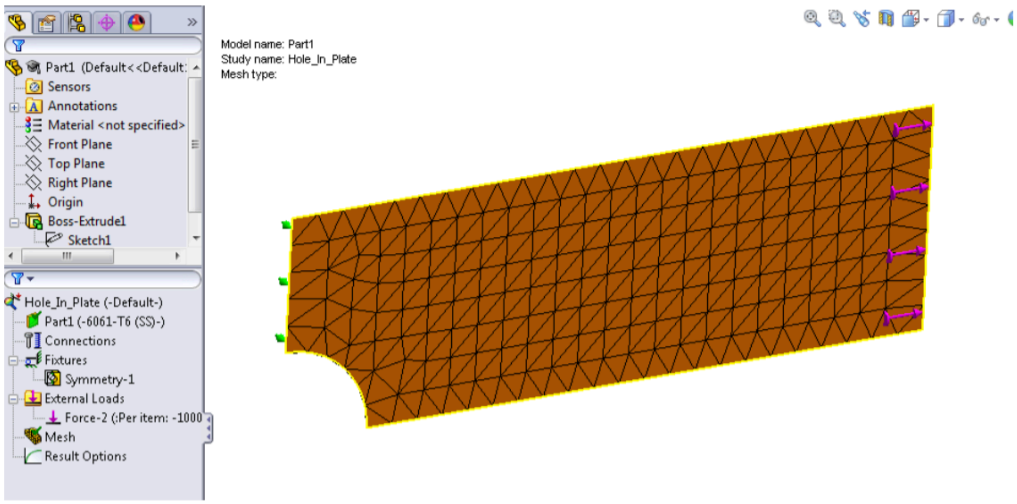

Figure 19: Finite element model using SolidWorks simulation software [55]

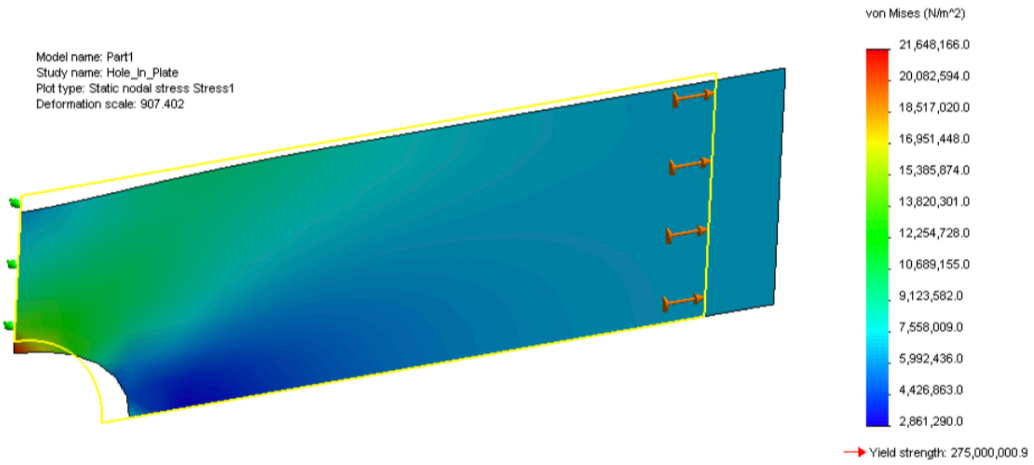

Figure 20: Finite element result (from model shown in prior figure) illustrating the von Mises stress profile using SolidWorks simulation software. [55]

1.5 3D Printing

1.5.1 3D Printing Technology

3D printing, or additive manufacturing (AM), is a manufacturing technology that has reshaped the traditional thinking for what could be manufactured and how. 3D printing, as opposed to subtractive manufacturing, allows for increased complexity while reducing waste. Also, 3D printing can substantially lower the skill and time it takes to produce a useful part or prototype from a computer-aided design or drawing. 3D printing can remove much of the challenges found in communicating a geometric design from a designer to the machinist, being that the process with 3D printing is significantly digitized. The process of 3D printing a part includes creating a computer model, then defining 3D printing parameters specific to the 3D printing technology (e.g., layer height, part orientation, temperature, etc.), printing the part, and finally post-processing the part as necessary (e.g., removing support structure, cleaning residue, sanding surfaces, etc.). Figure

21 illustrates the 3D printing process [56]. 3D printing parameters will vary depending on the technology, the material used, and the desired resolution, among other factors, that may be important to the designer. In this section, different 3D printing technologies will be reviewed.

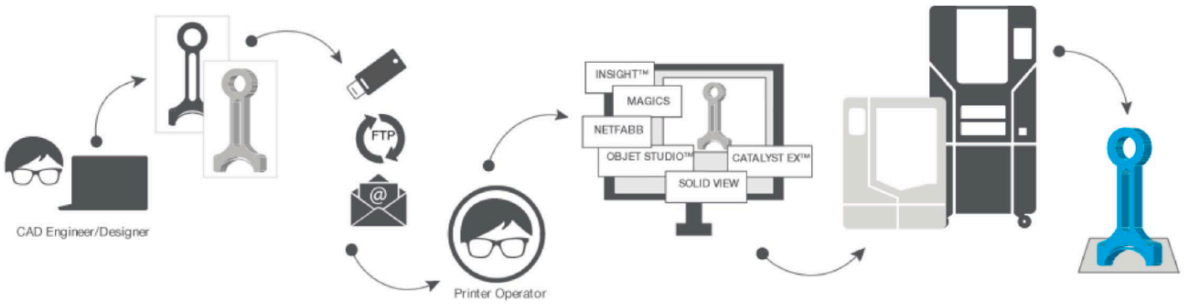

Figure 21: 3D printing process schematic [56]

Fused Deposition Modeling (FDM)

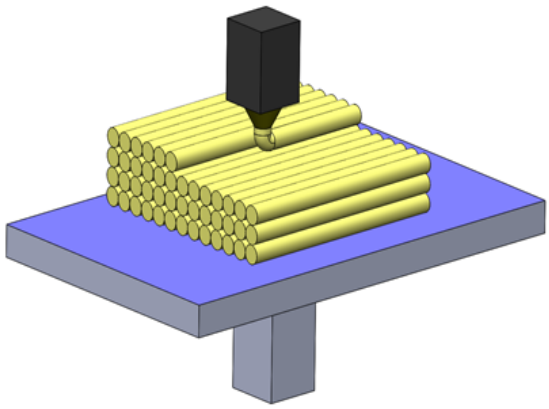

Figure 22: Fused deposition modeling (FDM) 3D printing schematic

Fused deposition modeling (FDM) is the most highly proliferated form of 3D printing due to the technology's ability to be sold at a low cost and large scale [57]. The technology uses a wide variety of thermoplastic materials such as polylactic acid (PLA) or acrylonitrile butadiene styrene

(ABS) [57]. These materials can be drawn into an extruder that melts the material and positions it, layer by layer so that the material can cool and harden in the desired location (see Figure 23).

Crump [58] designed and patented the first FDM printer and quickly carried it into the founding of a large company, 3D Systems Incorporated. Figure 23 shows an illustration from the 1992 issued patent with the extruder and build plate clearly visible [58]. This FDM system looks very similar to the many current commercially available 3D printers as many companies have been able to leverage the technology now that the patent has expired.

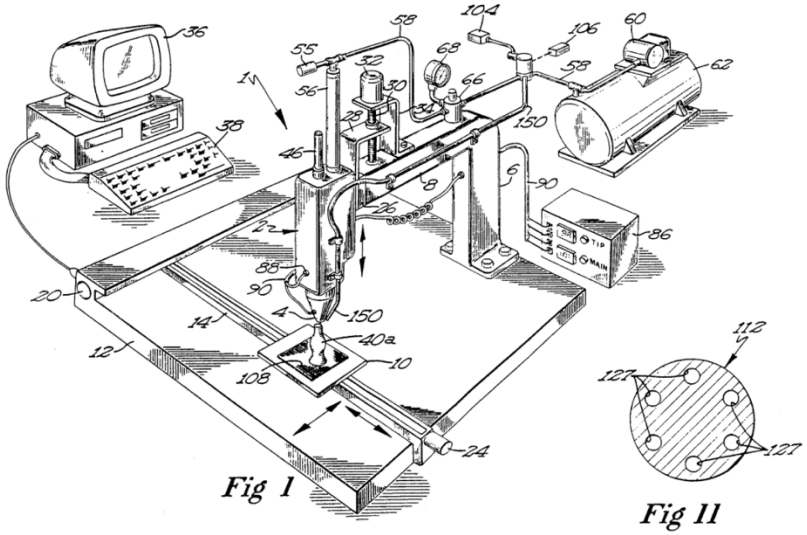

Figure 23: Fused deposition modeling (FDM) schematic from patent. [58]

Stereolithography Apparatus (SLA)

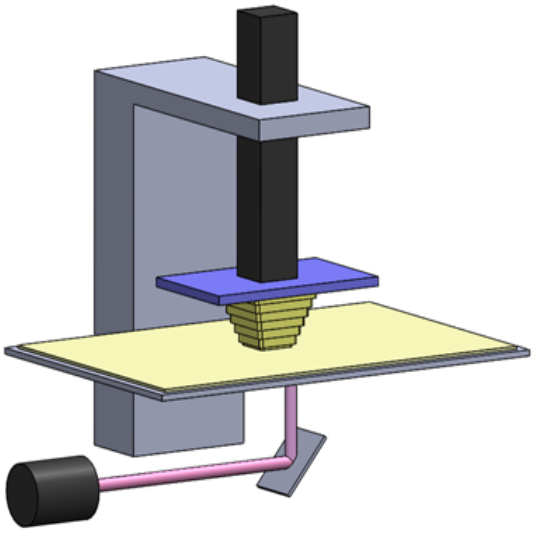

Figure 24: Stereolithography apparatus (SLA) 3D printing schematic

Stereolithography Apparatus (SLA) 3D printing currently allows for a relatively high level of resolution using an ultra-violet (UV) light or UV laser light to cure, or harden, a liquid photopolymer resin [59]. This hardening is, again, performed layer-by-layer in order to build the desired geometry (see Figure 24).

Hull [60] designed and patented the first SLA printer and quickly carried it into the founding of a large company, Stratasys Incorporated. Figure 25 shows an illustration from the 1986 patent with the laser, resin bath, and build plate clearly visible. Stratasys and 3D systems companies have each developed and acquired many impactful technologies in the 3D printing space.

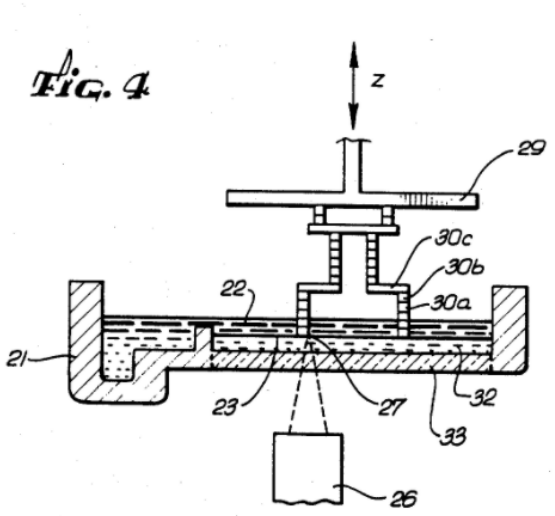

Figure 25: Stereolithography Apparatus (SLA) 3D printing schematic from patent [60]

Material Jetting (MJ)

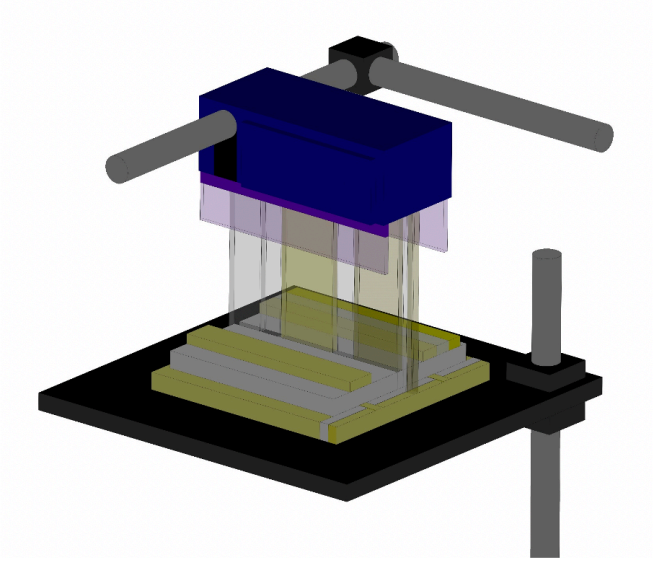

Figure 26: Material Jet (MJ) 3D printing schematic

Material Jet (MJ) 3D printing has been made, more recently, commercially available and allows for high quality prints and the potential for “digital materials”, or the smooth mixing of

materials within a single part. MJ 3D printing jets, or sprays, photopolymer resin through an array of nozzles onto a surface and cures the layer with a UV light. This is analogous to a 2D inkjet printer commonly used in the office environment, but instead of ink being used, photopolymer resin is used and instead of only color being mixed between the jetted materials, a multitude of material properties can be mixed leading to the smooth transition of color or changes in flexibility within a part. Again, this jetting and curing is performed layer-by-layer to create the final 3D object (see Figure 26).

Kritchman et al. designed and patented the first MJ printer. Figure 27 shows an illustration from the 2002 patent [61] where the resin material is jetted from the nozzle array to create the part layers.

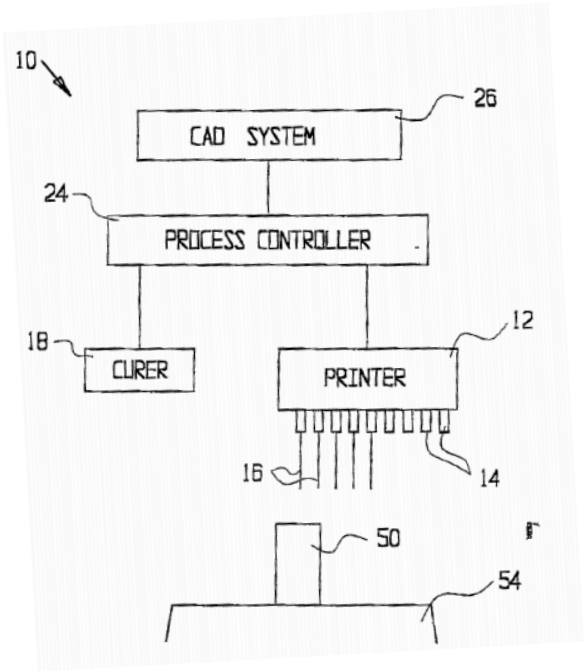

Figure 27: Material Jet (MJ) 3D printing schematic from patent [61]

The technologies reviewed in the previous section have turned into a large variety of commercially available 3D printers. Figure 28 shows three printers utilizing the three technologies

previously discussed: Replicator using FDM, Form 2 using SLA, and Connex using MJ. These printers range in prices and are used around the world to develop innovative products, including medical devices.

Figure 28: Commercially available 3D printers [62-64]

1.5.2 3D Printing in Medicine

3D printing is increasingly utilized in medical research and industry. As previously discussed, the FDA has been strongly encouraged to address the sudden push toward this enabling and new manufacturing technology. The FDA has done so through providing guidance on "Technical Considerations for Additive Manufactured Medical Devices" [44]. It is important to note that their guiding document only provides a high-level overview of considerations. Figure 29 shows the general 3D printing workflow provided by the guidance document with some considerations added on top of their workflow that can easily affect the reliability of the part being manufactured with a specific technology, fused deposition modeling 3D printing.

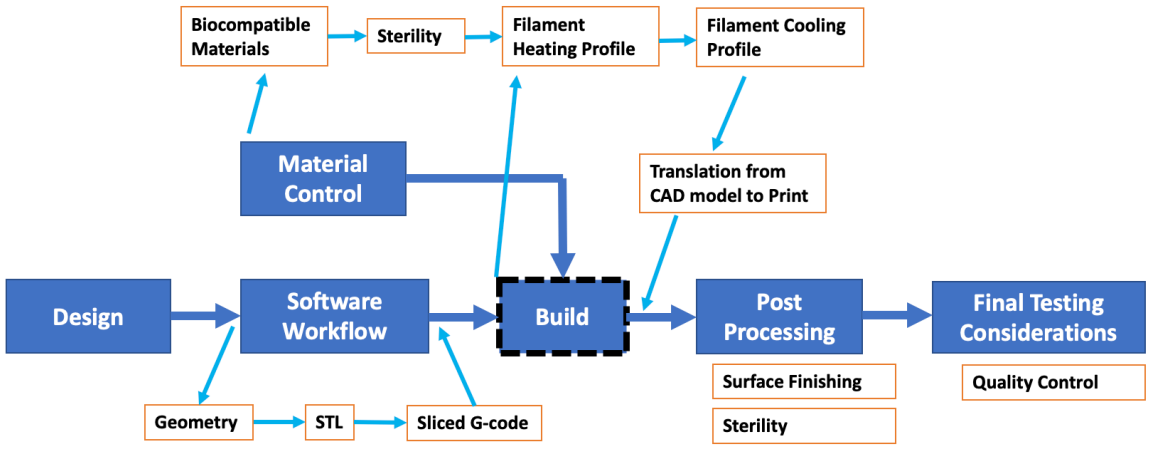

Figure 29: Flow chart of the Additive Manufacturing Process per FDA Technical Guidance (modified from [44] to include aspects of the FDM process)

Even among such variety in technology there is a clear need for 3D printing in medicine as illustrated in Figure 30 [65]. Figure 30 plots the increased citations of 3D printing or Additive manufacturing in journals especially relevant to the medical community posted through PubMed. The fused deposition modeling technology only accounts for a small portion of utilized 3D printing technologies discussed in the medical oriented publications.

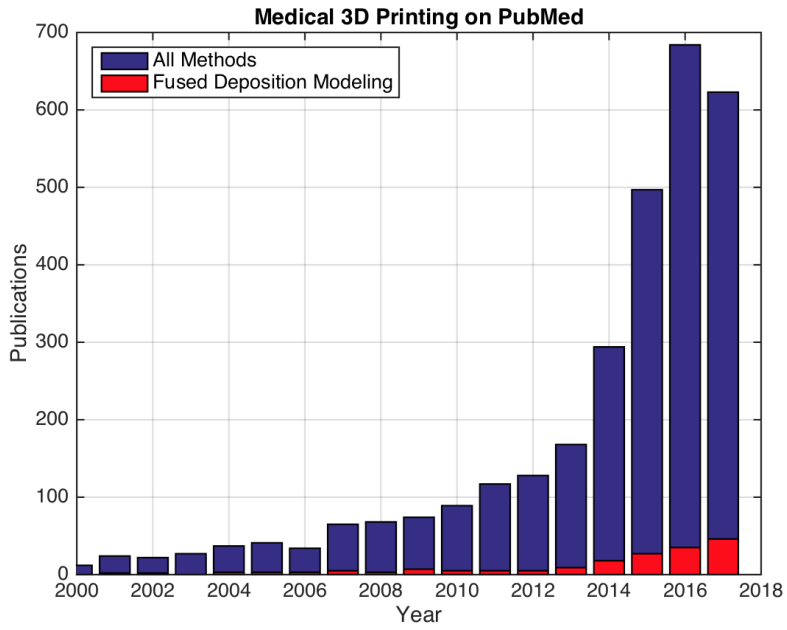

Figure 30: Publications in PubMed discussing 3D printing. (modified from [65])

3D printing has already proven useful or shown promise in a variety of medical communities, most notably, in surgical planning, medical devices, bioprinting, and drug deliver [65-67]. In the Talke Biomedical Device Lab, 3D printing has been used primarily as a prototyping tool in the fields of gastroenterology, ophthalmology, and surgery, building flexible endoscope over tubes, expandable stents, bronchoscope transmissions, and ergonomics device enclosures, among other areas [68-72]. The impacts of 3D printing on medicine continue to grow. With the mentioned uncertainty it is very important to understand the mechanical nature of the 3D printed material as it is put to medical use. This “mechanical nature”, or constitutive material property, can be modeled mathematically to enable further analytical or numerical assessment of a proposed medical device design.

1.6 Summary

There have been significant medical advances in the fields of cardiac electrophysiology and gastroenterology. RF ablation has been used to treat atrial fibrillation patients. Esophageal thermal lesions may occur due to the delivery of high intensity RF ablation energy to the atrial tissue along with the proximity of the left atrium and the esophagus. These thermal lesions have led to a number of other medical problems for the patient. A medical device should be designed to optimally prevent esophageal thermal damage.

The design process, as it pertains to the development of medical devices, was discussed. The medical device ecosystem, including the regulatory and reimbursement pathways, device standards, safety measures, and measurements of reliability, were also reviewed. Computer aided

analysis and design tools were discussed along with advanced manufacturing techniques, like 3D printing.

In the following chapters the problem of esophageal thermal damage will be addressed by implementing the described design process. Computer-aided analysis and design tools will assist the design process and novel technologies will be proposed and investigated as they aim to meet this important medical need.

References

[1] FDA Website "How to determine if your product is a medical device" - https://www.fda.gov/medical-devices/classify-your-medical-device/how-determine-if-your-product-medical-device.

[2] Chugh, Sumeet S., Rasmus Havmoeller, Kumar Narayanan, David Singh, Michiel Rienstra, Emelia J. Benjamin, Richard F. Gillum et al. "Worldwide epidemiology of atrial fibrillation: a Global Burden of Disease 2010 Study." Circulation 129, no. 8 (2014): 837-847.

[3] Jaïs, Pierre, Bruno Cauchemez, Laurent Macle, Emile Daoud, Paul Khairy, Rajesh Subbiah, Mélèze Hocini et al. "Catheter ablation versus antiarrhythmic drugs for atrial fibrillation: the A4 study." Circulation 118, no. 24 (2008): 2498-2505.

[4] Steinberg, Jonathan S., Pierre Jais, and Hugh Calkins. Practical guide to catheter ablation of atrial fibrillation. John Wiley & Sons, 2015.

[5] Chen, Yi-He, Zhao-Yang Lu, Yin Xiang, Jian-Wen Hou, Qian Wang, Hui Lin, and Yi-Gang Li. "Cryoablation vs. radiofrequency ablation for treatment of paroxysmal atrial fibrillation: a systematic review and meta-analysis." EP Europace 19, no. 5 (2017): 784-794.

[6] Spragg, David, and Hugh Calkins. "Catheter ablation for atrial fibrillation: past, present, and future." Practical Guide to Catheter Ablation of Atrial Fibrillation (2015): 7.

[7] Kaneshiro, Takashi, Yoshiyuki Matsumoto, Naoko Hijioka, Minoru Nodera, Shinya Yamada, Masashi Kamioka, Akiomi Yoshihisa, Hiroshi Ohkawara, Hitoshi Suzuki, and Yasuchika Takeishi. "Distinct Forms of Esophageal Lesions After Radiofrequency and Cryoballoon Pulmonary Vein Isolation." JACC: Clinical Electrophysiology 4, no. 12 (2018): 1642-1643.

[8] Zhang, Pei, Yue-Yue Zhang, Qian Ye, Ru-Hong Jiang, Qiang Liu, Yang Ye, Jia-Guo Wu et al. "Characteristics of atrial fibrillation patients suffering esophageal injury caused by ablation for atrial fibrillation." Scientific reports 10, no. 1 (2020): 1-9.

[9] Zhang, Ping, and Yi Bian. "Cerebral arterial air embolism secondary to iatrogenic left atrial-esophageal fistula: a case report." BMC neurology 20, no. 1 (2020): 1-4.

[10] Carroll, Brett J., FERNANDO M. CONTRERAS‐VALDES, E. Kevin Heist, Conor D. Barrett, Stephan B. Danik, Jeremy N. Ruskin, and Moussa Mansour. "Multi‐sensor esophageal temperature probe used during radiofrequency ablation for atrial fibrillation is associated with increased intraluminal temperature detection and increased risk of esophageal injury compared to single‐sensor probe." Journal of cardiovascular electrophysiology 24, no. 9 (2013): 958-964.

[11] Elkhatib, Imad, Syed Fehmi, Mary L. Krinsky, Thomas J. Savides, and Gregory Feld. "Tu1360 Endoscopic Mechanical Displacement of the Esophagus During Atrial Fibrillation Catheter Ablation." Gastrointestinal Endoscopy 79, no. 5 (2014): AB511-AB512.

[12] Koruth, Jacob S., Vivek Y. Reddy, Marc A. Miller, Kalpesh K. Patel, James O. Coffey, Avi Fischer, J. Anthony Gomes, Srinivas Dukkipati, A. N. D. R. E. D'AVILA, and Alexander Mittnacht. "Mechanical esophageal displacement during catheter ablation for atrial fibrillation." Journal of cardiovascular electrophysiology 23, no. 2 (2012): 147-154.

[13] Parikh, Valay, Vijay Swarup, Jacob Hantla, Venkat Vuddanda, Tawseef Dar, Bharath Yarlagadda, Luigi Di Biase, Amin Al-Ahmad, Andrea Natale, and Dhanunjaya Lakkireddy. "Feasibility, safety, and efficacy of a novel preshaped nitinol esophageal deviator to successfully deflect the esophagus and ablate left atrium without esophageal temperature rise during atrial fibrillation ablation: the DEFLECT GUT study." Heart Rhythm 15, no. 9 (2018): 1321-1327.

[14] Us - FDA - Bandages - https://www.accessdata.fda.gov/scripts/cdrh/cfdocs/cfcfr/cfrsearch.cfm?fr=880.5240.

[15] Dhivya, Selvaraj, Viswanadha Vijaya Padma, and Elango Santhini. "Wound dressings–a review." BioMedicine 5, no. 4 (2015).

[16] Banerjee, Jaideep, Piya Das Ghatak, Sashwati Roy, Savita Khanna, Emily K. Sequin, Karen Bellman, Bryan C. Dickinson et al. "Improvement of human keratinocyte migration by a redox active bioelectric dressing." PLoS One 9, no. 3 (2014): e89239.

[17] Marino, Robert A., Unni MM Mooppan, and Hong, Kim. "History of urethral catheters and their balloons: drainage, anchorage, dilation, and hemostasis." Journal of endourology 7, no. 2 (1993): 89-92.

[18] Mould, Richard Francis. "The early history of x-ray diagnosis with emphasis on the contributions of physics 1895-1915." Physics in Medicine & Biology 40, no. 11 (1995): 1741.

[19] Kligfield, Paul. "The centennial of the Einthoven electrocardiogram." Journal of electrocardiology 35, no. 4 (2002): 123-129.

[20] Ward, Catherine, Susannah Henderson, and Neil H. Metcalfe. "A short history on pacemakers." International journal of cardiology 169, no. 4 (2013): 244-248.

[21] Mueller, Richard L., and Timothy A. Sanborn. "The history of interventional cardiology: cardiac catheterization, angioplasty, and related interventions." American heart journal 129, no. 1 (1995): 146-172.

[22] Scheinman, Melvin M., Michael M. Laks, John DiMarco, and Vance Plumb. "Current role of catheter ablative procedures in patients with cardiac arrhythmias. A report for health professionals from the Subcommittee on Electrocardiography and Electrophysiology, American Heart Association." Circulation 83, no. 6 (1991): 2146-2153.

[23] Lin, Tina, Feifan Ouyang, Karl-Heinz Kuck, and Roland Tilz. "THERMOCOOL® SMARTTOUCH® CATHETER–The Evidence So Far for Contact Force Technology and the Role of VISITAG™ MODULE." Arrhythmia & electrophysiology review 3, no. 1 (2014): 44.

[24] Abbott Tacticath - https://www.cardiovascular.abbott/int/en/hcp/products/electrophysiology/tacticath-family-of-contact-force-ablation-catheters.html.

[25] Medtronic - PVAC gold -https://europe.medtronic.com/xd-en/healthcare-professionals/products/cardiac-rhythm/ablation-atrial-fibrillation/pulmonary-vein-ablation-catheter-gold.html.

[26] Keçe, Fehmi, Katja Zeppenfeld, and Serge A. Trines. "The impact of advances in atrial fibrillation ablation devices on the incidence and prevention of complications." Arrhythmia & electrophysiology review 7, no. 3 (2018): 169.

[27] Terricabras, Maria, Jonathan P. Piccini, and Atul Verma. "Ablation of persistent atrial fibrillation: Challenges and solutions." Journal of cardiovascular electrophysiology 31, no. 7 (2020): 1809-1821.

[28] Rottner, Laura, Daniela Waddell, Tina Lin, Andreas Metzner, and Andreas Rillig. "Innovative tools for atrial fibrillation ablation." Expert review of medical devices 17, no. 6 (2020): 555-563.

[29] Halm, Ulrich, Thomas Gaspar, Markus Zachäus, Stephan Sack, Arash Arya, Christopher Piorkowski, Ingrid Knigge, Gerhard Hindricks, and Daniela Husser. "Thermal esophageal lesions after radiofrequency catheter ablation of left atrial arrhythmias." American Journal of Gastroenterology 105, no. 3 (2010): 551-556.

[30] Su, Wilber, Qinling Zhang, William Reichert, Zeshan Ahmad, Emrie Tomaiko, and Xi Su. "Minimal Dose of Cryoballoon Ablation Leading to Atrioesophageal Fistula Formation." HeartRhythm Case Reports (2020).

[31] Engel, Rainer ME. "Philipp Bozzini—the father of endoscopy." Journal of endourology 17, no. 10 (2003): 859-862.

[32] Ramai, Daryl, Karl Zakhia, Denzil Etienne, and Madhavi Reddy. "Philipp Bozzini (1773–1809): the earliest description of endoscopy." Journal of medical biography 26, no. 2 (2018): 137-141.

[33] Fuchs, K. H. "Minimally invasive surgery." Endoscopy 34, no. 02 (2002): 154-159.

[34] Kohli, Divyanshoo R., and John Baillie. "How endoscopes work." In Clinical Gastrointestinal Endoscopy, pp. 24-31, 2019.

[35] Shigley, Joseph Edward, Larry D. Mitchell, and H. Saunders. "Mechanical engineering design." (1985): 145-145.

[36] MAE 207: Soft Robotics - Deborah Forster Slides on “The Double Diamond (DD) of Design” - Presented 20 January 2017.

[37] Yock, Paul G., Stefanos Zenios, Josh Makower, Todd J. Brinton, Uday N. Kumar, FT Jay Watkins, Lyn Denend, Thomas M. Krummel, and Christine Q. Kurihara. Biodesign: the process of innovating medical technologies. Cambridge University Press, 2015.

[38] Teixeira, Marie B. Design controls for the medical device industry. CRC press, 2019.

[39] Johnson, Judith.FDA Regulation of Medical Devices (2016) - https://fas.org/sgp/crs/misc/R42130.pdf.

[40] FDA Investigational Device Exemtion - https://www.fda.gov/medical-devices/how-study-and-market-your-device/investigational-device-exemption-ide.

[41] ISO Standards 10993-1:2018 - https://www.iso.org/standard/68936.html.

[42] Williams, David F. "There is no such thing as a biocompatible material." Biomaterials 35, no. 38 (2014): 10009-10014.

[43] Current Good Manufacturing Practices: FDA (2020) - https://www.fda.gov/drugs/pharmaceutical-quality-resources/current-good-manufacturing-practice-cgmp-regulations.

[44] Technical Considerations for Additive Manufactured Medical Devices: FDA (2017) - https://www.fda.gov/regulatory-information/search-fda-guidance-documents/technical-considerations-additive-manufactured-medical-devices.

[45] Dhillon, Balbir S. Design reliability: fundamentals and applications. CRC press, 1999.

[46] Kececioglu, Dimitri. Reliability and life testing handbook. Vol. 2. DEStech Publications, Inc, 2002.

[47] Jarcho, Daniel G. "Premarket Approval and Federal Preemption of Product Liability Claims in the Wake of Medtronic, Inc. v. Lohr." Food & Drug LJ 51 (1996): 613.

[48] Kececioglu, Dimitri. Reliability engineering handbook. Vol. 1. DEStech Publications, Inc, 2002.

[49] NAMSA Regulatory Guidance on Esophageal Deflection Device (2017).

[50] US Patent office general patent information: https://www.uspto.gov/patents/basics.

[51] MAE 207 Presentation by Josh Harrison - Patent and Patent Lab - UC San Diego (2020).

[52] Sutherland, Ivan E. "Sketchpad a man-machine graphical communication system." Simulation 2, no. 5 (1964): R-3.

[53] Hughes, Thomas JR. The finite element method: linear static and dynamic finite element analysis. Courier Corporation, 2012.

[54] Cook, Robert D. Concepts and applications of finite element analysis. John wiley & sons, 2007.

[55] MAE 150 UCSD Hole in the Plate Tutorial, K. Morris, F.E. Talke, V.A. Lubarda (2015).

[56] 3D printing process - https://www.informationweek.com/cloud/grabcads-print-cloud-speeds-up-3d-printing/d/d-id/1325717?.

[57] Liu, Zengguang, Yanqing Wang, Beicheng Wu, Chunzhi Cui, Yu Guo, and Cheng Yan. "A critical review of fused deposition modeling 3D printing technology in manufacturing polylactic acid parts." The International Journal of Advanced Manufacturing Technology 102, no. 9 (2019): 2877-2889.

[58] Crump, S. Scott. "Apparatus and method for creating three-dimensional objects." U.S. Patent 5,121,329, issued June 9, 1992.

[59] Melchels, Ferry PW, Jan Feijen, and Dirk W. Grijpma. "A review on stereolithography and its applications in biomedical engineering." Biomaterials 31, no. 24 (2010): 6121-6130.

[60] Hull, Charles W. "Apparatus for production of three-dimensional objects by stereolithography." United States Patent, Appl., No. 638905, Filed (1984).

[61] Kritchman, Elisha, Hanan Gothait, and Gershon Miller. "System and method for printing and supporting three dimensional objects." U.S. Patent Application 10/101,089, filed November 21, 2002.

[62] MakerBot Replicator - https://www.makerbot.com/3d-printers/replicator/.

[63] FormLab Form 2 - https://formlabs.com/3d-printers/form-2/.

[64] Stratasys Connex Object 350 - https://www.stratasys.com/connex3.

[65] Chepelev, Leonid, Andreas Giannopoulos, Anji Tang, Dimitrios Mitsouras, and Frank J. Rybicki. "Medical 3D printing: methods to standardize terminology and report trends." 3D printing in medicine 3, no. 1 (2017): 1-9.

[66] Ventola, C. Lee. "Medical applications for 3D printing: current and projected uses." Pharmacy and Therapeutics 39, no. 10 (2014): 704.

[67] Kalaskar, Deepak M., ed. 3D printing in medicine. Woodhead Publishing, 2017.

[68] Pandit, Anay Mahesh. "Design and manufacturing of a disposable endoscope and an overtube using 3-D printing technology." MS diss., UC San Diego, 2017.

[69] Phan, Alex, Phuong Truong, Andrew Camp, Kerrianne Stewart, Benjamin Suen, Robert N. Weinreb, and Frank E. Talke. "A wireless handheld pressure measurement system for in vivo monitoring of intraocular pressure in rabbits." IEEE Transactions on Biomedical Engineering 67, no. 3 (2019): 931-937.

[70] Gotlib, Oren, Karcher Morris, Frederick E. Spada, Madhu Alagiri, Katy Patras, and Frank E. Talke. "Investigation of Zinc-Silver Oxide-Thermoplastic Composite for Application in a Biofilm Retardant Urinary Catheter." In ASME 2019 28th Conference on Information Storage and Processing Systems. American Society of Mechanical Engineers Digital Collection, 2019.

[71] Ringel, Lars, Karcher Morris, Thomas J. Savides, and Frank Talke. “Sa 1912 Development of a new endoscope distal attachment cap for converting a front viewing scope into a side viewing scope.” Gastrointestinal Endoscopy 87, no. 6 (2018): AB246-AB247.

[72] Morris, Karcher, Minghui Zhao, Jenny Lam, Garth Jacobsen, Santiago Horgan, and Frank E. Talke. "A Wearable Neck Measurement Device and Monitoring System to Improve Ergonomic Performance of Surgeons." In Information Storage and Processing Systems, vol. 59124, p. V001T09A002. American Society of Mechanical Engineers, 2019.

Chapter 2 Initial Design of the Esophageal Deflection Device

2.1 Proof of Concept for a Modified Overtube Design

In order to prevent the esophageal thermal damage caused by atrial ablation procedures, our research team at the Talke Biomedical Device Lab has aimed to deflect the esophagus away from the heart. A wide variety of potential technical solutions presented themselves early in the design process including endoscope-like manipulators, pressurized balloons, and magnetic actuators, for example. Medical practitioners often prefer a device that is simple to use and requires very little training. A simple device can also reduce surgeon fatigue and reduce overall operation time for a procedure to deflect the esophagus. A relatively simple design idea was derived from an already ubiquitous tool in gastroenterology, the esophageal Gaurdus® overtube by U.S. Endoscopy [1]. A precurved overtube, as opposed to an initially straight overtube, could be straightened, inserted in the esophagus, and activated to assume the precurved shape, ultimately deflecting the esophagus.

The commercially available overtube, shown in Figure 31, is most commonly used in endoscopy to provide a constant opening through the mouth, into the gastrointestinal tract. The overtube allows for easy reinsertion of an endoscope and protection of the tract tissue [1]. The overtube technology consists of two parts, an outer tube and an inner tube. Once the assembled device is fully inserted into the esophagus the inner tube is removed so that the channel is as large

as anatomically feasible. At a 2cm outer diameter, the outer tube also provides a meaningful anatomical constraint for future design consideration.

Figure 31: Guardus Overtube by U.S. Endoscopy [1]

A modified overtube was designed with similar dimensions as the clinically used overtube from Figure 31. The modified overtube design included a natural, or initial, curvature. Material Jet (MJ) 3D printing, was employed to manufacture a flexible part. Stiffness can be varied using "digital materials" on the Connex Objet 350 3D printer. The part was 3D printed using a propriety photopolymer material known as "TangoBlackPlus", which cures with a rubber-like flexibility. Once the modified overtube was 3D printed and post processed by cleaning off support material, the commercially available inner tube was inserted into the inner lumen, effectively straightening the overtube. As the insertion tube was removed, the modified overtube assumed its initial curvature. The proof of concept was validated through the design, 3D print, and an initial test (see Figure 32).

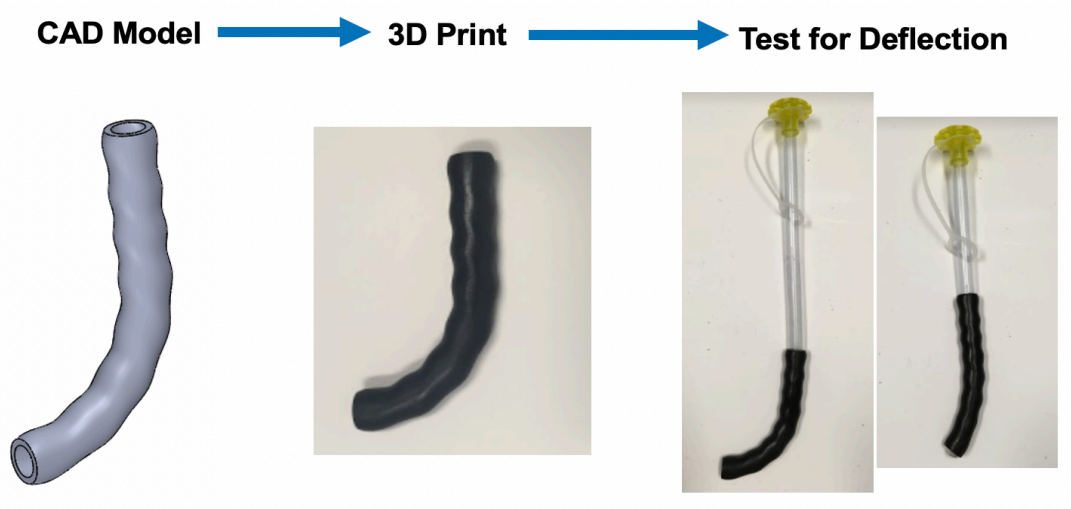

Figure 32: Proof of concept: CAD Model, 3D print, and deflection test

The proposed concept was shared with medical practitioners who have witnessed the need to prevent esophageal damage and have used endoscopes to deflect the esophagus during the ablation procedure. Their qualitative feedback led to a series of design features and changes that are explored in this and later chapters. Many of these features have been first published in the patent, “Esophageal Deflection Device” assigned to the Regents of the University of California, US20200029822A1 [2]. This chapter will also review many of the claims presented in the patented technology.

2.2 Design Features of the Esophageal Deflection Device Outer Tube and Inner Rod

A number of functional changes are needed to be made from the initial proof of concept in order to design an effective and clinically relevant Esophageal Deflection Device (EDD). Anatomical considerations are necessary to develop the proper device geometry. These include the diameter of the esophagus and the distance from the mouth to the portion of the esophagus that

needs to be deflected. Tribological factors must be considered as the device must navigate down the curvature from the mouth into the esophagus and slide along tissue without causing discomfort or damage. Usability factors must also be considered as the medical practitioner using the device must be able to easily operate and control it. The initial design and prototype from the previous section was iterated upon and further modified to address these concerns.

Figure 33 shows the design of a modified outer tube which considers many of the aforementioned constraints. The outer tube has a length larger than the distance from the mouth to the position of the esophagus that needs to be deflected. The device also has an outer diameter small enough to be easily insert into the esophagus, yet large enough to provide large areas of contact capable of distributing forces along the esophagus wall tissue, lowering potentially harmful contact pressure. The outer tube walls are a moderate thickness that can be varied to provide adequate stiffness and flexibility, and an inner lumen for an insertion rod and potentially other diagnostic or therapeutic medical equipment. The handle of the design should consider ergonomics of the medical practitioner, improving usability factors. In the device shown in Figure 33, the handle incorporates holes so that markings of any inserted item can be monitored and positioned to ensure the device is inserted the proper distance. A bellowed design was incorporated to prevent unwanted buckling during the insertion process.

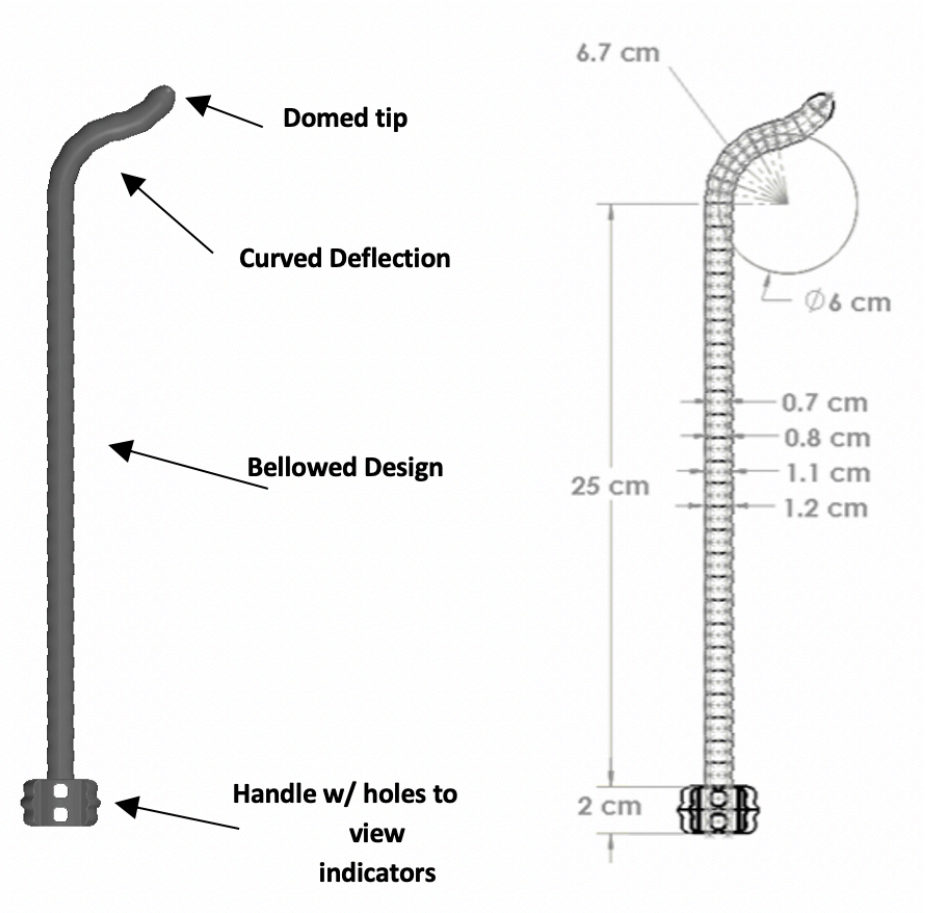

Figure 33: Modified EDD outer tube geometry

The curvature in Figure 33 is J-shaped, although various curvatures can be envisioned, such as the U-shaped example shown in Figure 34a. The designed curvature must be positioned to a reasonable distance from the handle, ~25-40 cm, so that the esophagus tissue near the heart is reachable. The J- and U-shaped designs as well as other compound variations can have different radii of curvature. The curve stiffness can be homogenously or heterogeneously varied along the tube, and the resistance to deflection is a function of curvature, outer tube cross section, and the material's mechanical properties. Figure 34b illustrates the changing of materials along the tube that can be incorporated with certain manufacturing techniques, i.e., 3D printing. The outer tube

material can include radio opaque markers to assist the surgeon with positioning of the device, as fluoroscopy is frequently used throughout the ablation surgeries for catheter placement in the heart. Figure 34c highlights varying dome structures on the distal end of the tube that improve tribological performance of the device upon insertion into the gastrointestinal tract. A hole on the tip of device can allow for "over-the-wire" insertion of the device, sometimes preferred by medical practitioners for insertion of medical devices into the gastrointestinal tract. The hole can provide an opening for the inner rod, which may improve tribological factors of increased flexibility or smoothness. The hole can be used by other medical equipment necessary to enter the esophagus or stomach during the procedure. Additional holes along the outer tube can be used to draw the esophageal walls into contact of the EDD through suction. Alternatively, the holes and inner lumen can also be used to introduce fluids or gas to the esophagus, which can be desirable for movement, cooling, or improved tribological function.

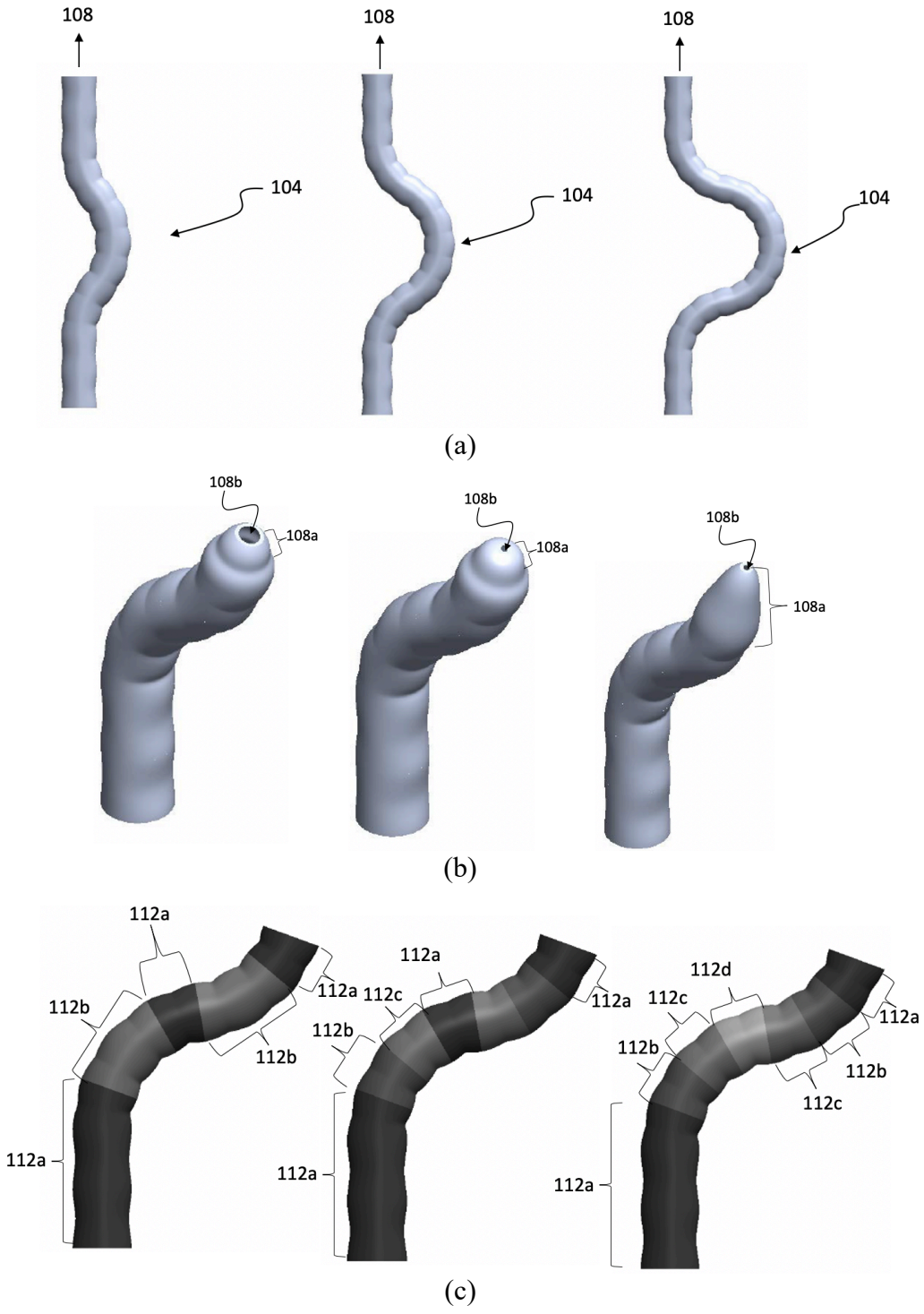

Figure 34: Outer tube Design variations described in Esophageal Deflection Device patent [2] illustrating (a) U-shaped curvature, (b) variant distal ends, and (c) varying tube stiffness.

By modifying the outer tube, the inner rod must also be re-designed. Figure 35 illustrates the proposed geometry for such a design. The length of the inner rod must extend the distance from the handle of the outer tube to at least the end of curved portion, but possibly longer and beyond the outer tube distal end. The outer diameter of the inner rod must be smaller than the inner diameter of the outer tube. A handle must be added to allow for the user to grip firmly and retract the inner rod from the outer tube. The inner rod must have enough stiffness to partially straighten the outer tube when inserted, but also have enough compliance, or flexibility, for seamless navigation into the gastrointestinal tract. The inner rod may also vary in stiffness along the length. Figure 36 illustrates a composite tip comprised of layers that can be optimized in stiffness as increased flexibility may be desirable at the distal portion of the tapered tip.

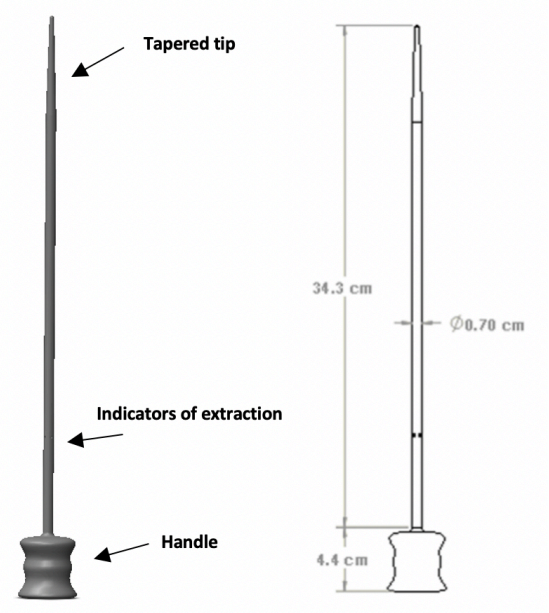

Figure 35: Modified EDD inner rod geometry

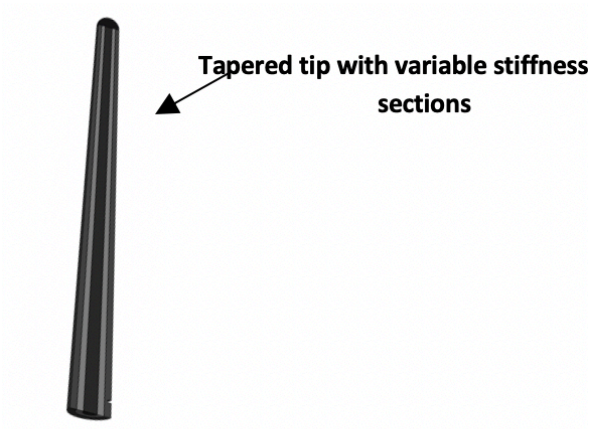

Figure 36: Modified EDD inner rod geometry

2.3 Manufactured EDD and Ex Vivo Proof of Concept

A prototype of the Esophageal Deflection Device (EDD), including the outer tube and inner rod, was manufactured with flexible, rubber-like 3D printed materials on a Connex Objet 350 3D printer. The outer tube consisted of a curved portion near the distal end, and the inner rod has a higher bending stiffness compared with the outer tube. The inner rod can be inserted into the outer tube, effectively straightening it. An example of this is shown in Figure 37.

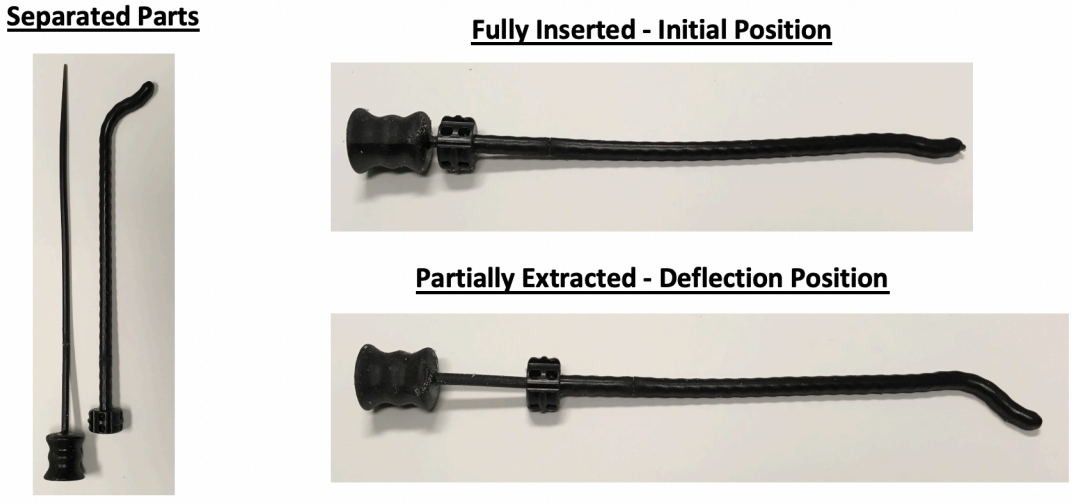

Figure 37: 3D printed Esophageal Deflection Device

In practice, the medical clinician would implement the following procedure to deflect an esophagus with the EDD.

1) The EDD is assembled, fully inserting the inner rod in the outer tube and effectively straightening the rod.
2) The assembled EDD is placed in the mouth and navigated down the esophagus
3) The EDD inner rod is retracted, partially or completely, allowing the outer tube to assume its initially curved shape and deflect the esophagus
4) The esophagus can be manipulated further by rotating the outer tube of the EDD, inserting it further into the esophagus or partially retracting it.
5) Once the ablation procedure is complete, both the EDD outer tube and inner rod may be slowly retracted.

This procedure was demonstrated in an ex vivo study in the Center for Future of Surgery at UC San Diego's School of Medicine. The EDD was assembled and inserted into porcine esophagus. It is shown in Figure 38 that the precurved outer tube tends toward its original shape, and in doing so, deflects the esophagus. The deflection does not necessarily need to be large. As seen in the figure, a deflection of about 1-2 cm is significant. It is important that the deflection is reliable even when there is other bodily connective tissue or constraints during the ablation procedure. It will be important to consider larger radii of curvature with different forms of curvature. It will also be important to understand the material used to prototype this device in terms of mechanical behavior due to deformation and deflection.

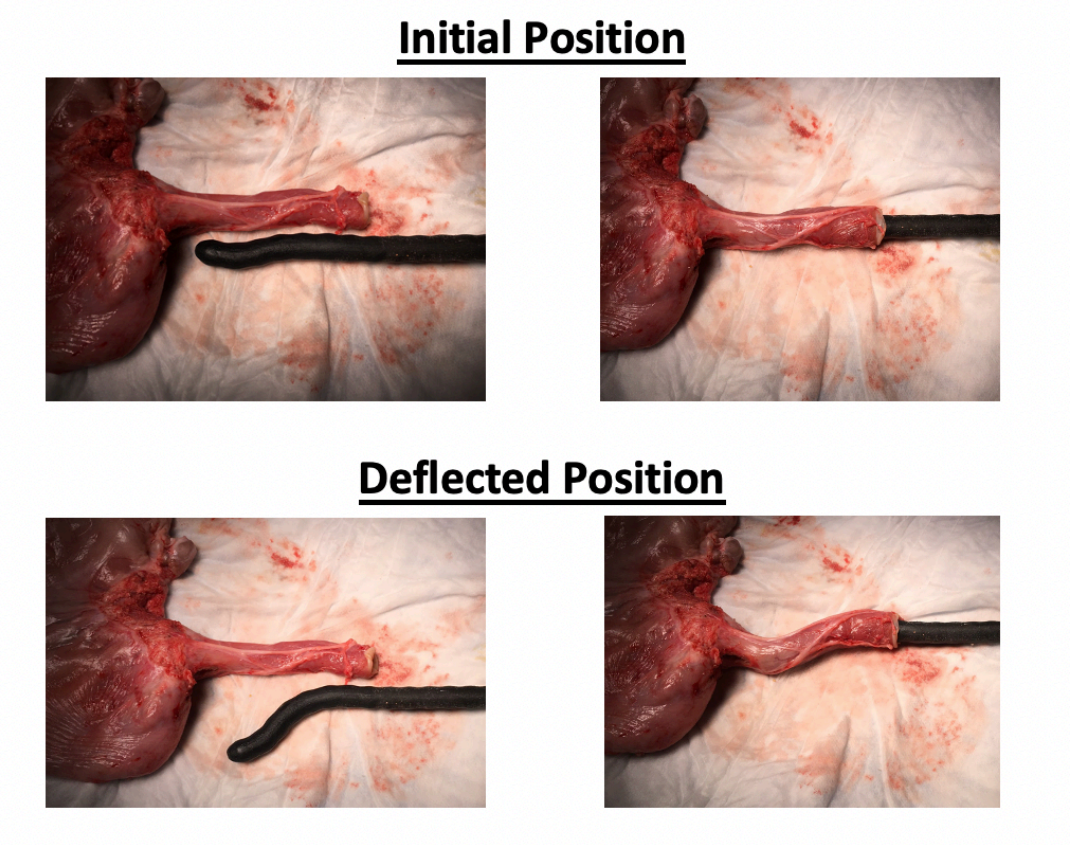

Figure 38: Ex vivo studies showing the deflection of porcine esophagus using the EDD

2.4 Addition of Thermal Sensing Technology on the EDD

Thermal sensing of the esophagus during atrial ablation is already the standard of care, with medical doctors commonly using devices like the Circa S-Cath [3]. It can be very useful to incorporate temperature sensors on the outer tube of the EDD. The sensors can be arranged in various patterns on the surface of the device and increase in density for the region expected to be closest to the heart enabling a higher spatial resolution and accuracy. With the sensors precisely

positioned, a three-dimensional heat map can be derived during use and based on these heat readings, doctors can decide on how to further manipulate the EDD and proceed with the procedure. Figures 39-41 show illustrations from [2] that indicate potential positioning of the sensors along the surface of the outer tube, in close proximity and preferably in contact to the esophageal wall. The sensors can be more densely populated near the curved portion since that is the expected location for the heart to be relative to the device.

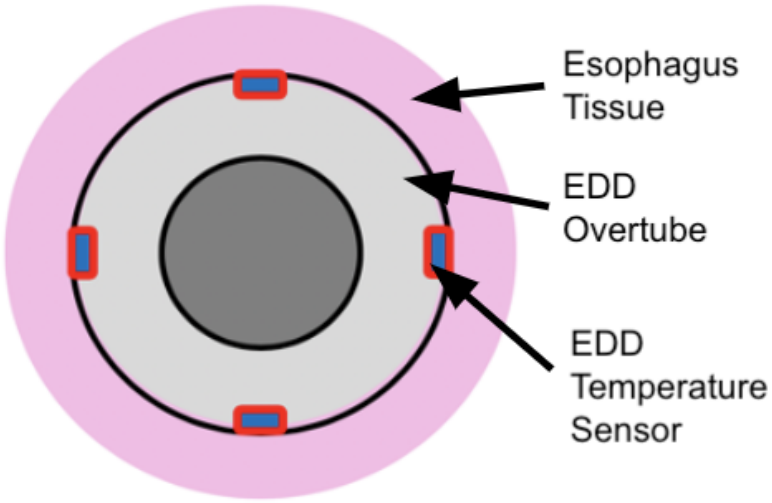

Figure 39: Temperature sensors surrounding outer tube of EDD circumferentially in order to contact esophagus wall [2].

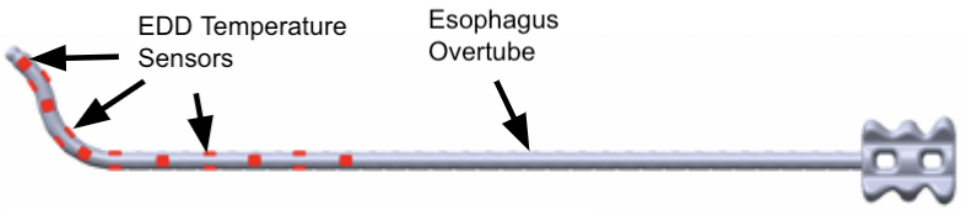

Figure 40: Temperature sensor array distributed axially along and circumferentially cross the outer tube of the EDD [2]

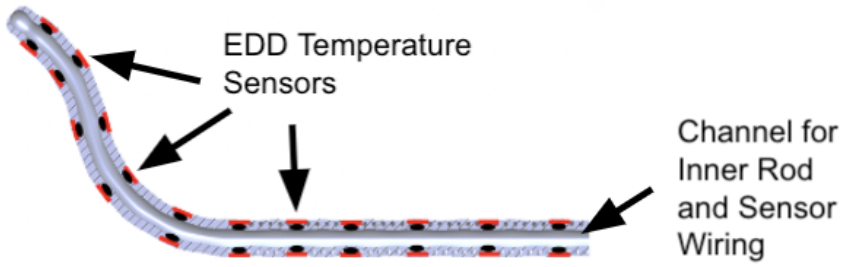

Figure 41: Temperature sensor array distributed cross section [2]

A combined approach for both deflecting and sensing has a few key advantages. The procedure can be simplified by having only one device to use instead of two. The sensors position can be pre-defined relative to the device and thus the esophagus. This is as opposed to the thermal sensors unintentionally lying next to the outer tube but on the opposite side of the heart. Furthermore, methods can be developed that assist the medical practitioner with placement or repositioning of the device as the thermal sensing can provide useful real-time feedback.

2.5 Review of the Claims in the Patent "Esophageal Deflection Device"

The following claims have been published in US20200029822A1 [2]. These claims clearly convey the novelty of certain aspects of the device, as they compare with "prior art", or the existing literature such as patents and journal articles. The claims in this patent cover both technical design aspects as well as methods to employ such a device. The technical aspects include the precurved outer tube and inner rod design for deflection and the temperature sensor array for the necessary

thermal sensing during an atrial ablation procedure. Each of the claims below can be further investigated including the ability to deflect and sense. These functions should be optimized and are functions of materials, geometry, sensor layout, and other technical aspects that will be discussed in later chapters of this thesis. The claims for US20200029822A1 "Esophageal Deflection Device" [2] are:

1. An esophageal deflection device, the device comprising: an elongate outer tube of biocompatible material having a proximal end and a distal end, the elongate outer tube being configured to contact walls of an esophagus, the elongate outer tube comprising a curved deflection between the distal end and the central portion, the elongate outer tube being flexible and resilient to maintain the curved deflection in a natural state and allow straightening of the elongate outer tube in response to force applied from within the elongate outer tube, the elongate outer tube being flexible enough to allow insertion and withdrawal from the esophagus, the curved deflection being stiffer than the esophagus such that the esophagus will conform to the shape of the curved deflection when the curved deflection is not straightened; and

an elongate insertion tube or rod having a distal end and a proximal end, the elongate insertion tube being dimensioned to slide within the elongate outer tube, at least a portion of the elongate insertion tube being stiffer than the curved deflection of the elongate outer tube to create the force applied from within the elongate outer tube to at least partially straighten the curved deflection of the elongate outer tube when the portion of the elongate insertion tube is within the curved deflection of the elongate outer tube, the elongate insertion tube being sufficiently flexible to allow insertion into the esophagus while the portion of the elongate insertion tube is within the curved deflection of the elongate outer tube.

2. The device of claim 1, further comprising:

an elongate outer tube handle at the proximal end of the elongate outer tube forming a grip for a practitioner;

an elongate insertion tube or rod handle at the proximal end of the elongate insertion tube or rod forming a grip for a practitioner.

3. The device of claim 1, wherein a length of the elongate outer tube from a central portion to the distal end is predetermined to place the curved deflection at a targeted esophagus location near the left atrium of the heart and the curved deflection is U-shaped or is compound curve shaped.

4. The device of claim 1, wherein the curved deflection of the elongate outer tube is immediately adjacent the distal end of the elongate outer tube and the curved deflection of the elongate outer tube is separated by a straight portion of the elongate outer tube from the distal end of the elongate outer tube.

5-**6**. (canceled)

7. The device of claim **5**, wherein the elongate outer tube comprises bellows and the curved deflection includes bellows having different stiffness.

8. The device of claim 1, comprising a domed tip at the distal end of the elongate outer tube with an opening in the domed tip.

9. (canceled)

10. The device of claim 8, wherein the distal end of the elongate rod or tube comprises a taper and the distal end and opening in the domed tip are sized to permit a portion of the taper to extend through the opening the in the domed tip.

11. The device of claim 1, wherein one or both of the elongate outer tube and the elongate insertion tube comprises a variable stiffness along its length.

12. (canceled)

13. The device of claim 1, comprising one or all of a depth insertion indicator, radio opaque marker, and a lumen in the insertion tube or rod.

14-**15**. (canceled)

16. The device of claim 1, wherein the insertion tube or rod comprises or consists of an endoscope.

17. The device of claim 1, wherein an outer diameter of the elongate outer tube is substantially matched to an esophagus inner diameter.

18. The device of claim 1, wherein an outer diameter of the elongate outer tube is at least half of an esophagus inner diameter.

19. The device of claim 1, wherein an outer diameter of the elongate outer tube is less than half of an esophagus inner diameter, the elongate outer tube further comprising suction ports for drawing a vacuum to draw esophagus walls into contact around the circumference of the elongate outer tube.

20. The device of claim 1, comprising a three-dimensional arrangement of plurality of temperature sensors disposed near an outermost surface of the elongate outer tube.

21. (canceled)

22. The device of claim 20, wherein the elongate outer tube comprises an outer coating and the temperature sensors are embedded in the coating.

23. The device of claim 20, wherein the temperature sensors are arranged in orthogonal pairs along the device's longitudinal axis, exceeding the average length and area that the heart is in contact with the esophagus.

24. The device of claim 20, wherein the temperature sensors are arranged in orthogonal pairs along the device's longitudinal axis, and increase in density in the region of curved deflection.

25. A method for conducting an esophageal deflection, the method comprising:

inserting an insertion rod or tube into an elongate outer tube to straighten a curved deflection in the elongate outer tube;

inserting the elongate outer tube into an esophagus with the insertion rod to place the straightened curved deflection in a targeted region of the esophagus near the left atrium; and

withdrawing the insertion rod or tube to allow the curved deflection to return to its natural shape and deflect the targeted region of the esophagus; wherein at least a portion of the elongate insertion tube is stiffer than the curved deflection of the elongate outer tube to create the force applied from within the elongate outer tube to at least partially straighten the curved deflection of the elongate outer tube.

26. The method of claim 25, further comprising: obtaining a three-dimensional heat map of the esophagus through a plurality of temperature sensors embedded near an outer surface of the elongate outer tube.

27. The method of claim 25, further comprising drawing a vacuum through a lumen in the insertion rod or tube through suction ports in the elongate outer tube to draw esophagus walls onto the circumference of the elongate outer tube.

28. The method of claim 25, further comprising introducing fluids or gas through a lumen in the insertion rod or tube.

29-32. (canceled)

2.6 Summary

The Esophageal Deflection Device (EDD) described in this section, was designed to deflect the esophagus during atrial ablation procedures. The EDD was manufactured using material jet (MJ) 3D printing. The deflection proof of concept was demonstrated using porcine esophagus tissue. A temperature sensing enabled device was also discussed.

3D printing enabled this prototype to be manufactured and iterated upon, advancing the design process. Major design decisions require the understanding of the device bending stiffness which is a function of both geometry and material. In order to make the most effective design decisions, the mechanical properties of the materials used need to be well understood and an accurate constitutive model is imperative for meaningful analytical or numerical studies of the device. The following chapter will explore how to best model the hyperelastic properties of the new 3D printed rubber-like material.

Chapter 2, in part, is a reprint of the materials as they appear in “Esophageal Deflection Device”, Karcher Morris, Scott Garner, Youyi Fu, Anay Pandit, Young Seo, Gregory Feld, Thomas Savides, Frank E. Talke, Ser. 62/468,697, 8 March 2018 (Published Patent (Pending) – US20200029822A1). The dissertation author was the primary investigator and author of this patent publication.

References

[1] Steris Guardus Overtube https://www.steris.com/healthcare/products/endoscopy-devices/foreign-body-management-devices/guardus-overtube.

[2] Morris, Karcher, Pandit, Anay M., Savides, Thomas J., Seo, Young W., Garner, Scott, Fu, Youyi, Feld, Gregory, and Talke, Frank E. "Esophageal deflection device." U.S. Patent Application 16/488,453, filed January 30, 2020.

[3] Circa Scientific - S Cath - https://www.circascientific.com/products/circa-s-cath-us/

Chapter 3 Uniaxial and Biaxial Testing of 3D Printed Hyperelastic Photopolymers

3.1 Introduction

Three-dimensional (3D) printing is extensively used in the early stages of product design as, for instance, in the design of medical devices [1-4] and soft robotic actuators [5-7]. In these applications, the knowledge of the material's properties of the 3D printed materials is essential since the materials often undergo large deformations while still supporting loads. Thus, the evaluation and characterization of the mechanical behavior of 3D printed materials is important for the design and prototyping process, and a detailed knowledge of the constitutive equations is essential [8, 9]. However, limited information and data related to the mechanical properties and the constitutive equations of 3D printed material is available in the open literature. Rubber-like photopolymers with a hyperelastic material response are among the most widely used materials for 3D printing [10].

Large deformations of hyperelastic materials have been studied by Mooney, [11] Rivlin [12], Treloar [13], and Ogden [14]. For these materials, the elastic modulus can no longer be considered as constant for all induced strains. Each of the mentioned models proposed a higher

order isotropic constitutive equation derived directly from extension ratios or the invariants of the Cauchy–Green deformation tensor relating principal extensions to strain energy.

To obtain accurate material models for hyperelastic materials, uniaxial, equibiaxial, or biaxial testing needs to be performed. Sasso et al. studied hyperelastic rubber-like materials using uniaxial and equibiaxial testing [15]. After fitting multiple material models, they validated their mechanical characterization by comparing planar tension testing with finite element modeling. Uniaxial tension testing of a commonly used 3D printed hyperelastic material, TangoPlus, has been performed by Liljenhjerte et al. [16]. They printed uniaxial coupons in two perpendicular directions to investigate the anisotropic behavior and differences in material model parameters and maximum extension. Subsequently, they used finite element analysis to validate their results. Wang et al. utilized 3D printing techniques to combine two 3D printed materials, VeroBlackPlus and TangoPlus, to design and manufacture phantom aortic tissue with similar mechanical properties [17]. Bodaghi et al. investigated thermomechanical properties of 3D printed material mixtures in order to design self-expanding/shrinking structures [18]. Uniaxial, tests were performed, and anisotropic material properties were identified.

Biaxial testing of hyperelastic material has also been performed by Seibert et al. [19]. Special care was taken to produce the coupons used in their biaxial testing, and a number of material models were implemented, including the Mooney–Rivlin model, to better understand the response of hyperelastic materials to large deformations. The present investigation extends the previous studies [11-19] by performing uniaxial and biaxial tests for a commonly used 3D printed photopolymer, TangoBlackPlus. The material coefficients of different material models are determined based upon uniaxial and biaxial testing data. Special emphasis was given to the design of the coupons for biaxial testing in order to ensure a homogenous strain field in the evaluation

area. Using the obtained material coefficients, we have applied finite element analysis to determine the deflection of a hollow tube undergoing large deformation to show the dependence of the results on the material models derived from biaxial and uniaxial tests.

3.1.1 Common Hyperelastic Material Models

The Mooney–Rivlin model is commonly used to describe hyperelastic materials. The strain energy function, W, can be described as follows assuming incompressibility and isotropy:

$$W(I_1, I_2) = C_{10}(I_1 - 3) + C_{01}(I_2 - 3) \tag{3.1}$$

where C_{10} and C_{01} are the material coefficients. I_1 and I_2 are the first and second principal invariants defined using the principle extension ratios. The invariants can be mathematically described using the Cauchy–Green deformation tensor, D_R, and the principal extension ratios λ_i:

$$I_1 = \mathrm{tr}(D_R) = \lambda_1^2 + \lambda_2^2 + \lambda_3^2, \tag{3.2}$$

$$I_2 = \frac{1}{2}\left[\mathrm{tr}\left(D_R^2\right) - \left(\mathrm{tr}\left(D_R^2\right)\right)^2\right] = \lambda_1^2\lambda_2^2 + \lambda_2^2\lambda_3^2 + \lambda_3^2\lambda_1^2, \tag{3.3}$$

$$I_3 = \det(D_R) = \lambda_1^2\lambda_2^2\lambda_3^2 \tag{3.4}$$

where $\lambda = \varepsilon + 1$. For ~~sim~~ple ex~~t~~ension, assuming incompressibility ($I_3 = 1$), and with $\lambda_1 = \lambda$, $\lambda_2 = \lambda_3 = 1/\sqrt{\lambda}$, the stress–stretch relation of the Mooney–Rivlin model can be simplified to:

$$\sigma = \left(2C_{10} + \frac{2C_{01}}{\lambda}\right)\left(\lambda^2 - \frac{1}{\lambda}\right) \tag{3.5}$$

Another commonly used model is the Neo-Hookean model, which is a special case of the Mooney–Rivlin model in which C_{01} reduces to 0.

The Ogden material model considers hyperelastic behavior found in many rubber-like polymers undergoing large deformations and strain. In this model, strain energy, W, directly depends on the principal extension ratios and is described as:

$$W(\lambda_1,\lambda_2,\lambda_3) = \sum_{p=1}^{N} \frac{\mu_p}{\alpha_p}\left(\lambda_1^{\alpha_p} + \lambda_2^{\alpha_p} + \lambda_3^{\alpha_p} - 3\right) \tag{3.6}$$

where μ_p and α_p are the material constants to be fitted, and N is a positive integer commonly assumed to be 3. This model can be simplified considering incompressibility and uniaxial tension resulting in the stress–stretch relation:

$$\sigma = \sum_{p=1}^{N} \mu_p\left(\lambda^{\alpha_p} - \lambda^{-\frac{1}{2}\alpha_p}\right) \tag{3.7}$$

The Ogden model is generally used to capture stress–stretch curve inflections of a polymer at large strains before failure; the latter behavior cannot be modeled with the Neo-Hookean or the Mooney–Rivlin model. Further details have already been published elsewhere [20,21].

3.2 Experimental Study

3D printing of test coupons was performed using material jet 3D printing [22]. This method, illustrated in Figure 42, enables the mixing of materials, as different types of photopolymers can

be jetted at various locations and layered on the “build” surface. In material jet 3D printing, an ultraviolet (UV) light is used to cure, or harden, the photopolymer, that is, crosslinking the monomers and polymer chains.

By using material jet technology and mixing different photopolymers, single 3D printed parts can be manufactured with continuous and gradual changes of mechanical properties. Stiffness properties can be varied smoothly from one point to another. Rigidity and flexibility of the printed material are not only a function of the geometry but also a function of the manufacturing process. The PolyJet material jet 3D printing process consists of four main steps: (1) photopolymer resin is jetted from an array of nozzles in specified locations onto a support, the so-called build plate, (2) an UV light cures the photopolymer sprayed onto the surface allowing crosslinking to occur, (3) a metal roller flattens and removes residual surface material, and (4) the build plate is lowered and another layer is deposited in a similar manner.

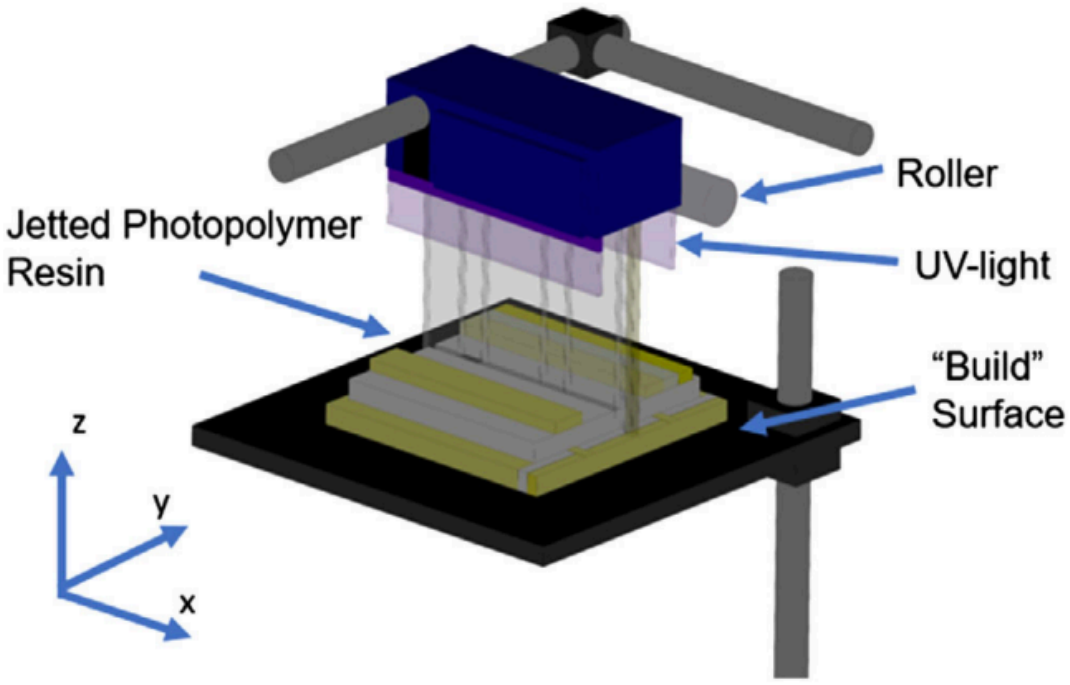

Figure 42: Material jet 3D printing schematic showing photopolymer jetting UV light, and xyz translational degrees of freedom.

Test coupons composed of TangoBlackPlus were manufactured using a commercially available material jet 3D printer (Stratasys Objet350 Connex3). The material properties of TangoBlackPlus as provided by Stratasys are shown in Table 3 [19].

Table 3: Material Properties for TangoBlackPlus as Specified By the Supplier [19].

	ASTM	Metric
Tensile strength (MPa)	D-412	0.8–1.5
Elongation at break (%)	D-412	170–220
Compressive set (%)	D-395	4–5
Shore hardness (Scale A)	D-2240	26–28
Tensile tear resistance (kg cm^{-1})	D-624	2–4
Polymerized density (g cm^{-3})	D-792	1.12–1.13

3.2.1 Uniaxial Testing

The Mooney Uniaxial coupons as shown in Figure 43 were fabricated according to ASTM D-412 standards for tensile testing of vulcanized rubber. Stepped, or jagged, edges are often found where curvature was intended due to inaccuracies caused by the 3D printing process. Because of this, minor coupon modifications were made to ensure a smooth curvature from the gripped portion to the neck on each end. The final design and the printed part are shown in Figure 43(a,b), respectively. The 3D printed orientation on the printer build plate is shown in Figure 43(c) indicating that uniaxial coupons were printed in transverse and longitudinal directions

corresponding to the build plate x- and y-directions. Uniaxial testing was performed using a commercially available tensile tester (MTS Criterion tester) with a SMT-250N load cell for increased sensitivity (Figure 44). A camera was used to detect strain using digital image correlation. The extension rate was kept constant at 0.05 mm s^{-1}.

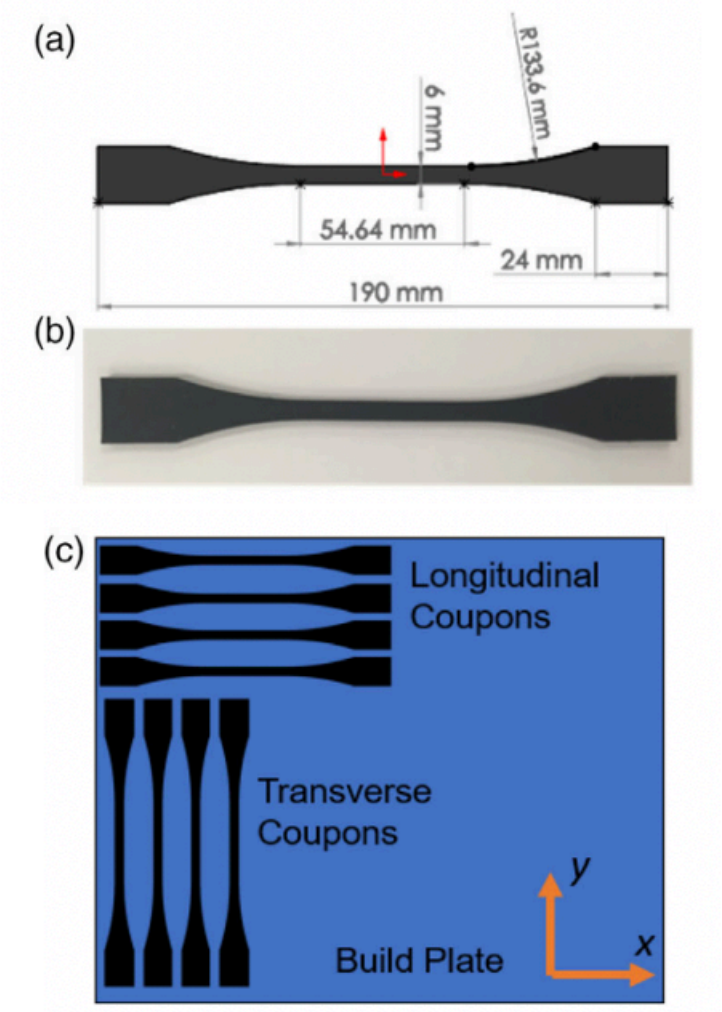

Figure 43: (a) CAD design for the uniaxial coupon, (b) 3D printed coupon prior to testing, and (c) schematic illustrating the placement of the coupons on the 3D printer build plate to study the influence of printing direction on mechanical properties.

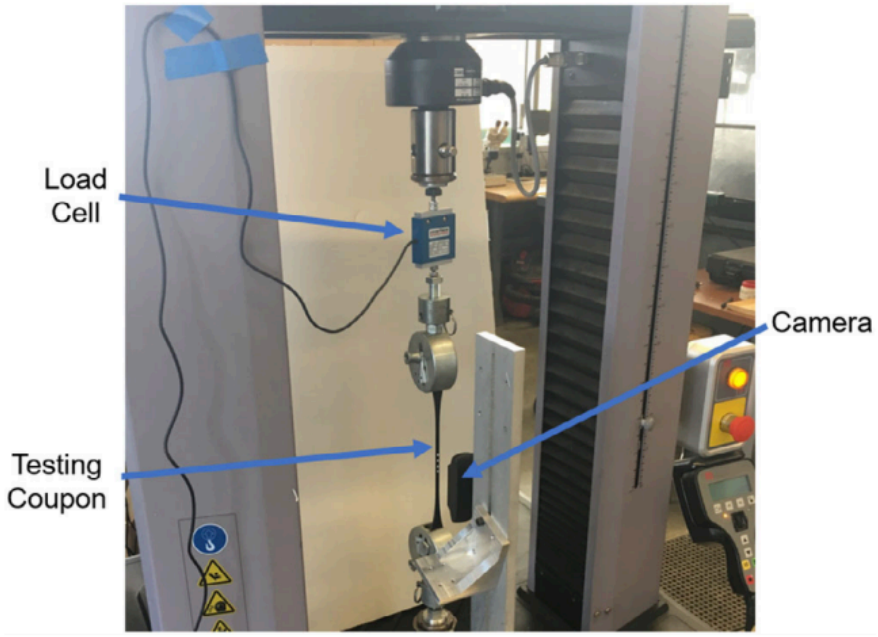

Figure 44: MTS criterion tester with loaded coupon and camera set up.

3.2.2 Biaxial Testing

The Mooney Novel biaxial coupons (Figure 45) were fabricated taking advantage of material mixing unique to material jet 3D printing. Biaxial testing of rubber-like materials is strongly affected by the clamping conditions of the sample coupon. The clamping regions (see Figure 45) were printed with a mixture of TangoBlackPlus and VeroClear while the center section was printed with pure TangoBlackPlus, which is the material of interest in this study. VeroClear is a PolyJet photopolymer that, when cured, has an approximately 10,000 times larger elastic modulus than TangoBlackPlus. Between the outside clamped areas and the softer inner area of interest made up of 100% TangoBlackPlus, a gradual transition occurs with step sizes ranging from 2.5 to 0.25 mm with a varying percentage of VeroClear and TangoBlackPlus to give a smooth gradient in stiffness [Figure 45(a)]. Cutouts are implemented in the coupon, as shown in Figure 45(a), to isolate the clamped region from the center region to be tested. This improved design

provides an increased amount of total strain as well as a uniform strain field at the center of the coupon. Biaxial coupons were printed and oriented with the x and y-axes, as shown in Figure 45(c). Special care was taken with all samples to remove support material without using sodium hydroxide-based solutions.

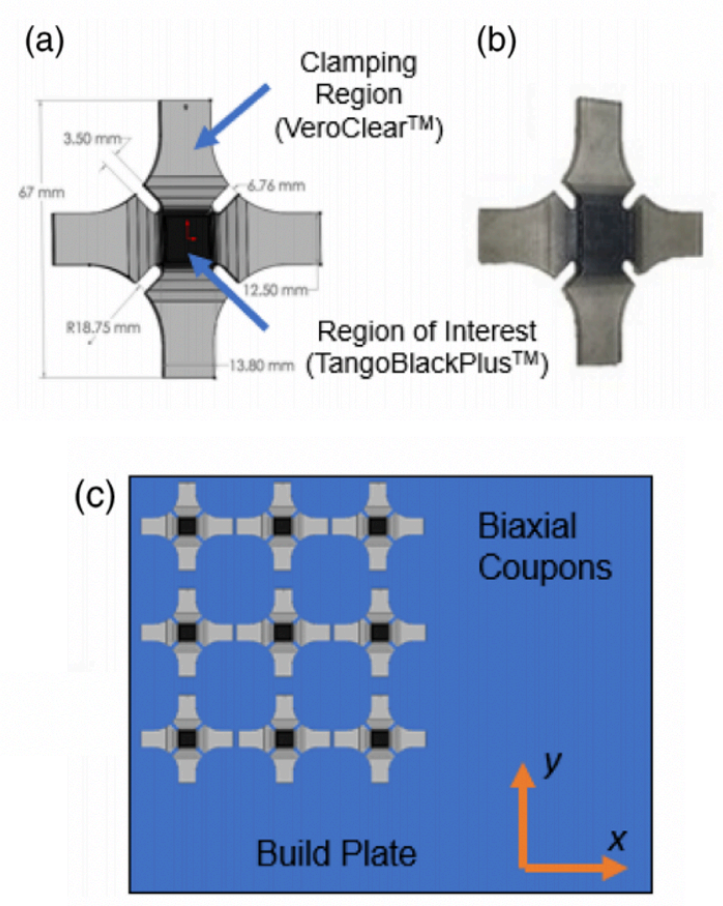

Figure 45: (a) CAD design for the biaxial coupon, (b) 3D printed coupon prior to testing, and (c) schematic illustrating the placement of the coupons on the 3D printer build plate to study the influence of printing direction on resulting mechanical properties.

Biaxial tests were performed using the custom-built biaxial testing apparatus [24] shown in Figure 46. The biaxial testing setup, described further in [24], used four stepper motors with individual spindle units. The motor and spindle system were arranged so that the middle section of the sample remained at the same position. Both axes were controlled independently of each

other, allowing the coupon to be exposed to any desired deformation state. The control of the setup was implemented in LabVIEW.

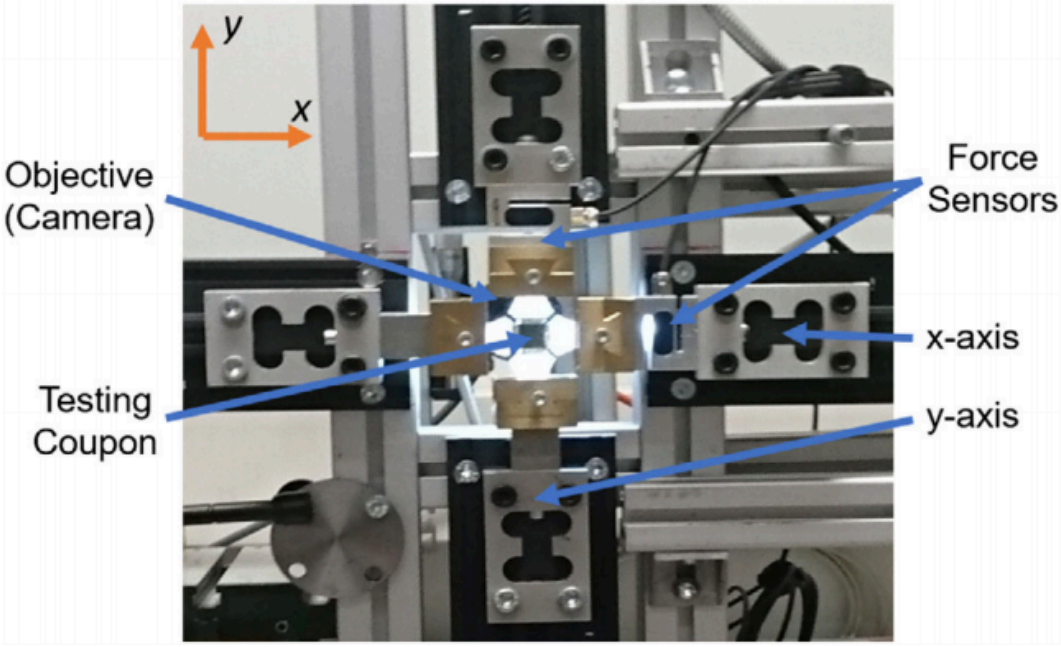

Figure 46: Biaxial testing apparatus with biaxial coupon.

The test procedure for biaxial testing was as follows: First, the sample was prestretched in the y-direction to a predefined value, leading to an essentially uniaxial deformation state in the y-direction. Thereafter, the y-displacement was kept constant for the remainder of the experiment, while the x-displacement was increased stepwise until rupture of the sample occurred. This procedure is equivalent to transforming an initial uniaxial deformation state into a complex biaxial deformation state. After each displacement increment, the sample was allowed to relax before forces in the x- and y-directions were measured using load cells.

In order to determine the strain in each direction for each step increment, a speckle pattern was initially spray coated on the surface of the sample. Correlation algorithms were then used to

compare the deformed speckle pattern after each stretching step with the initial speckle pattern, using commercially available software (ISTRA 4D [Dantec Dynamics], Skovlunde, Denmark). The strain in the z-direction was calculated from the strain in the x- and y-directions and by the condition of incompressibility. The cross-sectional area was calculated assuming homogeneous deformation in the center of the coupon. Assuming a principal axis system, the Cauchy stress was determined by dividing the measured forces by the current cross-sectional area perpendicular to each.

3.3 Results and Discussion

Stress–stretch curves of longitudinally and transversely 3D printed TangoBlackPlus coupons are shown in Figure 47(a,b), respectively, for uniaxial testing. From Figure 47(a,b), we have calculated that the elastic modulus is approximately 0.35 MPa at 50% strain with an elongation of approximately 70% at break. These results do not depend on the printing direction. The Mooney–Rivlin coefficients for longitudinally and transversely printed coupons are:

$$C_{10} = 0.008 \pm 0.004\text{MPa}, C_{01} = 0.0970 \pm 0.006\ MPa \quad longitudinal$$

$$C_{10} = 0.009 \pm 0.004\text{MPa}, C_{01} = 0.094 \pm 0.005\ MPa \quad transverse$$

Clearly, the Mooney–Rivlin material coefficients do not depend on the printing direction. A similar conclusion can be drawn for the Neo-Hookean material coefficients, given by:

$$C_{10} = 0.071 \pm 0.003\ MPa \quad longitudinal$$

$$C_{10} = 0.071 \pm 0.004\ MPa \quad transverse$$

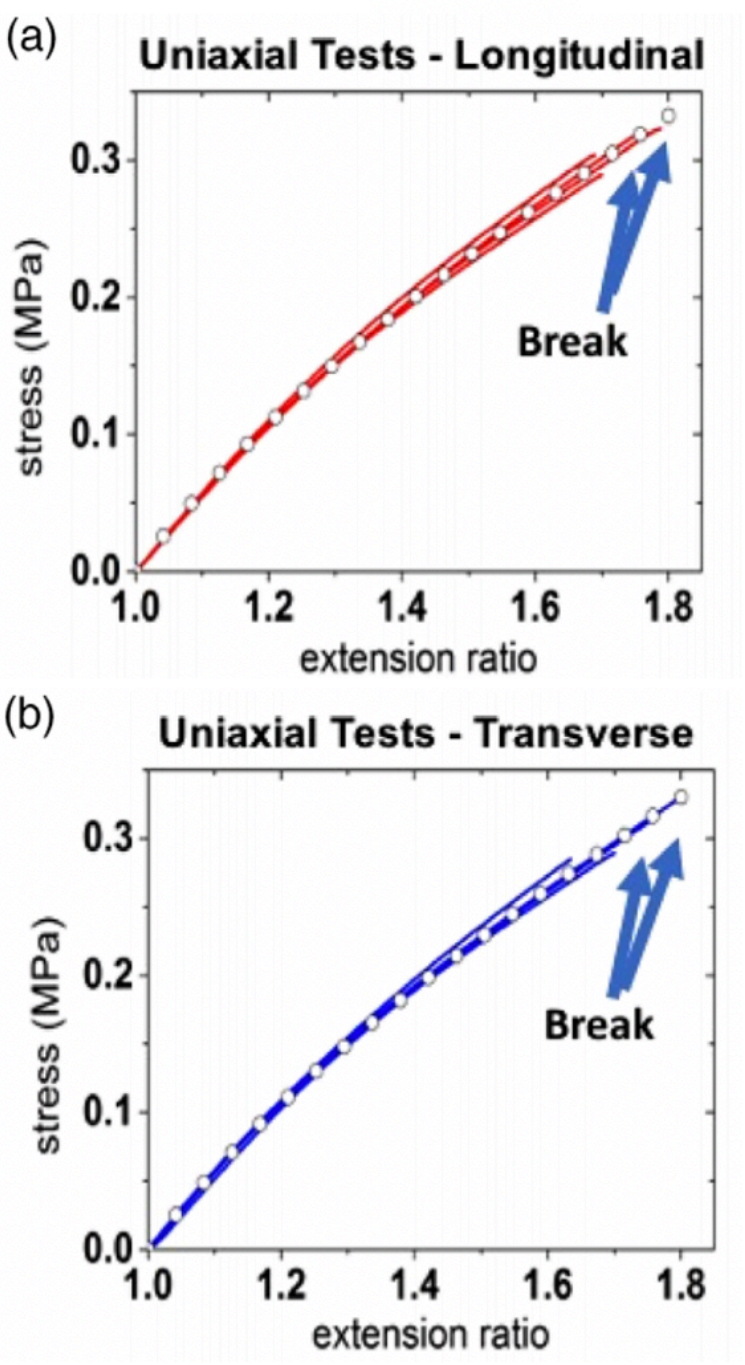

Figure 47: Uniaxial testing results for (a) longitudinally and (b) transversely printed coupons and their respective coupons after break (c,d). The solid lines in (a) and (b) represent experimental data, while the open circle represents the Mooney-Rivlin fit.

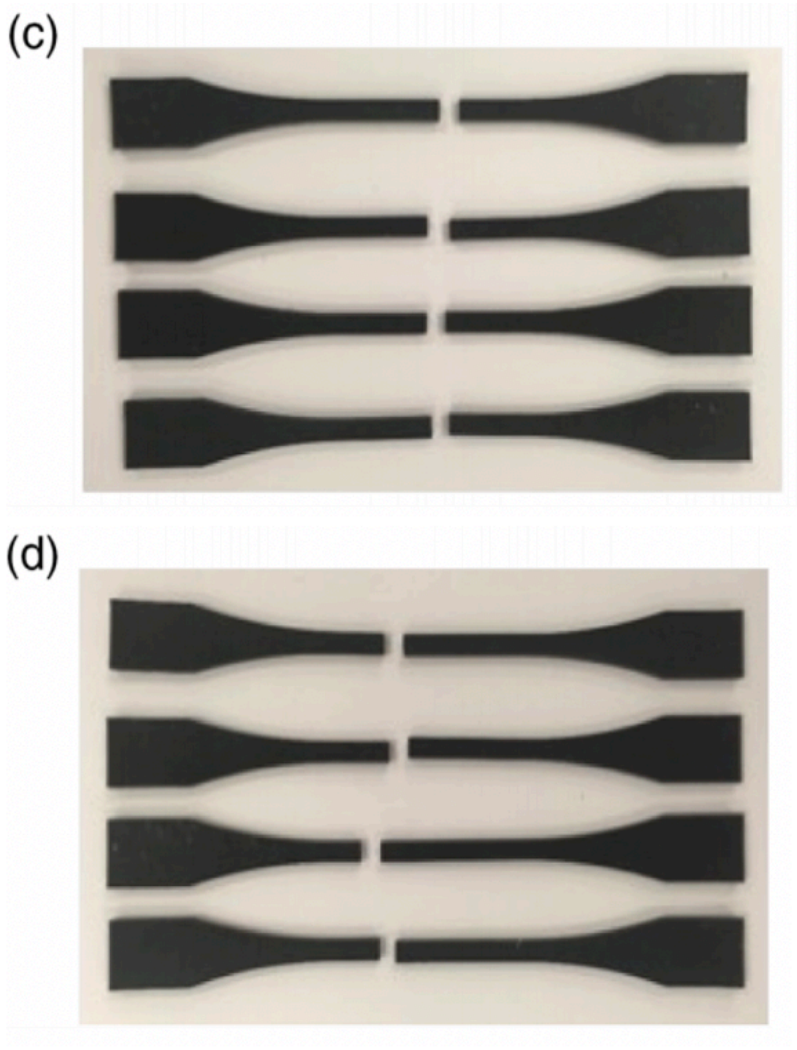

Figure 47 Continued.

After elongating to break, scanning electron microscopy (SEM) was used to image the surface of the broken cross sections. Independent of the coupon's printing direction, individual laminates, or layers, can be seen normal to the x-direction for longitudinally printed coupons [Figure 48(a)] and, similarly, normal to the y-direction for transversely printed coupons. Layering, due to the 3D printing process, is visibly normal to the z axis in Figure 48(b). We observe that the thickness of each individual layer varies slightly and is approximately 20 μm.

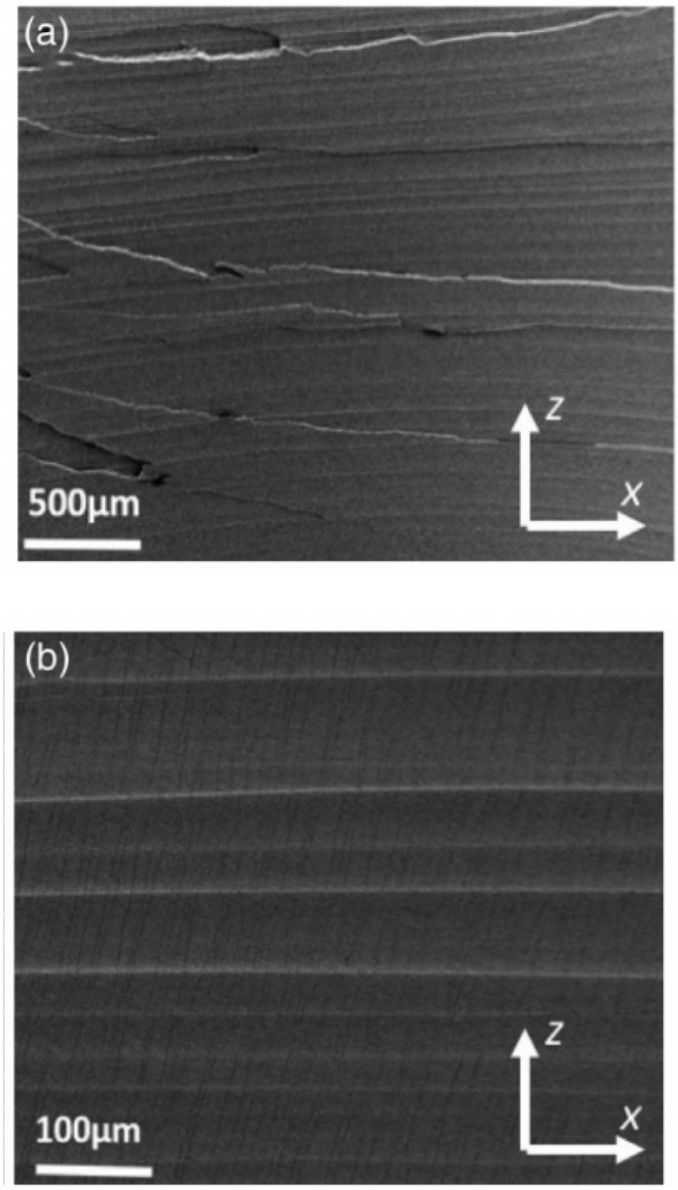

Figure 48: SEM micrographs of uniaxial coupons after testing which illustrate (a) lamination of the interface from rupturing and (b) layering caused by 3D printed process. The TangoBlackPlus photopolymer has been deposited and cured layer-by-layer normal to the z-direction.

The SEM micrographs illustrate a microstructure unique to additive manufacturing of photopolymers. Again, the difference in the microstructure of transversely and longitudinally 3D printed coupons was found to be minor.

Figure 49 shows time-dependent plots for displacement and force in the x- and y-direction for biaxial testing as a function of time. As can be seen in Figure 49(a), the biaxial test coupon was first prestretched in the y-direction. After a holding time of 300 s, the displacement in the x-direction was increased stepwise. The prestretching in the y-direction induced a time-dependent response in both the x-and y-direction as shown in Figure 49(b) due to relaxation. The stepwise increase of displacement in the x-direction leads to a stepwise increase of the force in the x- and y-directions. As can be seen from Figure 49, at a time of 1000 s when the displacements in the x- and y- directions are equal, the forces in the x- and y-directions are equal. A holding time of 90 s for each individual step was selected to allow complete relaxation to occur. The displacement and force measurements at the end of each holding time step are plotted versus time in Figure 49(c,d), respectively.

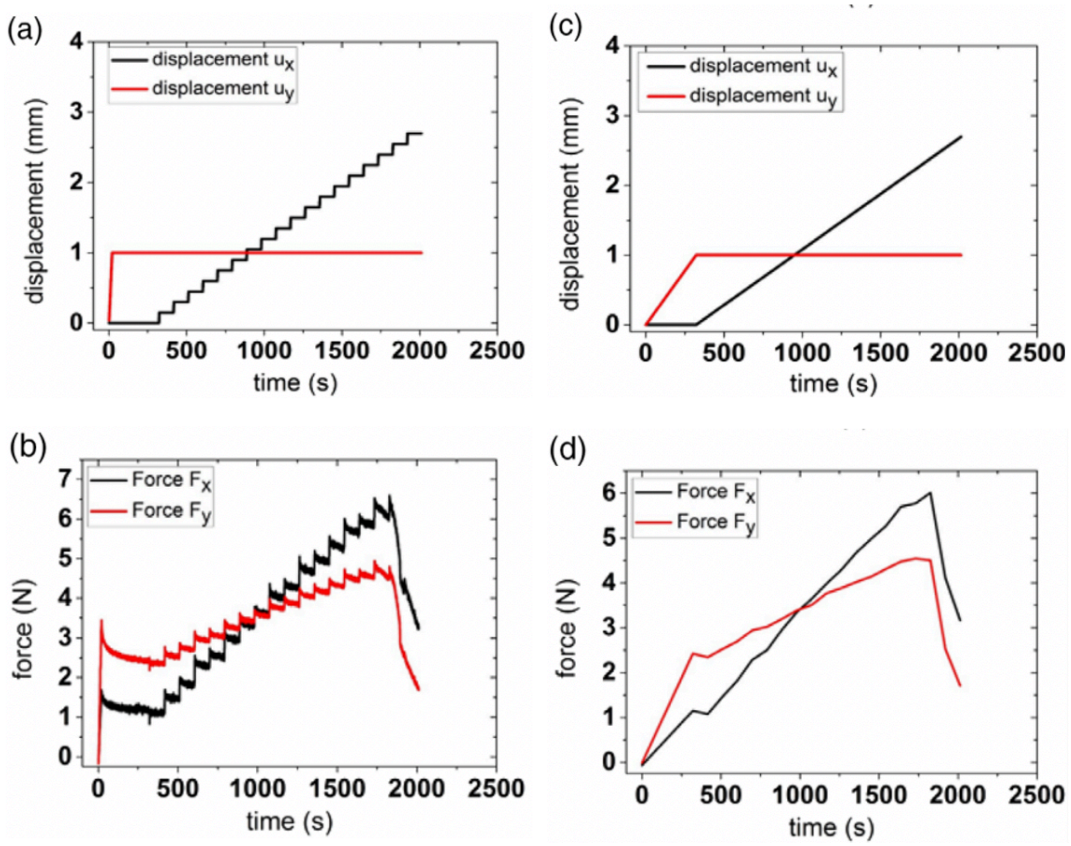

Figure 49: (a) Displacement and (b) force versus time plots showing the pre-stretching in y-direction and the stepwise stretching in x-direction as well as the respective force response in both directions. (c,d) Smoothened displacement- and force-time curves, respectively.

Figure 50(a) shows typical strain measurement results using digital from Figure 50(a), the strain field is uniform in the middle of image correlation. For each individual step increase, a new image the sample. In Figure 50(b), the measured strain is plotted versus was acquired to estimate the respective strain. As can be seen the total number of steps. We observe that prestretching in the y-direction leads to an initial increase of strain in the y-direction and a negative initial strain in the x-direction. Increasing the strain subsequently in the x-direction causes a decrease of the strain in the y-direction.

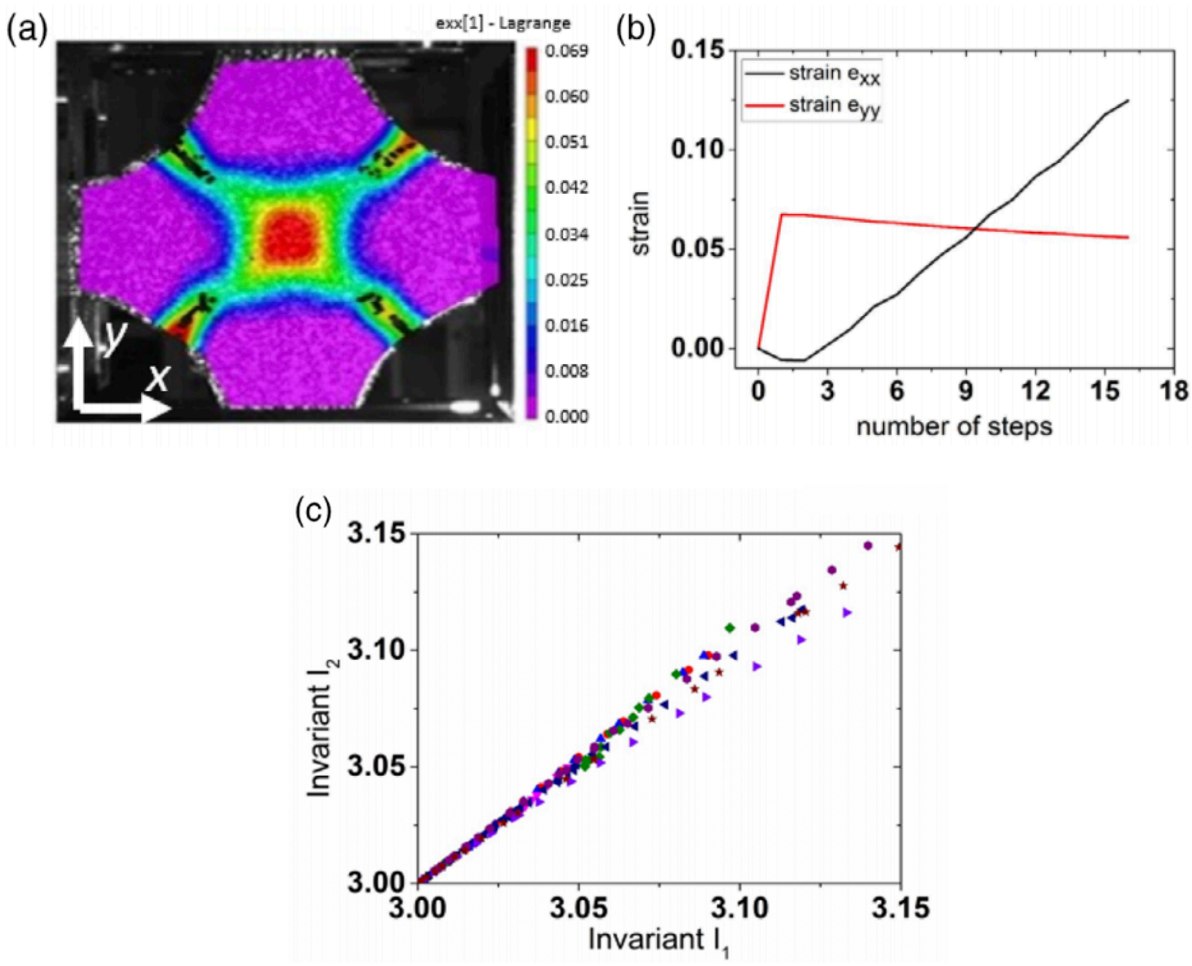

Figure 50: (a) Strain measurements (Lagrange) of biaxial coupon undergoing equibiaxial load using digital image correlation with a speckle pattern, (b) strain versus number of individual steps, and (c) derived invariants I_1, and I_2 based upon biaxial testing.

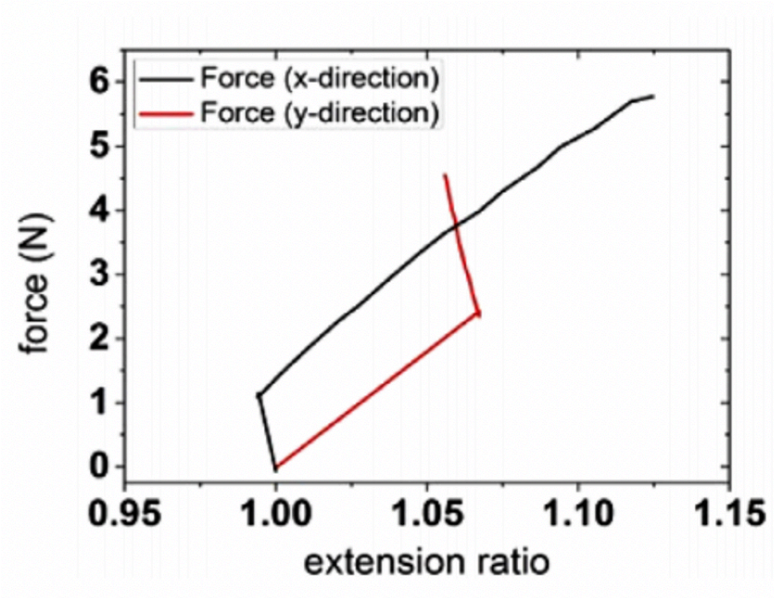

(a)

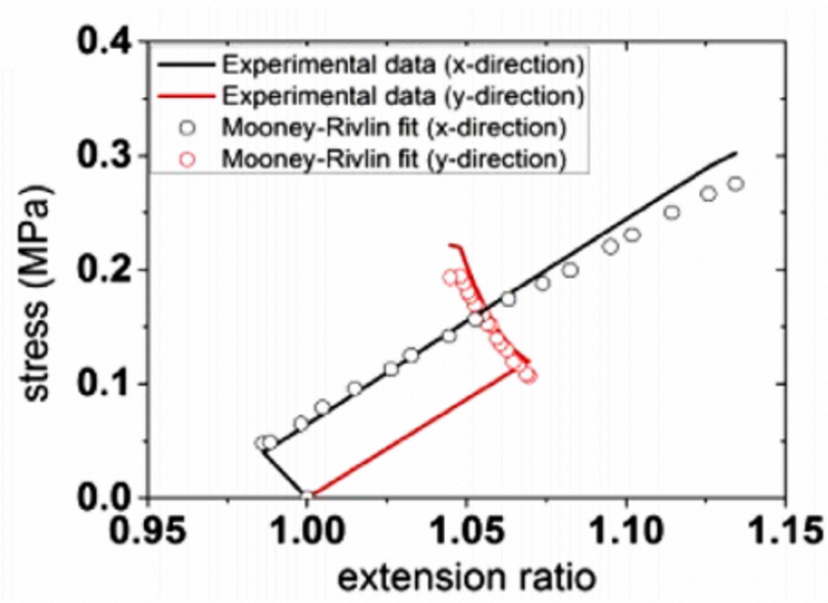

(b)

Figure 51: (a) Force versus extension ratio for a selected value of prestretching in the y-direction. (b) Experimental results and numerical fit for the first-order Mooney-Rivlin model.

Figure 50(c) shows a plot of the first and second principal invariants of the Cauchy–Green strain tensor as calculated from nine biaxial tests. Each point represents a unique deformation state of the coupon induced by different initial prestretching magnitudes in the y-direction. We note that a multitude of deformation states is observed for the first and second invariant using biaxial testing.

Combining the force response, plotted in Figure 49(d), and the strain measurements, given in Figure 50(b), we obtain a plot of force versus extension ratio [Figure 51(a)].

Due to the prestretching in the y-direction, the force in the x-direction increases initially while the extension ratio decreases [Figure 51(a)]. Thereafter, the force in the x-direction increases with an increase in the extension ratio. The force response in the y-direction shows first an increase due to prestretching. Then, as the force in the y-direction increases, a slight decrease in extension ratio is shown, which can be correlated with the stepwise stretching in the x-direction and the Poisson's ratio [Figure 51(a)]. Figure 51(b) shows the parameter fit to a selected biaxial test. Using data from biaxial testing, we derived both material coefficients C_{10} and C_{01} of the Mooney–Rivlin model. It is important to state that only biaxial testing allows for a unique identification of both coefficients. Across the nine biaxial tests with varying prestretching, the representative Mooney–Rivlin coefficients were found to be:

$$C_{10} = 0.1021\ MPa,\ C_{01} = 0.1473\ MPa$$

From the results above, we observe that the coefficients of the material models vary depending on the test used to derive them. In particular, our results show a significant difference in the Mooney–Rivlin coefficients depending on whether the parameters were derived from uniaxial testing or biaxial testing. Since incompressibility is assumed for strain calculations in uniaxial testing, the second invariant depends on the first invariant. Because of this, the first

Mooney–Rivlin coefficients C_{10} and C_{01} cannot be uniquely defined from uniaxial testing. The Mooney–Rivlin coefficients based upon data from uniaxial testing agree well with results presented by Liljenhjerte et al. [16], in which it was found that material jet 3D printed materials have a similar response in both the longitudinal and the transverse directions for uniaxial tests. Liljenhjerte et al. found that elongation at break is a function of the orientation of the printed samples [16]. Our uniaxial results correspond to an elongation of approximately 70% at break irrespective of the printing direction. Reasons for this discrepancy seem to be related to the hyperelastic characteristics of the photopolymer resin or to differences in the 3D printing process. Differences in the design of the coupons may also have influenced elongation at break by decreasing the likelihood of fracture at the curved edges near the clamped regions.

Uniaxial and biaxial testing results indicated that the material behaved quasi-isotropic with respect to the printing directions used in this study. The major benefit of performing biaxial tests as opposed to uniaxial tests is that the coefficients of the Mooney–Rivlin model can be uniquely derived from a large number of deformation states. Thus, both coefficients of the Mooney–Rivlin model (C_{10} and C_{01}) were fitted and found to be significant. In contrast, if a bulk material is deformed in simple extension, then a one-parameter Neo-Hookean or Mooney– Rivlin model based upon only uniaxial data is the only choice for parameter estimation. However, in the case of a complex deformation state, the simplified Neo-Hookean or Mooney–Rivlin models are insufficient and biaxial testing is necessary to capture the influence of both invariants through the C_{10} and C_{01} coefficients. Thus, it is apparent that the evaluation of a multiplicity of deformation states is desirable and leads to a more accurate material model as compared to uniaxial testing.

Table 4: Implemented Material Models for Device Deflection [23].

Model	Input parameters (MPa)
Linear elastic (min)	$E = 0.66$
Linear elastic (max)	$E = 2.14$
Neo-Hookean (uniaxial)	$C_{10} = 0.071$
Mooney–Rivlin (uniaxial)	$C_{10} = 0.009$ $C_{01} = 0.096$
Mooney–Rivlin (biaxial)	$C_{10} = 0.1021$ $C_{01} = 0.1473$

After evaluation of the material parameters, we have used the elastic modulus for TangoBlackPlus as provided by the supplier (minimum and maximum values in Table 4) as well as our derived material coefficients as material input parameters for a finite element simulation for the flattening of a curved hollow tube (Figure 52) undergoing large deformations.

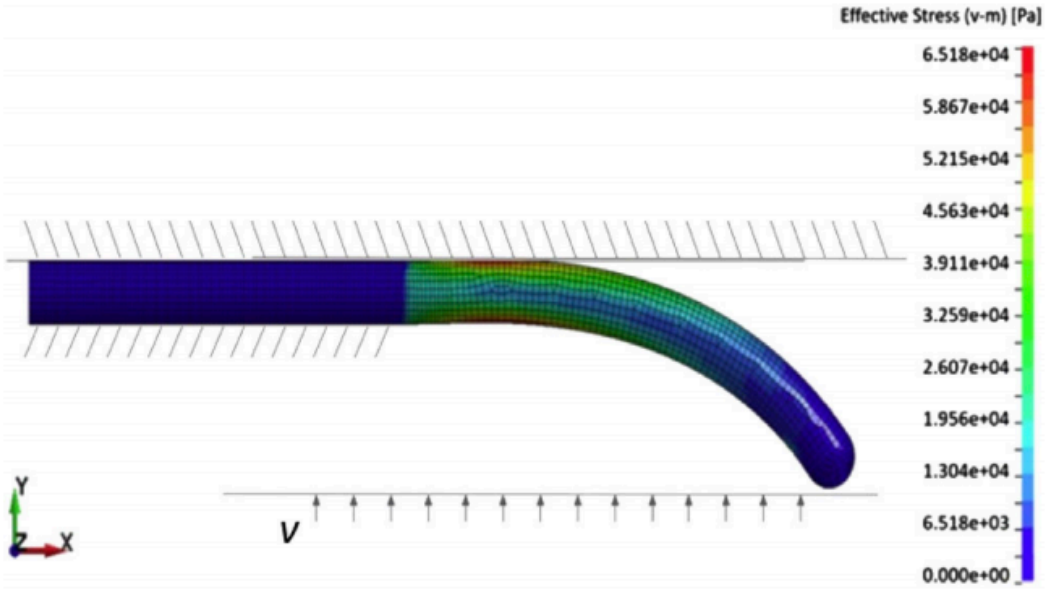

Figure 52: Finite element simulation of a curved cylindrical tube being straightened with illustrated boundary conditions.

This test case was motivated by our present work on 3D printed disposable endoscope-like devices [25]. Due to the large deformation attained by these devices during use, complex deformation states are observed and the question arises as to how large the influence of the material parameters used is on simulation results.

The curved hollow tube geometry was comprised of straight and curved sections with an inner and outer diameter of 8 and 12 mm, respectively. The curved portion had an initial radius of curvature of 30 mm. A slight inflection at the end tip of the curve was added to aid in the initial flattening of the device in the transient simulation. The calculations of the maximum force required for straightening the tube were performed with LS-DYNA. Solid eight-node brick elements were used to mesh the geometry. The straight section of the tube was constrained in all six degrees of freedom. The upper surface was assumed to be stationary, while the lower surface was moved slowly at a velocity, v, against the curved tube to straighten it.

LS-DYNA incorporates a variety of material models including linear elastic, Neo-Hookean, and the two-parameter Mooney– Rivlin model. Using these models together with the data provided by the supplier and our experimental data (Table 4), we have plotted in Figure 53, the maximum forces on the moving rigid wall during straightening of the curved tube.

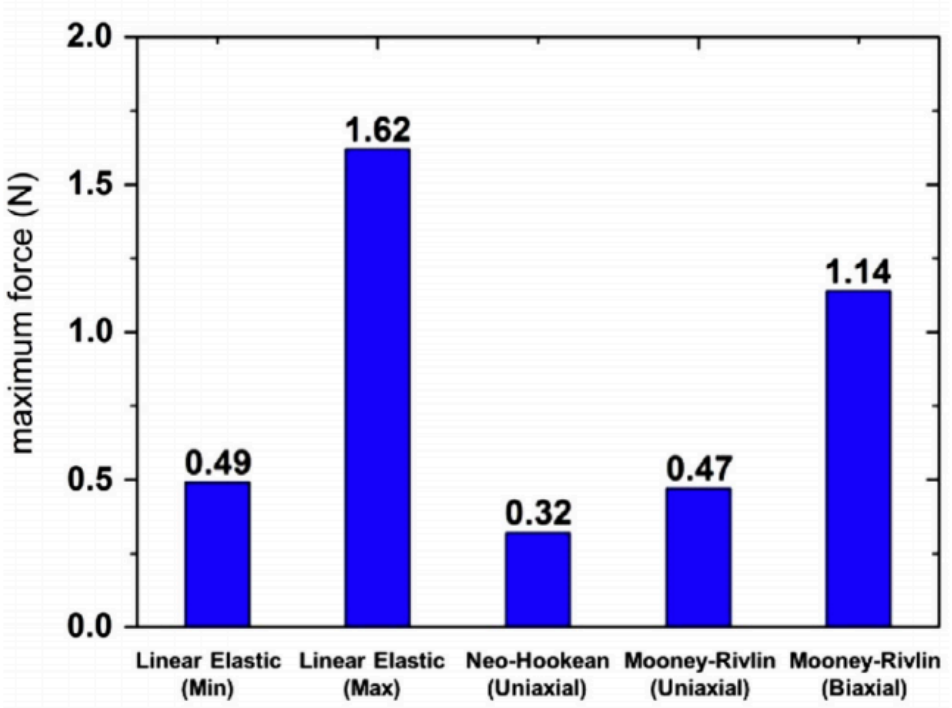

Figure 53: Maximum force simulation results for different material models.

We observe from Figure 53 that the resulting maximum force differs significantly from model to model. Using the maximum and minimum value of the elastic moduli as provided by the supplier of TangoBlackPlus, we observe forces of 1.62 and 0.49 N, respectively. These values are an approximation for the two extreme values. The Neo-Hookean model and the Mooney–Rivlin model based upon data from uniaxial testing predict forces of about 0.32 and 0.47 N, respectively. These values are comparable with the force value predicted by the minimum elastic modulus given by the supplier. In contrast, the Mooney–Rivlin model based upon data from biaxial testing predicts a force of about 1.14 N, which is higher than the results based upon data from the uniaxial tests but lower than the linear elastic maximum. It is interesting to note that both material models based upon data from uniaxial testing give values close to the lower limit determined with the minimum elastic modulus. On the other hand, the material model based upon biaxial testing

predicts an increase in the maximum force by about a factor of 2. Since one material coefficient (as derived by uniaxial testing) is not sufficient to accurately describe a hyperelastic material behavior, it is justifiable to conjecture that the force response using the Mooney–Rivlin model based upon biaxial data is more realistic than the results using simplified material models. Clearly, material models and the method of how to derive their coefficients are important input parameters that have a large influence on simulation results. Consequently, special attention needs to be paid to the selection of the right material model derived from appropriate mechanical testing methods when performing finite element simulation. In this context, it is important to emphasize that more accurate and reliable material models can assist with the design of rubber-like 3D printed devices, such as medical devices or robotic actuators, which may undergo even more complex deformations [25-27]. The knowledge and use of these improved material properties will greatly improve the design process.

3.4 Conclusions

The nonlinear material response of a 3D printed photopolymer (TangoBlackPlus) was studied using uniaxial and biaxial testing. Coupons printed in two different printing directions were investigated. The material coefficients derived for the Neo-Hookean and Mooney–Rivlin model based upon uniaxial and biaxial data were used as input material parameters for a finite element analysis of a curved hollow tube undergoing large deformations. From the experiments and subsequent finite element simulation, we conclude:

1. Based upon uniaxial testing, the elastic modulus was about0.35 MPa at 50% strain with an elongation of approximately 70% at break. The results did not depend on the printing direction.

2. Biaxial testing indicated that the material response was quasi-isotropic with respect to the printing directions used in this study. Both coefficients of the Mooney–Rivlin model (C_{10} and C_{01}) were fitted and found to be unique and significant. The major benefit of performing biaxial testing was that the coefficients of the Mooney–Rivlin model can be derived from a large number of deformation states.

3. Based upon biaxial testing, the Mooney–Rivlin coefficients C_{10} and C_{01} for TangoBlackPlus were determined to be 0.1021 and 0.1473 MPa, respectively.

4. A simple finite element simulation investigating the deformation behavior of a curved hollow tube and assessing the maximum force necessary to straighten it demonstrated that material models and the method for how to derive their coefficients are important input parameters that influence simulation results substantially. Consequently, special attention needs to be paid to the selection of the right material models derived by appropriate mechanical testing methods when performing finite element simulation.

Chapter 3, in part, is a reprint of the materials as they appear in "Uniaxial and biaxial testing of 3D printed hyperelastic photopolymers." Morris, K., Rosenkranz, A., Seibert, H., Ringel, L., Diebels, S., Talke, F. E. (2020), Journal of Applied Polymer Science, 137, 48400. The dissertation author was the primary investigator and author of this patent publication.

References

[1] CDRH. Technical Considerations for Additive Manufactured Medical Devices - Guidance for Industry and Food and Drug Administration Staff https://www.fda.gov/downloads/MedicalDevices/DeviceRegulationandGuidance/GuidanceDocuments/UCM499809.pdf, accessed: November, 2018.

[2] Morrison, Robert J., Scott J. Hollister, Matthew F. Niedner, Maryam Ghadimi Mahani, Albert H. Park, Deepak K. Mehta, Richard G. Ohye, and Glenn E. Green. "Mitigation of tracheobronchomalacia with 3D-printed personalized medical devices in pediatric patients." Science translational medicine 7, no. 285 (2015): 285ra64-285ra64.

[3] Ventola, C. Lee. "Medical applications for 3D printing: current and projected uses." Pharmacy and Therapeutics 39, no. 10 (2014): 704.

[4] Rybicki, Frank J., and Gerald T. Grant. "3D printing in medicine." Cham: Springer International Publishing (2017).

[5] Bartlett, Nicholas W., Michael T. Tolley, Johannes TB Overvelde, James C. Weaver, Bobak Mosadegh, Katia Bertoldi, George M. Whitesides, and Robert J. Wood. "A 3D-printed, functionally graded soft robot powered by combustion." Science 349, no. 6244 (2015): 161-165.

[6] Rossiter, Jonathan, Peter Walters, and Boyko Stoimenov. "Printing 3D dielectric elastomer actuators for soft robotics." In Electroactive polymer actuators and devices (EAPAD) 2009, vol. 7287, p. 72870H. International Society for Optics and Photonics, 2009.

[7] Zolfagharian, Ali, Abbas Z. Kouzani, Sui Yang Khoo, Amir Ali Amiri Moghadam, Ian Gibson, and Akif Kaynak. "Evolution of 3D printed soft actuators." Sensors and Actuators A: Physical 250 (2016): 258-272.

[8] Khoo, Zhong Xun, Joanne Ee Mei Teoh, Yong Liu, Chee Kai Chua, Shoufeng Yang, Jia An, Kah Fai Leong, and Wai Yee Yeong. "3D printing of smart materials: A review on recent progresses in 4D printing." Virtual and Physical Prototyping 10, no. 3 (2015): 103-122.

[9] Tymrak, B. M., Megan Kreiger, and Joshua M. Pearce. "Mechanical properties of components fabricated with open-source 3-D printers under realistic environmental conditions." Materials & Design 58 (2014): 242-246.

[10] Ngo, Tuan D., Alireza Kashani, Gabriele Imbalzano, Kate TQ Nguyen, and David Hui. "Additive manufacturing (3D printing): A review of materials, methods, applications and challenges." Composites Part B: Engineering 143 (2018): 172-196.

[11] Mooney, Melvin. "A theory of large elastic deformation." Journal of applied physics 11, no. 9 (1940): 582-592.

[12] Rivlin, R. S. "Large elastic deformations of isotropic materials IV. Further developments of the general theory." Philosophical Transactions of the Royal Society of London. Series A, Mathematical and Physical Sciences 241, no. 835 (1948): 379-397.

[13] Treloar, Leslie Ronald George. "The physics of rubber elasticity." (1975).

[14] Ogden, Raymond William. "Large deformation isotropic elasticity–on the correlation of theory and experiment for incompressible rubberlike solids." Proceedings of the Royal Society of London. A. Mathematical and Physical Sciences 326, no. 1567 (1972): 565-584.

[15] Sasso, M., G. Palmieri, G. Chiappini, and D. Amodio. "Characterization of hyperelastic rubber-like materials by biaxial and uniaxial stretching tests based on optical methods." Polymer Testing 27, no. 8 (2008): 995-1004..

[16] Liljenhjerte, Johannes, Priyank Upadhyaya, and S. Kumar. "Hyperelastic strain measurements and constitutive parameters identification of 3d printed soft polymers by image processing." Additive Manufacturing 11 (2016): 40-48.

[17] Wang, Kan, Yuanshuo Zhao, Yung-Hang Chang, Zhen Qian, Chuck Zhang, Ben Wang, Mani A. Vannan, and Mao-Jiun Wang. "Controlling the mechanical behavior of dual-material 3D printed meta-materials for patient-specific tissue-mimicking phantoms." Materials & Design 90 (2016): 704-712.

[18] Bodaghi, M., A. R. Damanpack, and W. H. Liao. "Self-expanding/shrinking structures by 4D printing." Smart Materials and Structures 25, no. 10 (2016): 105034.

[19] Seibert, Henning, Tobias Scheffer, and S. Diebels. "Biaxial Testing of Elastomers." Technische Mechanik-European Journal of Engineering Mechanics 34, no. 2 (2014): 72-89.

[20] Boyce, Mary C., and Ellen M. Arruda. "Constitutive models of rubber elasticity: a review." Rubber chemistry and technology 73, no. 3 (2000): 504-523.

[21] Hackett, Robert M. Hyperelasticity primer. Cham: Springer International Publishing, 2016.

[22] Gothait, H. “Apparatus and method for three dimensional model printing” (Objet Geometries Inc.) US6259962B1, 2001.

[23] Stratasys Material Testing Data for TangoBlackPlusTM PolyJet Material. http://usglobalimages.stratasys.com/Main/Files/Material_Spec_Sheets/MSS_PJ_PJMaterialsDataSheet.pdf?v=635785205440671440 , accessed: November, 2018.

[24] Johlitz, Michael, and Stefan Diebels. "Characterisation of a polymer using biaxial tension tests. Part I: Hyperelasticity." Archive of Applied Mechanics 81, no. 10 (2011): 1333-1349.

[25] Morris, Karcher, Pandit, Anay M., Savides, Thomas J., Seo, Young W., Garner, Scott, Fu, Youyi, Feld, Gregory, and Talke, Frank E. "Esophageal deflection device." U.S. Patent Application 16/488,453, filed January 30, 2020.

[26] De Greef, Aline, Pierre Lambert, and Alain Delchambre. "Towards flexible medical instruments: Review of flexible fluidic actuators." Precision engineering 33, no. 4 (2009): 311-321.

[27] Suzumori, Koichi, Toshihiro Maeda, H. Wantabe, and Toshiaki Hisada. "Fiberless flexible microactuator designed by finite-element method." IEEE/ASME transactions on mechatronics 2, no. 4 (1997): 281-286.

Chapter 4 Toward a Final Design of the Esophageal Deflection Device

4.1 Introduction

Atrial fibrillation (AF) is a common heart condition that affects tens of millions of people worldwide [1]. Cardiac electrophysiologists treat this disease with cardiac ablation, where a radiofrequency (RF) ablation catheter is inserted intravenously to thermally ablate the defective heart tissue. The esophagus lies directly behind the left atrium and is in close proximity to the heart during the ablation procedure. This close proximity of the esophagus poses a significant medical risk to the patient since it can lead to thermal injury of the esophagus [2,3]. To address the risk of thermal injury, clinicians currently use endoscopes, endotracheal stylets, or nitinol embedded rods to move the esophagus temporarily away from the heart [4-6]. These approaches pose additional risks to the esophagus, are time consuming, or require that an internist is on standby during the ablation procedure, which results in an increase of cost to the hospital.

In this paper, a new device, the so-called Esophageal Deflection Device (EDD), is designed to protect the esophagus during ablation procedures by mechanically moving the esophagus away from the heart [7-9]. The EDD consists of two parts, a pre-curved flexible tube and an insertion rod. Prior to the procedure, the insertion rod is positioned inside the pre-curved tube, thereby straightening the tube for easy insertion. After the tube and insertion rod are inserted into the esophagus, the rod is pulled out and the tube reassumes its original pre-curved shape. During the

process of reassuming its initial curvature, the tube applies a pressure to the esophageal wall and moves the esophagus away from the ablation site.

Medical devices have made use of pre-curved tubes in many applications, most notably in surgical robotics. Morimoto et al. [10], investigated experimentally the use of pre-curved concentric tubes for application in neurosurgery. Webster et al. [11] studied the mechanics of pre-curved tubes using Euler Bernoulli beam theory and analyzed the deflection of multiple concentric tubes with various sizes and curvatures. Rucker et al. [12] implemented an analytical model for the geometry considered in [10] to account for large deformation of pre-curved tubes. Their analytical developments are founded from Antman's work [13] on Cosserat rod theory. Baek et al. [14] used finite element analysis to further study interaction of concentric tubes. Morimoto and Okamura [15] expanded the work of Webster et al. [11] by comparing beam mechanics theory to their experimental results measuring the curvature of initially pre-curved concentric tubes.

In the present work, we study thin polymeric tubes used in the Esophageal Deflection Device and investigate the effect of material and design parameters on the maximum stress and maximum force caused by the flattening of the pre-curved tubes. A nonlinear constitutive equation of the Mooney Rivlin type was used for the tube material, with material parameters determined experimentally from uniaxial tensile tests. Pre-curved tubes were thermoformed and tested to evaluate the deformation of the tube with different curvatures and cross sections. A finite element simulation was developed to model the deformation of the tube, and its dependence on the materials properties. The analytical, experimental, and numerical results are discussed along with their applications to the final medical product.

4.2 Medical Background

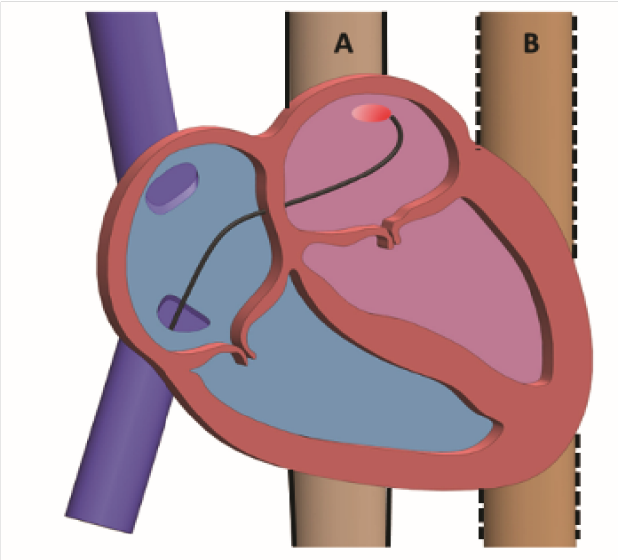

Figure 54: Schematic illustrating esophagus location A (undesirable) and location B (desirable) relative to the heart during a catheter ablation procedure.

Atrial Fibrillation (AF) is a common heart arrhythmia, or irregularity of the heart rate, which leads to a variety of health problems including chest pain, fatigue, or an increased likelihood of heart failure [1]. The mechanisms that cause AF are complex and are associated with irregularities of the electrical conduction system of the heart and atrial tissue characteristics [2]. Atrial ablation is a procedure that ablates defective heart tissue thermally. Ablation regions can be targeted by placing electrodes within the heart to perform, for example, pulmonary vein isolation that prevents irregular heart rate [2]. During the ablation procedure, esophageal tissue can be thermally damaged due to its proximity to the heart [3,16]. A rare and potentially fatal outcome of atrial ablation is the forming of an atrio-esophageal fistula, i.e., the creation of an opening between the heart and the esophagus due to the proximity and heat exchange between the left atrial wall and the esophagus [17,18]. It is common practice to utilize a temperature probe to measure luminal

esophageal temperature during the ablation procedure. If the temperature rise is above a safe value, the cardiac electrophysiologist performing the procedure will stop the ablation and move the esophagus away from the ablation region.

A schematic of the heart and neighboring esophagus is shown in Figure 54. Position A is the undeflected position of the esophagus, while position B is the deflected position of the esophagus, after moving it away from the ablation region. The esophagus is composed of two primary layers, a soft flexible muscular tissue and a more durable inner mucosa lining, with a thickness of approximately 3 mm for the muscle layer, and 2 mm for the mucosa layer [19]. The properties of human tissue and their variations within the esophagus and heart have been investigated [19, 20]. These studies note the resilience of the esophageal tissue. Clinically used stents have also shown to expand radially and exert forces on the esophagus greater than 80 N when deployed at a diameter of 15 mm [21]. Moreover, Evonich et al. [22] showed, through experimental tensile tests of porcine tissue, that the structural integrity of esophageal tissue will remain intact even after thermal damage from ablation. To help in the analysis and understanding of this ablation procedure including thermal damage, finite element models have been designed to simulate the heat transfer from the ablation site to the esophagus [8,9,17,18]. Esophagus tissue has also been investigated using finite element analysis by taking into account the thick, foldable esophageal walls [23]. Furthermore, the relationship between an atrial retractor and the surrounding heart tissue has been examined by finite element simulations in [20].

4.3 U-shaped Design of the EDD

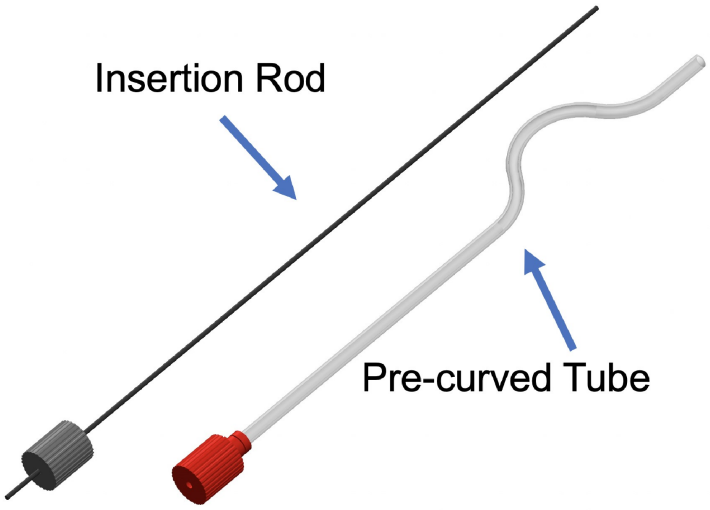

Figure 55: Computer aided design model of an esophageal deflection device (EDD) with tube and insertion rod.

Figure 55 shows a 3D model of our Esophageal Deflection Device originally proposed in [7,9]. The device consists of a pre-curved flexible tube and an insertion rod. The pre-curved tube is straightened by the rod prior to its insertion in the esophagus. After insertion of the assembled device, the inner rod is pulled out, causing the deflection of the esophagus, as the tube tends to reassume its original curved shape. To manipulate the position of the esophagus during the procedure, the EDD may have to be inserted further, retracted, or twisted. After completion of the procedure, the EDD can be retrieved by slowly pulling on the handle of the assembled device. The inner rod may be fully inserted if more precise control of the esophagus position is desired by the surgeon during retrieval of the EDD.

To deflect the esophagus, important design parameters of the EDD are the tube's cross section (outer and inner diameter of the tube), the radius of curvature of the tube, and the bending

stiff ness and strength properties of the material used. The assembled device including the tube and inner rod should be made flexible enough to navigate through the mouth and into the esophagus. We describe in this paper the idealized case of a rigid insertion rod to make our point clear. However, the inner rod must be flexible enough to cannulate the esophagus and does not need to be homogenous or uniform in its cross section. The design of the EDD must also take into consideration the mobility of the esophagus due to its interactions with adjacent soft tissue [21] and anatomical conditions including the diameter of the esophagus, the size of the heart, and the distance from the mouth. The tube should not exert pressure or forces on the inner esophageal wall that would exceed the limits tolerated by the human tissue. The quality and mechanical performance of the device should be tested further, beyond the force and deflection properties, to ensure patient safety. Tests for safe and reliable use should also be examined for anatomical variations of patients including children versus adults, and variability in tissue material properties. To satisfy FDA required ISO 10993 standards, the materials used in the EDD must be of biomedical grade and quality [24].

The assembled esophageal deflection device is inserted through the mouth into the esophagus. As the insertion rod is retracted, the tube reassumes almost fully its original curved shape (Figure 56), depending on the position and stiffness of the surrounding tissue. In our EDD, the radius of curvature for all curved portions of the tube is $R = R_1$, and the distance between the two ends of the curved portions of the tube is L_0. The inner and outer radii of the hollow circular cross section of the tube are a and b, respectively. The change in the shape of the EDD tube from its initial curved position to the straight position by insertion of the stiff rod can be calculated by applying two pairs of opposite couples M and $2M$ at the cross sections corresponding to inflection points of the original curved shape of the tube. The magnitude of the couple M is chosen to

eliminate the initial curvature of the tube ($\pm 1/R$). When the insertion rod is removed, the EDD goes back to its original shape and applies a pressure along the inner esophageal wall, thereby moving the esophagus away from the ablation site.

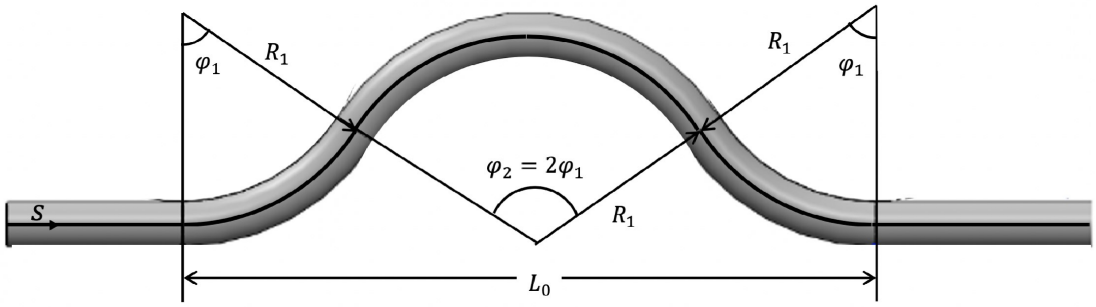

Figure 56: Schematic of pre-curved tube with geometric design parameters: the distance between the two ends of the curved portions of the tube is L_0, the radius of curvature is $R = R_1$ for all curved portions of the tube, and the corresponding angles are φ_1 and $\varphi_2 = 2\varphi_1$, so that $L_0 = 4R_1\varphi_1$.

4.4 Constitutive Equation for a Rubber-like Material

Correct constitutive equations are needed to model the EDD tube mechanical response during its deformation. If the tube material undergoes only small (infinitesimal) elastic strain, the stress σ is proportional to strain ϵ. For uniaxial stress, $\sigma = E\epsilon$, where E is the elastic modulus of the material. For the EDD tube under consideration, strains can be large and a nonlinear relationship between stress and strain must be considered to describe its mechanical response.

Hyperelastic material models of isotropic nonlinear elasticity are based on the elastic strain energy function $W = W(\lambda_1,\lambda_2,\lambda_3)$, where $\lambda_1,\lambda_2,\lambda_3$ are the principal stretch ratios (the eigenvalues of the stretch tensor $\mathbf{V} = \mathbf{B}^{1/2}$, where $\mathbf{B}$ is the right Cauchy Green deformation tensor $\mathbf{B}$). For the

Mooney Rivlin isotropic and incompressible material model, the strain energy W is of the form [25,26]

$$W = C_1(I_B - 3) + C_2(II_B - 3), \tag{4.4.1}$$

where I_B and II_B are the invariants of **B**, while C_1 and C_2 are the material parameters determined from experimental data. In the case of uniaxial stress, the stretch ratios in an incompressible isotropic material are $\lambda_1 = \lambda$, $\lambda_2 = \lambda_3 = 1/\sqrt{\lambda}$, where $\lambda = l/l_0$ is the ratio of the elongated and original length of the specimen. The right Cauchy Green deformation tensor **B** consequently becomes

$$\mathbf{B} = \begin{bmatrix} \lambda_1^2 & 0 & 0 \\ 0 & \lambda_2^2 & 0 \\ 0 & 0 & \lambda_3^2 \end{bmatrix} = \begin{bmatrix} \lambda^2 & 0 & 0 \\ 0 & 1/\lambda & 0 \\ 0 & 0 & 1/\lambda \end{bmatrix}, \tag{4.4.2}$$

with the corresponding invariants

$$\begin{aligned} I_B &= \lambda_1^2 + \lambda_2^2 + \lambda_3^2 = \lambda^2 + \frac{2}{\lambda}, \\ II_B &= \lambda_1^2\lambda_2^2 + \lambda_2^2\lambda_3^2 + \lambda_3^2\lambda_1^2 = 2\lambda + \frac{1}{\lambda^2} \end{aligned} \tag{4.4.3}$$

The stress expression follows from the general expression for the Cauchy stress tensor σ of isotropic and incompressible hyperelasticity [25,26],

$$\boldsymbol{\sigma} = -p\mathbf{I} + 2\left(\frac{\partial W}{\partial I_B}\mathbf{B} - \frac{\partial W}{\partial II_B}\mathbf{B}^{-1}\right), \tag{4.4.4}$$

where the pressure p can be determined by solving the boundary value problem under consideration; **I** is the identity tensor, and the exponent −1stands for the inverse. The substitution

of (4.4.1) (4.4.3) into (4.4.4) gives the expression for the applied longitudinal stress in a uniaxial tension,

$$\sigma = -p + 2\left(C_1\lambda^2 - \frac{C_2}{\lambda^2}\right). \tag{4.4.5}$$

Because the normal stress in the orthogonal direction is equal to zero under uniaxial tension, it also follows from (4.4.4) that

$$0 = -p + 2\left(\frac{C_1}{\lambda} - C_2\lambda\right) \quad \Rightarrow \quad p = 2\left(\frac{C_1}{\lambda} - C_2\lambda\right). \tag{4.4.6}$$

By substituting the expression for p from (4.4.6) into (4.4.5), the stress–stretch relationship is found to be

$$\sigma = 2C_1\left(\lambda^2 - \frac{1}{\lambda}\right) + 2C_2\left(\lambda - \frac{1}{\lambda^2}\right). \tag{4.4.7}$$

4.5 EDD Tube Material

Ethylene Vinyl Acetate (EVA) was chosen as a material for the EDD tube since EVA has been used previously in biomedical applications, is easily available, and has good mechanical properties. Table 5 lists materials properties of commercially available EVA-tubes [Hudson Extrusions, Inc].

Table 5: Material properties provided by supplier.

Property	Nominal Value Unit	Test Method
Melt Mass-Flow Rate (MFR) (190°C/2.16 kg)	2.3 g/10 min	ASTM D 1238
Vinyl Acetate Content	18.0 wt%	
Density	0.941 g/cm³	ASTM D 1505
Durometer Hardness (Shore D)	37	DIN 5305
Tensile Strength at Yield	4.5 MPa	ASTM D 638
Tensile Strength at Break	25 MPa	ASTM D 638
Ultimate Elongation	820 %	ASTM D 638
Vicat Softening Temperature	62°C	ASTM D 1525

The stress strain relationship for the specific rubber-like, EVA co-polymer is not fully defined in Table 5, but is needed for evaluating the mechanical features of the EDD. In order to identify a constitutive model that properly describes its stress strain relationship, uniaxial tensile tests were performed by creating EVA specimens from flattened tube cutouts, and testing them uniaxially (Figure 57), while adhering to ASTM D-412 standards [27].

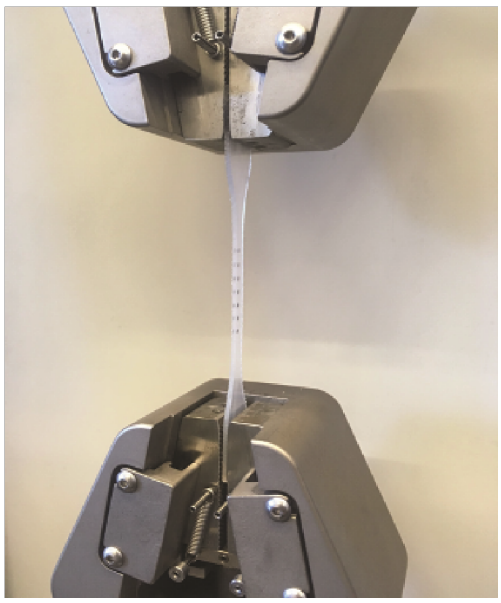

Figure 57: Uniaxial tensile testing of ethylene vinyl acetate tube material [MTS-Criterion tester]. The initial length of the specimen is $l_0 = 140$ mm, and the initial dimensions of the rectangular cross section are 3 mm x 1.59 mm.

Figure 58 shows the stress vs. stretch ratio for up to 15% tensile strain $\epsilon = \Delta l/l_0$ for five uniaxial specimens, where l_0 is the initial length of the specimen, l is its current length, and $\Delta l = l - l_0$ is the length change. The maximum stretch ratio considered was $\lambda_{max} = l/l_0 = 1.15$, which corresponds to maximum strain in the tube of length $L = 84$ mm and initial radius of curvature $R_0 = 27$ mm when it is straightened out by two end couples, as discussed in the next section. The material response is initially linear, but becomes increasingly nonlinear as the strain increases. To analytically describe this behavior, we adopted the Mooney Rivlin constitutive model and determined the material parameters C_1 and C_2 by requiring that (a) the constitutive expression must reproduce the experimentally observed initial elastic modulus $E = 52.8$ MPa (slope of the stress strain curve at zero strain), and (b) the applied stress at strain $\epsilon = 0.15$ is $\sigma = 3.71$ MPa, as experimentally observed. Thus, we required that

$$6(C_1 + C_2) = 52.8 \text{ MPa}, \qquad 2C_1\left(1.15^2 - \frac{1}{1.15}\right) + 2C_2\left(1.15 - \frac{1}{1.15^2}\right) = 3.71 \text{ MPa}. \tag{4.5.1}$$

This gives

$$C_1 = -27.4\,\text{MPa}, \quad C_2 = 36.2\,\text{MPa}. \tag{4.5.2}$$

We note that these values of the parameters C_1 and C_2 are intended to be used only for $0.95 \leq \lambda \leq 1.15$. For very large values of the stretch ratio λ, other values of C_1 and C_2 will be needed, but these large values of the stretch ratio are not of interest in the present work.

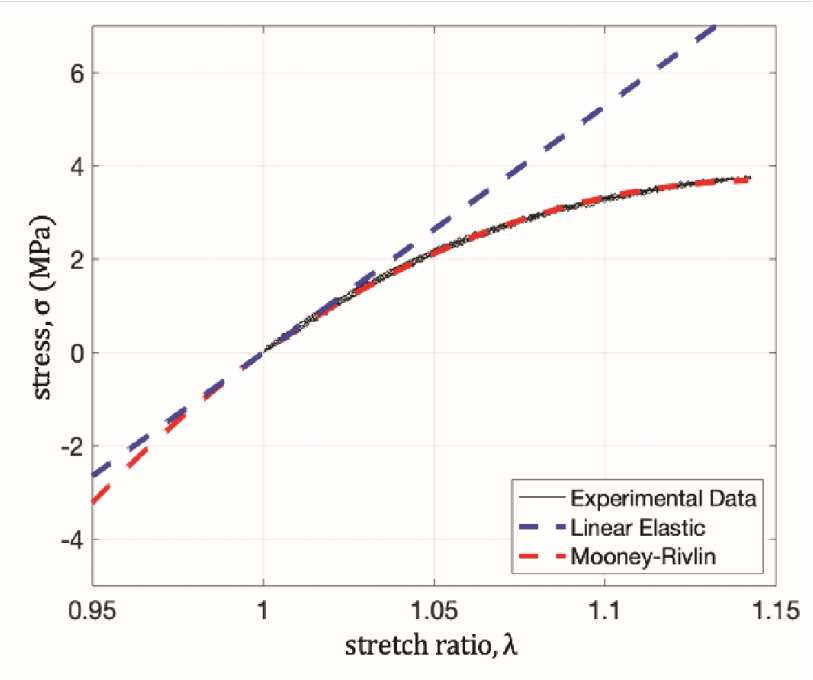

Figure 58: Experimental results for linear and Mooney Rivlin models from EVA uniaxial tensile tests in the range of stretch ratio $0.95 \leq \lambda \leq 1.15$.

4.6 Moment Curvature Relationship

Consider a pure bending of a slender circularly curved tube whose length along the centroids of the cross sections is L_0. The initial radius of curvature of the centroidal axis is R_0, such that $R_0\varphi_0 = L_0$, where φ_0 is the angle spanned by two end cross section of the tube (Figure 59b). Each cross section is a hollow cylindrical cross section, made by two concentric circles of inner and outer radii a and b, respectively.

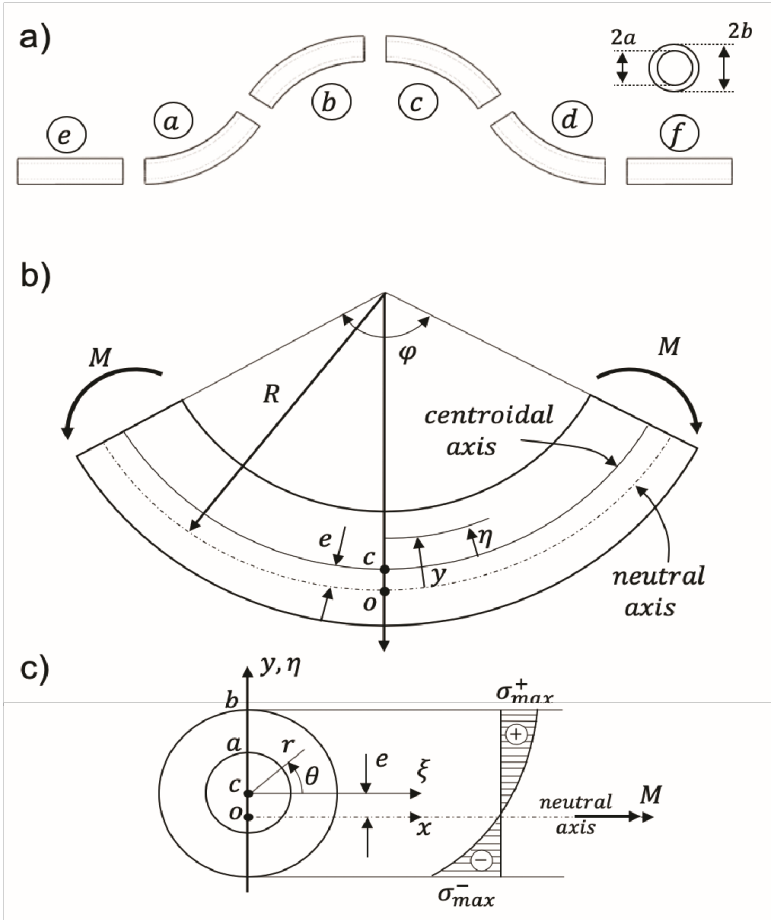

Figure 59: (a) The EDD separated into four equivalent sections a , b , c and d , and the straight sections e and f at the beginning and the end of the tube. (b) Generalized tube configuration with applied end moments M, the radius of curvature R, and other geometric parameters utilized in the analysis. (c) Cross section of the curved tube with the stress distribution along the vertical axis. The axis ξ passes through the centroid C of the cross section, while the neutral axis x passes through the point O at the distance e below the centroidal ξ axis.

Upon application of two end bending moments M in the vertical plane of symmetry, the tube bends and a longitudinal section in the vertical plane of symmetry becomes circular with the radius of curvature R of the longitudinal neutral axis of the tube, such that $R\varphi = L_0$. The neutral axis of each cross section is defined by the condition that $\sigma = 0$ along this axis. We adopt a simplified curved beam analysis in which we consider the normal stress orthogonal to the cross

section of the beam only. If we locate the coordinate origin of the cross section at the point in the middle of the neutral axis, then the strain at a distance y from the neutral axis can be expressed as

$$\epsilon(y) = y\Delta\kappa\,, \quad \Delta\kappa = \frac{1}{R_0} - \frac{1}{R}, \tag{4.6.1}$$

where $\Delta\kappa$ is the change in curvature. Because the stretch ratio λ is related to strain ϵ by

$$\lambda = 1 + \epsilon = 1 + y\Delta\kappa, \tag{4.6.2}$$

the substitution of (4.6.2) into (4.4.7) gives

$$\sigma = 2C_1\left[(1+y\Delta\kappa)^2 - \frac{1}{1+y\Delta\kappa}\right] + 2C_2\left[1 + y\Delta\kappa - \frac{1}{(1+y\Delta\kappa)^2}\right]. \tag{4.6.3}$$

Under pure bending, the net normal force in each cross section of the tube must vanish, and the moment of the normal stresses $\sigma = \sigma(y)$ for any point must be equal to M, i.e.,

$$N = \int_A \sigma\,\mathrm{d}A = 0\,, \quad M = \int_A \eta\sigma\,\mathrm{d}A\,, \tag{4.6.4}$$

where the centroid of the cross section is conveniently used as the reference point for the moment calculation. The vertical distances from the centroid of the cross section (η) and from the neutral axis (y) are related by

$$y = \eta + e \tag{4.6.5}$$

with e being the vertical distance between the axes x and ξ, as shown in Figure 59c. Upon the substitution of (4.6.5) into the first expression in (4.6.4), we obtain

$$C_1\left[\int_A (1+y\Delta\kappa)^2\mathrm{d}A - \int_A \frac{\mathrm{d}A}{1+y\Delta\kappa}\right] + C_2\left[\int_A (1+y\Delta\kappa)\,\mathrm{d}A - \int_A \frac{\mathrm{d}A}{(1+y\Delta\kappa)^2}\right] = 0. \tag{4.6.6}$$

Because (ξ,η) are the centroidal axes of the cross section, it follows that

$$\int_A \eta \, \mathrm{d}A = 0\,, \quad \int_A \eta^2 \, \mathrm{d}A = I_\xi = \frac{\pi}{4}\,(b^4 - a^4)\,, \quad A = \pi(b^2 - a^2) \,. \tag{4.6.7}$$

The small ovalization of the circular cross section caused by the Poisson-type effects in bending have been ignored; for the analysis of three-dimensional stress state and anticlastic curvature effects in pure bending of nonlinearly elastic prismatic beams with rectangular cross section, see [28]. Thus, after performing the integrations in (4.6.6), this equation becomes

$$C_1(I_1 - J_1) + C_2(I_2 - J_2) = 0, \tag{4.6.8}$$

where

$$\begin{aligned}
I_1 &= \int_A (1 + y\Delta\kappa)^2 \mathrm{d}A = \alpha^2 A + I_\xi(\Delta\kappa)^2\,, \\
I_2 &= \int_A (1 + y\Delta\kappa)\,\mathrm{d}A = \alpha A\,, \quad \alpha = 1 + e\Delta\kappa\,, \\
J_1 &= \int_A \frac{\mathrm{d}A}{1 + y\Delta\kappa} = \frac{2\pi}{(\Delta\kappa)^2}\,B_1\,, \quad B_1 = \sqrt{\alpha^2 - a^2(\Delta\kappa)^2} - \sqrt{\alpha^2 - b^2(\Delta\kappa)^2}\,, \\
J_2 &= \int_A \frac{\mathrm{d}A}{(1 + y\Delta\kappa)^2} = -\frac{2\pi\alpha}{(\Delta\kappa)^2}\,B_2\,, \quad B_2 = \frac{1}{\sqrt{\alpha^2 - a^2(\Delta\kappa)^2}} - \frac{1}{\sqrt{\alpha^2 - b^2(\Delta\kappa)^2}}
\end{aligned} \tag{4.6.9}$$

For a given $\Delta\kappa$, equation (4.6.9) can be solved numerically for the value of the eccentricity e corresponding to $\Delta\kappa$. The numerical results for the $e = e(\Delta\kappa)$ relationship are shown in Figure 60a.

We next proceed with the derivation of the moment curvature relationship. The substitution of (4.6.4) into the second expression in (4.6.3) gives

$$M = 2C_1\left[\int_A \eta(1 + y\Delta\kappa)^2 \mathrm{d}A - \int_A \frac{\eta\,\mathrm{d}A}{1 + y\Delta\kappa}\right] + 2C_2\left[\int_A \eta(1 + y\Delta\kappa)\,\mathrm{d}A - \int_A \frac{\eta\,\mathrm{d}A}{(1 + y\Delta\kappa)^2}\right]. \tag{4.6.10}$$

Upon performing the integrations, (4.6.10) can be expressed in the form

$$M = 2C_1(I_3 - J_3) + 2C_2(I_4 - J_4) \tag{4.6.11}$$

where

$$
\begin{aligned}
I_3 &= \int_A \eta(1+y\Delta\kappa)^2 \mathrm{d}A = 2\alpha I_\xi \Delta\kappa\,, \\
I_4 &= \int_A \eta(1+y\Delta\kappa)\,\mathrm{d}A = I_\xi \Delta\kappa\,, \\
J_3 &= \int_A \frac{\eta\,\mathrm{d}A}{1+y\Delta\kappa} = \frac{A}{\Delta\kappa} - \frac{2\pi\alpha}{(\Delta\kappa)^3}\,B_1\,, \\
J_4 &= \int_A \frac{\eta\,\mathrm{d}A}{(1+y\Delta\kappa)^2} = \frac{2\pi}{(\Delta\kappa)^3}\,(B_1+\alpha^2 B_2)
\end{aligned}
\tag{4.6.12}
$$

Expression (4.6.11) is the desired moment curvature relationship. The corresponding variation $M = M(\Delta\kappa)$ is shown in Figure 60b. The solid curve corresponds to the nonlinear Mooney Rivlin model and the dashed line to the linear elastic material model. In the latter case (4.6.11) reduces to

$$M = EI_\xi \Delta\kappa, \tag{4.6.13}$$

since the stress $\sigma = \sigma(y)$ is in this case is $\sigma = 6(C_1 + C_2)\epsilon = E\epsilon$, while $e = 0$. For the nonlinear Mooney Rivlin model, the stress varies nonlinearly along the y direction according to (4.6.3), which is sketched in Figure 59c.

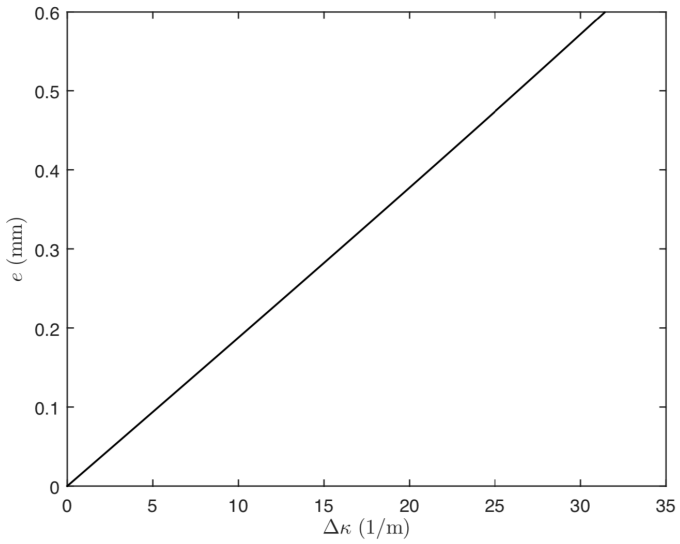

(a)

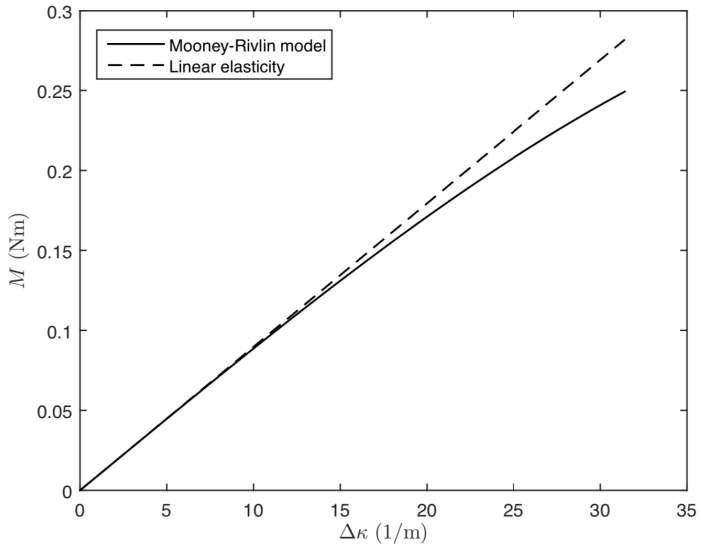

(b)

Figure 60: (a) The eccentricity e vs. the change in curvature $\Delta\kappa$ in the case of Mooney Rivlin material model. (b) The applied moment M vs. the change in curvature $\Delta\kappa$ in the case of Mooney Rivlin material model.

4.6.1 Straightening of a Precurved EVA Tube

If a curved tube of initial radius of curvature R_0 is straightened-out by two end couples M, then $R \to \infty$ and $\Delta\kappa = R_0^{-1}$. The corresponding value of M is obtained from (4.6.11) and (4.6.11) by replacing $\Delta\kappa$ with $1/R_0$. For example, if $R_0 = 40$ mm, the moment needed to straighten-out the tube is $M = 0.2079$ Nm. If the material of the tube was linearly elastic in the entire range of bending, the corresponding moment would have been $M = EI_\xi/R_0 = 0.2243$ Nm. In these calculations the inner and outer radii of the tube were assumed to be given by $a = 2.38$ mm and $b = 3.97$ mm, so that $A = 31.72\text{mm}^2$ and $I_\xi = 170\text{mm}^4$, while $E = 52.8$ MPa.

The normal stress follows from (4.6.3) by replacing there $\Delta\kappa$ with $1/R_0$, which gives

$$\sigma = 2C_1\left[(1+y/R_0)^2 - \frac{1}{1+y/R_0}\right] + 2C_2\left[(1+y/R_0) - \frac{1}{(1+y/R_0)^2}\right]. \tag{4.6.14}$$

The magnitudes of the maximum tensile and compressive stresses in this case are

$$\sigma_{\max}^{+} = 3.47\,\text{MPa}\,, \quad \sigma_{\max}^{-} = 6.45\,\text{MPa}\,, \tag{4.6.15}$$

corresponding to $y^+ = 4.4$ mm and $y^- = -3.5$ mm, as shown in Figure 59c.

4.6.2 Straightening of a Doubly Precurved EVA Tube

Figure 61b shows a straightened configuration of a doubly pre-curved EVA tube shown in Figure 61a. Since the pre-curved portions of the tube are circular, the straightening into a perfectly straight configuration can be accomplished by the application of two pairs of concentrated couples of moments M_1 and M_2, because only pure bending by concentrated end couples transforms a circularly pre-curved tube into a straight tube. The magnitude of the moment M_1 is obtained from (4.6.11) and (4.6.11) by replacing $\Delta\kappa$ with $1/R_1$, while the magnitude of the moment $M_2 - M_1$ is obtained from (4.6.11) and (4.6.11) by replacing $\Delta\kappa$ with $1/R_2$, because the central portion of the

tube of radius R_2 is under the bending moment $M_2 - M_1$ (Figure 61c). For example, if $R_1 = R_2$, the bending moment $M_2 = 2M_1$, regardless of the values of the angles φ_1 and φ_2. The straightened-out configuration of a pre-curved tube is the most critical configuration of the tube, in which the stresses attain their greatest values, because upon the removal of the inserted straight rod, the tube is reverting to its original curved shape, releasing its strain energy and relaxing the stresses caused by the inserted rod. In the case of the cross section of the tube with inner and outer radii a = 2.38 mm and b = 3.97 mm, the maximum stresses are σ_{max}^{+} = 3.28 MPa and σ_{max}^{-} = 5.65 MPa in the case of the radii of curvature $R_1 = R_2$ = 45 mm, while σ_{max}^{+} = 2.59 MPa and σ_{max}^{-} = 3.73 MPa in the case of the radii of curvature $R_1 = R_2$ = 65 mm.

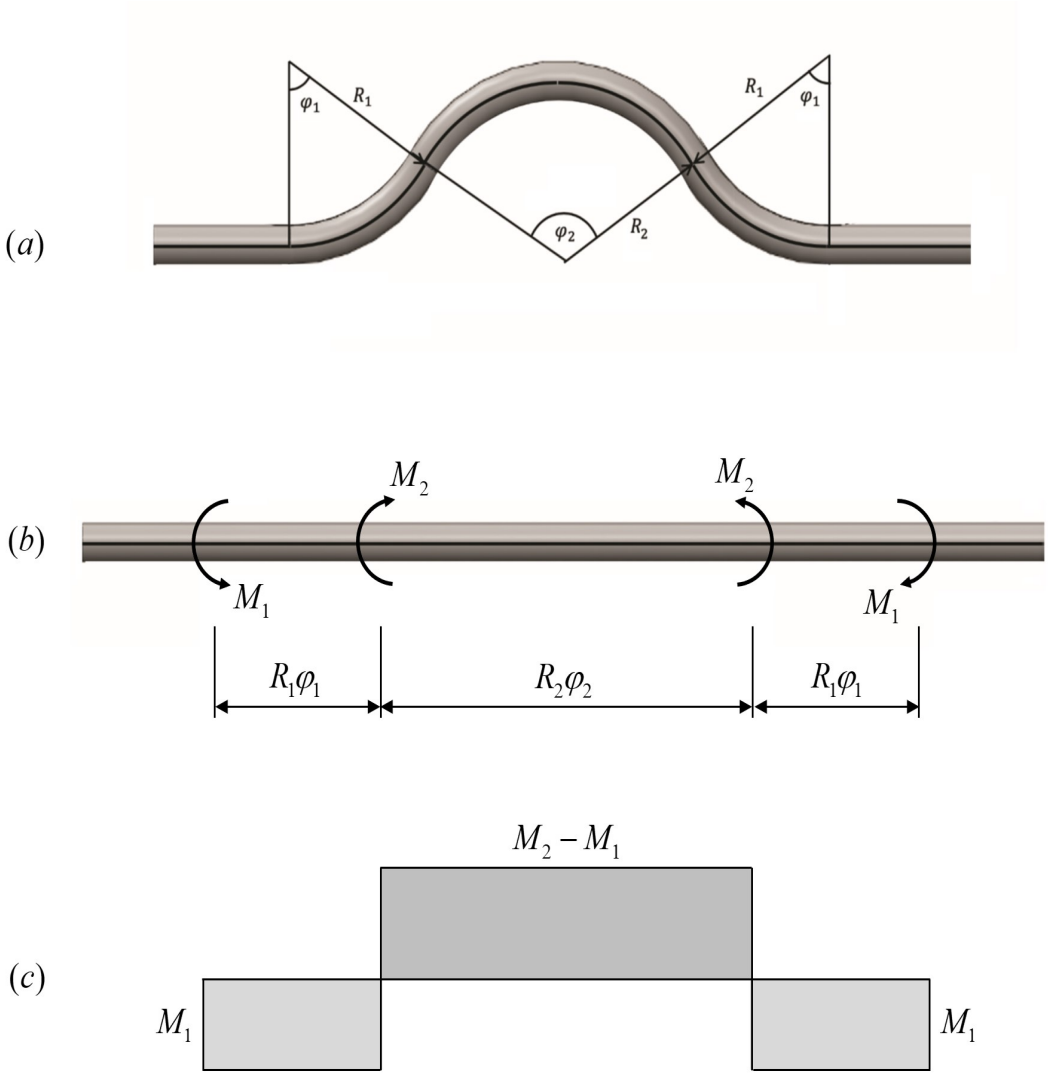

Figure 61: (a) The initial pre-curved configuration of the EVA tube. (b) The straightened-out configuration of the tube produced by the application of two pairs of couples M_1 and M_2. (c) The moment diagram along the straightened axis of the tube.

4.7 Experimental Measurement of Force vs. Deflection of Precurved EVA tubes

Straight EVA tubes were thermoformed in 3D printed molds (Figure 62) to attain curved geometry similar to that used in the EDD. The thermoforming process consisted of cutting and fitting the tubes into the mold, heating the mold with the tubes in an oven at 70 ◦C for 1 hour, and, finally, cooling the tubes outside of the oven (Figure 63). A sample set of tubes with different precurved radii are shown in Figure 64. The test set-up for measuring the force vs. displacement of pre-curved EVA tubes is shown in Figure 65. The setup consists of a load cell (SMT 250N), a tube mount, and a vertical actuator arm. One end of the tube is clamped into the mount while the other end of the tube can deflect against a at surface on the mount. The curved portion of the tube contacts the stationary surface of the load cell. The actuator arm moves the tube mount downward at a speed of approximately 0.1 mm/s and, as the distance decreases between the at surface on the load cell and the tube mount. Figure 66 shows the tube in a nearly straightened position between the load cell and the tube mount. The force applied by the deforming tube is measured using the load cell until the tube is straightened.

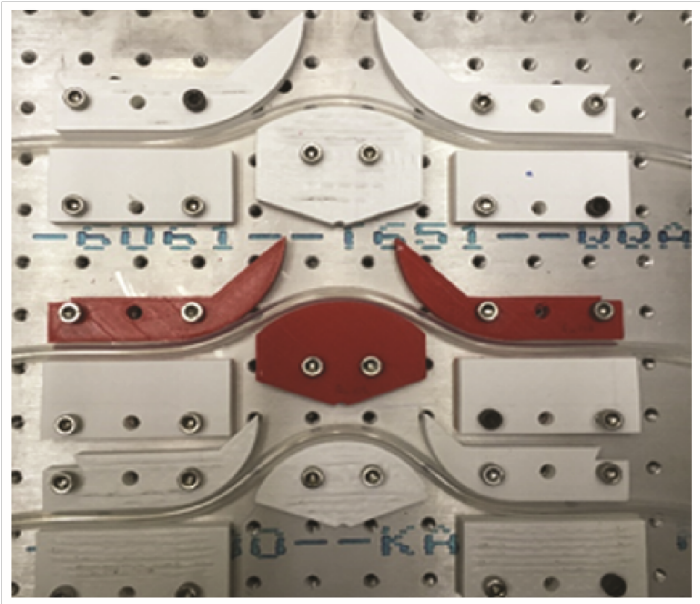

Figure 62: Thermoform mold and EVA tubes for different radii of curvature.

Figure 63: Talke Lab Oven for Thermoforming

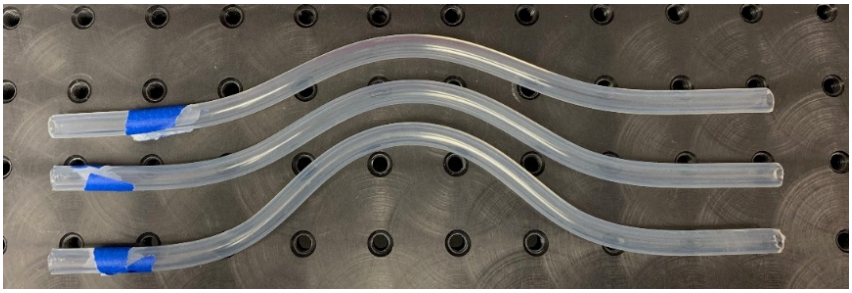

Figure 64: EVA tube cut after thermoforming.

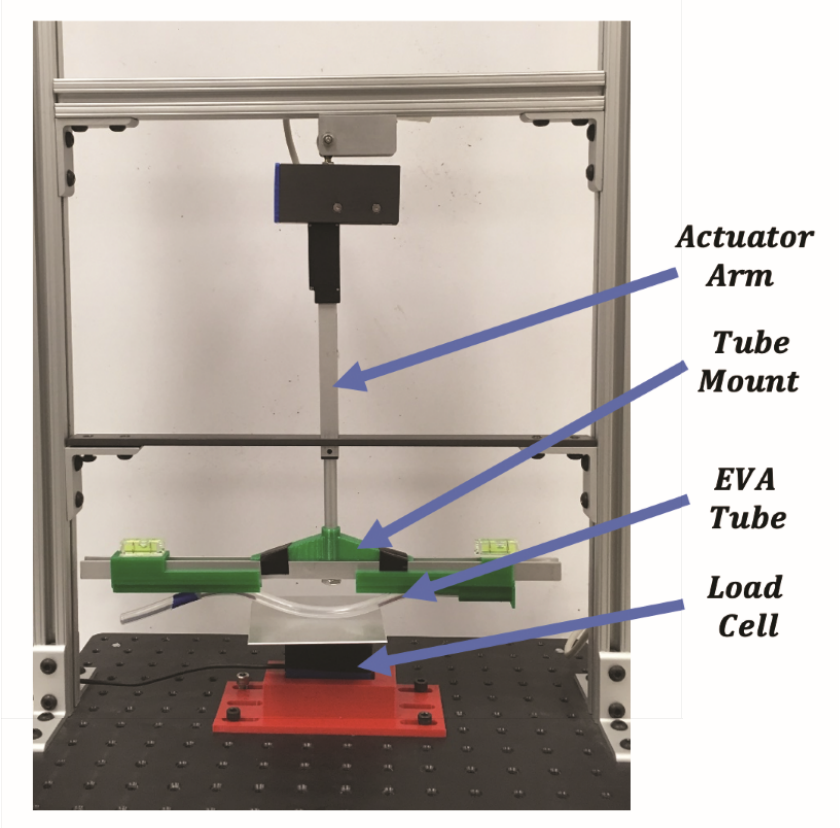

Figure 65: Set-up for measurement of force vs. deflection of preformed deflected EVA tubes.

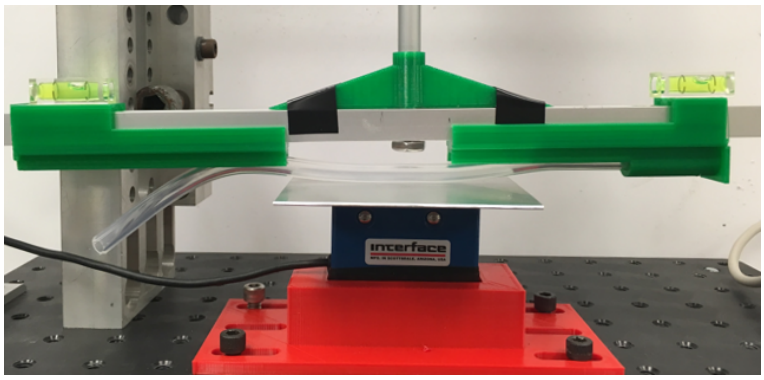

Figure 66: Experimental deformed EVA tube with load cell measurement.

In Figure 67 a and b, the force vs. displacement is shown for EVA tubes of 7.9 mm and 9.5 mm outer diameter, respectively, with initial radius of curvature (RoC) of 45 mm, 55 mm, and 65 mm, respectively. From Figure 67, we observe that the displacement required to generate a particular force increases with decreasing radius of curvature. The tube with a 9.5 mm outer diameter produces a larger force than the tube with 7.5 mm outer diameter keeping all other parameters the same. The tube with a 9.5 mm outer diameter exerts a maximum force of approximately two times that of the tube with a 7.9 mm outer diameter, for all three pre-formed curvatures.

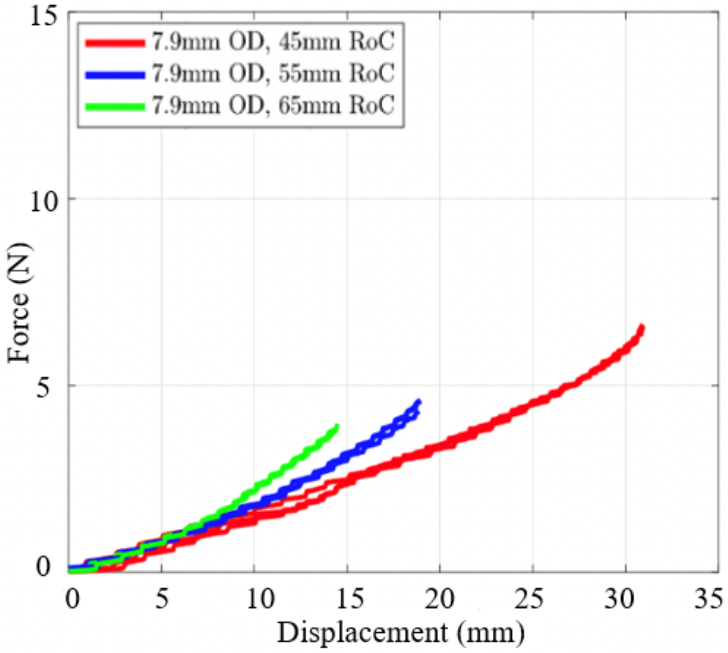

(a)

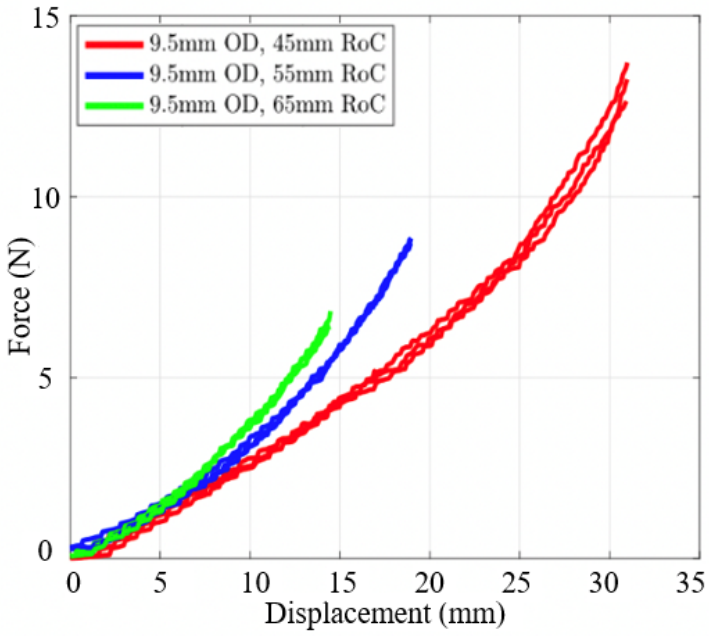

(b)

Figure 67: Experimentally determined force vs. displacement for: (a) 7.9 mm outer diameter and (b) 9.5 mm outer diameter tube with pre-curved radius of curvature (RoC) of 45 mm, 55 mm, and 65 mm.

4.8 Finite Element Model of Outer Tube Deformation

To complement and validate the analytical and experimental results shown in the previous sections, a finite element model was developed simulating the straightening of a pre-curved EVA tube. As shown in Figure 68, the pre-curved and initially stress-free tube is confined between two rigid walls *w*1 and *w*2. The left end of the tube is constrained in all six degrees of freedom, while the right end of the tube is free to move. The surface *w*1 is displaced slowly toward surface *w*2, thereby straightening the tube. The force exerted by the tube on surface *w*2 is determined.

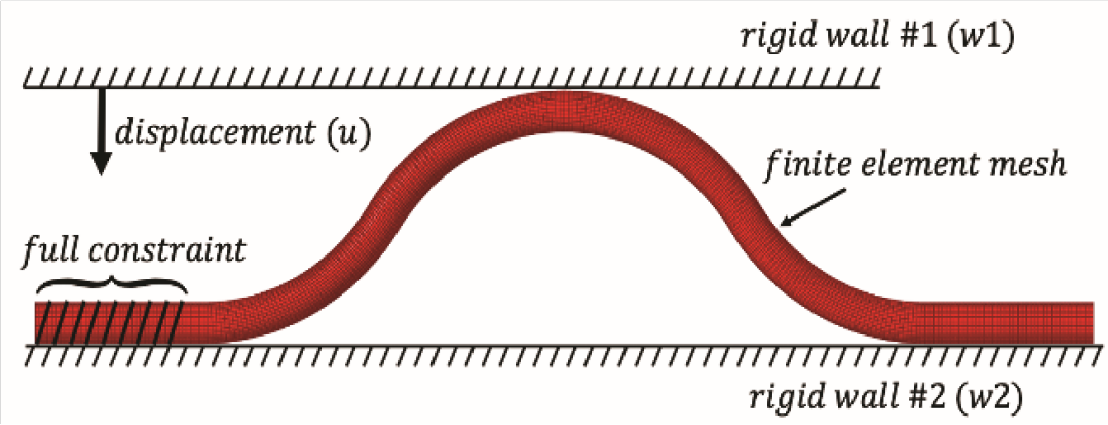

Figure 68: Schematic of geometry and boundary conditions.

The pre-curved tube geometry was first obtained in 3D (SolidWorks) and meshed using a commercially available finite element program (Hypermesh). Stress and strain as a function of displacement were then obtained using an explicit transient solver (LS-DYNA). All three software packages are commercially available. The mesh for the pre-curved tubes utilized approximately 70,000 8-node quadrilateral elements. Both the linear material model and the nonlinear Mooney Rivlin model were used, with material parameters determined from the experimental results of section 4.7. The initial position of the tube (see Figure 68 and Figure 69a) corresponds to the case

that the insertion rod is completely removed, while the final position of the tube in Figure 69c corresponds to the case that the (rigid) insertion rod is fully inserted in the EDD. The deformation of a tube being straightened by two rigid walls is physically comparable to the tube being straightened by a rigid inner rod. Clearly, our model contains the extreme limiting cases occurring during use of the EDD during the procedure. Figure 69a-c show the von Mises stress along the length of the tube for the initial, intermediate, and final position of the rigid wall w1. From Figure 69, we observe that the von Mises stress varies significantly along the length of the tube. As expected, the largest von Mises stresses occur furthest away from the neutral axis in the *y* direction.

Figure 70 shows force vs. displacement and von Mises stress vs. displacement of pre-curved EVA tubes using the Mooney Rivlin constitutive equation. We observe that the force increases as the displacement increases for all tubes. We also observe that tubes with a smaller radius of curvature have a larger maximum force. In addition, we observe that the force and the maximum von Mises stress increases as the area moment increases. The maximum von Mises stress varies only a small amount for tubes having different radii of curvature keeping all other parameters constant. On the other hand, tubes with smaller radius of curvature have a larger final value of the von Mises stress, because they deflect a larger total distance compared to the tubes with larger radii of curvature, similar to the trend observed for the simulated force. The numerical results provide insight into the effect of design parameters of the tube on the mechanical performance of the EDD tube. By changing the cross section and the radius of curvature, the force applied against the esophageal wall can vary significantly and, in some cases, the stress can exceed the elastic limit.

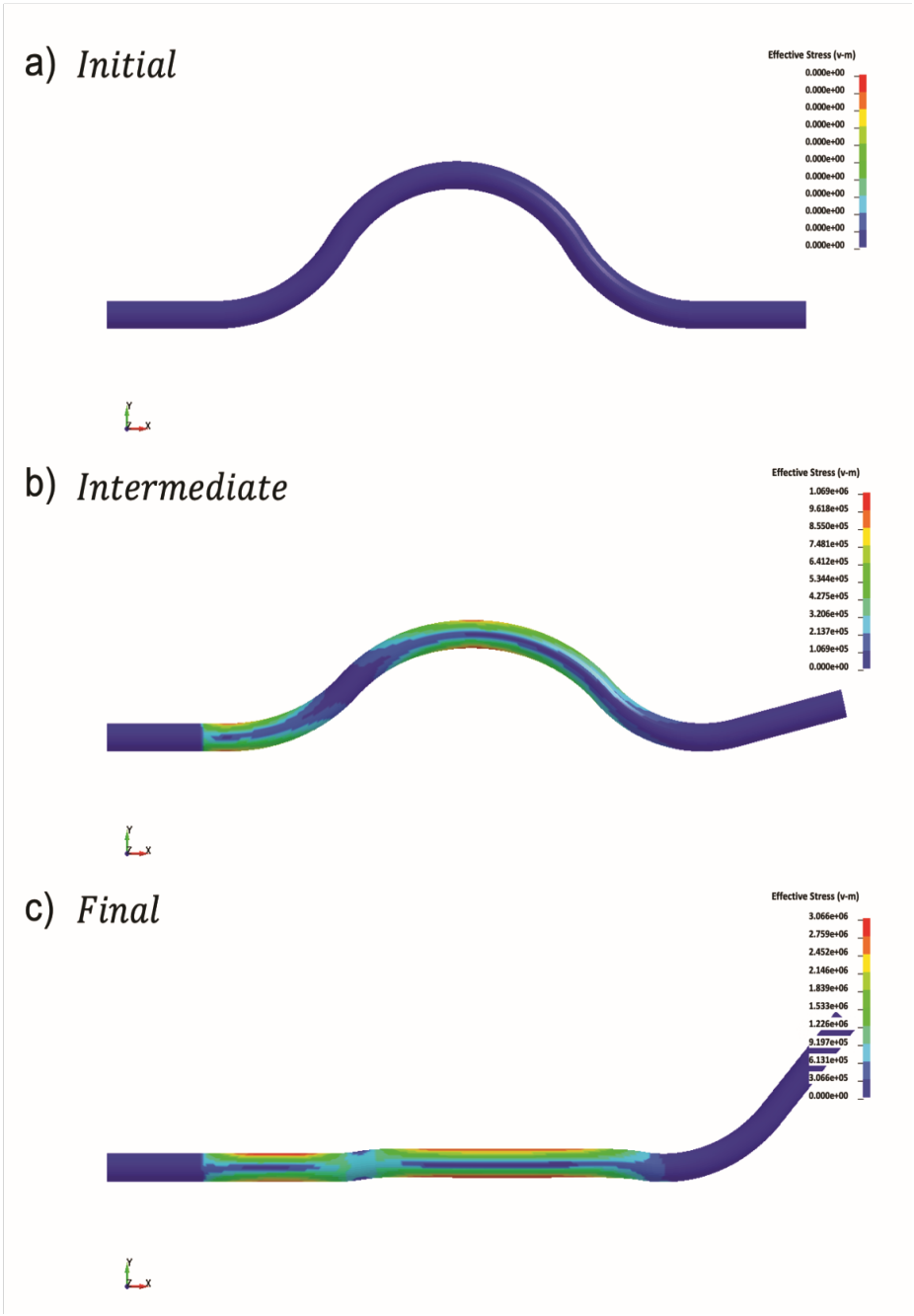

Figure 69: The von Mises stress distribution along the length of the tube during its deflection.

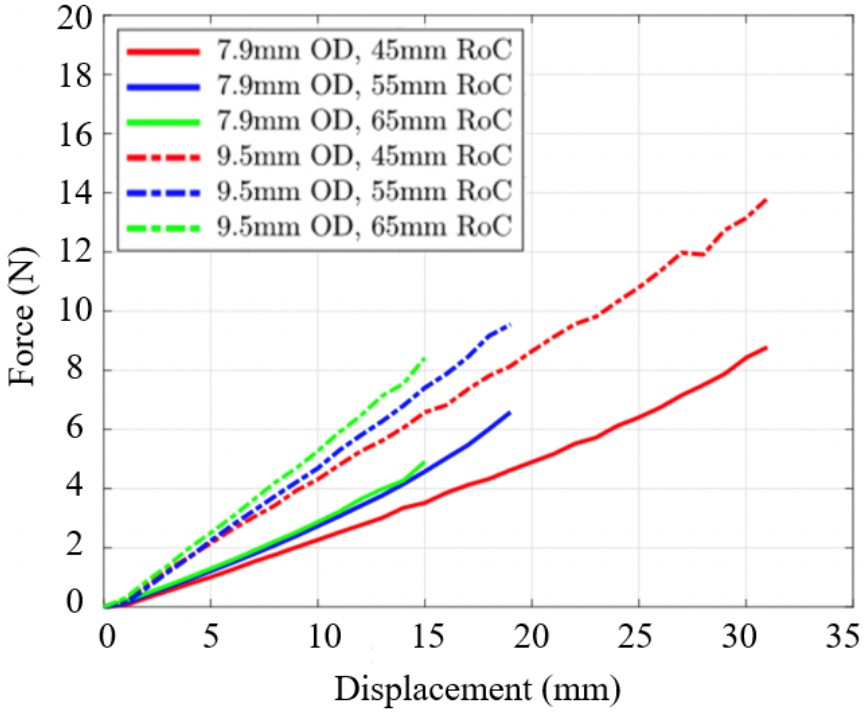

(a)

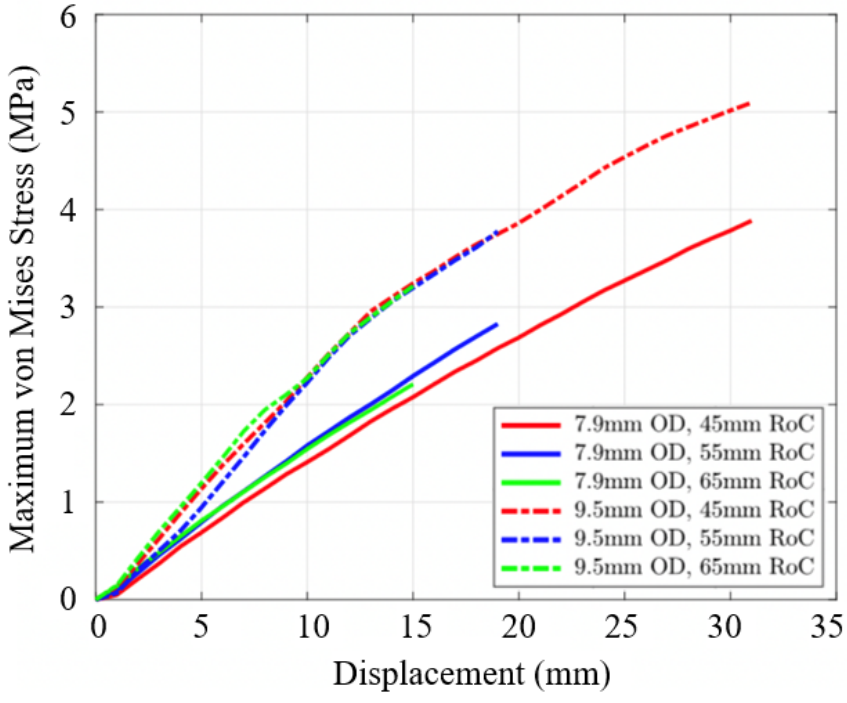

(b)

Figure 70: The finite element results for the (a) force vs. displacement and (b) maximum von Mises stress vs. displacement using the nonlinear Mooney Rivlin material model.

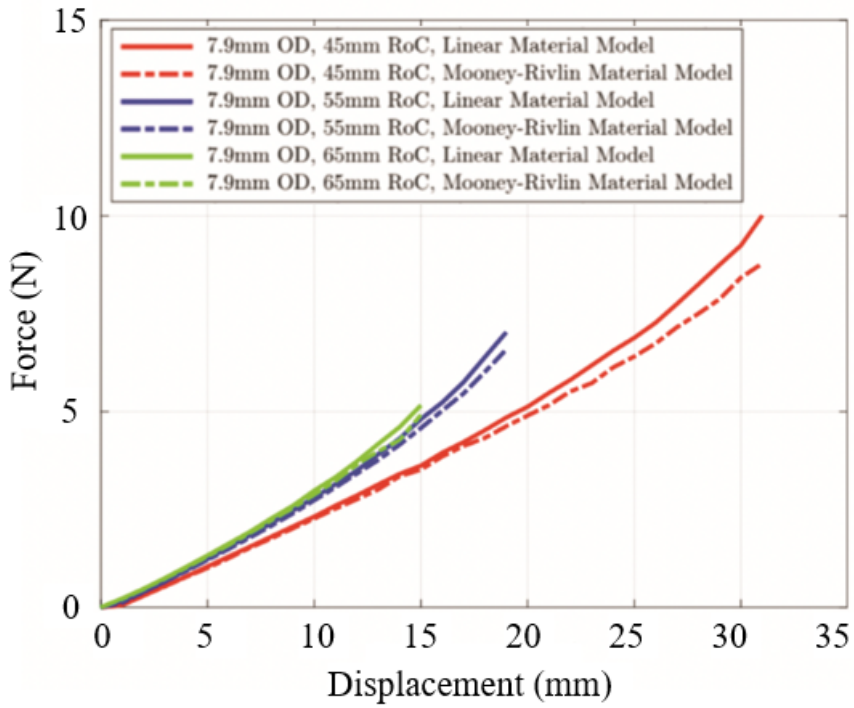

(a)

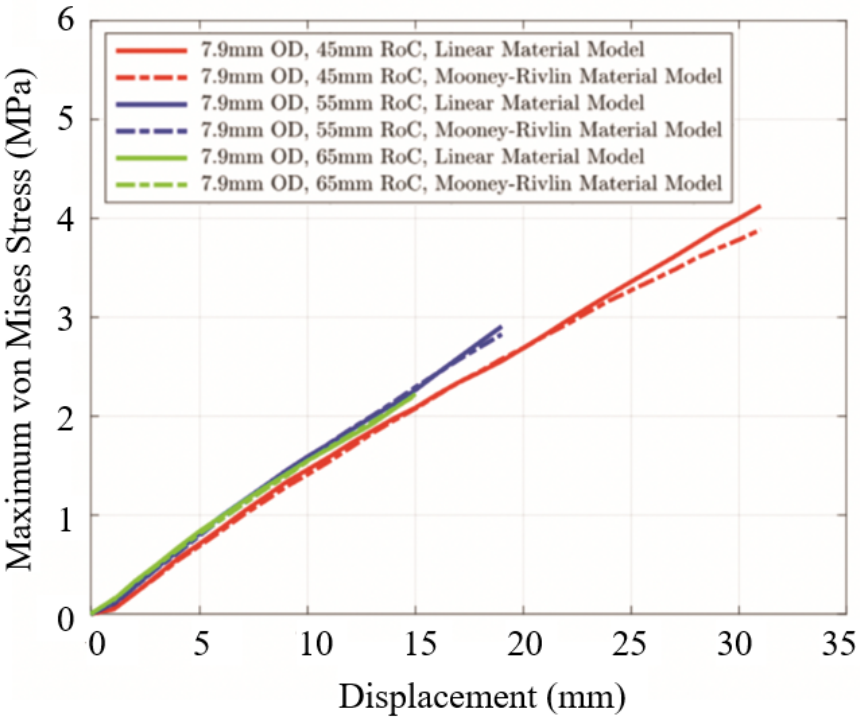

(b)

Figure 71: Comparison of (a) force vs. displacement and (b) maximum von Mises stress vs. displacement for linear and nonlinear Mooney Rivlin material models (7.9 mm diameter tubes).

In Figure 71, the von Mises stress vs. displacement is shown including the comparison between the linear and the nonlinear material models in the simulation. As expected, for small values of displacement there is only a small difference in the calculated values of the force and the maximum von Mises stress for the two models. As the displacement increases, the differences become more pronounced. The linear model overestimates the values of the force and the maximum von Mises stress for a given amount of displacement.

The cross-section of the EDD outer tube before and after deformation was analyzed using the simulation described above. Results are illustrated in Figure 72 and Figure 73, and reveal that the neutral axis does indeed shift away from the centroidal axis as assumed in the analytical section. The figures also show that the inner and outer diameter do not significantly change during bending. If a thinner outer tube wall was implemented, or a more compliant material was chosen, this assumption may no longer apply. This finite element result validates those assumptions found in the mathematical analysis by clearly showing the deformation and stress distribution.

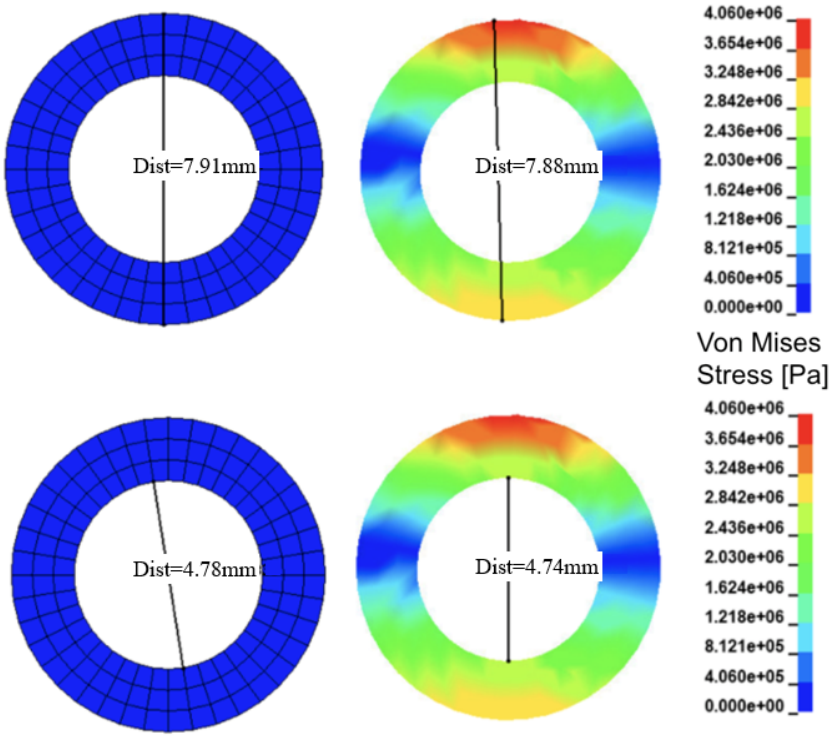

Figure 72: Cross-section analysis measuring vertical distance for outer and inner diameters.

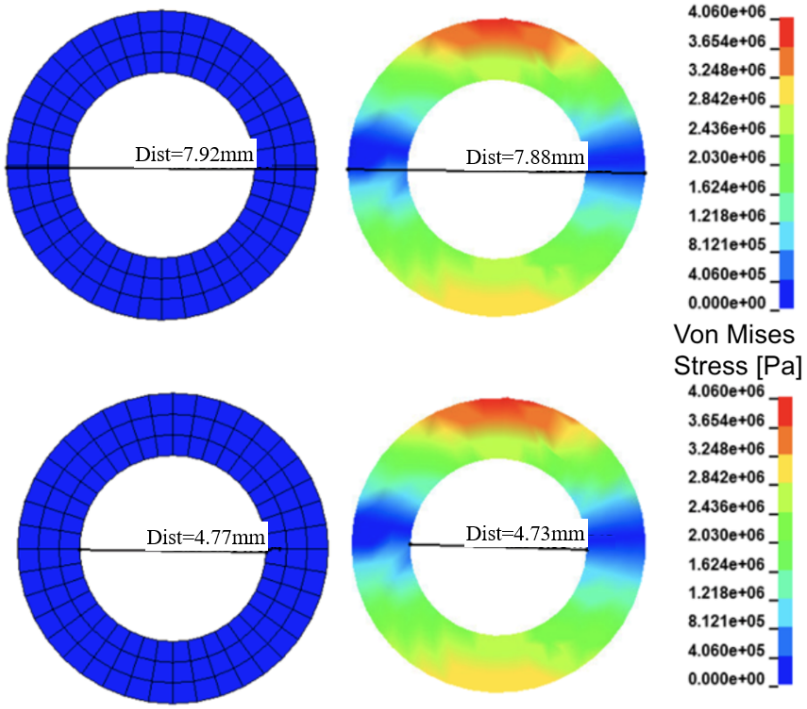

Figure 73: Cross-section analysis measuring horizontal distance for outer and inner diameters.

4.9 Ex Vivo Testing of the EDD

In order to fully translate the EDD so that it may be used in a clinical setting, it is important to understand how the device will perform under more realistic conditions, beyond the bench testing setup. The human body introduces a complex set of boundary conditions, including that of the EDD being inserted into a soft flexible esophagus which is connected to the stomach (or lower esophageal sphincter) and the pharynx on either end while held at body temperature (~37°C). Following the bench and numerical tests, ex vivo testing introduces new relevant boundary conditions. Porcine tissue is clamped into a temperature-controlled water bath. An esophageal deflection device is deployed into the porcine esophagus ex vivo set up. The deflection and applied force properties for EDDs comprised of varying cross sections and curvatures are investigated.

4.9.1 Ex Vivo EDD Deflection Measurement

Porcine esophagus and stomach tissue have been excised and integrated into the ex vivo experimental set up shown in Figure 74. Clamping points have been set up in expected locations for the lower esophageal sphincter on one end and the pharynx for the other. A port is inserted into the wall of the water bath providing access to the inner esophageal lumen. A temperature controller holds the water bath at 37°C, or body temperature, for the duration of the experiments. A camera is placed above the set up to optically measure deflection.

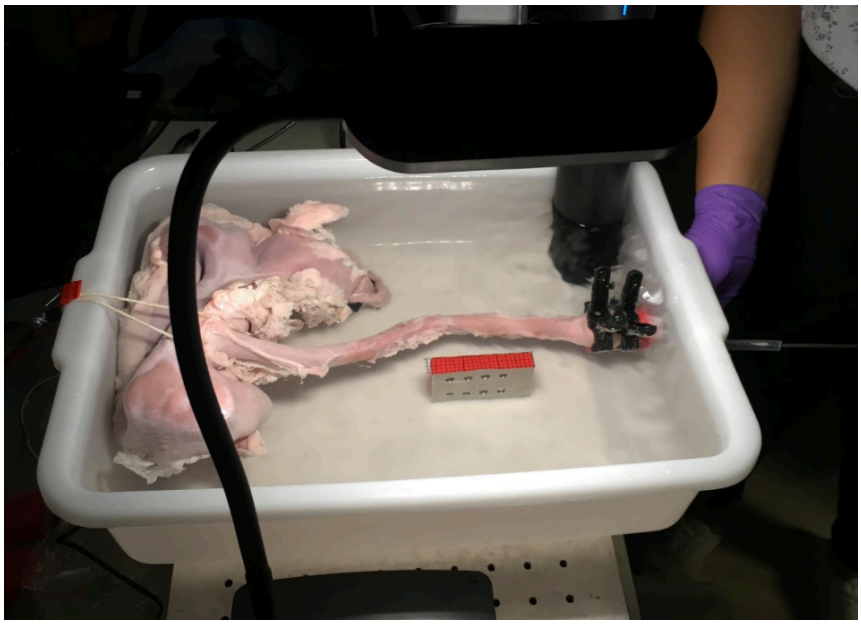

Figure 74: Experimental setup for ex vivo deflection measurements.

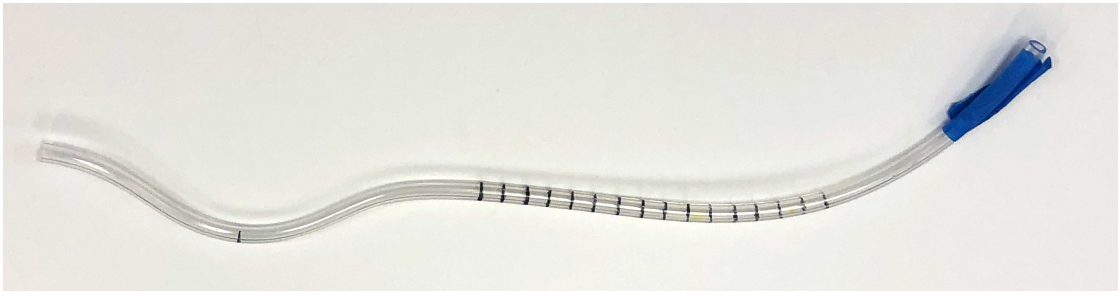

Figure 75: An EVA EDD Tube used in ex vivo studies.

To study deflection of the esophagus in an ex vivo setting as a function of EDD cross section and curvature, multiple EDD EVA outer tubes were thermoformed and prepared. Figure 75 shows a typical prepared EDD outer tube with markings for repeatable insertion depths. Three cross sections were studied (outer diameters of 6.4mm, 7.9mm, and 9.5mm with wall thickness of 1.6mm) as well as three radii of curvature (45mm, 55mm, and 65mm). For each test, the EDD was assembled by inserting the inner rod into the outer pre-curved tube. The assembled EDD was then inserted into the porcine esophageal lumen through the wall port. Once positioned, the inner rod was retracted, allowing the outer tube to re-assume its predefined curvature. Deflection was

measured optically. Finally, the inner rod was re-inserted, and the assembled device was pulled from the esophagus. The procedure was repeated three times for each tube cross section and curvature setting.

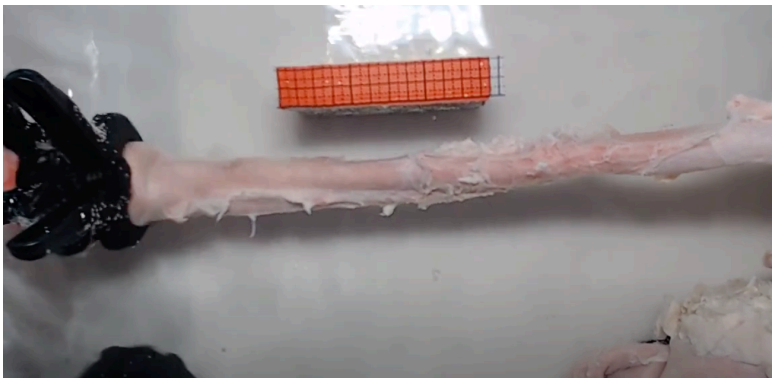

(a)

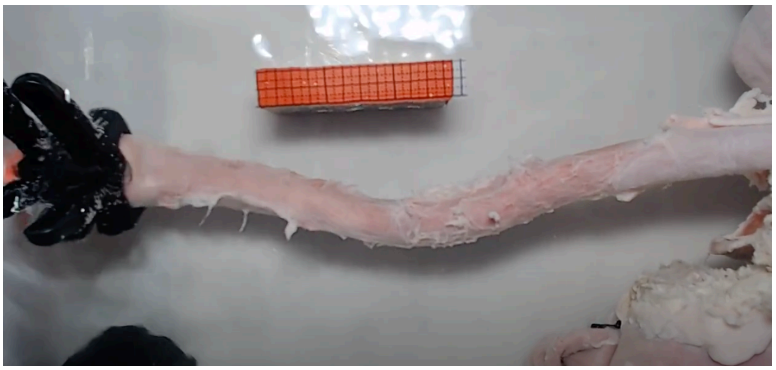

(b)

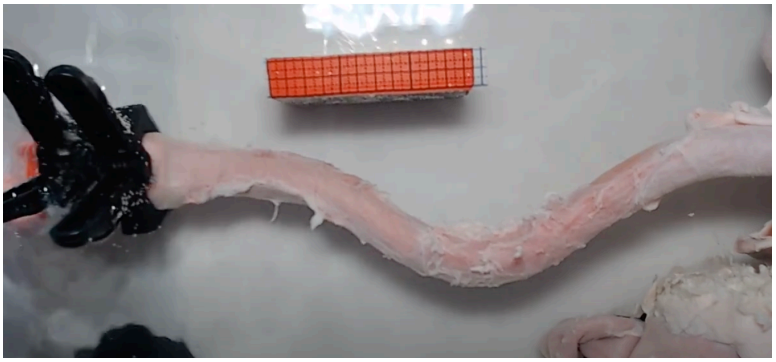

(c)

Figure 76: Photographs of esophagus deflection during test with (a) no deflection, (b) deflection using a tube with 65mm radius of curvature, (c) deflection using a tube with 45mm radius of curvature.

Figure 76 illustrates the esophagus (a) without deflection, (b) using a deployed EDD with a 65mm radius of pre-curvature, and (c) using a deployed EDD with a 45mm radius of pre-curvature. Deflection is clearly visible in the photographs provided and MATLAB image processing techniques were implemented to automatically measure deflection with the varying EDD parameters.

Figure 77(a) shows deflection as a function of EDD outer tube radius of curvature. Deflection increases as the radius of curvature decreases. The data shows between a 3-3.5 cm deflection for the EDDs with a 45mm radius of curvature and a 1.7-2.3cm deflection for the EDDs with a 65mm radius of curvature. Figure 77(b) shows deflection as a function of EDD cross section. Deflection varies insignificantly as a function of EDD outer tube cross section.

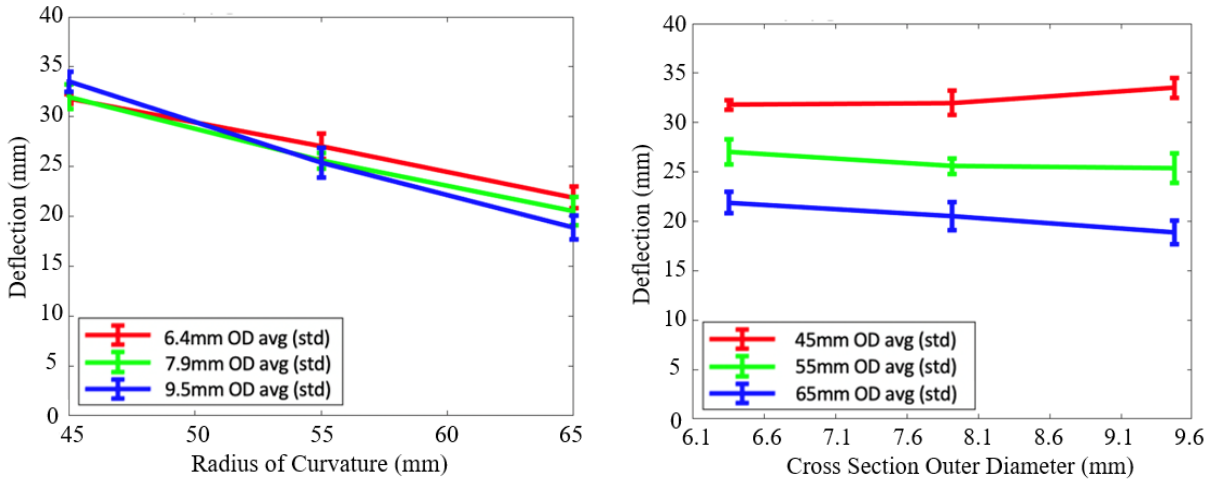

(a) (b)

Figure 77: Experimental results for the (a) measured deflection as a function of the (a) radius of curvature and (b) cross section outer diameter for the inserted tubes.

4.9.2 Ex Vivo EDD Force Measurements

The experimental setup described in the previous section was modified to measure the force exerted on the esophagus from the outer tube re-assuming its pre-curved geometry in the ex vivo environment. Figure 78 shows the porcine esophagus tissue clamped into place and submerged into temperature regulated water. A load cell is mounted to a support structure and attached to an extendable bar with a flat surface on the end. The flat surface is lowered into contact with the esophagus, while the esophagus is in its undeflected state.

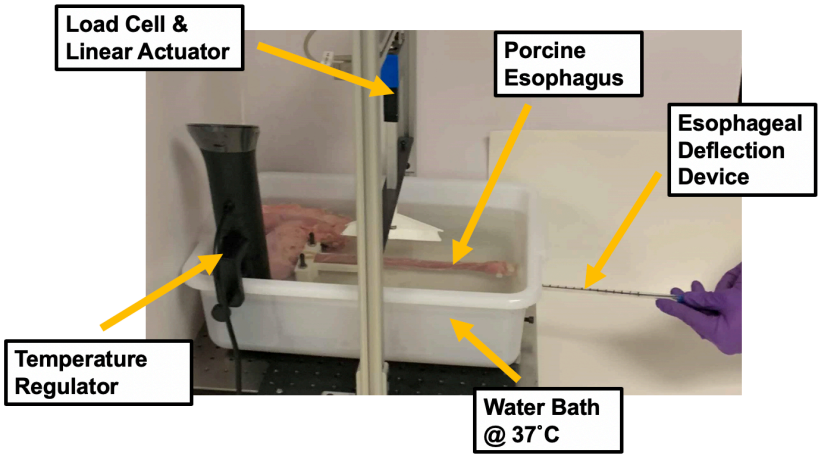

Figure 78: Experimental setup for ex vivo force measurements.

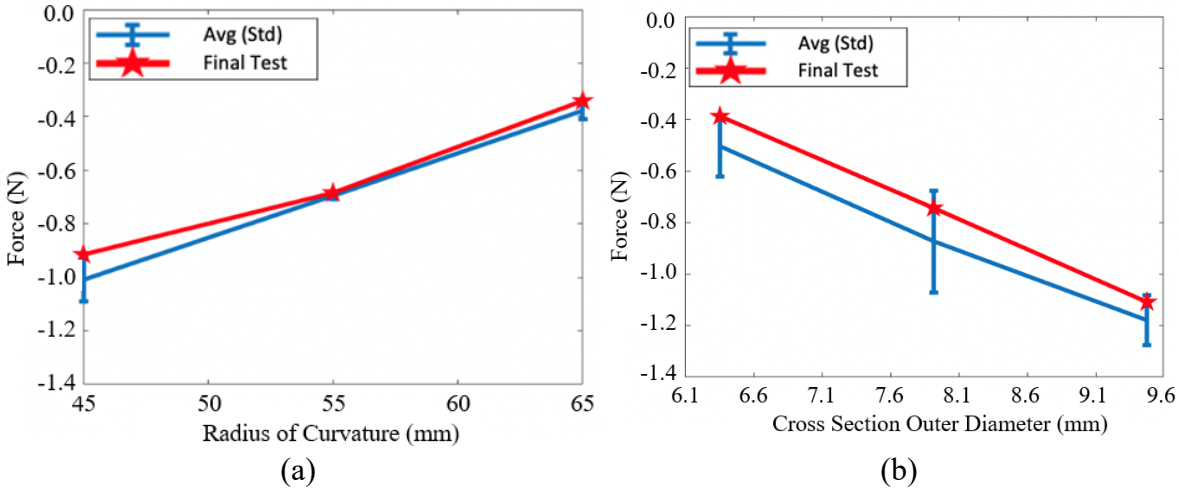

Figure 79: Experimental results for the measured force as (a) function of the radius of curvature for the inserted tubes and (b) a function of cross section outer diameter for the inserted tubes.

Figure 79 shows the forces against the flat surface for EDD tubes with (a) varying radii of curvature from 45mm to 65mm and (b) varying cross section outer diameter from 6.4mm to 9.5mm. Similar to the previous analysis, the absolute value of the force decreases as the radius of curvature increases and the absolute value of the force increases as the cross section outer diameter increases.

4.10 Discussion and Conclusions

The design parameters of the Esophageal Deflection Device (EDD) strongly influence the performance of the device. The EDD tube exerts forces along the esophageal wall after the insertion rod is removed, thereby deflecting the esophagus. In this paper, the performance of the esophageal deflection device has been studied analytically by evaluating the nonlinear displacements of pre-curved EVA tubes under the action of applied moments. In addition, the displacement of pre-curved EVA tubes has been investigated experimentally using an actuator that applied a known displacement on the tube. Finally, we have simulated the deformation of EVA tubes using finite element analysis. The results from the theoretical, numerical and experimental analysis show that material properties and design parameters such as the radius of curvature of the tube and the cross section of the tube determine the deformation of the tube as well as the internal stresses and strains while the initially curved tube is straightened.

The hyperelastic (Mooney-Rivlin) constitutive model, investigated in section 4.5, proved to be of importance in both the analytical and numerical studies. In particular, we observed that an increase in the change of curvature causes the predictions from the linear and nonlinear material models to differ significantly. For the tubes used in this study, the differences became noticeable at an approximate change in curvature of 15 m^{-1}. Additional parameters not studied in this paper

may affect the performance characteristics and constitutive equation when the medical device is used clinically. These parameters include viscoelastic effects, as well as thermoelastic effects. A material with a slower response in releasing its strain energy may make the device easier and safer to use. Temperature of the human body as opposed to room temperature of the experiment, can make the device less stiff and, in turn, prevent the device from effectively moving the esophagus. The constitutive equation for the EDD tube material, EVA, needs to be investigated at elevated temperature conditions.

In our analytical evaluation, the curvature remained circular, and the tube cross section remained circular as the tube straightened. The numerical model relaxed those geometrical constraints. Similar results were obtained numerically, but it is clear that the geometric non-linearity observed in the numerical study can affect the stress distribution both along the tube length as well as across the cross section.

In the analytical model, the tube deformation was investigated by changing the curvature due to applied end moments until the tube was straightened. In the experimental and numerical analysis, the tube deformation was investigated by confining the tube between two rigid walls, with one of the walls moving towards the other surface, in order to straighten the tube. The applied boundary conditions are important for understanding the stress and strain states in the tube and to provide a resulting moment or force, but they do not reveal the effects on the esophageal soft tissue and the body tissue surrounding it. Further experimental and numerical studies should include changing of boundary conditions to address worst-case scenarios and extreme anatomical conditions. With the aim of moving the esophagus safely and reliably, it would be desirable to enhance the model and investigate the interactions of the tube with the soft tissue. Future ex vivo studies (e.g., using a porcine model) could provide useful results for this application. In all

investigations, the consideration of how design changes affect patient safety must be of primary concern.

In summary, the conclusions of our study are as follows.

- The EDD has been designed and manufactured to exert a force on the esophagus and defect it away from the ablation site during the procedure.
- Previous esophageal deflection devices have required expensive and complicated manufacturing methods [4-6]. A low-cost EVA tube thermoforming process has been implemented to vary the dimensions of the EDD tube curvature and cross section.
- Previously published properties for the EVA tube material, shown in Table 5, are inadequate for modeling the constitutive response during deformation of the EDD due to the large deformation states that are beyond the linear elastic range (>1%).
- Uniaxial tensile tests were performed on the specific EVA formulation provided by the supplier and after thermoforming. We observe that the EVA tube material is hyperelastic with estimated Mooney Rivlin parameters $C_1 = -27.4$ MPa and $C_2 = 36.2$ MPa. In the range of infinitesimal strain, EVA can be modeled as a linearly elastic material with a modulus of elasticity $E = 52.8$ MPa.
- Moment curvature and stress curvature relationships were determined analytically using both linear and nonlinear constitutive equations. The analytical approach reveals a direct relationship between design features and product performance including the effect of curvature, cross section, and radial location on applied moment and stresses. Maximum stress values for one proposed design in a straightened state were found to be $\sigma_{max}^{+} = 3.28$ MPa and $\sigma_{max}^{-} = 5.65$ MPa, respectively, indicating a small amount of plastic deformation.

- Experimental measurements of the force exerted by the tube during straightening range from 0 to 14 N. The force was shown to depend on the deformation state during straightening as well as the initial radius of curvature and cross section of the tube.

- A numerical model, incorporating linear and nonlinear material models, was developed using finite element analysis to simulate the deformation of pre-curved tubes and determine the stress strain behavior of the pre-curved tubes in the EDD. This model can be extended to evaluate different geometries, materials, or boundary conditions.

- The analytical and numerical model revealed levels of von Mises stress beyond the elastic limit. Those limits should be avoided when finalizing the EDD design to prevent plastic deformation.

- Significant differences between the tube deformation predictions based on linear and nonlinear material models occurred at a large change in curvature ($> 15 m^{-1}$) for both the analytical and numerical studies. A non-linear material model is necessary to accurately model the expected deformation of the EDD.

- Ex vivo studies were performed to provide a more realistic setting for how the EDD will operate. Force results were lower due to different boundary conditions including esophagus contact points and higher environmental temperature. The higher environmental temperature resulted in some softening of the EVA material. This should be studied further.

- Additional studies should be undertaken to investigate the performance of the device during ex-vivo and in-vivo testing, including a more detailed and accurate description of the interactions of the device with surrounding soft tissue at body temperature. Patient safety is of upmost importance when translating this device for clinical use.

Chapter 4, in part, is a reprint of the materials as they appear in "Design of an esophageal deflection device for use during atrial ablation procedures." Morris, K., Lubarda, V.A., Talke, F.E. Journal of Materials Research and Technology, 9(6) pp. 13801-12, 2020. The dissertation author was the primary investigator and author of this patent publication.

References

[1] Chugh S.S., Havmoeller R., Narayanan K., Singh D., Rienstra M., Benjamin E.J., et al. Worldwide Epidemiology of Atrial Fibrillation: A Global Burden of Disease 2010 Study. Circulation. 2013;129(8):83747. https://doi.org/10.1161/CIRCULATIONAHA.113.005119].

[2] Spragg D., Calkins H. Catheter Ablation for Atrial Fibrillation: Past, Present, and Future. In: Steinberg JS, Jaïs P, Calkins H, editors. Practical Guide to Catheter Ablation of Atrial Fibrillation. Hoboken: John Riley & Sons; 2015, p. 715. https://doi.org/10.1002/9781118658369.ch02.

[3] Kaneshiro T., Matsumoto Y., Hijioka N., Nodera M., Yamada S., Kamioka M., et al. Distinct Forms of Esophageal Lesions After Radiofrequency and Cryoballoon Pulmonary Vein Isolation. JACC: Clinical Electrophysiology. 2018;4(12):1642-3 https://doi.org/10.1016/j.jacep.2018.08.006.

[4] Elkhatib I., Syed F., Krinsky M.L., Savides T.J., Feld G. Endoscopic Mechanical Displacement of the Esophagus During Atrial Fibrillation Catheter Ablation. Gastrointestinal Endoscopy. 2014;79(5):AB51112. https://doi.org/10.1016/j.gie.2014.02.806.

[5] Koruth J.S., Reddy V.Y., Miller M.A., Patel K.K., Coey J.O., Fischer A., et al. Mechanical Esophageal Displacement during Catheter Ablation for Atrial Fibrillation. Journal of Cardiovascular Electrophysiology. 2012;23(2):14754. https://doi.org/10.1111/j.1540-8167.2011.02162.x 15.

[6] Parikh V., Swarup V., Hantla J., Vuddanda V., Dar T., Yarlagadda B., et al. Feasibility, Safety, and Efficacy of a Novel Preshaped Nitinol Esophageal Deviator to Successfully Deflect the Esophagus and Ablate Left Atrium without Esophageal Temperature Rise during Atrial Fibrillation Ablation: The DEFLECT GUT Study. Heart Rhythm. 2018;15(9):132127. https://doi.org/10.1016/j.hrthm.2018.04.017.

[7] Morris K., Savides T., Feld G., Seo Y., Fu Y., Talke F.E. Esophageal Deflection Device, Published Patent (Pending) 2020; US 2020/0029822.

[8] Garner S., Morris K., Pegan R., Savides T.J., and Talke F.E. Development of a Luminal Esophageal Temperature Monitoring Device for Use During Treatment for Atrial Fibrillation. In: American Society for Mechanical Engineers, organizer. Proceedings of the ASME-JSME 2018 Joint International Conference on Information Storage and Processing Systems and Micromechatronics for Information and Precision Equipment; 2018 Aug 2930, San Francisco, USA. p. 13 https://doi.org/10.1115/ISPS-MIPE2018-8578.

[9] Garner S. Development of A Luminal Esophageal Temperature Monitoring Device for Use During Treatment of Atrial Fibrillation. [M.Sc. Dissertation]. La Jolla: University of California, San Diego; 2018.

[10] Morimoto T.K.., Greer J.D., Hawkes, E.W., Hsieh M.H., Okamura, A.M. Toward the Design of Personalized Continuum Surgical Robots. Annals of Biomedical Engineering. 2018;46:152233. https://doi.org/10.1007/s10439-018-2062-2.

[11] Webster R.J., Okamura A.M., Cowan N.J. Toward Active Cannulas: Miniature Snake-like Surgical Robots. In: Institute of Electrical and Electronics Engineers, organizer. Proceedings of the IEEE/RSJ International Conference on Intelligent Robots and Systems; 2006 Oct 915, Beijing, China. p. 285763. https://doi.org/10.1109/IROS.2006.282073.

[12] Rucker D.C., Jones B.A., Webster R.J. A Geometrically Exact Model for Externally Loaded Concentric- Tube Continuum Robots. IEEE Transactions on Robotics. 2010;26(5):76980. https://doi.org/10.1109/TRO.2010.2062570.

[13] Antman S.S. Nonlinear Problems of Elasticity. 2nd. ed. New York: Springer; 2005. https://doi.org/10.1007/0-387-27649-1.

[14] Baek C., Yoon K., Kim D. Finite Element Modeling of Concentric Tube Continuum Robots. Structural Engineering and Mechanics. 2016;57(5):80921. https://doi.org/10.12989/sem.2016.57.5.809.

[15] Morimoto T.K., Okamura A.M. Design of 3-D Printed Concentric Tube Robots. IEEE Transactions on Robotics. 2016;32(6):141930. https://doi.org/10.1109/TRO.2016.2602368.

[16] Biase L.D., Saenz L.C., Burkhardt D.J., Vacca M., Elayi C.S., Barrett C.D., et al. Esophageal Capsule Endoscopy after Radio frequency Catheter Ablation for Atrial Fibrillation: Documented Higher Risk of Luminal Esophageal Damage with General Anesthesia as Compared with Conscious Sedation. Circulation: Arrhythmia and Electrophysiology. 2009;2(2):10812. https://doi.org/10.1161/CIRCEP.108.815266.

[17] Zhang P., Zhang Y.Y., Ye Q., Jiang R.H., Liu Q., Ye Y., Wu J.G., Sheng X., Fu G.S., Cha Y.M., Jiang C.Y. Characteristics of Atrial Fibrillation Patients Suffering Esophageal Injury Caused

by Ablation for Atrial Fibrillation. Scientific Reports. 2020;10:2751. https://doi.org/10.1038/s41598-020-59539-6.

[18] Berjano E.J., Hornero F. What Affects Esophageal Injury during Radiofrequency Ablation of the Left Atrium? An Engineering Study Based on Finite-Element Analysis. Physiological Measurement. 2005; 26(5):83748. https://doi.org/10.1088/0967-3334/26/5/020.

[19] Liao D., Frøkjær J.B., Yang J., Zhao J., Drewes A.M., Gilja O.H., Gregersen H. Three-Dimensional Surface Model Analysis in the Gastrointestinal Tract. World Journal of Gastroenterology. 2006;12(19):287075. https://doi.org/10.3748/wjg.v12.i18.2870.

[20] Jernigan S.R., Buckner G.D., Eischen J.W., Cormier D.R. Finite Element Modeling of the Left Atrium 16 to Facilitate the Design of an Endoscopic Atrial Retractor. Journal of Biomechanical Engineering 2007;129(6):825-37. https://doi.org/10.1115/1.2801650.

[21] Natali A.N., Carniel E.L., Gregersen H. Biomechanical Behaviour of Oesophageal Tissues: Material and Structural Conguration, Experimental Data and Constitutive Analysis. Medical Engineering and Physics. 2009;31(9):105662. https://doi.org/10.1016/j.medengphy.2009.07.003.

[22] US Food and Drug Administration. Use of International Standard ISO 10993-1, https:// www.fda.gov/downloads/medicaldevices/deviceregulationandguidance/guidancedocuments/ucm 348890; 2020 [accessed 25 March 2020].

[23] Ogden R.W. Nonlinear Elasticity, Anisotropy, Material Stability and Residual Stresses in Soft Tissue. In: Holzapfel GA, Ogden RW, editors. Vienna, Springer; 2003, p. 65108 https://doi.org/10.1007/978- 3-7091-2736-03.

[24] Lubarda V.A. Elastoplasticity Theory. Boca Raton, CRC Press; 2001.

[25] Morris K.M, Rosenkranz A., Seibert H., Ringel L., Diebels S., Talke F.E. Uniaxial and Biaxial Testing of 3D Printed Hyperelastic Photopolymers. Journal of Applied Polymer Science. 2019;48400. https://doi.org/10.1002/app.48400.

Chapter 5 Temperature Measurement in the Esophagus during Ablation Procedures

5.1 Introduction

Human heart tissue is damaged irreversibly at temperatures higher than 50°C, i.e., at temperatures of approximately 13°C above body temperature [1]. In catheter ablation procedures, the application of heat to the left atrial tissue can lead to heating of the esophageal tissue [2], since the esophagus is in close proximity to the heart (see Figure 80). Heating can produce lesions or ulcerations on the esophagus tissue and, in the worst case, lead to the formation of a so-called atrioesophageal fistula [3,4]. Atrioesophageal fistulae have a high mortality rate [4]. To prevent thermal damage of the esophagus, it is important to measure the temperature of the esophageal tissue during an ablation procedure and stop the procedure when a critical temperature is reached.

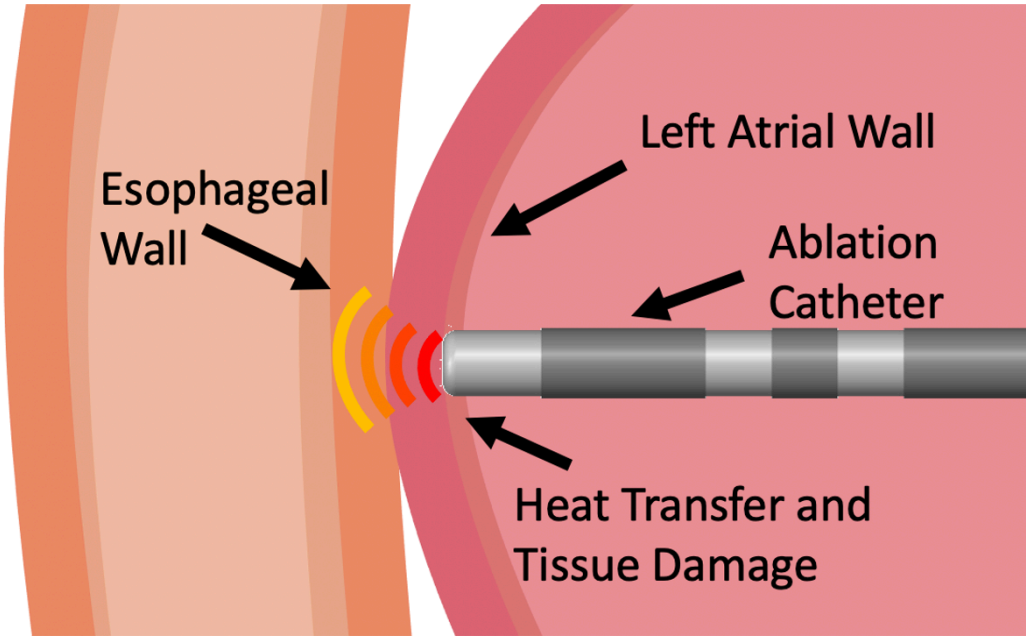

Figure 80: The esophagus being heated during cardiac ablation procedures.

To accomplish the measurement of the luminal esophageal temperature (LET), it is necessary to insert temperature probes into the esophagus through the nose or the mouth [4, 5]. It has been shown by [2] that an increase of the inner esophageal wall temperature above 40°C corresponds to the development of thermal lesions in the esophagus. To avoid thermal lesions, medical doctors will, in general, stop the ablation procedure once the esophagus temperature measurement device indicates a rise in temperature greater than ~1°C above body temperature. The medical clinicians may attempt ablation again or aim to move the esophagus away from its position adjacent to the heart. The design of esophagus temperature probes, including the placement of the sensors, is a complicated design problem and requires the understanding of heat transfer in human tissue to prevent thermal damage.

A number of temperature measurement devices have been designed and are commercially available. A typical example is the Circa S-Cath® catheter that is used for esophageal temperature

measurement [5] (see Figure 81). The device has twelve sensors positioned along its length and can be inserted into the esophagus through the mouth. After insertion, a wire can be pulled from the device to allow the catheter to attain a sinusoidal shape pushing the sensors against the esophagus inner wall (Figure 81). The temperature sensors are labeled in Figure 81 and placed incrementally along the sinusoidal catheter.

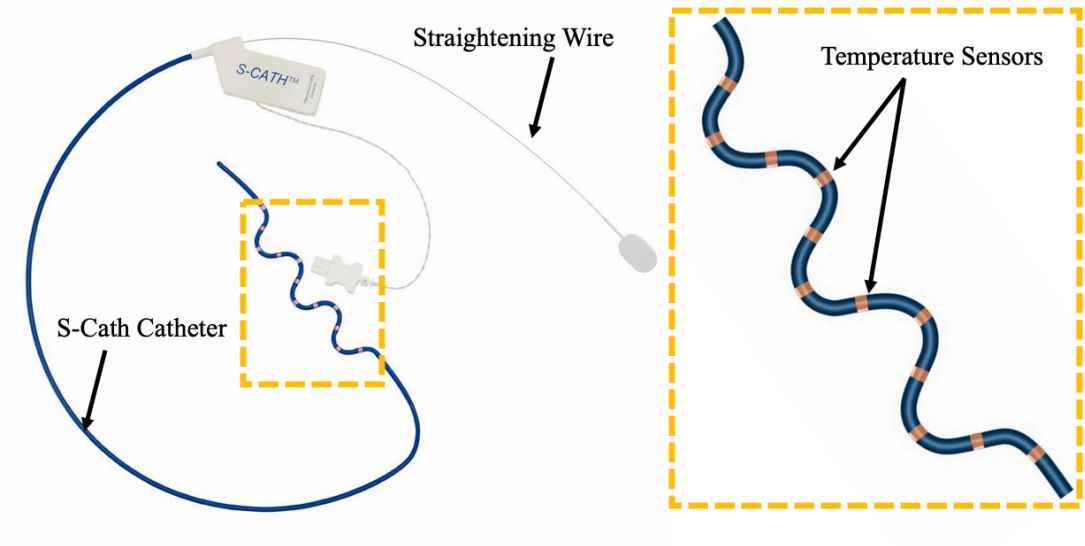

Figure 81: (a) Circa S-Cath with pulled straightening wire, and (b) Circa S-Cath temperature sensor array [6].

To obtain reliable temperature measurements the sensors must be positioned against the inner esophageal wall and against the part of the esophageal tissue that is closest to the ablation site. In this chapter, we discuss the combination of the esophageal deflection device (EDD) [7, 8] and temperature sensors. A new medical device design is discussed which incorporates the EDD with the Circa S-Cath. Using newly designed temperature sensor arrays adhered to a flexible silicone sheet, the effect of thermal sensor placement on the measurement of the esophagus temperature is studied experimentally.

5.2 Esophageal Deflection Device with Temperature Sensors

In order to reliably sense the inner esophageal wall temperature during cardiac ablation procedures, incorporation of temperature sensors in the esophageal deflection device (EDD) is proposed. The EDD can be manufactured to include temperature sensors. Several advantages are present if the EDD incorporates its own temperature sensing technology, as opposed to using a separate device. It can be more difficult on the medical practitioner to introduce and use multiple devices. The devices can conflict with one another, for example, if the EDD blocks the thermal sensors from measuring at the ideal location. Figure 82a shows the precurved outer tube of the EDD described in [7, 8], as well as the Circa S-Cath device. The S-Cath protrudes out of the trailing edge of the device, on the side of the EDD which is most likely to be closer to the left atrium ablation site.

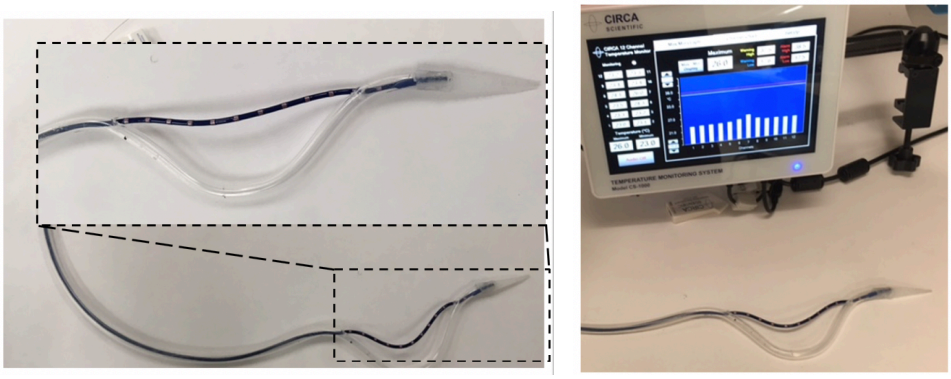

(a) (b)

Figure 82: (a) Modified EDD combined with Circa Scientific S-Cath Device and (b) Circa S-Cath monitor with measurement sensing system next to Modified EDD combined with Circa Scientific S-Cath Device.

Figure 82b shows the combined EDD and S-Cath as well as the commercially available Circa monitoring system. The bar chart on the monitoring system shows each temperature sensor measurement and, once one sensor detects a temperature above a specified value, the monitoring system will sound an alarm and flash.

The sensors position plays an important role in the devices ability to detect temperature rise. In order to optimize the thermal sensing of the device, it is necessary to understand the heat transfer through the atrium and esophagus tissue.

5.3 Background for Tissue Heat Transfer during Radiofrequency Catheter Ablation

Thermal energy transport through human tissue requires information on the anatomical structure of the human body, internal and external heat sources, and thermal properties of the tissue. Important material properties include tissue density, thermal conductivity, and specific heat. The energy balance equation for heat transfer can be written as:

$$\frac{d}{dt}Q_s = \frac{d}{dt}Q_g + \frac{d}{dt}Q_l + \frac{d}{dt}W \tag{5.1}$$

where $\frac{d}{dt}Q_s$ is the rate of heat energy stored, $\frac{d}{dt}Q_g$ is the rate of heat energy gained, $\frac{d}{dt}Q_l$ is the rate of heat energy lost, and $\frac{d}{dt}W$ is the rate of work done by the tissue [7].

The rate of heat energy stored in tissue can be defined as:

$$\frac{d}{dt}Q_s = \rho c \frac{\partial T}{\partial t} \tag{5.2}$$

where ρ, c, and T are the tissues' mass density, specific heat, and temperature.

The rate of heat energy gained or heat energy lost is commonly described through conduction and convection. Conduction is the transfer of heat through materials while convection is the transfer of heat between a solid and fluid. Conduction and convection are mathematically defined by:

$$\frac{d}{dt}Q_{g/l\,(conduction)} = \frac{\partial}{\partial x}\left(k_x\frac{\partial T}{\partial x}\right) + \frac{\partial}{\partial y}\left(k_y\frac{\partial T}{\partial y}\right) + \frac{\partial}{\partial y}\left(k_z\frac{\partial T}{\partial y}\right) \tag{5.3}$$

$$\frac{d}{dt}Q_{g/l\,(convection)} = hA(T - T_\infty) \tag{5.4}$$

where k_x, k_y, k_z are the thermal conductivity constants, while h is the heat convection coefficient, A is the surface area between the solid and fluid interaction, and T_∞ is the ambient temperature of the fluid. If the tissue is thermally isotropic, then $k_x = k_y = k_z$.

A number of models have been developed from the energy balance equation using conduction and convection components to describe the nature of heat transfer in tissue [9]. The general Pennes's Bio-heat transfer (BHT) equation [9, 10] is commonly used in tissue heat transfer analysis and accounts for tissue thermal conductivity, specific heat, density, arterial blood flow and metabolic heat generation. The Pennes's BHT equation is written as:

$$\rho c\frac{\partial T}{\partial t} = \nabla(k\nabla T) + w_b c_b(T_a - T) + q_m \tag{5.5}$$

where

$$\nabla(k\nabla T) = \frac{\partial}{\partial x}\left(k_x\frac{\partial T}{\partial x}\right) + \frac{\partial}{\partial y}\left(k_y\frac{\partial T}{\partial y}\right) + \frac{\partial}{\partial y}\left(k_z\frac{\partial T}{\partial y}\right) \tag{5.6}$$

and ρ, c, and k are the tissues' mass density, specific and thermal conductivity, respectively. T is the temperature and T_a is the temperature of the arterial blood. w_b and c_b are the mass flow rate and specific heat of the blood and q_m is the metabolic heat generation. Through equation 5.6, it shown that differences in temperature can cause heat transfer in x-, y-, and z-directions. When measuring temperature rise on the esophagus wall, it is useful to measure longitudinally along the esophagus as well as circumferentially. Similarly, when modeling heat transfer in the esophagus and atrial tissue, a 3-dimensional model is preferred, so that any non-uniformity in the x-, y-, and z-directions could be modelled and the temperature changes in each direction can be evaluated.

5.3.1 Radiofrequency Catheters and Additional Heat Transfer Effects

For this study, an additional heat source term q_{hs} is necessary to represent heat generating from a radiofrequency ablation catheter. A typical cardiac RF ablation catheter is shown in Figure 83 [11].

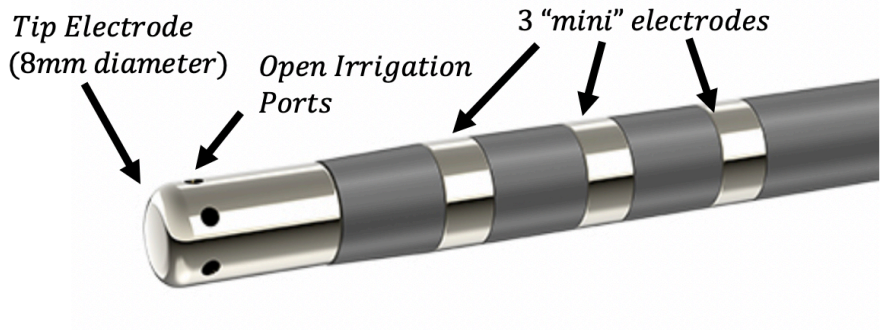

Figure 83: Typical cardiac RF ablation catheter. Figure modified from [11].

RF ablation catheters are used in other medical areas, as, for example, in gastroenterology [12], oncology [13], and pain management [14]. Figure 84 shows different applications of RF ablation to heat tissue rapidly.

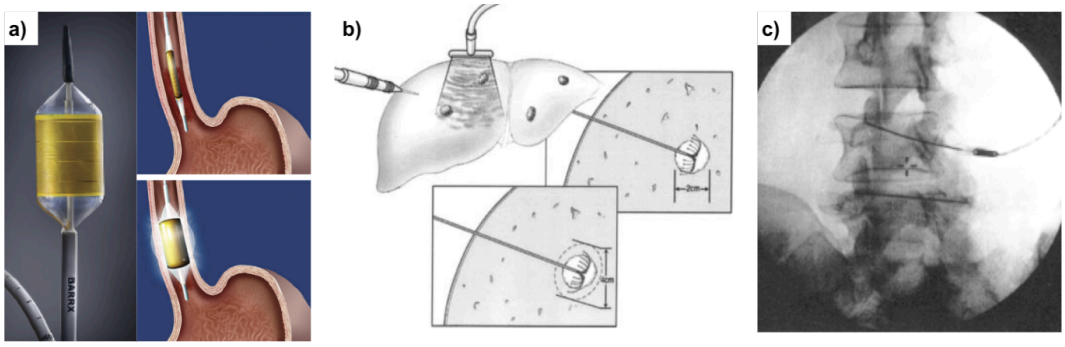

Figure 84: Radiofrequency ablation in use to treat a) an esophageal condition (Barrett's esophagus) [12], b) a malign tumor in the liver [13], c) pain caused by nerves in the spinal cord [14].

The ablation catheter contacts the tissue and applies electrical currents oscillating at radiofrequencies (~500MHz). Due to the high current density in the adjacent tissue, resistive heating occurs. The defining equation for q_{hs} from an RF ablation catheter, as detailed in [15,16] is written as:

$$q_{hs} = \sigma(\nabla\emptyset)^2 \tag{5.8}$$

where q_{hs} is a function of the electrical conductivity σ and the electrical potential $\emptyset$. The electrical field intensity is strongest near the catheter tip and disperses through the human body toward a ground pad usually located nearby on the patient's skin. A schematic is shown in Figure 84a illustrating the radiofrequency ablation setup including a ground pad.

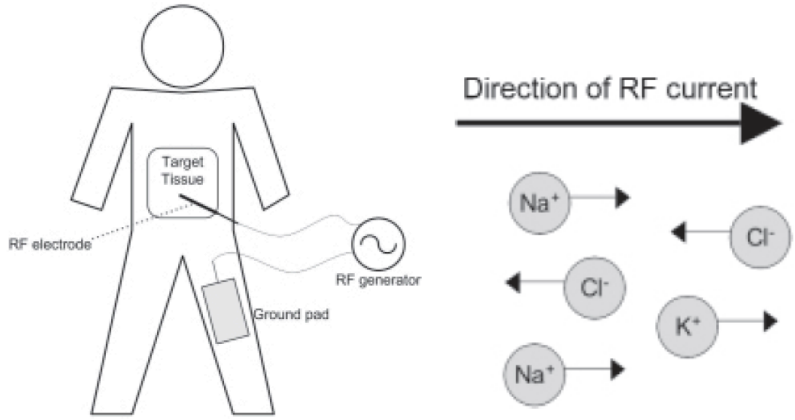

(a) (b)

Figure 85: (a) Illustration of RF ablation set up including ground pad and (b) schematic showing positive and negative charged ions moving dependent on RF current [17]

Figure 85b illustrates the desirable movement of ions within the tissue (i.e., Na^+, K^+, Cl^-), which is dependent on the radiofrequency electrical potential including magnitude and direction (or polarization). As the ions rapidly move, Joule heating (or resistive heating) occurs due to friction. The heat generated is the highest through Joule heating (mathematically described with equation 5.8). Joule heat generation is the strongest near the electrode tip of the catheter.

As RF catheters come into contact with the atrial tissue, there may be other effects heating or cooling the catheter electrode tip and the surrounding tissue. Figure 86 shows several potential effects driven by blood flow and irrigation fluids. The irrigation fluids, such as saline liquid, can be designed to cool the catheter tip through internal cooling, or cool the catheter tip and the surrounding material and tissue through external cooling.

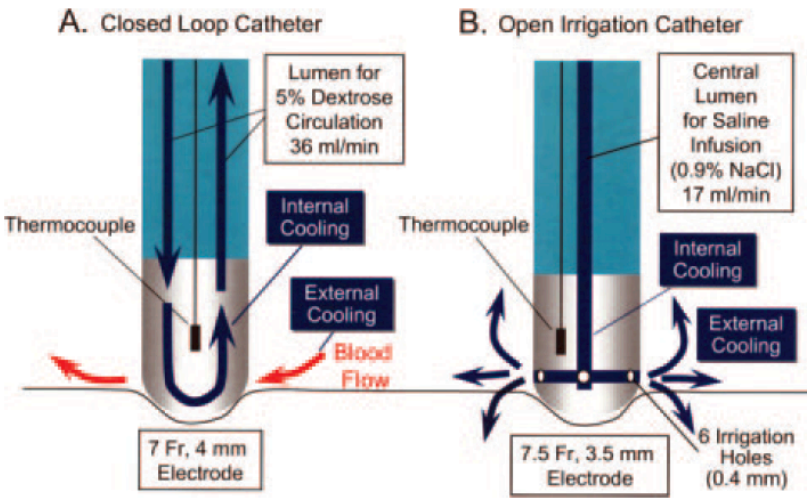

Figure 86: Example of two Cardiac RF Ablation Catheters with (a) closed loop internal cooling and (b) internal cooling and open irrigation external cooling [18].

Also shown in Figure 86 is the direction of blood in the atrial chamber. Blood flow in the arteries and metabolic heat generation shown in the BHT equation are negligible when compared to the RF heat source [19]. However, the convective heat transfer at the atrial wall should also be considered. The pulsatile blood flow velocity can range between 0.1 m/s and 0.5 m/s. It varies significantly with the location in the heart [18,20]. As the temperature difference increases between the blood and the heated tissue, the effect of heat transfer from the tissue to the blood proportionally increases. The equation for heat transfer q_{bf} at blood-atrium interface is

$$q_{bf} = h_{bf} A (T - T_{blood}) \tag{5.7}$$

where h_{bf} is the convective constant for blood flow on the inner atrial wall and T_{blood} is the temperature of the blood. These terms could be extended to include catheter irrigation fluids.

After incorporating the terms for the RF ablation heat source and the atrial wall convection, and dismissing the terms for arterial blood flow and metabolic heat generation, the modified bio-heat transfer equation is given as:

$$\rho c \frac{\partial T}{\partial t} = \nabla(k\nabla T) + h_{bf} A(T - T_{blood}) + \sigma(\nabla \emptyset)^2 \tag{5.9}$$

where the last term denotes the effect of the radiofrequency heat source.

An RF ablation catheter with some common technical specifications is shown in Figure 87 [21]. An important feature on current RF ablation catheters is the temperature sensors, e.g., "3x Distal Thermocouples", located at the contact point between the RF electrode and the atrial tissue. This temperature is monitored throughout the procedure.

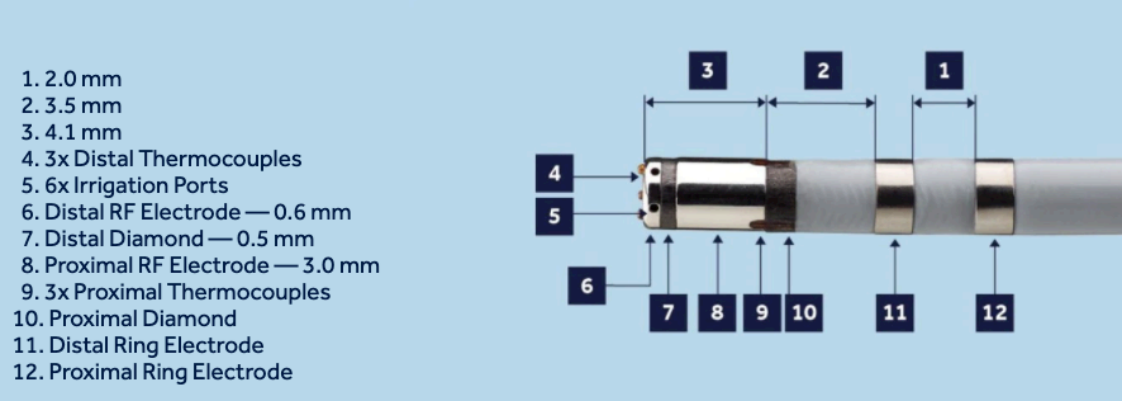

Figure 87: Current RF Ablation catheter with specifications [21]

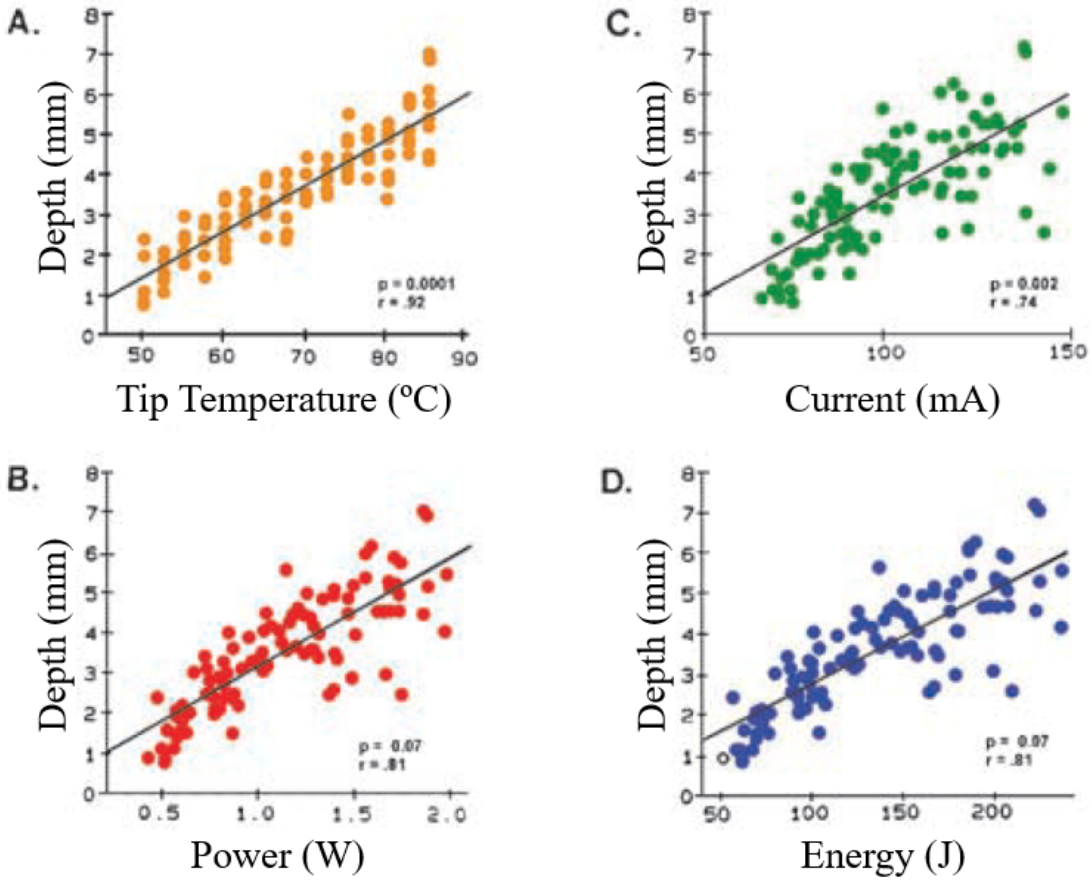

Figure 88: Lesion depth from RF catheter ablation as a function of a) tip temperature (tissue/electrode interface), b) power, c) current, and d) energy [22,23]

Figure 88a plots the lesion depth as a function of tip temperature experimentally using RF ablation on canine right ventricular tissue [22,23]. Figure 88b-c similarly plots the lesion depth as a function of power, current, and energy. The 4 parameters are measured and available to the cardiac electrophysiologist during the procedure, but the lesion depth is uncertain at any point in time. During RF ablation, there are a number of additional factors including, for example, tissue damage, scarring, catheter heating, and contact force between the catheter and tissue, that can complicate how much heat is generated and at what depth [22,23].

In this thesis, a first-order experimental study has been performed to understand heat transfer through esophagus and heart tissue. To simplify the complexity of RF heat generation, a

constant-temperature heat source was used in the experiment. With this our heat transfer equation simplifies to:

$$\rho c \frac{\partial T}{\partial t} = \nabla(k \nabla T) + h_{bf} A (T - T_{blood}) \tag{5.10}$$

where boundary conditions can be adjusted according to the temperature of the heat source. The experiments investigating heat transfer across atrial and esophageal tissue are described in the following sections.

5.4 Experimental Study – Linear (1D) Temperature Sensor Array

An experimental study was conducted ex vivo to measure the temperature on the inner esophagus wall after heat was supplied to adjacent atrial tissue [24,25]. A schematic of this study is shown in Figure 89. With a constant temperature heat source on the atrial wall and a linear, discrete set of temperature sensors on the inner esophageal wall, temperature can be monitored spatially (1D), away from the heat source, and temporally during and after the application of a heat source. Flow of blood or liquid is not considered in this experiment.

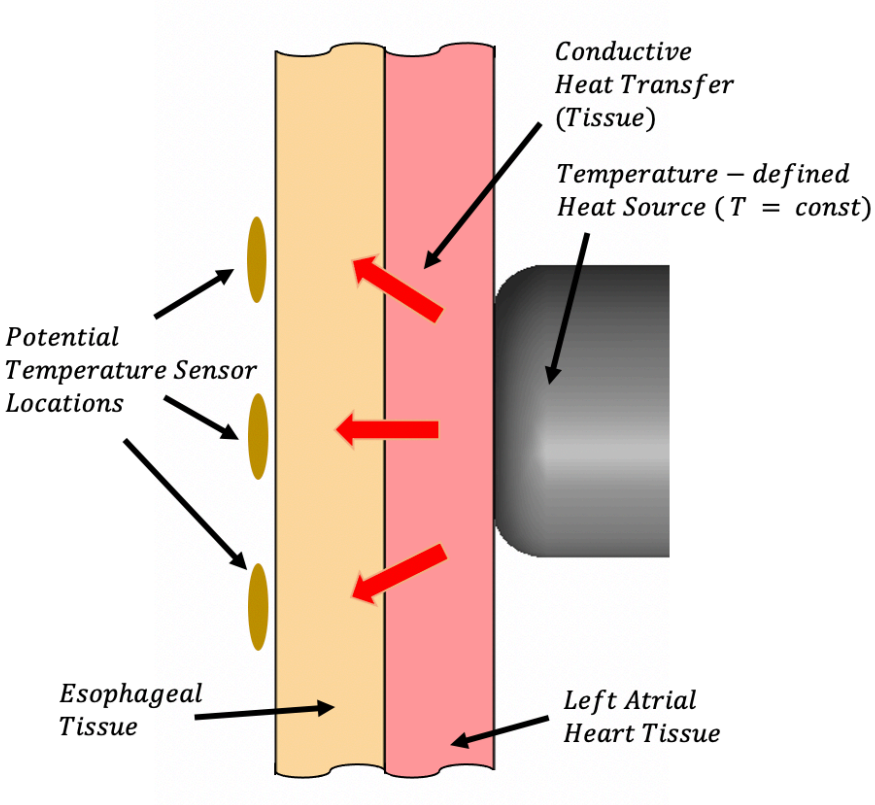

Figure 89: Schematic of heat transfer caused by catheter ablation in the left atrium with heat transfer affecting the esophagus

Temperature sensors (10kΩ NTC thermistors) were attached to a flexible silicone surface to measure the 1D (in-line) temperature distribution as heat is transferred from the inner atrial wall to the inner esophageal wall (see Figure 90). A linear sensor array, similar to the one shown in Figure 90, can be attached to the esophageal deflection device [24,25].

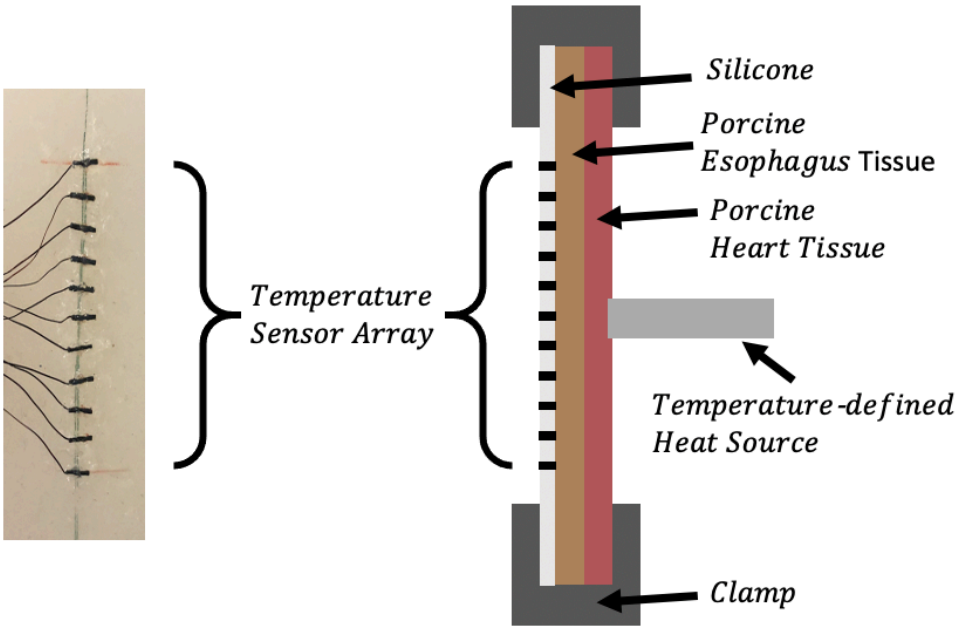

Figure 90: Linear temperature sensors adhered to silicone sheet and a schematic of experimental setup with linear temperature sensor array, esophagus tissue, heart tissue, and the temperature-defined heat source.

The temperature sensor array is clamped to the porcine esophageal and atrial tissue layers. The sensors collected data at approximately 5Hz using a 10-bit ADC microcontroller and MATLAB software while a heat source was introduced to the inner atrial wall. The heat source had a metallic contact interface of 8mm diameter and was temperature controlled, i.e., a constant temperature could be attained.

A typical result for the temperature distribution as a function of time is plotted in Figure 91. The temperature for each of the 11 linearly distributed sensors was measured as a function of time for approximately 6 minutes. For this experiment, the heat source was introduced at t = 30s between sensors 5 and 6 (on the atrial wall side). A temperature rise is first observed by sensor 5 approximately 15 seconds after the heat source is activated. Then, shortly thereafter, sensor 6 detects a temperature rise. With an additional delay of approximately 20s, sensor 4 and sensor 7

also show an increase in temperature. Within 30s, the temperature at sensor 5 rises an additional 13°C beyond the initial 22°C. At 60s, the heat source is removed, and the temperatures begin to rise less rapidly and then decline.

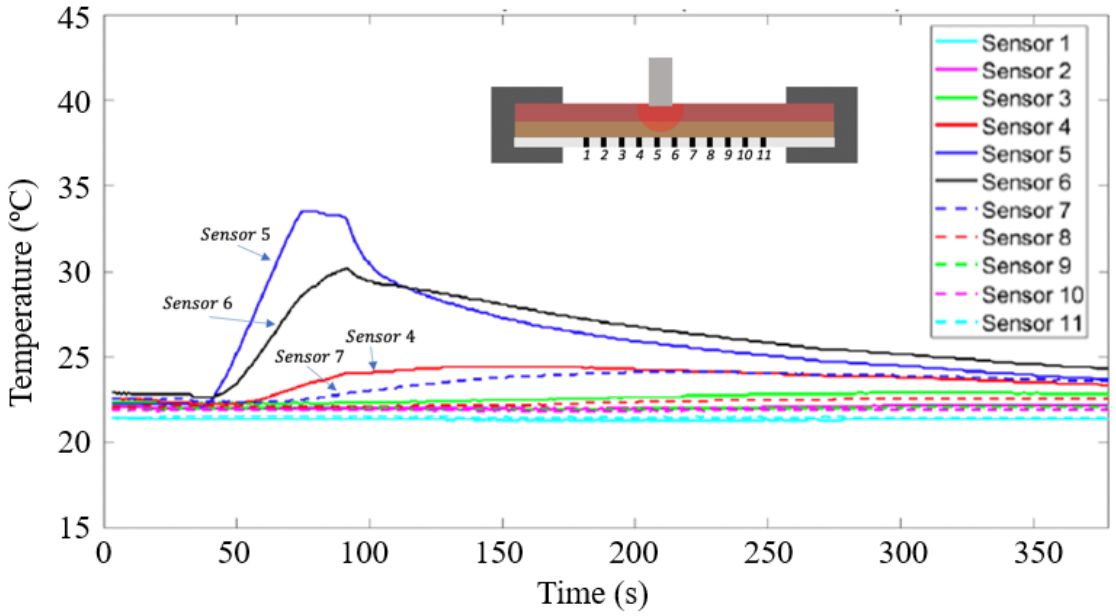

Figure 91: Temperature sensor array measurements Linear sensor array and experimental setup [24, 25]

5.5 Design of 2D Temperature Sensor Array

Figure 92 illustrates an EDD design with incorporated sensors. These sensors can be more densely arranged in regions of highest interest. Cost and difficulty of manufacturing should be considered and an optimal number of sensors along with their position is necessary.

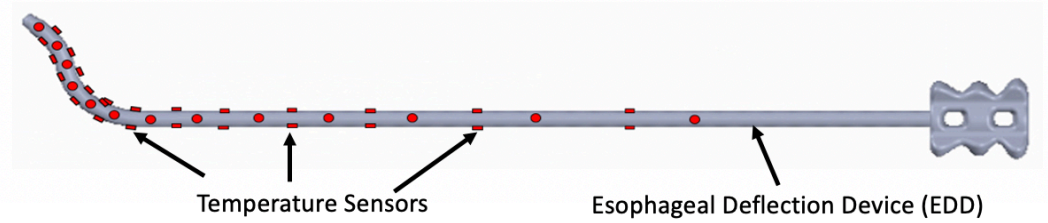

Figure 92: Sensors positioned in 2D (axially and circumferentially) on the proposed esophageal deflection device [8]

A significant challenge is knowing the location where a temperature rise is likely to occur. Having a 2D pattern, where temperature sensors can be wrapped around the EDD, is an ideal approach. In the following section, temperature sensors are positioned in a 2D pattern on a silicone sheet and tested experimentally, measuring temperatures on the inner esophageal wall.

5.5.1 2D Temperature Sensor Array and Experimental Setup

A 2D temperature sensor array is shown in Figure 93a. 15 NTC thermistors were embedded into the surface of silicone so that the sensor surface protruded slightly from the flexible substrate. The center of each sensor is separated by 5mm horizontally and by 7.5mm vertically to create the 2D pattern shown. Figure 93b shows the thermistor voltage divider setup, using 4.7kOhm resistors and an Arduino microcontroller to act as a power source (5V) and an analog to digital convertor (10bit). The microcontroller communicates temperature data through a serial port at 10Hz to a local computer.

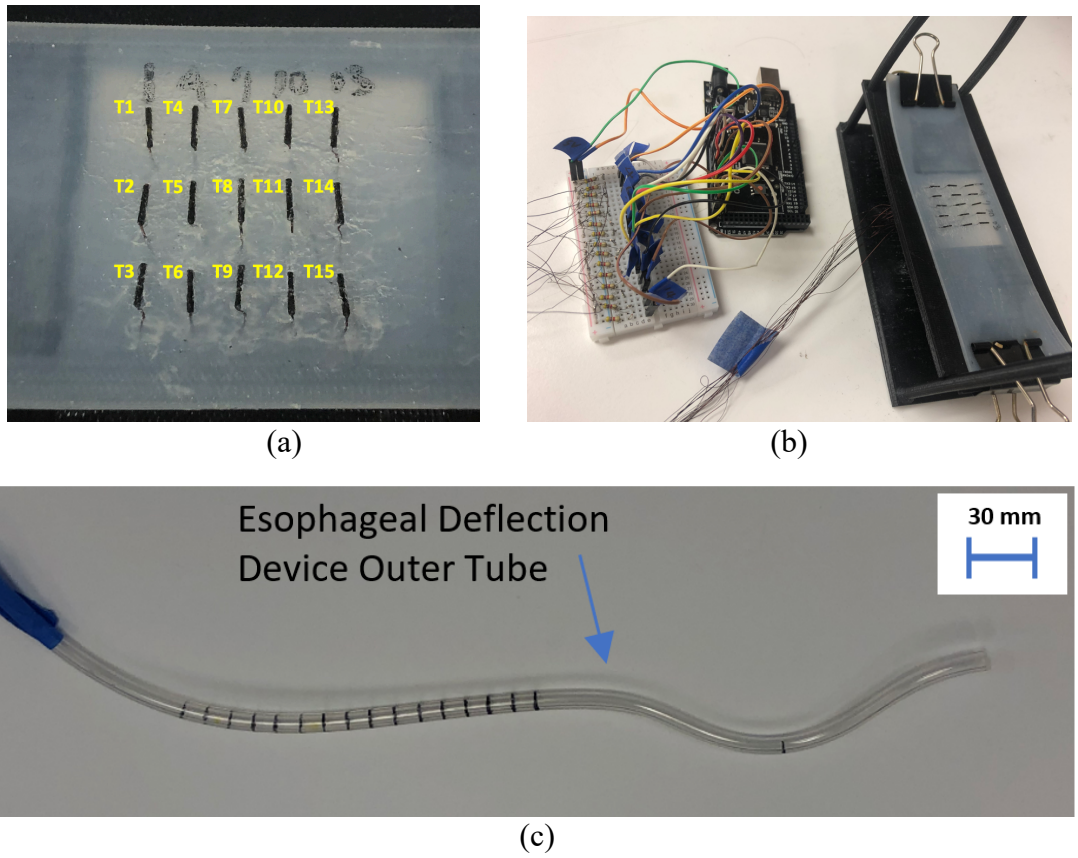

Figure 93: (a) 2D pattern for temperature sensor array using NTC thermistors embedded into silicone surface, (b) mounted 2D temperature sensor array with voltage divider setup and Arduino microcontroller, and (c) an esophageal deflection device outer tube created from thermoformed EVA.

An ex vivo experimental study was performed using porcine esophagus and atrial tissue to test the 2D temperature sensor array. An aluminum cylinder of 8mm diameter was used as the heat source, together with a flexible polyimide resistive heater element and thermistors to control the temperature at approximately 50ºC. The response of the sensor array to an increase in temperature was examined by monitoring the tissue temperature. First, a study was performed with an environmental temperature of approximately 24ºC and heat conduction through esophagus tissue only, through atrial tissue only, and through combined atrial and esophagus tissue. Then, the combined atrial and esophagus tissue were held underwater in a temperature-controlled bath of

approximately 36ºC. The experimental setup for the underwater study is shown in Figure 94 with the atrial and esophageal tissue attached to the 2D sensor array.

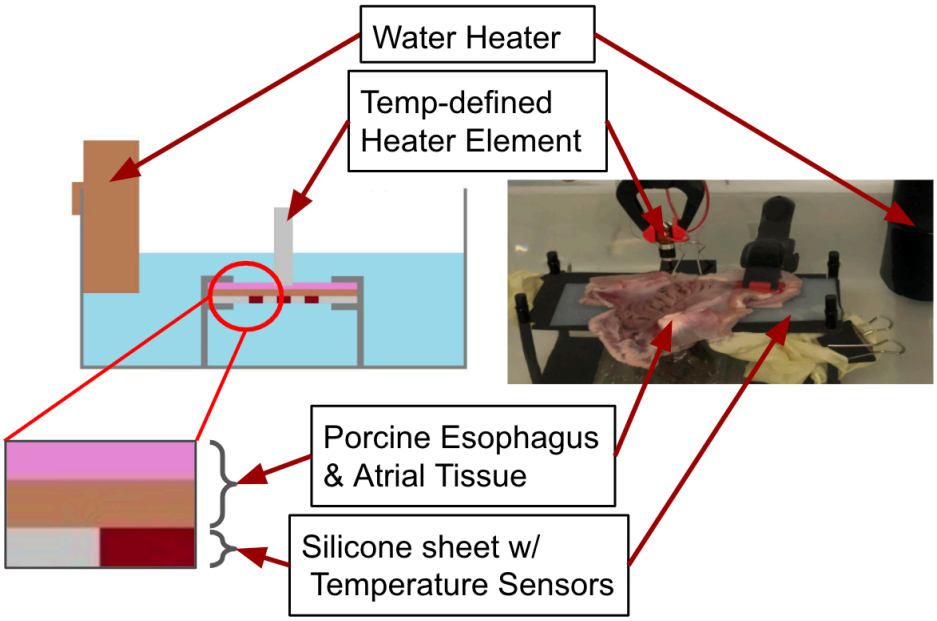

Figure 94: Experimental setup for 2D Temperature Sensor Array

5.5.2 Results

Temperature as a function of time is shown in Figure 95 for temperature sensor 8 (middle sensor) from three ex vivo experiments. For these experiments, the environmental (air) temperature was approximately 24ºC and three combinations of tissue were tested: (1) atrial (heart) tissue only, (2) esophagus tissue only, and (3) combined atrial and esophagus tissue. The maximum temperature observed 60 seconds after initiating contact between the heat source (~50ºC) and tissue was approximately 45ºC for experiments with esophagus tissue only and atrial tissue only, and approximately 35ºC for combined atrial and esophagus tissue. For the combined tissue, temperature sensor 8 observed an 11ºC difference between the initial and final temperature measurements.

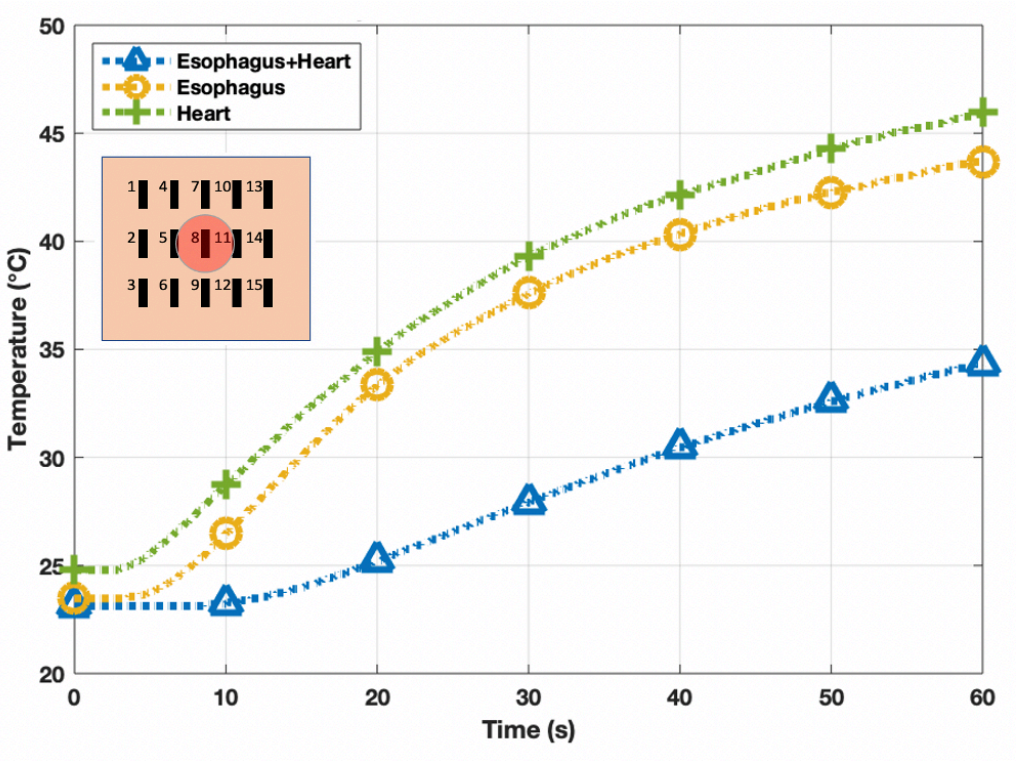

Figure 95: Temperature sensor data as a function of time for 15 thermistor array.

Temperature as a function of time is shown in Figure 96 for all 15 thermistors in an ex vivo experiment. For these experiments, the environmental (water) temperature was approximately 36ºC. 60 seconds after initiating contact between the heat source (~50ºC) and tissue, the maximum temperature observed was approximately 41ºC and detected at T8 (middle temperature sensor). For these underwater ex vivo conditions, a 5ºC difference was observed between the initial and final temperatures measured by T8. Adjacent temperature sensors, T5 and T11, measured 39ºC and 40ºC, respectively, 60 seconds after initiating contact. Significant temperature rises were not observed from any sensor until approximately 10 seconds after initiating contact. Other sensors, besides T5, T8, and T11, either showed a further delayed response, or no response at all.

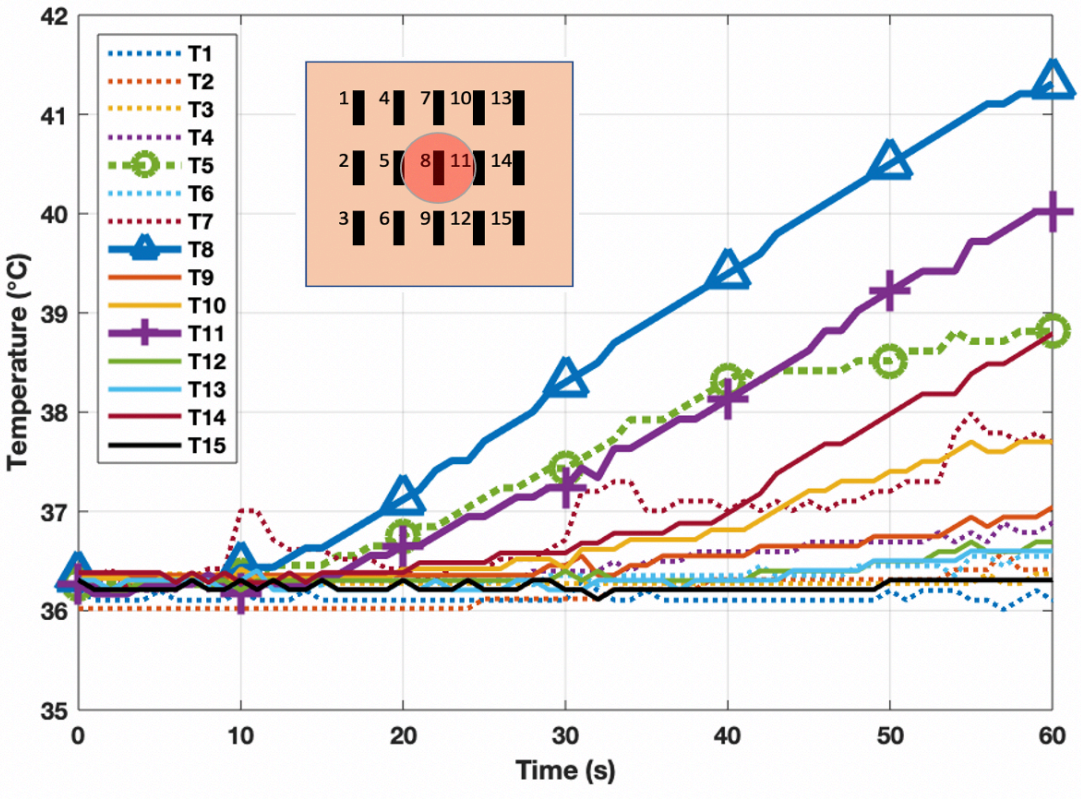

Figure 96: Temperature sensor data as a function of time for 15 thermistor array.

Figure 97 illustrates similar results as in Figure 96, but at times 0s, 20s, 40s, and 60s, respectively. The importance of sensor position and spacing can easily be seen by looking at the data for 20 seconds into the experiment. Here, only three of the 15 sensors register a temperature rise, i.e., only the sensors located directly behind the heat source location show a temperature rise. In fact, even after 60 seconds, several sensors do not yet register a significant temperature rise.

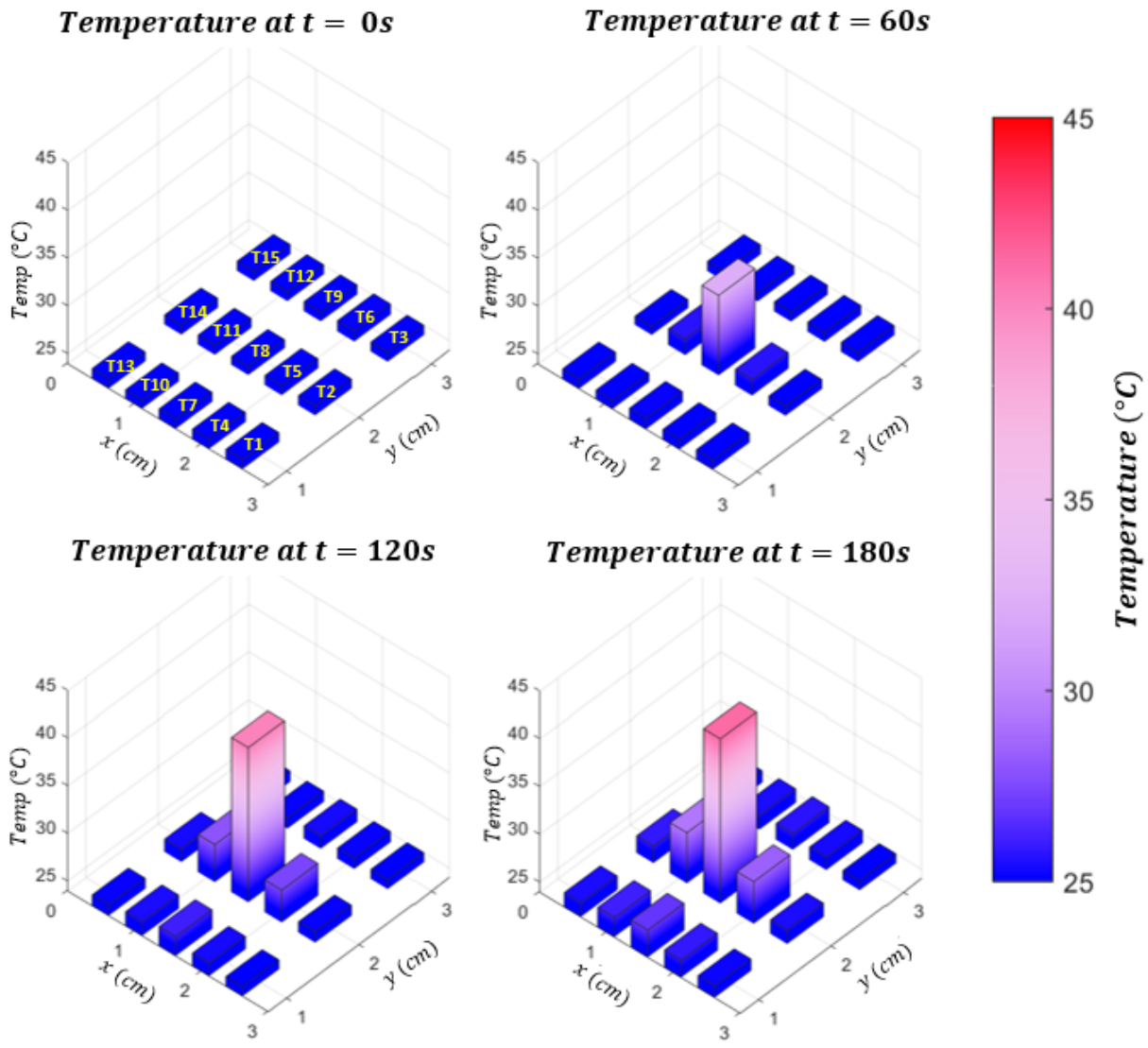

Figure 97: Spatial temperature distribution for 15 sensors at 0s, 20s, 40s and 60s.

The 2D temperature sensor array on a sheet of silicone was used to measure temperature rise in the x- and y-directions. The importance of sensor position and spacing was revealed through a number of ex vivo experiments. After 60 seconds, the temperature rise is small even if measuring directly behind the heat source. If temperature sensors are positioned further away from the heat source, they are not likely to measure a rise in temperature. This is important information since medical doctors will stop the procedure once a temperature rise of greater than 1ºC is observed.

Through the use of many temperature sensors, positioned on the surface of an EDD, a temperature increase can be observed with sufficient resolution and accuracy. The number of sensors that can be used is limited by cost and manufacturing restrictions. Sensor position can be further optimized using thermal mapping techniques and materials with increased thermal conductivity.

5.6 Summary

Thermal damage of the esophagus is a significant problem during ablation procedures. As an EDD is used to protect the esophagus from thermal damage, it is important to observe the inner esophagus walls for an undesirable temperature increase. Heat transfer through the esophagus and atrial tissue was investigated. A 2D temperature sensor array positioned onto a silicone sheet can be wrapped around the EDD to monitor temperature rise and heat transfer between the different layers of tissue. The sensor array was tested experimentally, ex vivo, using porcine tissue. Results showed an increase in temperature on the inner esophagus wall after a heat source was applied to the atrial tissue. The spatial temperature distribution was captured with the sensor array. The response of the temperature sensor depends on its position relative to the heat source.

In this experimental study, the temperatures of the inner esophageal wall were investigated. It is important to know the expected temperature difference between the inner and outer esophagus wall. It is also important to evaluate how the heat transfer can be affected by changes in geometry, material, or boundary conditions (e.g., the heat source). To evaluate these parameters, we develop in the next chapter a numerical model for the heat transfer between a heat source and esophagus and heart tissue.

Chapter 5, in part are a reprint of the materials as they appear in “Experimental and Numerical Investigation of Heat Transfer through Porcine Heart and Esophageal Tissue” Morris, K., Hu, S., Kohanfars, M., and Talke, F.E., Proceedings for ASME 2021 Conference on Information Storage and Processing Systems. Online Virtual. June 2–3, 2021.

References

[1] Terricabras, Maria, Jonathan P. Piccini, and Atul Verma. "Ablation of persistent atrial fibrillation: Challenges and solutions." Journal of cardiovascular electrophysiology 31.7 (2020): 1809-1821.

[2] Halm, Ulrich, Thomas Gaspar, Markus Zachäus, Stephan Sack, Arash Arya, Christopher Piorkowski, Ingrid Knigge, Gerhard Hindricks, and Daniela Husser. "Thermal esophageal lesions after radiofrequency catheter ablation of left atrial arrhythmias." American Journal of Gastroenterology 105, no. 3 (2010): 551-556.

[3] Zhang, Ping, and Yi Bian. "Cerebral arterial air embolism secondary to iatrogenic left atrial-esophageal fistula: a case report." BMC neurology 20.1 (2020): 1-4.

[4] Koranne, Ketan, Indranill Basu-Ray, Valay Parikh, Mark Pollet, Suwei Wang, Nilesh Mathuria, Dhanunjaya Lakkireddy, and Jie Cheng. "Esophageal temperature monitoring during radiofrequency ablation of atrial fibrillation: a meta-analysis." Journal of atrial fibrillation 9, no. 4 (2016).

[5] Carroll, Brett J., FERNANDO M. CONTRERAS‐VALDES, E. Kevin Heist, Conor D. Barrett, Stephan B. Danik, Jeremy N. Ruskin, and Moussa Mansour. "Multi‐sensor esophageal temperature probe used during radiofrequency ablation for atrial fibrillation is associated with increased intraluminal temperature detection and increased risk of esophageal injury compared to single‐sensor probe." Journal of cardiovascular electrophysiology 24, no. 9 (2013): 958-964.

[6] Circa Scientific Website - https://www.circascientific.com/circa-s-cath-tm/

[7] Morris, Karcher, Vlado A. Lubarda, and Frank E. Talke. "Design of an esophageal deflection device for use during atrial ablation procedures." Journal of Materials Research and Technology 9.6 (2020): 13801-13812.

[8] Morris, Karcher, Garner, Scott, Fu, Youyi, Seo, Young Woo, Pandit, Anay M., Feld, Gregory, Savides, Thomas, Talke, Frank E., Esophageal deflection device. US20200029822A1-Patent Pending, filed January 30, 2020.

[9] Hristov, Jordan. "Bio-heat models revisited: concepts, derivations, nondimensalization and fractionalization approaches." Frontiers in Physics 7 (2019): 189.

[10] Pennes, Harry H. "Analysis of tissue and arterial blood temperatures in the resting human forearm." Journal of applied physiology 1.2 (1948): 93-122.

Yokoyama, Katsuaki, Hiroshi Nakagawa, Fred HM Wittkampf, Jan V. Pitha, Ralph Lazzara, and Warren M. Jackman. "CLINICAL PERSPECTIVE." Circulation 113, no. 1 (2006): 11-19.

[11] Boston Scientific Website - https://www.bostonscientific.com/en-US/medical-specialties/electrophysiology/cardiac-mapping-system/cardiac-ablation-catheters/open-irrigated-mifi-ablation-catheter.html.

[12] Sharma, Virender K., Kenneth K. Wang, Bergein F. Overholt, Charles J. Lightdale, M. Brian Fennerty, Patrick J. Dean, Douglas K. Pleskow et al. "Balloon-based, circumferential, endoscopic radiofrequency ablation of Barrett's esophagus: 1-year follow-up of 100 patients (with video)." Gastrointestinal endoscopy 65, no. 2 (2007): 185-195.

[13] Curley, Steven A. "Radiofrequency ablation of malignant liver tumors." Annals of Surgical Oncology 10, no. 4 (2003): 338-347.

[14] Kapural, Leonardo, and Nagy Mekhail. "Radiofrequency ablation for chronic pain control." Current Pain and Headache Reports 5, no. 6 (2001): 517-525.

[15] Erez, Aaron, and Avraham Shitzer. "Controlled destruction and temperature distributions in biological tissues subjected to monoactive electrocoagulation." (1980): 42-49.

[16] Rivera, Maria J., Juan A. López Molina, Macarena Trujillo, Vicente Romero-García, and Enrique J. Berjano. "Analytical validation of COMSOL Multiphysics for theoretical models of Radiofrequency ablation including the Hyperbolic Bioheat transfer equation." In 2010 Annual International Conference of the IEEE Engineering in Medicine and Biology, pp. 3214-3217. IEEE, 2010.

[17] Haemmerich, Dieter. "Biophysics of radiofrequency ablation." Critical Reviews™ in Biomedical Engineering 38, no. 1 (2010).

[18] Yokoyama, Katsuaki, Hiroshi Nakagawa, Fred HM Wittkampf, Jan V. Pitha, Ralph Lazzara, and Warren M. Jackman. "CLINICAL PERSPECTIVE: Comparison of Electrode Cooling Between Internal and Open Irrigation in Radiofrequency Ablation Lesion Depth and Incidence of Thrombus and Steam Pop" Circulation 113, no. 1 (2006): 11-19.

[19] Erez, Aaron, and Avraham Shitzer. "Controlled destruction and temperature distributions in biological tissues subjected to monoactive electrocoagulation." (1980): 42-49.

[20] Yokoyama, Katsuaki, Hiroshi Nakagawa, Dipen C. Shah, Hendrik Lambert, Giovanni Leo, Nicolas Aeby, Atsushi Ikeda et al. "Novel contact force sensor incorporated in irrigated radiofrequency ablation catheter predicts lesion size and incidence of steam pop and thrombus." Circulation: Arrhythmia and Electrophysiology 1, no. 5 (2008): 354-362.

[21] Medtronic RF Ablation Website: https://europe.medtronic.com/xd-en/healthcare-professionals/products/cardiac-rhythm/ablation-atrial-fibrillation/diamondtemp-ablation-catheters.html.

[22] Haines, David. "Biophysics of ablation: application to technology." Journal of cardiovascular electrophysiology 15 (2004): S2-S11.

[23] Haines, David E., and Denny D. Watson. "Tissue heating during radiofrequency catheter ablation: a thermodynamic model and observations in isolated perfused and superfused canine right ventricular free wall." Pacing and Clinical Electrophysiology 12, no. 6 (1989): 962-976.

[24] Garner, Scott, Karcher Morris, Raul Pegan, Thomas Savides, and Frank E. Talke. Development of a Luminal Esophageal Temperature Monitoring Device for Use During Treatment for Atrial Fibrillation. Vol. 51937. American Society of Mechanical Engineers, 2018.

[25] S. Garner, Development of A Luminal Esophageal Temperature Monitoring Device for Use During Treatment of Atrial Fibrillation, UC San Diego, MS Thesis (2018).

Chapter 6 Numerical Simulation of Heat Transfer in the Left Atrium and Esophagus

6.1 Introduction

Numerical simulations have previously been performed to study the heat transfer during cardiac ablation procedures. Berjano and Hornero [1] modeled the tissue heat transfer using ANSYS, a commercially available finite element software. Their model explored effects of geometric and heat source parameters on the temperature distribution within the atrial tissue as a function of time. Their work laid the foundation to explore how thermal injury to the esophagus can occur [2]. Berjano [3] reviewed the field of ablation modeling and discussed the challenges that need to be addressed in future research. Berjano and Hornero [4] simulated numerically how a cooled balloon placed in the esophagus could help prevent thermal injury. Perez et al. [5] investigated how temperature probes in the esophagus could affect heating due to radiofrequency (RF) interactions with the thermistors. González-Suárez explored how the use of open-irrigated catheters can affect the flow field [6].

In this chapter, we develop a finite element model for the heat transfer from the left atrium to the inner esophagus wall based off of our experimental investigation of thermal sensing on the

inner esophagus wall where the temperature sensors will be positioned. We investigate the temperature distribution through the tissue and study the optimum position of temperature sensors on the inner esophagus wall. We investigate how convection affects the temperature rise through the heart and esophagus tissue. Additionally, we study the effects of ramping of the heat source temperature.

The primary objective of the esophageal deflection and thermal monitoring device is to prevent thermal injury of the esophagus. The results of the heat transfer simulations are useful for optimizing the layout of the temperature sensors on the esophageal deflection device (EDD).

6.2 Finite Element Model

LS-DYNA is a commercially available software. It supports a transient finite element solver for 3D heat transfer problems. This software is ideal for investigating the heat transfer through heart and esophagus tissue. LS-DYNA uses implicit methods for the solution of the heat equation described in the previous chapter [7]. The Galerkin formulation for the transient heat conduction equation, shown in equation 7.1, is used in LS-DYNA together with the implicit time stepping Crank Nicolson Method. The first term in eq. 7.1 describes the change in internal energy. The second term describes the heat flux in and out of a volume element. The third term describes the energy generation inside the volume element while the last and final term describes the energy transfer at the surface.

$$\int_\Omega w_j \rho c \frac{\partial T}{\partial t} d\Omega = -\int_\Omega \nabla^T w_j k \nabla T d\Omega + \int_\Omega w_j Q d\Omega + \int_\Gamma w_j q d\Gamma \tag{7.1}$$

The terms w_j denote the shape functions which are identical to the weight functions.

Figure 98 shows the geometry of the esophagus tissue thickness t_{eso}, left atrium tissue thickness t_{hrt}, the diameter D_{hs} and depth d_{hs} of the heat source. L_w is the width and L_h is the height of the tissues being considered. The model for the heat transfer between the ablation catheter and the inner esophagus considers two tissue layers (heart and esophagus tissue) with the ablator on the inner atrial wall while the temperature sensors are on the inner esophagus wall. The model was designed using SolidWorks (commercially available software). The model was then meshed, material models were chosen, and boundary conditions were applied using Hypermesh (commercially available software). The mesh consisted of approximately 25,000 3D 8-node brick elements. A set of nodes on or in the heart tissue surface were defined as the ablation heat source, where a constant temperature was defined.

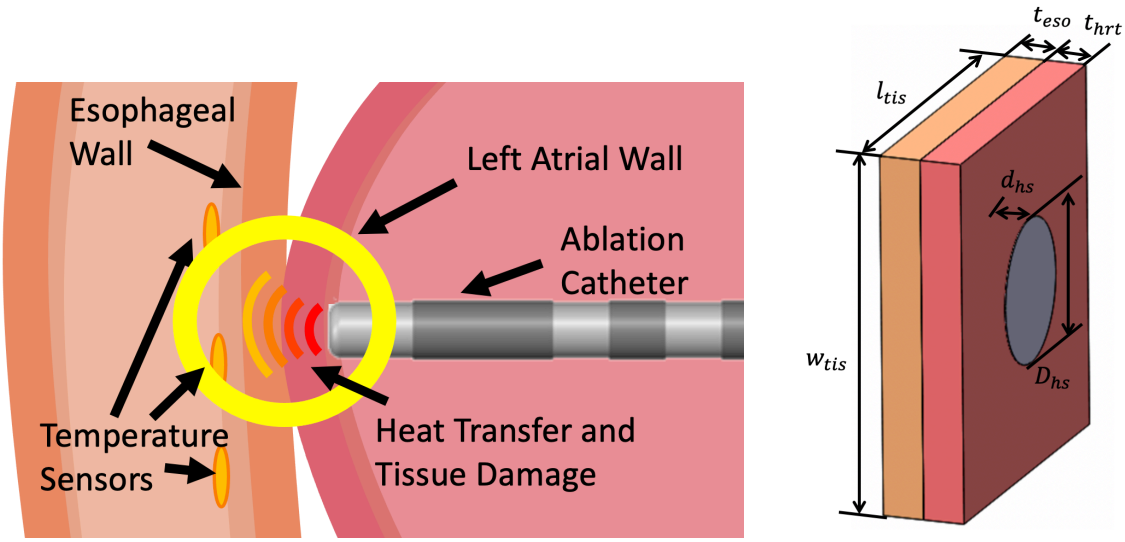

Figure 98: Esophagus and heart tissue layer geometry with heat source contact geometry.

Biological tissue, e.g., esophagus and heart tissue, has anisotropic thermal conductivity [8]. However, in this study, the heart tissue and esophagus tissue were assumed to be thermally isotropic. Material properties such as density, specific heat, and thermal conductivity are required for the esophagus and heart tissue. These properties are shown in Table 6 [9]. LS-DYNA supports

material models that incorporate thermo-elastic-plastic properties, as many stress-strain constitutive models depend on temperature [10]. In this study, we focus on the heat transfer aspects of the tissue and ignore the mechanical stress and strain effects of the modelled tissue. An initial temperature was set for all nodes, at 37°C. The radiofrequency ablation catheter was modeled as a circular area of 8mm diameter. The applied temperatures were nominally set at 75°C for the specified heat source nodes.

Table 6: Material Parameters for Heart and Esophagus Tissue [9]

Tissue Material	Density, ρ $\left(\frac{kg}{m^3}\right)$	Thermal Conductivity, κ $\left(\frac{W}{m * K}\right)$	Specific Heat Capacity, c $\left(\frac{J}{kg * K}\right)$
Heart (Left Atrium)	1200	0.7	3200
Esophagus	1000	0.4	3700

The temperature distribution between the inner and outer esophageal lumen was investigated as a function of heat source temperature and location, tissue material properties and time. The resulting heat transfer and temperature distribution profiles allow the designer to make design decisions about the placement of the temperature sensors.

6.3 Tissue with Heat Conduction

Heat conduction is the primary contributor of heat transfer for the ablation problem we are investigating. Heat is conducted from the ablation tip of the ablator to the surrounding atrial and esophageal tissue (see Figure 98). In this section, we consider conduction only, i.e., heat transfer from the blood flow in the left atrium is neglected. This corresponds to our experimental set up

discussed in chapter 5 (see Figure 90). In the following section, we include heat convection and study the combined effect of conduction and convection.

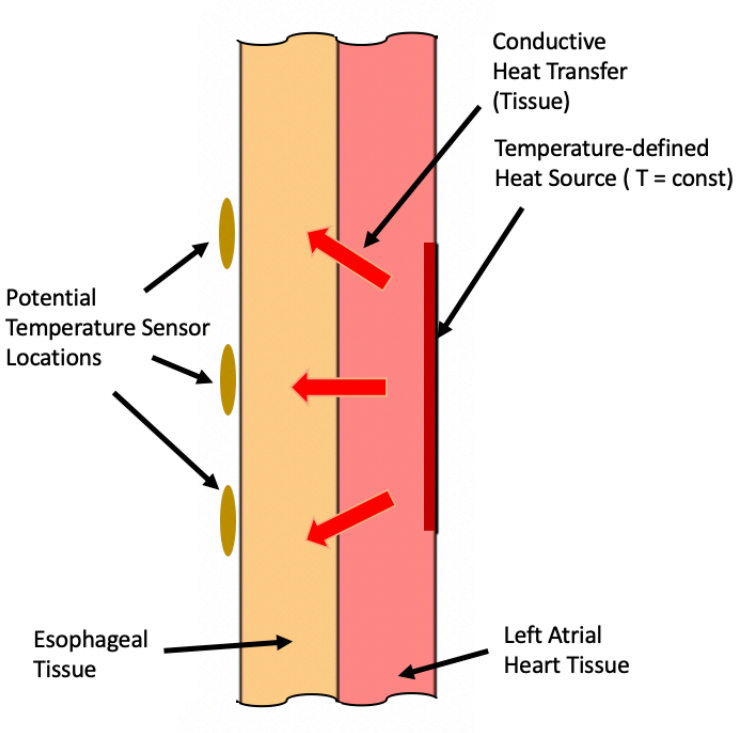

Figure 99: Esophagus and heart tissue layer geometry with heat source and conduction heat transfer.

The finite element model was initiated with all nodes set at body temperature of 37°C. The ablation tip is modelled as a circular area of 8mm diameter on the surface ($d_{hs} = 0$) of the heart tissue (see Figure 99) at a constant temperature of 75°C. We first consider the case of heat conduction only, where blood flow is neglected. This corresponds to two of the three experimental set ups in Chapter 5. Figure 100a shows the temperature distribution of the cross section of the heart and esophagus tissue 30 seconds after the start of ablation. Figure 100b shows the

temperature distribution on the outer esophagus wall (equivalent to the outer atrial wall) and the inner esophagus wall (where the temperature sensors should ideally be positioned).

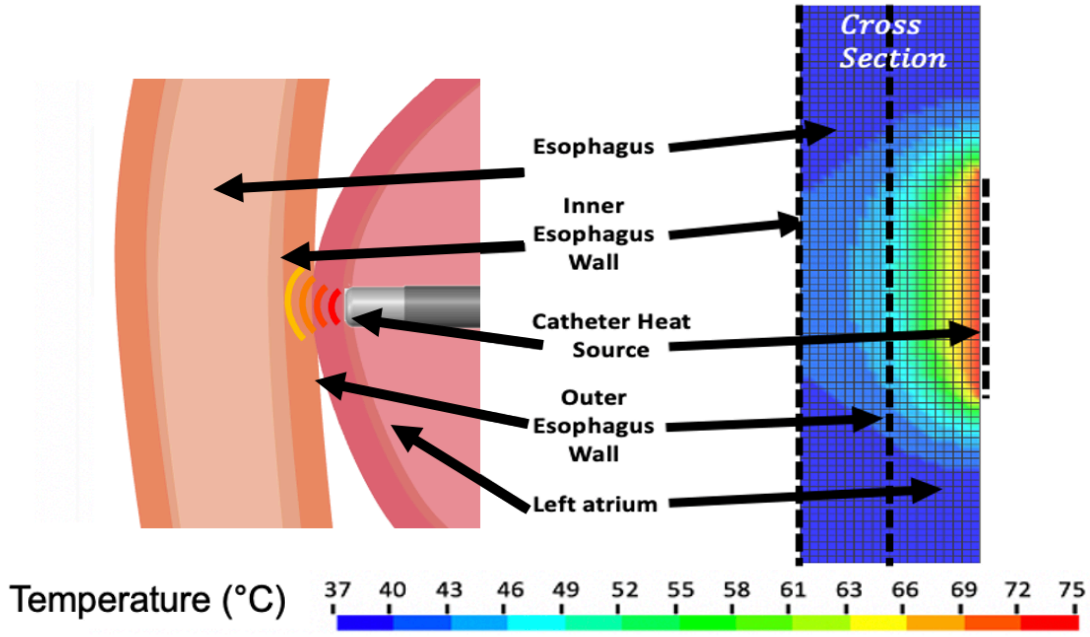

(a)

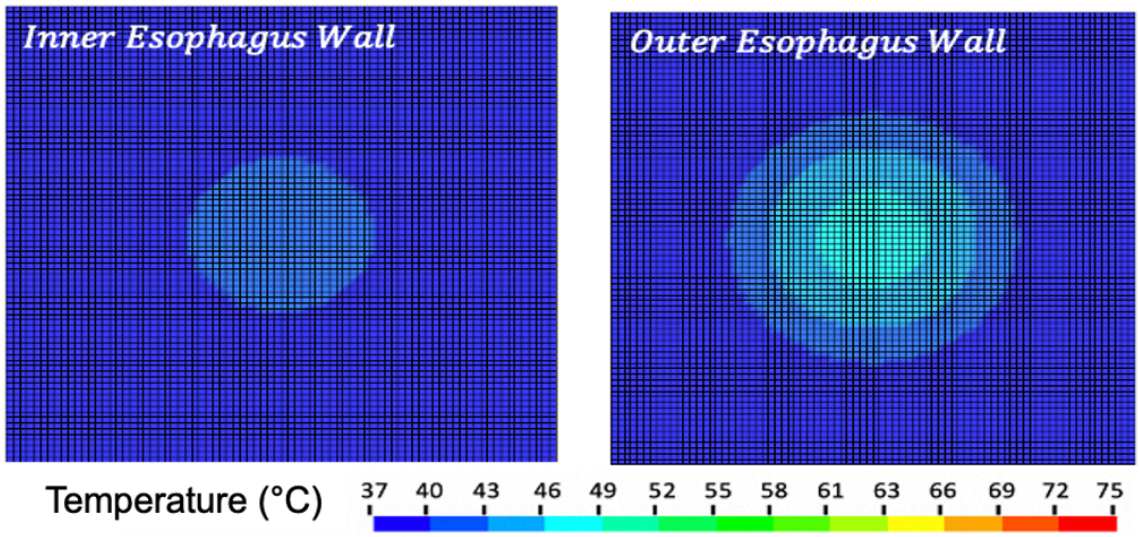

(b)

Figure 100: Temperature distribution 30s into ablation simulation with a constant temperature of 75°C applied on an 8mm diameter area of the inner atrial wall.

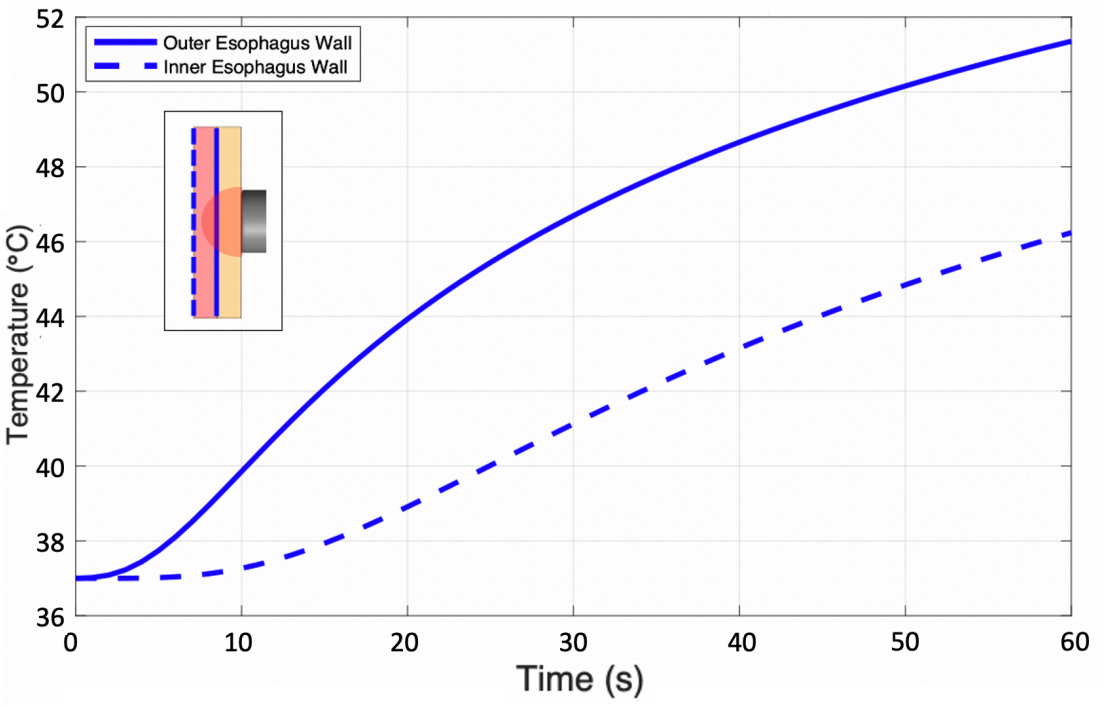

Figure 101: Maximum temperature on the inner and outer esophagus walls as a function of time.

Figure 101 shows the maximum temperature on the inner and outer esophagus walls as a function of time. We observe that the esophagus temperature reaches nearly 51°C (a rise of 14°C) after only 60 seconds. A rise of 1°C is not observed on the inner esophagus wall until approximately 15 seconds into the simulation. At a temperature rise of 1°C, if measured by the esophagus temperature probe, a medical doctor will stop the ablation procedure out of concern for esophageal damage. A temperature difference of approximately 5°C between the outer and inner esophagus is observed after 60 seconds.

Figure 102 shows the predicted temperatures at the inner esophagus wall for a position at the center of the heat source, 5mm off center of the heat source, and 10mm off center of the heat source. These are potential locations for temperature sensors. If placed 10mm off center, a sensor may not detect a 1°C rise until nearly 60 seconds into the ablation procedure, under these specific conditions. If the sensors placed on the inner esophagus wall, closer to the ablation heat source, a

temperature rise of 1°C will be observed much earlier. For the case simulated, 14 seconds was required to observe a 1°C temperature rise at the location closest to the heat source, as compared with 23s and 53s, respectively, at the locations 5mm and 10mm from the center.

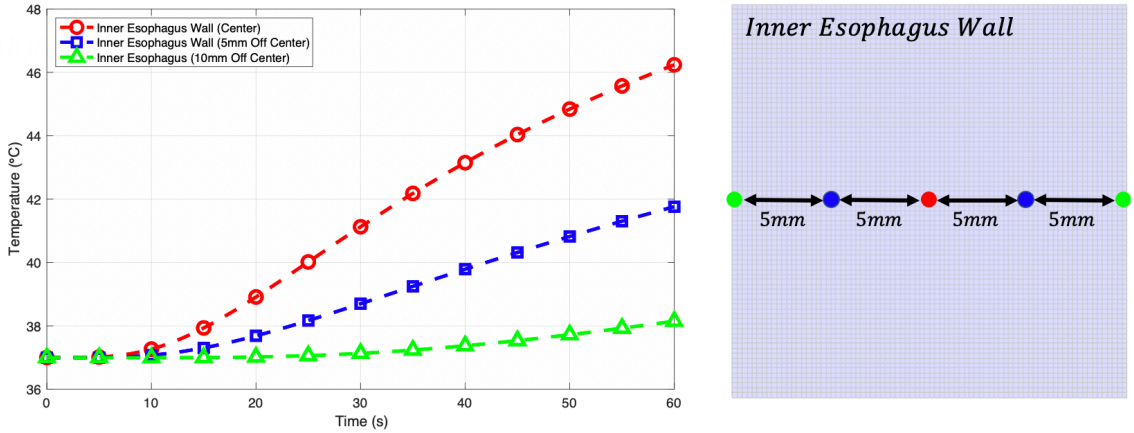

Figure 102: Simulated temperature at the specific nodes on the inner esophagus wall.

6.4 Numerical Simulation of Heat Transfer Including Heat Convection

In this section, convection is included in the heat transfer model under investigation. The spatial and temporal temperature distribution is obtained. The results are discussed and compared with the case of heat conduction only. Finally, the temperature at the interface between the ablation catheter and heart tissue is investigated, along with the temperature increase as a function of the heat source depth under the atrial surface, and the heat source ramp-up temperature profile. The primary objective of this study is to develop an improved understanding of heat transfer during cardiac ablation so that the designed temperature sensor array can optimally detect dangerous temperature rises.

6.4.1 Heat Convection

Heat convection between the atrial wall and the blood flowing through the heart can have an effect on the temperature distribution (see Figure 103). Blood flow in the heart is pulsatile flow driven by the cardiac cycle. The temperature of the blood is lower (~37°C) than the temperature of the heart tissue (>50°C), i.e., heat transfer occurs from the tissue to the blood, ultimately lowering the tissue temperature during the procedure. Tangwongsan et al. [11] experimentally measured the velocity of the blood in the left atrium of porcine tissue in vivo. Their results provide an estimate for the heat transfer coefficient due to convection. From [11], we use h = 2000 W/m^2°C. This estimate is a first order estimate knowing the complexity of blood flow in the heart [12].

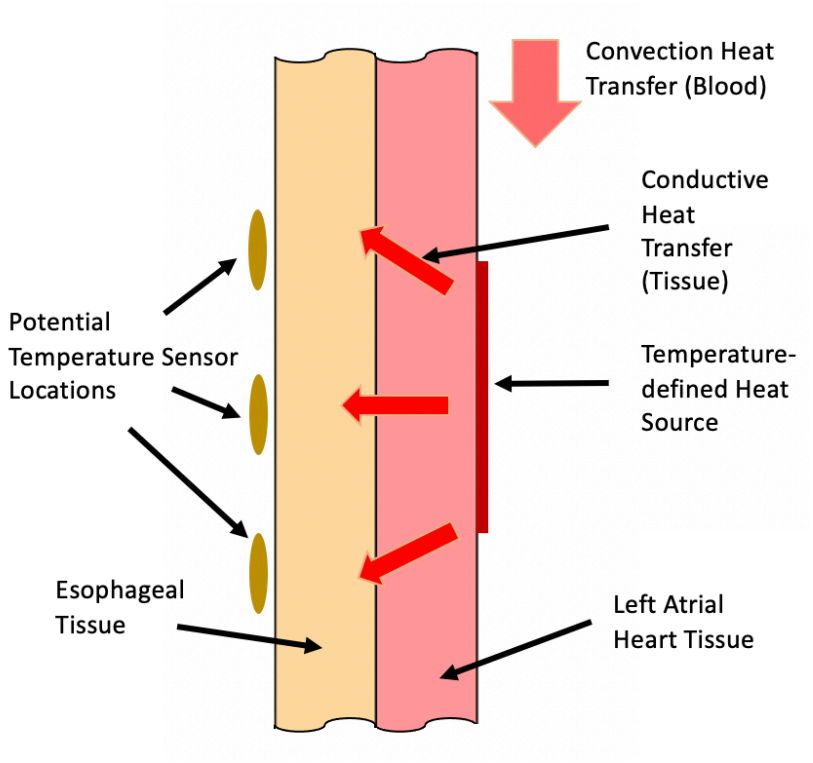

Figure 103: Esophagus and heart tissue layer geometry with heat source and conduction and convection heat transfer.

Convection reduces the temperature in the tissue, as is shown in Figure 104. The value of the coefficient of convection was also investigated in [13]. The coefficient depends strongly on the local velocity of blood in the neighborhood of the catheter tip. The side-by-side comparison of the temperature distribution in Figure 104 shows that convection is important in determining the tissue temperature. To improve the accuracy of the model, the thermal model needs to be coupled with a model of the fluid flow in the heart, and data for the convective heat transfer coefficient as a function of velocity are needed.

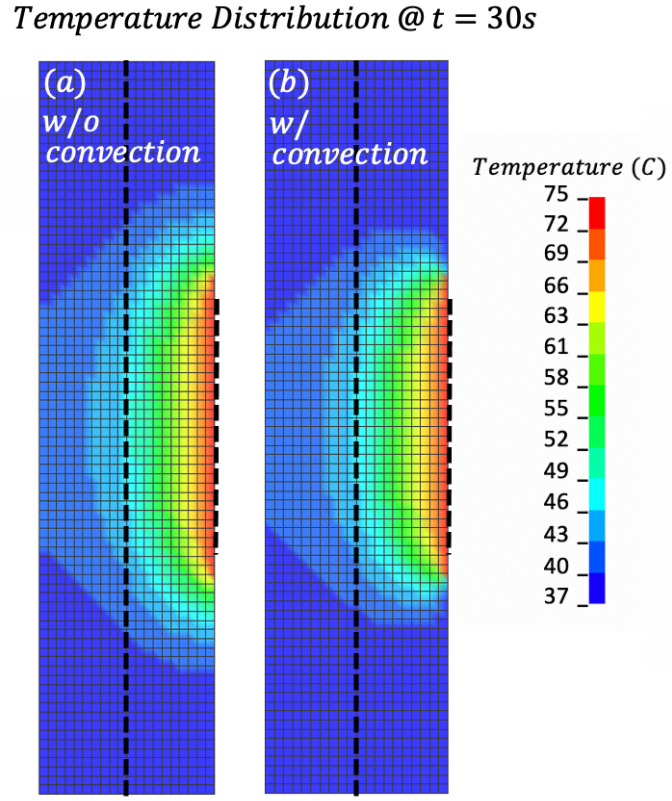

Figure 104: Temperature distribution in heart and esophagus for a) conduction only, and b) conduction and convection simulation 30s into ablation simulation. A constant temperature of 75°C is applied over an 8mm diameter area of the inner atrial wall.

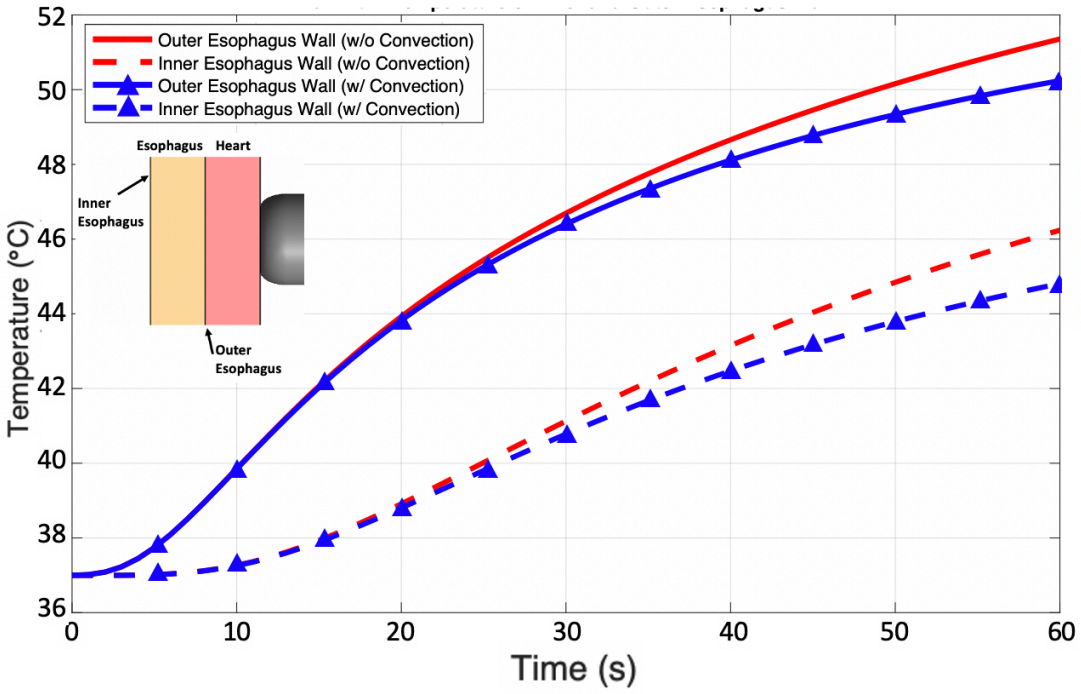

Figure 105: Maximum temperature on the inner and outer esophagus walls for a) conduction only and b) conduction and convection as a function of time.

Figure 105 shows the maximum temperature on the inner and outer esophagus walls as a function of time for the case of a) conduction only and, b) conduction and convection. We observe that the maximum temperature is higher if only conduction is considered. If convection is included, the temperature is lowered substantially. The maximum temperature difference between the two models is on the order of 2°C after 60 seconds.

6.4.2 Spatial Temperature Distribution

Figure 106 shows the temperature distribution at time steps of 0s, 5s, 15s, 30s, 45s and 60s for conduction and convection. At each time step, the temperature distribution is shown on the cross section, the outer esophageal wall, and the inner esophageal wall. We observe from Figure 106 that the temperature increase at the inner esophageal wall is delayed due to the thickness of

the esophagus and heart tissue. In Figure 106, temperatures above 50°C indicate damaged tissue [1]. Clearly, the model predicts that the outer esophagus would be thermally damaged after 60 seconds.

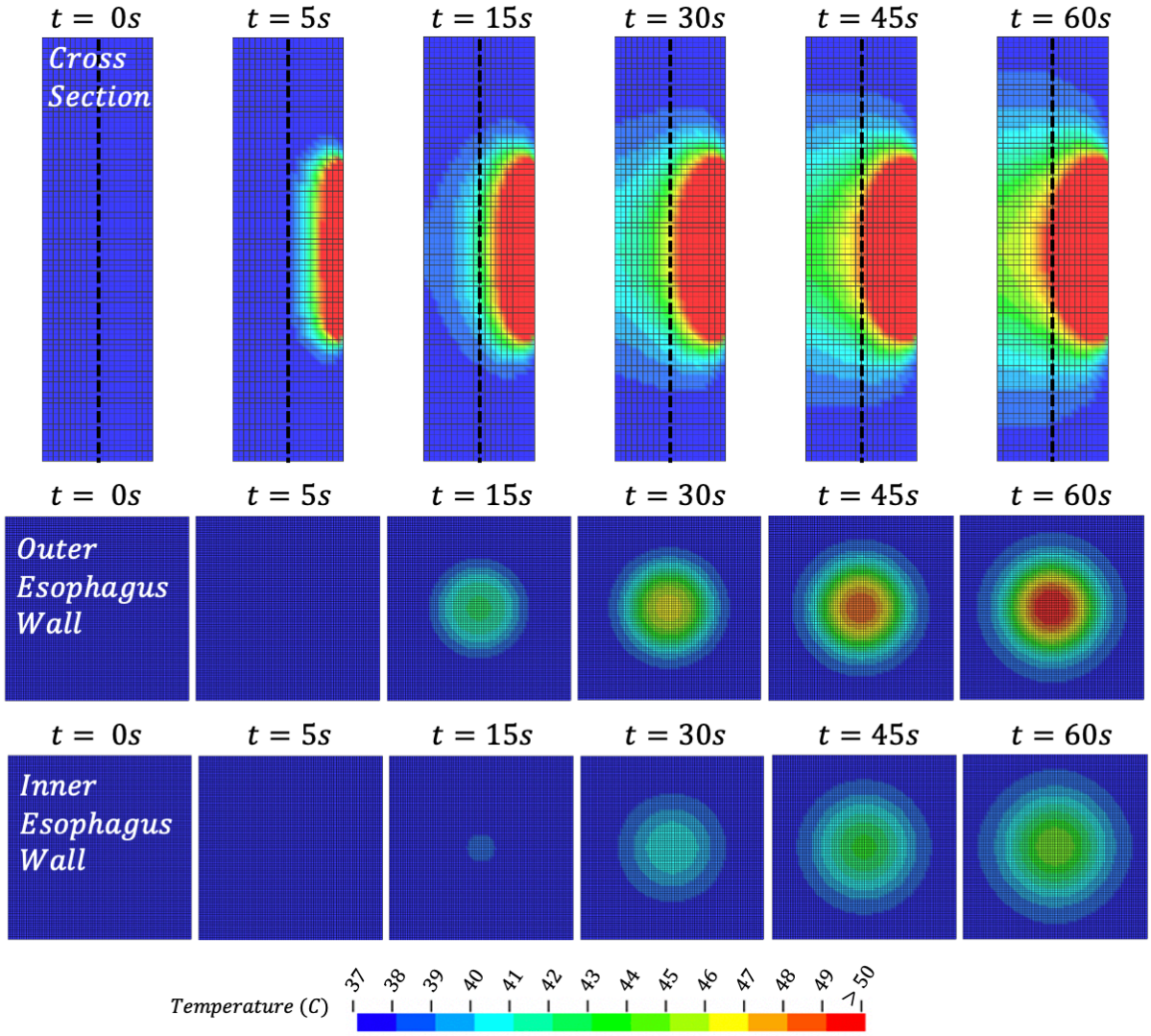

Figure 106: Temperature distribution at the cross section (column 1), the heart / esophagus interface (column 2), and the inner esophageal wall (column 3) during the first 60 seconds with an applied 75°C constant temperature on an 8mm diameter area of the inner atrial wall.

The difference in maximum temperature between the inner and outer esophagus is plotted in Figure 107 as a function of time. We observe that the temperature difference increases rapidly in the first 20 seconds of the ablation procedure. The rapid increase does not leave much time for

a medical clinician to respond to a rise in temperature, since they can only observe portions of the inner esophagus wall. Figure 107 shows a difference of approximately 5°C between the inner and outer walls of the esophagus at 60 seconds into the ablation.

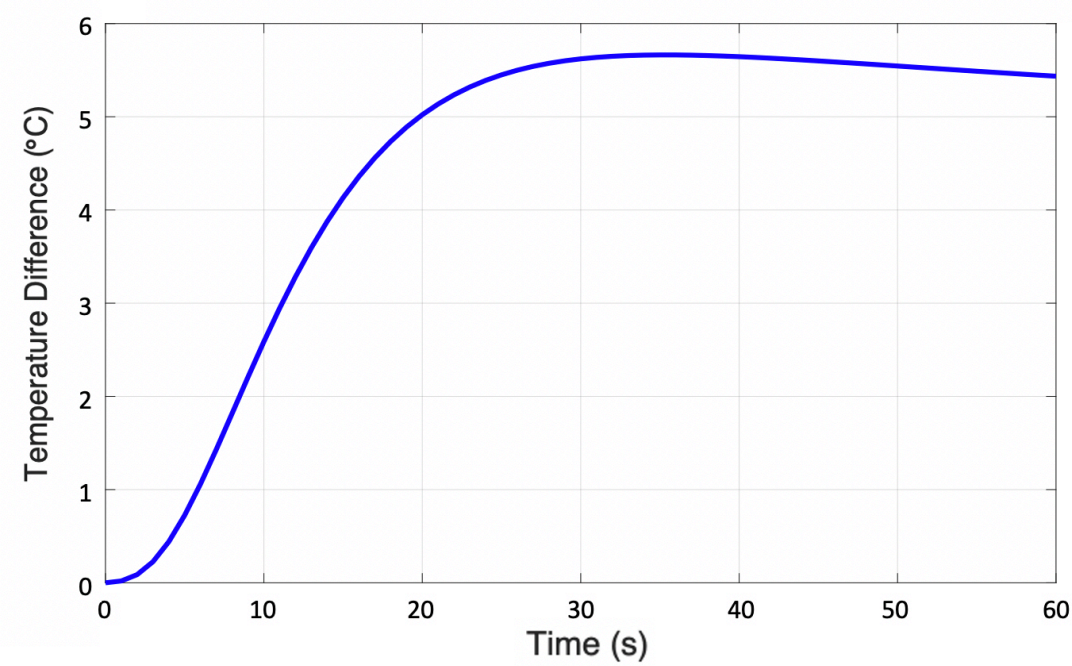

Figure 107: Maximum temperature difference between the inner and outer esophagus walls as a function of time.

6.4.3 Effect of Temperature of Catheter Tip

The temperature experienced by the tissue depends strongly on the temperature at the interface between the catheter tip and the heart tissue. We have evaluated the temperature rise of the tissue for catheter temperatures of 50°C, 75°C, and 100°C, respectively. These values are typical target temperatures used in RF ablation procedures [1 (experiment)]. The experimental study in chapter 6 used a catheter input temperature of approximately 50°C, although higher temperatures have also been used in clinical testing. Figure 108 shows the temperature

distribution of the tissue after 60 seconds of ablation time, for catheter interface temperatures of 50°C, 75°C, and 100°C, respectively. We observe that thermal damage on the outer esophagus occurs for both the 75°C and the 100°C interface temperatures. Both the 75°C and the 100°C, respectively, can lead to thermal damage on the outer esophagus.

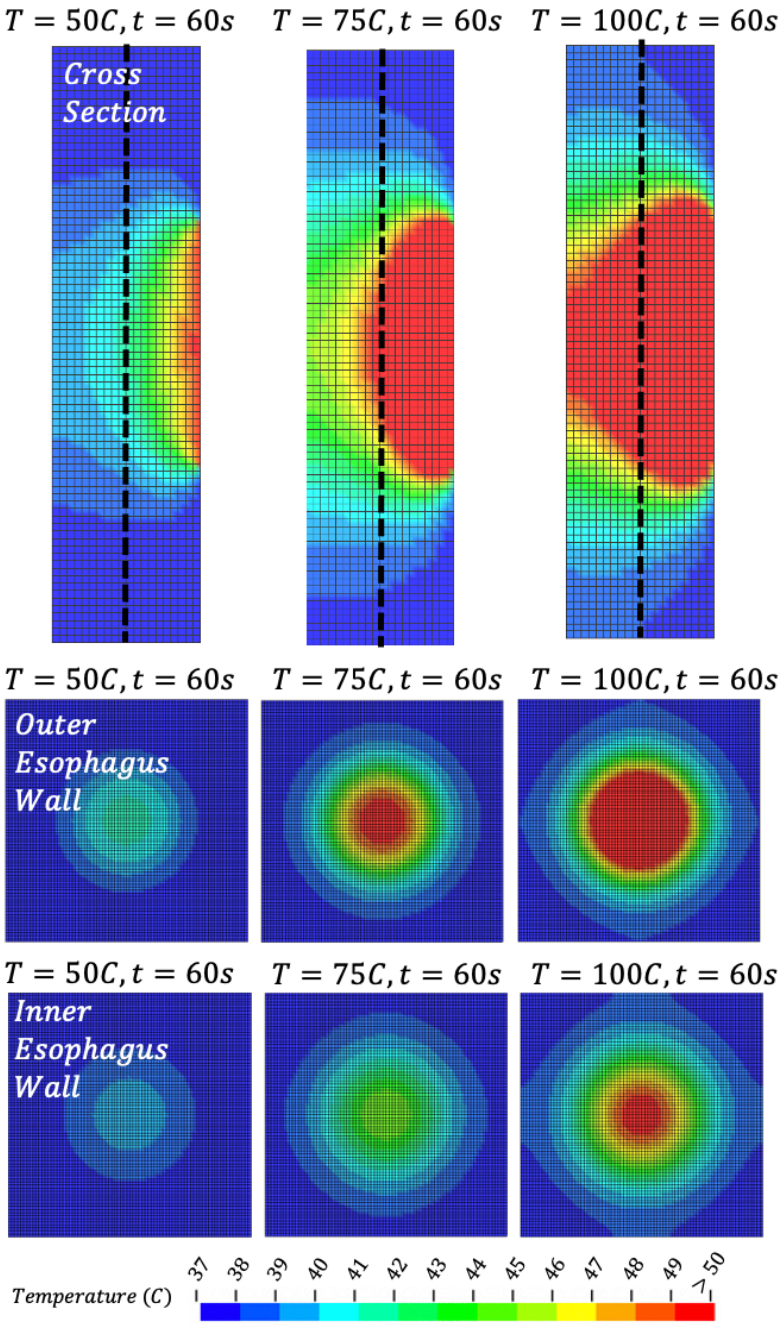

Figure 108: Temperature distributions of tissue for temperatures of 50°C, 75°C, 100°C, respectively, at the catheter/tissue interface.

Figure 109 shows the temperature distribution for the 50°C, 75°C, and 100°C input temperatures at the time corresponding to the moment when the inner esophageal wall observes a 1°C across an region at least 10 mm in length. 10mm was chosen as a potential distance for temperature sensors to be separated by on the inner esophageal wall. Under the modelled conditions, it will take approximately 42 seconds to observe the 10mm span of a 1°C rise on the inner esophagus wall when 50°C is applied at the atrial wall. When 75°C and 100°C is applied at the atrial wall, 24 seconds and 18 seconds are required, respectively to observe the same 1°C rise across a 10mm span on the inner esophagus wall. It is ideal to have the temperature sensor directly behind the heat source. In practice, however, the temperature sensors are spread out to cover more area, or reduced in number to lower cost and increase product feasibility.

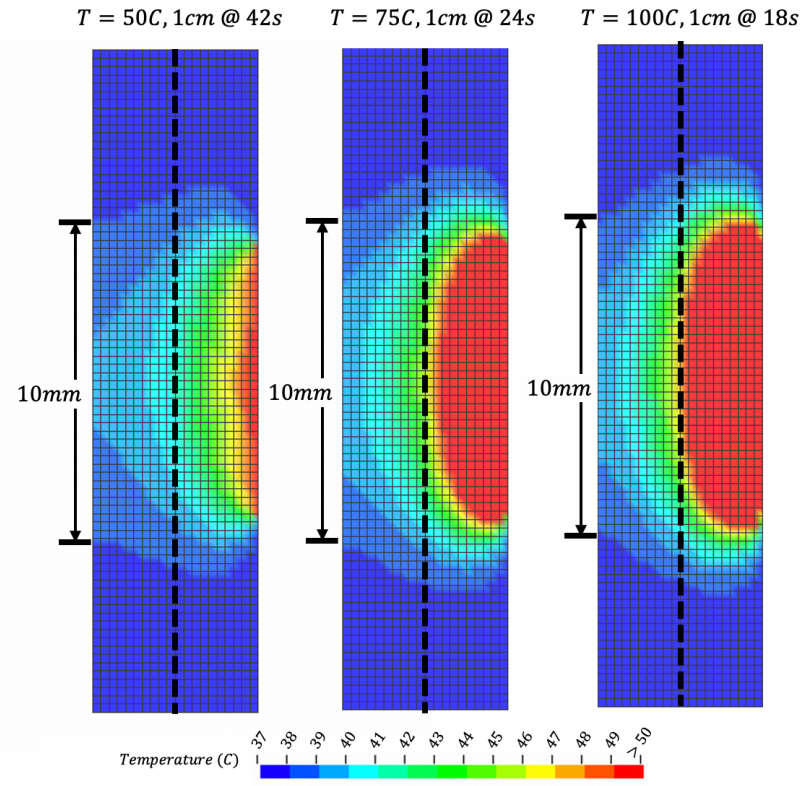

Figure 109: Cross section temperature distributions at the instant of time where nodes covering a 10mm diameter circular area on the inner esophagus wall detect a temperature rise greater than or equal to 1°C above body temperature.

If the catheter tip temperature is 75°C or 100°C (see Figure 109), the outer esophagus reaches a temperature that causes irreversible damage before all of the nodes covering a 10mm diameter circular area on the inner esophagus wall detect a temperature rise greater than or equal to 1°C above body temperature. If the temperature sensors on the inner esophagus wall are spaced more than 10mm apart and the heat source is applied between them, it is possible that the outer esophagus is thermally damaged before the sensor measures a significant increase in temperature.

6.4.4 Sensitivity of Tissue Thermal Conductivity Parameter on the Maximum Temperature

Figure 110 shows the effect of changing the thermal conductivity coefficient by 10% from its nominal value (Table 6). We observe the maximum temperatures vary by ~1% for both the inner esophagus and outer esophagus after a 60s simulation ablation. The thermal conductivity coefficient is an important parameter and has been shown to vary due to thermal damage [14]. For an improved model, the coefficient of heat conductivity should be updated during ablation process to account for changing materials parameters.

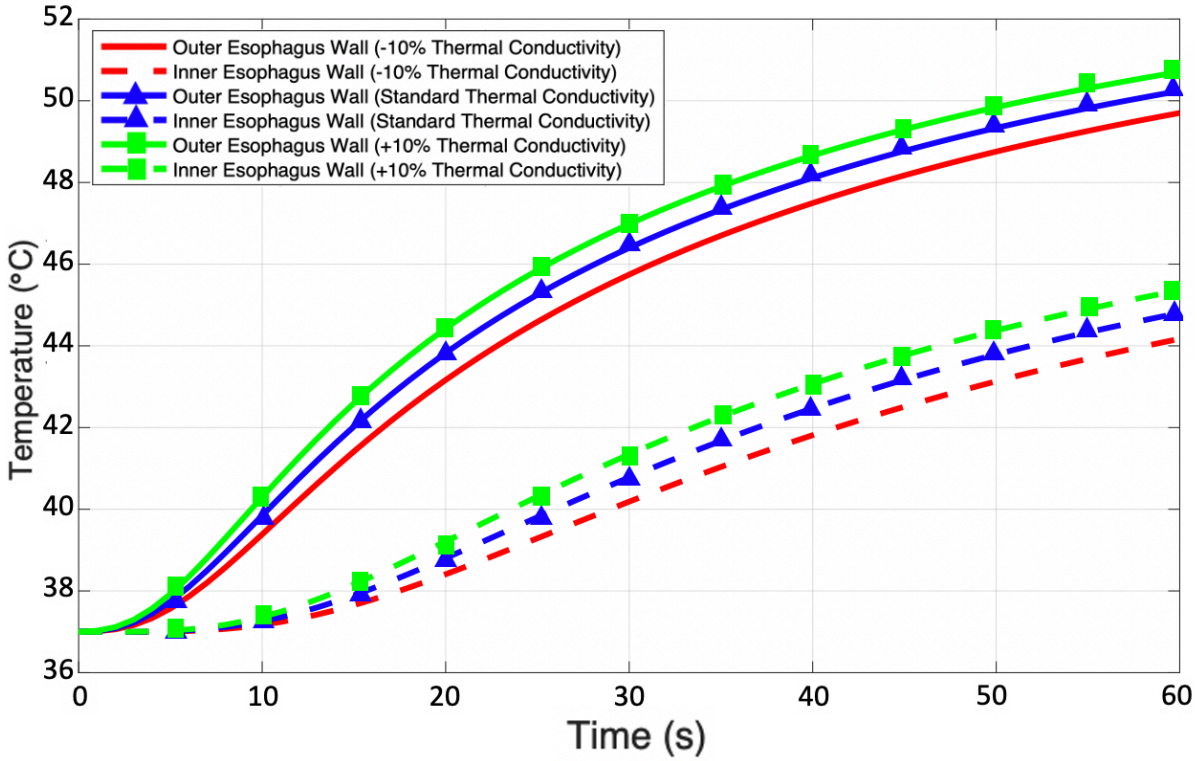

Figure 110: Maximum temperature on the inner and outer esophagus walls as a function of time with varying thermal conductivity parameters (+/- 10%).

6.4.5 Effect of Catheter Heat Source Depth and Ramping of Applied Catheter Temperature

The radiofrequency energy applied by the ablation catheter uses the principle of "Joule heating" [15], as described in the previous chapter. High current density, or the large flow of electrons close to the catheter/tissue interface, heats the tissue through resistive, or a friction-like, heating. The clinician operating the catheter can also slowly increase the current as they monitor the resistance (or impedance) between the radiofrequency ablation catheter and the grounding pad. Instead of catheter/tissue interface temperature remaining constant, the interface temperature has been estimated to ramp up from the initial temperature of 37°C to significantly higher values around 100°C. Prior models have shown "worst case" constant temperatures at or near the surface.

Figure 111 shows the effects of changing the temperature ramp profile of the heat source on the temperature distribution at the outer and inner esophageal walls. Figure 111a plots the three simulated temperature ramp profiles as a function of time. Figure 111b and Figure 111c illustrate the temperature differences between the inner and outer esophagus walls for the different input temperature profiles.

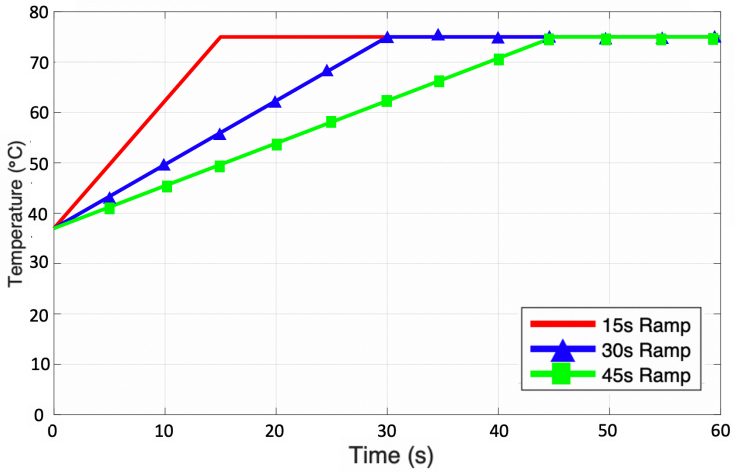

(a)

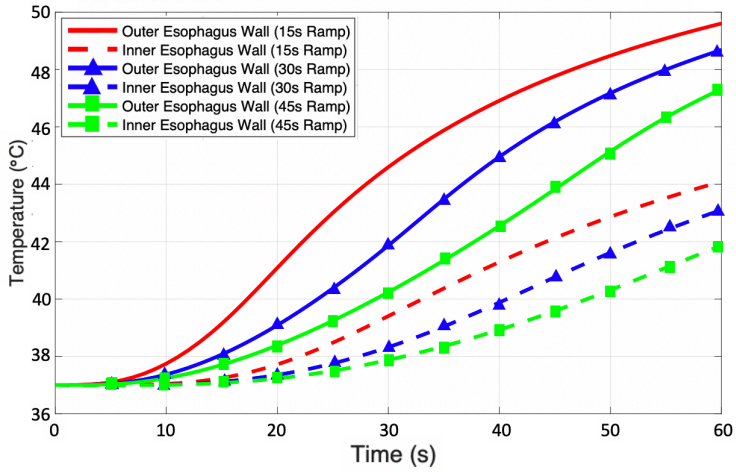

(b)

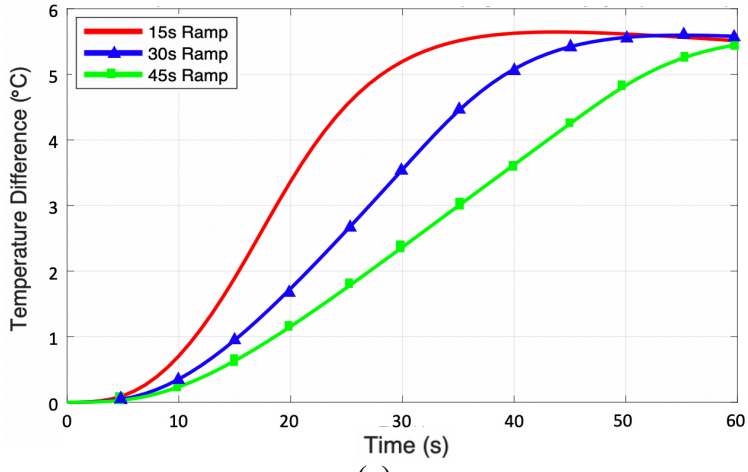

(c)

Figure 111: (a) Varying temperature "ramp" input profiles. (b) Maximum temperature on the inner and outer esophagus walls as a function of time with varying temperature ramp profiles (15s, 30s, 45s ramp profiles) and (c) the absolute difference between maximum temperatures of the inner and outer esophageal walls as a function of time with varying temperature ramp profiles.

The results in Figure 111 indicate that the temperature profile of the ablation catheter has a significant effect on the temperature of the tissue as a function of time. Since the clinician is concerned about the outer esophagus temperature, even though they can measure only the inner esophagus temperature, it is important to predict the different between the outer and inner esophagus temperature. It is desirable to have a small difference so that the clinician has a lower possibility of accidentally burning the esophagus. Figure 111c shows that this difference is smallest for a longer period of time when the ramp-up profile is slowest, e.g., for 45 seconds instead of 15 seconds. Clinicians often aim for a quicker heat rise [2]. However, since there is uncertainty about the position of the esophagus relative to the heart and the ablation heat source, a slower ramp-up profile of the ablation heat source may allow for an earlier detection of a temperature increase reaching the esophagus.

The highest temperature in the tissue can be found a small distance below the heart tissue surface when using a radiofrequency ablation catheter. To simulate this effect, we varied the model's boundary conditions by defining the temperature profile for nodes at a 0.5mm and 1.0mm distance from the inner atrial wall. Figure 112 shows the cross-section temperature distribution when the nodes used to define the heat source are 1.0mm from the inner atrial wall. Tissue thermal damage is illustrated in the figure as temperatures that rise above 50°C.

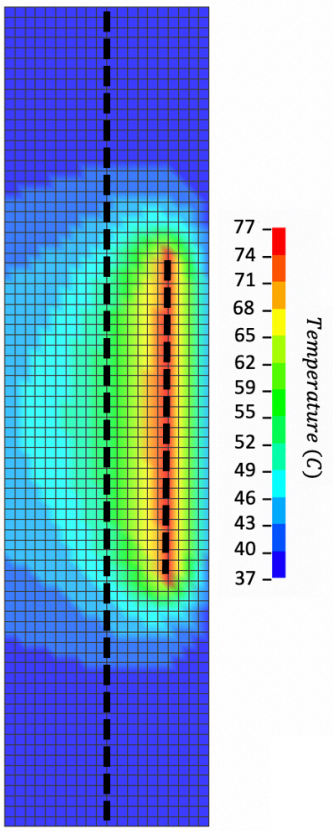

Figure 112: Temperature distribution at cross section illustrating heat source depth of 1.0mm at time = 30s.

Figure 113a shows the maximum temperature of the outer and inner esophagus walls as a function of time when the heat source distance from the inner atrial surface varies from 0.0mm to 0.5mm and 1.0mm, respectively. This distance, or heat source depth, has a significant effect on the difference between the maximum temperature of the inner and outer esophageal walls. As shown in Figure 113b, the maximum temperature difference between the inner and outer esophageal walls is much larger when the heat source depth increases. Since, in a clinical setting, temperature can only be measured on the inner wall of the esophagus, the large difference between the temperatures of the inner and outer esophagus walls is a cause for concern.

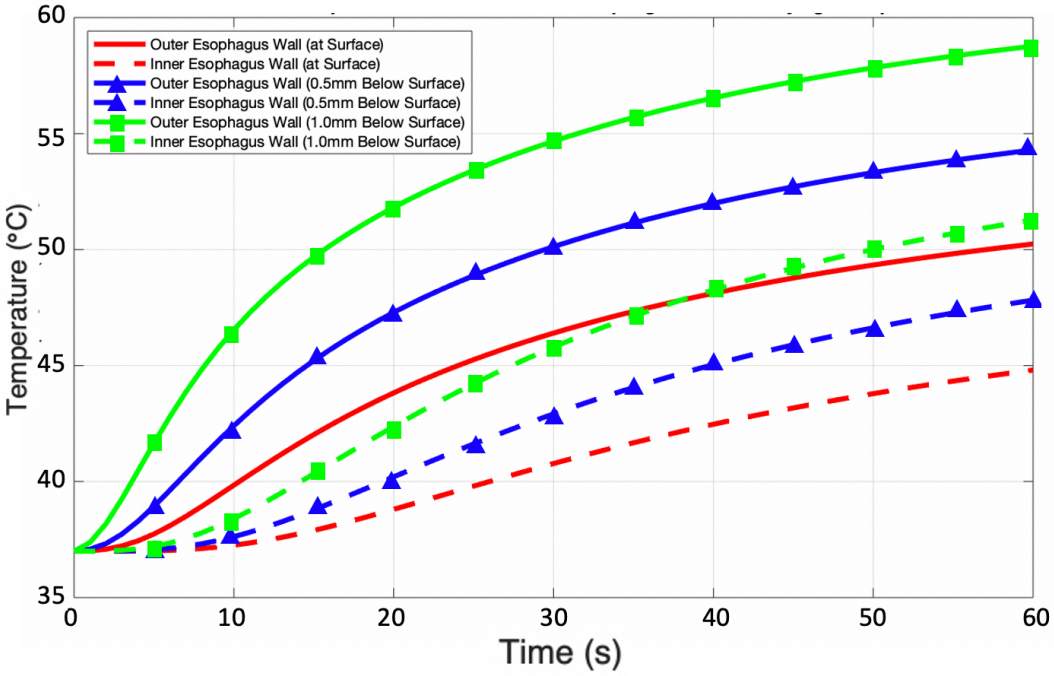

(a)

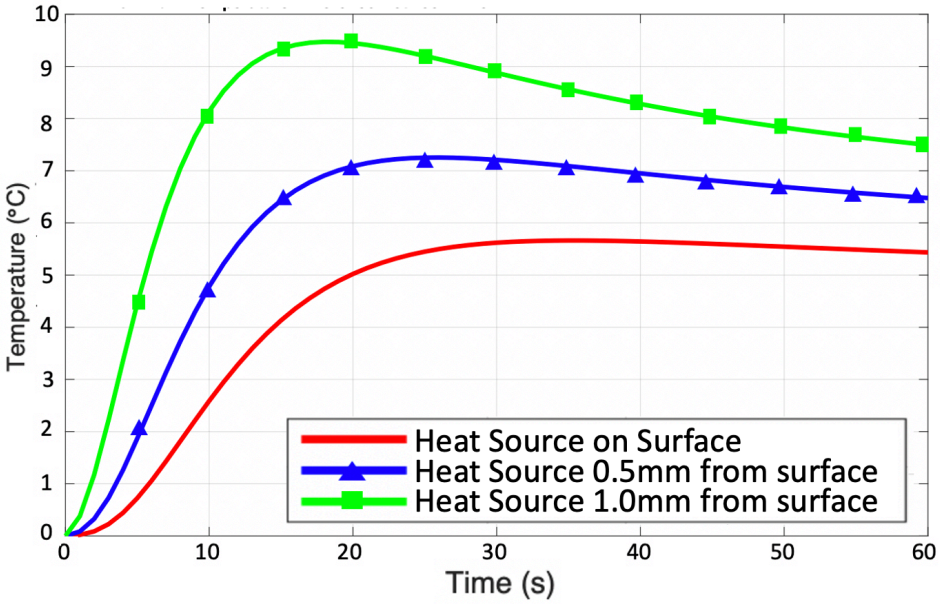

(b)

Figure 113: (a) Maximum temperature on the inner and outer esophagus walls as a function of time with ablation heat source depth d_{hs} (surface, 0.5mm, 1.0mm) and (b) the absolute difference between maximum temperatures of the inner and outer esophageal walls as a function of time with ablation heat source depth d_{hs}.

6.5 Discussion

The spacing of the temperature sensors on the inner esophageal wall is a very important design parameter when developing a temperature sensing EDD. A large temperature difference between the inner and outer esophageal walls is of concern to a medical practitioner. If the temperature sensors do not yet pick up a temperature rise, and the cardiac electrophysiologist continues ablating, it is possible that the outer esophagus can be thermally damaged.

The ability of the sensors to predict esophageal damage will depend on the parameters modeled including the temperature input value and ramp profile. A slower ramping profile can provide enough time for the sensors placed on the inner esophagus to detect a small 1°C rise. The temperature distribution over timer is sensitive to the nature of convection and conduction defined by their respective constants, k and h, in the model. Both constants can be influenced by physiological changes from device interaction. For example, the convection term can change due to blood flow variations on the inner atrial wall caused by the RF catheter, or additionally, the conduction term can change due to tissue properties variations after reaching irreversible thermal damage [14].

It is desirable to have a deflection device that incorporates temperature sensors at optimal locations. This would increase the likelihood of detecting a rise in temperature and, thus, the prediction of formation of thermal lesion.

The numerical and experimental results show a comparable temperature rise and temperature distributions on the inner esophagus wall. The numerical model provides insight into the temperature distribution throughout the tissue, including the outer esophagus wall. This is important information as the medical clinician might only be able to monitor the inner esophagus wall but must also prevent outer esophagus wall thermal damage. Experimental sensors and

numerical nodes closer in proximity to the ablation heat source show smaller delay in detecting a temperature rise. The temperature sensor array attached to the esophageal deflection device must take these observations into account.

6.6 Summary

In this chapter, a numerical study was performed using finite element analysis to complement the experimental evaluation (see Chapter 5) of the 2D temperature sensor array designed for use in cardiac ablation procedures. The aim of this device is to measure the temperature at the inner esophagus to ensure that the entire esophagus (inner and outer) is safe from thermal damage throughout the cardiac ablation procedure. The numerical study provided insight into how heat transfers through the atrial and esophageal tissue. The experimental study was concerned with the temperature measurement at the inner esophageal wall and the inner atrial wall. The finite element model depends significantly on the material models and boundary conditions. It was shown that the sensor spacing is an important design parameter since the sensor location determines whether the device will be capable of detecting a temperature rise on the inner esophageal surface.

Chapter 6, in part are a reprint of the materials as they appear in “Experimental and Numerical Investigation of Heat Transfer through Porcine Heart and Esophageal Tissue” Morris, K., Hu, S., Kohanfars, M., and Talke, F.E., Proceedings for ASME 2021 Conference on Information Storage and Processing Systems. Online Virtual. June 2–3, 2021.

References

[1] Berjano, Enrique J., and Fernando Hornero. "Thermal-electrical modeling for epicardial atrial radiofrequency ablation." IEEE transactions on biomedical engineering 51.8 (2004): 1348-1357.

[2] Berjano, Enrique J., and Fernando Hornero. "What affects esophageal injury during radiofrequency ablation of the left atrium? An engineering study based on finite-element analysis." Physiological measurement 26.5 (2005): 837.

[3] Berjano, Enrique J. "Theoretical modeling for radiofrequency ablation: state-of-the-art and challenges for the future." Biomedical engineering online 5.1 (2006): 1-17.

[4] Berjano, Enrique J., and Fernando Hornero. "A cooled intraesophageal balloon to prevent thermal injury during endocardial surgical radiofrequency ablation of the left atrium: a finite element study." Physics in Medicine & Biology 50.20 (2005): N269.

[5] Pérez, Juan J., Andre D'Avila, Arash Aryana, and Enrique Berjano. "Electrical and thermal effects of esophageal temperature probes on radiofrequency catheter ablation of atrial fibrillation: results from a computational modeling study." Journal of cardiovascular electrophysiology 26, no. 5 (2015): 556-564.

[6] González-Suárez, Ana, Enrique Berjano, Jose M. Guerra, and Luca Gerardo-Giorda. "Computational modeling of open-irrigated electrodes for radiofrequency cardiac ablation including blood motion-saline flow interaction." PloS one 11, no. 3 (2016): e0150356.

[7] LS-DYNA Theory Manual (2020) https://www.lstc.com/download/manuals.

[8] Yue, Kai, Liang Cheng, Lina Yang, Bitao Jin, and Xinxin Zhang. "Thermal Conductivity Measurement of Anisotropic Biological Tissue In Vitro." International Journal of Thermophysics 38, no. 6 (2017): 92.

[9] Fasano, Antonio, Luca Anfuso, Giuseppe Arena, and Claudio Pandozi. "Thermal field in cryoablation procedures for pulmonary veins isolation: importance of esophageal temperature monitoring." Journal of atrial fibrillation 9, no. 6 (2017).

[10] LS-DYNA Manual Vol. II - Material Models (2020) https://www.lstc.com/download/manuals

[11] Tangwongsan, Chanchana, James A. Will, John G. Webster, Kenneth L. Meredith, and David M. Mahvi. "In vivo measurement of swine endocardial convective heat transfer coefficient." IEEE transactions on biomedical engineering 51, no. 8 (2004): 1478-1486.

[12] Vedula, Vijay, Richard George, Laurent Younes, and Rajat Mittal. "Hemodynamics in the left atrium and its effect on ventricular flow patterns." Journal of biomechanical engineering 137, no. 11 (2015).

[13] Yokoyama, Katsuaki, Hiroshi Nakagawa, Dipen C. Shah, Hendrik Lambert, Giovanni Leo, Nicolas Aeby, Atsushi Ikeda et al. "Novel contact force sensor incorporated in irrigated

radiofrequency ablation catheter predicts lesion size and incidence of steam pop and thrombus." Circulation: Arrhythmia and Electrophysiology 1, no. 5 (2008): 354-362.

[14] Pearce, John A. "Models for thermal damage in tissues: processes and applications." Critical Reviews™ in Biomedical Engineering 38.1 (2010).

[15] Kunwar, Anil, Peter Råback, Shengyan Shang, Prafulla Bahadur Malla, Xueguan Song, Yunpeng Wang, and Haitao Ma. "A Computational Model for Simulation of Temperature during Radio-Frequency Ablation of Biological Tissue." In 2018 IEEE International Conference on Computational Electromagnetics (ICCEM), pp. 1-3. IEEE, 2018.

Chapter 7 Summary, Conclusions, and Future Work

7.1 Summary and Conclusions

In this dissertation, a medical problem was described, namely, thermal damage of the esophagus caused by heat transfer during radiofrequency ablation procedures. Cardiac electrophysiologists have tried to find a better way to protect the esophagus during increasingly common ablation procedures. Methods, tools, and equipment were discussed as they relate to the design and prototyping of a medical device. For endoscope-like devices, it is important to have soft flexible materials during the medical device prototyping phase. Material jet, photopolymer 3D printing was employed to produce so-called Esophageal Deflection Devices (EDDs). In order to accurately model such a device, hyperelastic constitutive models were developed for the soft photopolymer material by uniaxial and biaxial testing. The EDD prototype transitioned to a biocompatible material, i.e., ethylene vinyl acetate (EVA), and a final pre-curvature. Then, the moment versus curvature and force versus deflection were mathematically, experimentally, and numerically modelled. The results detailed the relationship between applied forces and cross section, material, and radius of curvature for the pre-curved, thermoformed EVA tubes.

Given the aim of protecting the esophagus during ablation procedures, it is important to measure the temperature on the inner esophagus wall. A thermal monitoring EDD was proposed, incorporating an array of thermistors. A silicone skin prototype was manufactured and tested using

excised porcine esophagus and atrial tissue. Heat was applied to the inner wall and the temperature response was measured. The importance of sensor location and spacing on the EDD was investigated. Furthermore, numerical models were developed and simulated to complement the experimental work. By validating the numerical model with the experiments and varying model input parameters and boundary conditions a better understanding of the heat transfer through the tissue was obtained. Temperatures at both the inner and outer esophageal walls were simulated as a function of time and heat source temperature profile. The effect of heat convection at the inner atrial wall on the tissue temperature was also investigated.

During the design and analysis of the Esophageal Deflection Device, it was revealed that a wide array of technical skills and scientific concepts were necessary, including but not limited to design methods, computer aided design, 3D printing, solid mechanics, material modeling, mathematical analysis, experimental design and analysis, numerical simulation, sensors, and tissue heat transfer. Potentially the most significant part of the design process, which drove much of the design, was the valuable and consistent feedback from the medical community throughout the entirety of the project.

7.2 Future Direction

The medical device industry, despite numerous federal regulations, moves very quickly in order to address a seemingly infinite number of medical challenges. UC San Diego's medical community, comprised of medical doctors, nurses, staff and engineers, has been growing in size and energy to complement that effort. With support from this academic community, our research

team aims to translate this Esophageal Deflection Device to a clinically-used product, along with other similar devices in the Talke Biomedical Device Lab, that meet important medical needs.

Specifically for the Esophageal Deflection Device, we need to translate the device fully, moving it “from benchtop to bedside”, so that we can impact the patient populations here and at other cardiology centers. There is a path for commercialization. Scientifically, the models for pre-curved tube deformation and tissue heat transfer can be expanded for this and other medical devices, as precurved concentric tubes have been increasingly used in surgery and radiofrequency catheter ablation is commonly used minimally invasive treatments, for example, in gastroenterology or pain medicine. Medical problems often arise that require a strong understanding of solid mechanics and heat transfer. It is important that engineers and clinicians work together to solve these problems. Additionally, the reliability of these new devices must be investigated.

The tissue heat transfer experiments proved valuable for evaluating our thermal monitoring Esophageal Deflection Device design, but the experiments used a temperature-controlled heat source enabled through conduction. It would be important to compare this experimental heat source device against radiofrequency ablation catheters, as well as cryoablation balloons and electroporation devices. Electroporation, or pulsed frequency ablation, is a novel approach to performing atrial ablations, relying on high current and shorter pulses to ablate the tissue. This technology may limit the need for an Esophageal Deflection Device, yet it is still important to understand how heat transfer and the location of the esophagus can affect temperature rises on the surface and the temperature profile within the tissue. It would be helpful to compare these techniques more directly using experimental setups like the ones shown in chapters 4 and 5 of this dissertation.

Our research team, the Talke Biomedical Device Lab, has learned a great deal in terms of medical device design, working on ophthalmic instrumentation, 3D printed endoscope caps, biofilm resistant urinary catheters, ergonomic measurement devices, detachable bronchoscopes, cervical expanders and other medical devices. The best and most important part is working cooperatively with the wonderful and brilliant medical doctors at UC San Diego. Our future direction will certainly be working alongside them.